Slab photonic crystal demultiplexers: analysis and design

by

Aref Bakhtazad ©

A thesis submitted in partial fulfillment of the requirements for the degree of

Doctor of Philosophy

Electrical and Computer Engineering Department

McGill University, Montreal, Canada

Your file Votre référence
ISBN: 978-0-494-32143-0
Our file Notre référence
ISBN: 978-0-494-32143-0

Abstract

The exploitation of the superprism phenomenon for optical demultiplexing using a slab photonic crystal on the silicon on insulator platform is the main subject of this thesis. The **S**-vector and **k**-vector superprisms are considered. Design equations for the **S**-vector superprism demultiplexer which fully take into account the nonlinear spectral dependence of beam propagation and dispersion are introduced. This allows wide-band coarse wavelength division multiplexing (CWDM) demultiplexers to be designed. Selecting minimum prism area as a metric, the best photonic crystal lattice, design parameters and prism geometry is sought. A full 3-D modeling approach using the plane wave expansion method is employed to ensure the practicality of the design. We show that the slab 1-D photonic crystal can provide the smallest superprism. Based on our result, an area of 1367 μm^2 is sufficient to resolve 4 standard CWDM channels (20nm channel spacing). We extend this approach by proposing a stratified photonic crystal which has 5 times less area for an 8 channel CWDM design.

We then propose the first fully integrated **k**-vector superprism layout. Design rules and equations are presented and we use these to obtain the design parameters that result in a minimum prism area. We show that an optimized 1-D photonic crystal **k**-vector superprism with the area of less than 0.1 mm^2 is sufficient to resolve 32 standard dense wavelength division multiplexing (DWDM) channels (100GHz channel spacing). The resulting chip size is approximately 4.5 times less than an equivalent etched grating demultiplexer.

We also demonstrate that fast lenses can be made using slab 1-D photonic crystal with angular periodicity.

We introduce an analytical approximation technique for slab 1-D photonic crystals based on the weighted index method. The variational nature of the method leads to acceptable results for moderate refractive index contrast materials. The method can also be extended to 2-D cases and to nonlinear systems.

The plane wave expansion (PWE) method and field matching have been combined to obtain a new method which is capable of obtaining all types of modes including the leaky modes of slab 1-D photonic crystals. The method requires fewer plane waves than the conventional PWE method but provides a better approximation. We compare our results with an accurate finite element method as a benchmark.

A report of our first attempt for the fabrication, post-possessing and optical characterization of the proposed **k**-vector superprism demultiplexer is also presented. We recommend the development of a cladding, and more accurate fabrication procedures for future investigations.

Sommaire

Le sujet principal de cette thèse est l'exploitation du phénomène de "super prisme" pour le démultiplexage optique à l'intérieur de cristaux photoniques planaires fabriqués à l'aide d'une technologie de silicone sur diélectrique. Deux approches sont considérées: la méthode du vecteur ***S*** et celle du vecteur **k**. Des équations pour la conception de supers prismes basés sur le vecteur ***S*** qui prennent en considération les effets spectraux non linéaires de la propagation des faisceaux et de la dispersion sont présentées. Celles-ci permettent la création de démultiplexeurs à large bande avec une séparation grossière des longueurs d'onde. La disposition des cristaux photoniques, la géométrie du prisme ainsi que d'autres paramètres de conception sont investigués afin de minimiser la surface du prisme. Un modèle tridimensionnel basé sur le développement des ondes planes est employé afin d'assurer la fonctionnalité du concept. Nous démontrons que les cristaux photoniques unidimensionnels forment les plus petits supers prismes. Selon nos résultats, une surface de 1367 μm^2 est suffisante pour résoudre quatre canaux séparés par 20 nm. Cette approche est extrapolée en proposant un cristal photonique stratifié dont la surface est cinq fois moins grande et qui peut résoudre huit canaux.

Ensuite, le premier super prisme complètement intégré basé sur l'approche du vecteur **k** est présenté. Les équations et les principes de conception sont introduits et utilisés pour minimiser l'aire du prisme. Il est démontré qu'un cristal photonique unidimensionnel avec une surface de moins de 0.1 mm^2 est suffisant pour résoudre 32 canaux espacés par 100 GHz. Ce circuit est environ 4,5 fois plus petit qu'un démultiplexeur à réseau intégré.

Il est aussi démontré que des lentilles rapides peuvent être fabriquées avec des cristaux photoniques unidimensionnels à périodicité angulaire.

Une technique d'approximation analytique pour les cristaux photoniques à une dimension basée sur la méthode des indexes pondérés est présentée. La nature de cette technique permet d'obtenir des résultats acceptables pour des contrastes d'index réfractif modérés. De plus, elle peut être étendue aux situations bidimensionnelles et aux systèmes non linéaires.

La méthode de développement des ondes planes et celle d'adaptation des champs furent combinées afin d'obtenir une nouvelle technique capable de résoudre tous les types de modes, incluant les modes de fuite, à l'intérieur des cristaux photoniques unidimensionnels. Cette technique requiert moins d'ondes planes que le développement traditionnel mais donne de meilleures approximations. Une méthode d'éléments finis est utilisée comme référence pour évaluer les résultats obtenus avec la nouvelle technique.

Les résultats de la fabrication, du post-traitement ainsi que de la caractérisation optique du super prisme basé sur le principe du vecteur **k** sont aussi présentés. Le développement d'une gaine et de meilleurs procédés de fabrication sont recommandés pour les travaux futurs.

Acknowledgements

I wish to acknowledge Prof. Andew Kirk for his support and supervision during the course of my study; also I want to thank Prof. Mark Andrews for his support during the first years of my study.

Thanks are due to François Marquis CEO & Founder of "Design Workshop Technologies" whose permission to acssess to the mask layout designer "DW2000" was particulary helpful. I also wish to thank Prof. Vincent Aimez for his kind help and his premission to use the faciities of Sherbrooke University. Thanks also to Dr. Po Dong and Dr. Aju Jugessuru for their help in the post-processing and characterization of the samples.

In the prepartaion of the thesis, I am grateful again to my supervisor for his time and his efforts. The efforts of my brother, Amid who reviewd the text is well acknowledged. I also appreciate Michaël Ménard for the French summary.

Finaly I am greatful to my wife, Mahshid for her kind paitience and support during the last year.

Table of Contents

List of Figures

List of Tables

List of Acronyms

1-D	One Dimension
2-D	Two Dimension
3-D	Three Dimension
6-D	Six Dimension
AWG	Array Waveguide Grating
CMOS	Complementary Metal Oxide Semiconductor
CWDM	Course Wavelength Division Multiplexing
DWDM	Dense Wavelength Division Multiplexing
FDTD	Finite Difference Time Domian
FFT	Fast Forier Transform
PLC	Plannar Lightwave Circuts
PWE	Plane Wave Expansion
SOI	Silicon On Insulator
TE	Transverse Electric
TM	Transverse Magnetic
PML	Prefectly Matched Layer

ITU	International Telecommunication Union
RCWA	Rigorous Coupled Wave Analysis
GRIN	Gradient Index
NRC	National Research of Canada
RIE	Reactice Ion Eatching
PECVD	Plasma Enhanced Convention Vapor Deposition
PMMA	PolyMethyl MethAcrylate
ESM	Electron Scanning Microscope
IR	InfraRed
DUT	Device Under Test
FEM	Finite Element Method
EPWE	Extended Plane Wave Expansion
SMP	Symmetric Multi-Processors

Chapter 1

INTRODUCTION

We explain the potential of the photonic crystal superprism for demultiplexing and compare it with other alternatives. Our proposed designs for both k-vector and S-vector superprisms are introduced. The original contributions of the thesis are outlined together with a description of its layout.

1.1 Introduction

During the last two decades, photonic crystals have been a focus of research interest because of their ability to control the flow of light on a very small length scale. Although the first motivation behind photonic crystals was to prohibit light from propagation (using 3-D photonic crystals where there is a full bandgap and wavelengths inside the bandgap [1]), the dispersive, anisotropic wave propagation inside photonic crystal at wavelengths below the bandedge has attracted significant attention too [2;3]. Wave propagation through a perfect uniform photonic crystal involves Bloch modes. Near the bandedge they are very dispersive, highly anisotropic, and also highly polarization dependent. This highly anomalous dispersion behavior of the Bloch modes leads to the extraordinary angular sensitivity which has been called the superprism phenomena [2]. The observation of 500 times more dispersion whilst impressive, was an indication of the emerging of new class of demultiplexers [2]. However, a 3-D photonic crystal is hard to make and it is not suitable for integrated optics. The planar counterpart is a promising choice owning to the fact that its fabrication resembles microelectronic pattering techniques. The compatibility with CMOS technology also makes the silicon on insulator (SOI) platform a suitable candidate. The slab photonic crystal is an optically thin dielectric slab perforated with a 2-D lattice of holes (or in the 1-D case, trenches). Light confinement within the slab is due to the refractive index contrast of the slab with substrate, and cladding. The observed dispersion in planar photonic crystal is 50 times more than in ordinary glasses [4]. This thesis is an exploration of the superprism phenomenon focusing on planar photonic crystals in the SOI platform for demultiplexing.

There are two types of dispersion with two distinct origins in photonic crystals. The one originating from group velocity is based on the sensitivity of the direction of the Bloch modes with wavelength (usually near the band edge) [5]. The **k**-vector superprism on the other hand is based on the angular dispersion of the light at the free space/photonic crystal interfaces [6-8].

1.2 S-vector superprism

Figure 1.2.1 shows the schematic of a PLC based **S**-vector superprism.

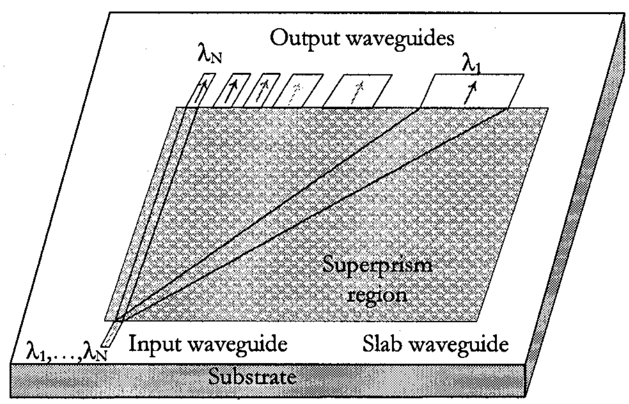

Figure 1.2.1 The schematic of PLC based **S**-vector superprism

The incident beam, after decomposing into highly localized Bloch modes, propagates through photonic crystal (but it looses its spatial coherence soon as it propagates through the photonic crystal). As the Bloch modes reach the opposite border of the photonic crystal, they loose some power and couple back to the free space wave and no further spatial separation occurs. Loss of spatial coherence and lack of dispersion effect outside photonic crystal makes a superprism based on group velocity dispersion (also known as **S**-vector superprism) too large for resolving DWDM wavelengths. For the CWDM applications (20nm channel spacing), the first order analysis estimation shows that the superprism area is comparable to the other alternatives (in this case PLC based Array Waveguide Grating, AWG) [8]. Figure 1.2.2 depicts the AWG layout on a high index contrast system of material [9]. Considering low diffraction orders and the difficulty of implementing small path differences in the waveguide array region, a typical device area (excluding input and output waveguides) is about 0.8 mm^2[9].

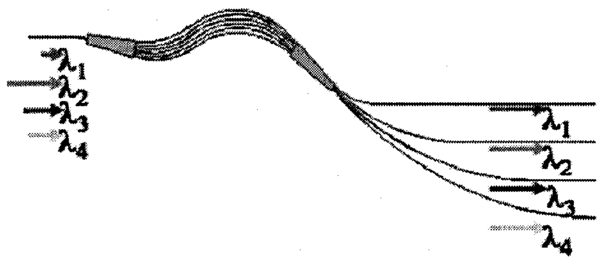

Figure 1.2.2 High refractive index contrast AWG for CWDM applications [9].

Through detail analysis of the wave dynamics in a photonic crystal, in chapter 6 we show that a 1-D photonic crystal 4-Channel CWDM demultiplexer can be optimized to provide the smallest photonic crystal size with the area of 1367 μm^2 (which is about 500 fold size reduction compared to the AWG alternative). 3-D modeling of the structure and inclusion of all non-linearities and practical micro-fabrication constraints ensure that the designs are realistic. Our analysis demonstrates that the other 2-D photonic crystals (in this case square and hexagonal lattices) prism areas are more than 10 times larger than the 1-D counterpart.

By folding and separating the propagation paths of different channels, we then propose the stratified photonic crystal to reduce the superprism area even further. A wider band CWDM demultiplexer (e.g. 8-channel) with reduced superprism area can be implemented in this way. This will be presented in chapter 7 where an 8-channel CWDM demultiplexer is designed with five-fold reduction in prism area. The prism area of 0.26 mm^2 is achieved with a square lattice. Our detailed analysis in chapter 6 and especially our novel proposal for stratification in chapter 7 show the potential capability of the **S**-vector superprism for wider band demultiplexing.

1.3 k-vector superprism

The **k**-vector superprism effect is a more recent approach and we are pioneers in its devolvement. The **k**-vector superprism uses the phase velocity dispersion of photonic crystals and is based on the angular dispersion of the refracted beam from a prism shaped photonic crystal area. The **k**-vector superprism has an advantage over the previous **S**-vector approach in that the beam separation can continue outside the photonic crystal region. In this way it is much closer to a conventional bulk dispersive prism and implies the possibility of using beam expanding and focusing optics with a small prism area. Figure 1.3.1 shows a schematic of our proposed device. In this example beam collimation and focusing is accomplished with etched mirrors.

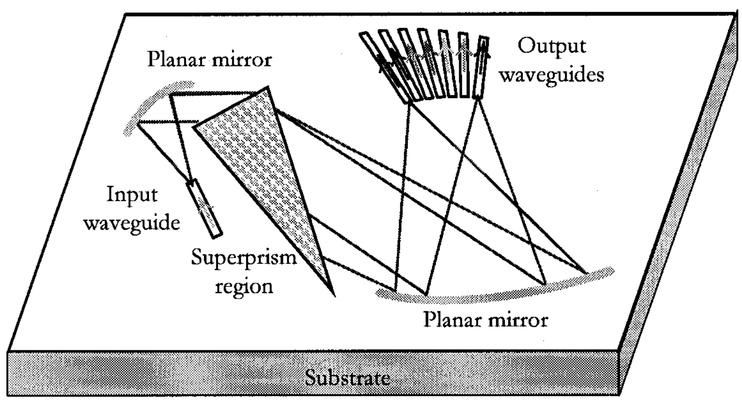

Figure 1.3.1 The schematic of a **k**-vector superprism

The application of the **k**-vector superprism phenomena which is described here will drastically reduce the sizes of DWDM demultiplexers. Several kinds of DWDM filters, such as PLC-based arrayed waveguide gratings (AWG's) [10;11] and etched grating demultiplexers (echelle grating) [12;13] have already been developed. Figure 1.3.2 shows a typical layout of AWG and Echelle grating for the high refractive index contrast material. For the AWG choice, the die size for a typical 32 DWDM channel demultiplexer (of 100GHz, ~0.8 nm channel spacing at the C band) using an SOI wafer with 0.5 μm top silicon layer is about $3\times 2.5 = 7.5\text{mm}^2$ (excluding the input/output waveguides sections). The grating order is 61, and TM polarization has been assumed. The AWG suffers from ghost beams due to the higher order diffraction images. For many applications, (AWG) devices face fundamental limits due to the physical size and extreme fabrication tolerances required to achieve higher channel counts and narrower channel spacing. Echelle gratings on the other hand by folding the input and output path and using the reflective grating, reduces the demultiplexer size considerably. The device size for implementation of a similar design using an echelle grating (excluding the input/output waveguide parts) is about $3 \times 1.5 = 4.5\,\mathrm{mm}^2$. The ghost image similar to the AWG case exists.

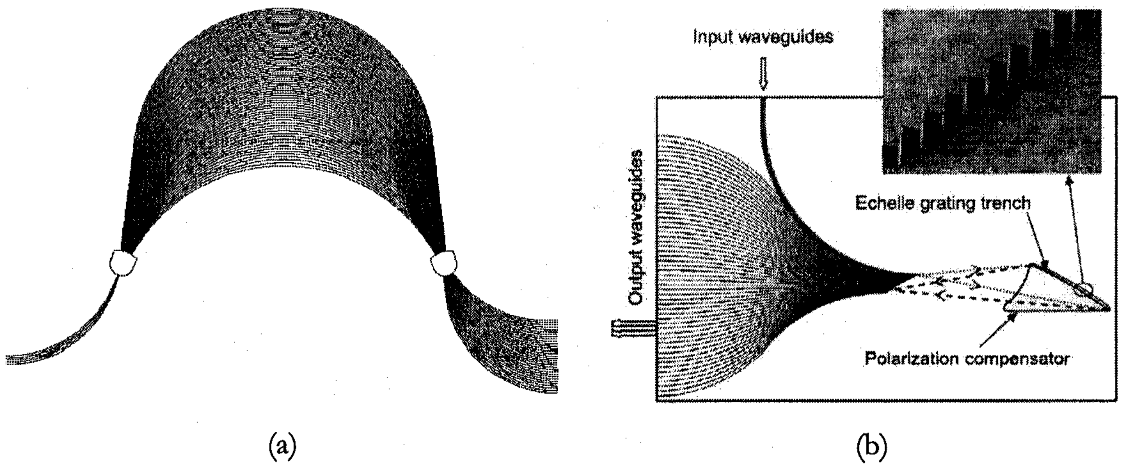

Figure 1.3.2 the layout of (a) a typical AWG for 32 DWDM channel, and (b) a typical echelle grating for 48 DWDM channel [13].

For the first time, this thesis presents a complete analysis, design, fabrication and of the **k**-vector superprism demultiplexer.

Detail design rules and optimization for **k**-vector superprism are presented in Chapter 8. The factors underlying the geometry, photonic crystal type and design parameters are also discussed. Compared with the 2-D photonic crystal of interest (in this case, 2-D square and 2-D hexagonal lattice), we have shown that the best photonic crystal that provides the smallest **k**-vector superprism is a 1-D photonic crystal. We have shown that an optimized 1-D photonic crystal superprism area of about $0.1\,\mathrm{mm}^2$ is enough to resolve 32 DWDM standard channels. Including two focusing elements (but again excluding the input/output regions) the device size would not be greater than $1\,\mathrm{mm}^2$. Compared to the nearest rival (echelle grating), it provides 4.5 times area reduction.

Also in this thesis, we proposed and design of a new class of 1-D photonic crystal lenses. As we will show in chapter 9, a fast lens with 130 μm focal length, and $f/\# = 1.3$ is achievable on SOI technology with 100 nm feature size. The etching area is only 658 μm^2.

The parametric mask design and implementation was another achievement, which is explained in chapter 10. Figure 1.3.3 shows a typical layout for 5x16 DWDM **k**-vector demultiplexer. An optical characterization bench has been designed and constructed for measurement of transmission spectra of **k**-vector demultiplexer. Ten different 16-channel DWDM demultiplexers have been designed, and sent for fabrication. The fabricated wafers were post-processed and tested. Unfortunately, the unsatisfactory fabrication quality prevented us from obtaining any meaningful results. The details of the characterization bench and our post-processing procedure together with some analysis of the fabricated samples and finally some recommendations for the next step of the project are presented in chapter 11.

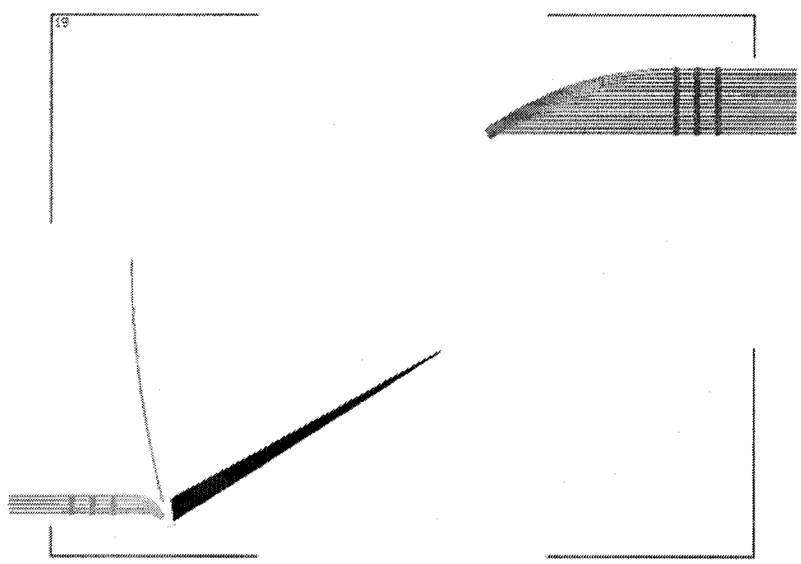

Figure 1.3.3 A typical mask layout for 5x16 **k**-vector superprism

1.4 Analysis and Modeling techniques

We devote the entire chapter 3 to the theory of 1-D photonic crystal. The availability of closed form equations for the wave vector diagram of the 1-D photonic crystal enables us to explain the very basic phenomenon behind **k**- and **S**-vector superprisms more easily.

In chapter 4, we develop an approximate analytical tool for slab 1-D photonic crystals. The well known weighted index method from conventional rectangular waveguide theory is adopted and modified for slab 1-D photonic crystals. It is basically a new variational technique suitable for rectangular type photonic crystals (such as slab 1-D, 2-D rectangular, 2-D rectangular slab and 3-D rectangular parallelepiped with similar atom type photonic crystals). The accuracy of the method (compared with the accurate finite element method) was satisfactory for the medium refractive index contrast material and it is acceptable for high contrast materials. The speed of the method and the low programming effort are the main advantage of such a method. The potential for tuning of **k**-vector superprism with optical power is also investigated using the method developed in this chapter.

3-D modeling of transmission through and reflection from the bulk slab photonic crystal is an open problem. Inclusion of many out of plane radiation modes into the calculation makes the modeling more cumbersome than the 2-D case with no radiation modes. Alternatively, one can find many leaky modes, and carry out mode matching at the interfaces. In order to do that, we need a method to obtain a spectrum of the modes at the desired wavelength. The conventional plane wave expansion method, with supercell definition is incapable of doing this. We have modified the method to be able to find the spectrum of modes. The accuracy of the method compared to an accurate finite elements method is excellent. The method and some results are explained in chapter 5.

Finally we present our comments regarding the future works in the chapter 12 and the benchmark finite element method is outlined in Appendix A.

References

[1] E . Yablonovitch, "Inhibited Spontaneous Emission in Solid-State Physics and Electronics," *Physical Review Letters*, vol. 58, no. 20, pp. 2059-2062, May1987.

[2] H . Kosaka, T. Kawashima, A. Tomita, M. Notomi, T. Tamamura, T. Sato, and S. Kawakami, "Superprism phenomena in photonic crystals," *Physical Review B*, vol. 58, no. 16, pp. 10096-10099, Oct.1998.

[3] H . Kosaka, T. Kawashima, A. Tomita, M. Notomi, T. Tamamura, T. Sato, and S. Kawakami, "Self-collimating phenomena in photonic crystals," *Applied Physics Letters*, vol. 74, no. 9, pp. 1212-1214, Mar.1999.

[4] T . F. Krauss, R. M. Delarue, and S. Brand, "Two-dimensional photonic-bandgap structures operating at near infrared wavelengths," *Nature*, vol. 383, no. 6602, pp. 699-702, Oct.1996.

[5] L . J. Wu, M. Mazilu, T. Karle, and T. F. Krauss, "Superprism phenomena in planar photonic crystals," *Ieee Journal of Quantum Electronics*, vol. 38, no. 7, pp. 915-918, July2002.

[6] A . Bakhtazad and A. G. Kirk, "Superprism effect with planar 1-D photonic crystal," *Proceedings of the SPIE*, vol. 5360, pp. 364-372, June2004.

[7] C . Y. Luo, M. Soljacic, and J. D. Joannopoulos, "Superprism effect based on phase velocities," *Optics Letters*, vol. 29, no. 7, pp. 745-747, Apr.2004.

[8] T . Matsumoto and T. Baba, "Photonic crystal **k**-vector superprism," *Journal of Lightwave Technology*, vol. 22, no. 3, pp. 917-922, Mar.2004.

[9] N . Yurt, K. Rausch, A. R. Kost, and N. Peyghambarian, "Design and fabrication of a broadband polarization and temperature insensitive arrayed waveguide grating on InP," *Optics Express*, vol. 13, no. 14, pp. 5535-5541, July2005.

[10] W . N. Ye, D.-X. Xu, S. Janz, P. Cheben, A. Delage, M. J. Picard, B. Lamontagne, and N. G. Tarr, "Stress-induced birefringence in silicon-on-insulator (SOI) waveguides," *Proc. SPIE*, vol. 5357, pp. 57-66, 2004.

[11] C . Dragone, "Efficient N X N Star Couplers Using Fourier Optics," *Journal of Lightwave Technology*, vol. 7, no. 3, pp. 479-489, Mar.1989.

[12] P . C. Clemens, G. Heise, R. Marz, H. Michel, A. Reichelt, and H. W. Schneider, "8-Channel Optical Demultiplexer Realized As Sio2/Si Flat-Field Spectrograph," *Ieee Photonics Technology Letters*, vol. 6, no. 9, pp. 1109-1111, Sept.1994.

[13] S . Janz, A. Balakrishnan, S. Charbonneau, P. Cheben, M. Cloutier, A. Delage, K. Dossou, L. Erickson, M. Gao, P. A. Krug, B. Lamontagne, M. Packirisamy, M. Pearson, and D. X. Xu, "Planar waveguide echelle gratings in silica-on-silicon," *Ieee Photonics Technology Letters*, vol. 16, no. 2, pp. 503-505, Feb.2004.

Chapter 2

LITERATURE REVIEW

In this chapter, we review the existing research materials on the modal analysis of photonic crystals. Those methods capable of obtaining wave vector diagrams for slab photonic crystals are on our focus. The methods for obtaining transmission and reflection coefficients have been discussed too. Previous researches on mode matching techniques (plane wave to Bloch mode) are surveyed. Restricting ourselves to the high refractive index contrast materials, the superprism history (both S-vector and k-vector) is presented. The waveguide focusing elements which are an important part of the k-vector superprism are reviewed too.

2.1 Modal analysis

Due to complexity of 3-D simulations, the first approach to solve the problem was to replace the slab photonic crystal layer by an equivalent one. Finding this equivalence has been done by simply ignoring the field confinement normal to the plane of photonic crystal layer, and solving the problem in two dimensions (treating the layer as a bulk). Whilst these methods are capable of providing physical understanding of the light propagation in photonic crystals, they are insufficient for the design of a realistic device (as we will discuss them briefly in section 6.6). Replacing the slab photonic crystal layer by an equivalent homogenous layer, one can consider field confinement in the vertical direction by solving Maxwell's equation in the slab waveguide. An equivalent layer can be obtained using homogenization methods, solving dispersion equation, which has been obtained analytically, or by discretizing the 2-D media and applying numerical methods directly, and so on.

methods belong to the analytical category, whilst plane wave expansion, finite difference time domain, spectral methods and transfer matrix methods are basically numerical techniques.

Effective medium theories are methods that seek to replace the slab photonic crystal with a homogenous anisotropic layer. In this way they reduce a complicated 2-D structure to 1-D modeling. This definition is very broad and many theories are beyond this idea, (e.g., homogenization theories are the well known one). We have used this idea successfully to reduce the reflection from bulk photonic crystal (Chapter 10 is devoted to this idea).

Effective index methods seeks to reduce a 3-D modeling problem to an equivalent 2-D one. The main theme of these methods is the assumption that separable field can be a good approximation to the reality. They are more suitable for low contrast slab photonic crystals. The spectrum of these methods starts with simply replacing the photonic crystal layer material by an equivalent one and solving 2-D photonic crystals, to one enhanced by variational methods which try to find the best separable solutions.

The plane wave expansion method is the outcome of the mature solid state theory. It is well suited to periodic structures with continuous potential (as we have in atoms in crystals). Implementation of Finite Difference Time Domain (FDTD) technique is more recent. Based on the time domain simulation, it is not necessary to save data on all mesh points during the simulation. This fact reduces the necessary computer storage dramatically. On the other hand, the existence of the Fast Fourier Transform (FFT) based technique makes the computational gap between time and frequency domains narrow. On the other hand, spectral domain techniques are also well known for their accuracies. They use the symmetry of the structure, which needs to be implemented only on a unit cell. This feature make them attractive, however their implementation with a computer program is more complicated.

2.1.1 *Analytical techniques*

There are two approximate analytical techniques in the literature for our cases. The first method is the effective medium theory that belongs to a more general family of approximations known as homogenization theories (which has wide applications on other branch of engineering). The second method is the effective index methods that have a good reputation in integrated optics as an easy and accurate enough for many applications. We will discuss both of them in the following sections.

2.1.1.1 *Homogenization techniques*

The aim of homogenization theory (effective medium theory) is to establish the macroscopic behavior of a system, which is microscopically heterogeneous, in order to describe some characteristics of the heterogeneous medium (for instance refractive index). This means that the heterogeneous material is replaced by a homogenous fictitious one (the 'homogenized' material), whose global (or overall) characteristics are as equivalent as the initial one. Homogenization theory or effective medium theory exploits this dual scale by introducing a small parameter χ that is defined by the ratio of two characteristic lengths associated with the two scales. When χ tends to zero (long wavelength or quasi-static limit), the properties of the material and of its homogenized version are identical. From the mathematical point of view, this signifies mainly that the solutions of a boundary value problem, depending on a small parameter χ, eventually converge to the solution of a limit boundary value problem, which is explicitly described.

Initially, various effective medium approaches like the Maxwell-Garnett approximation (basically a Clausius-Mosotti relation) were used [1], however later it was realized that there were inadequate and that the micro-geometry of the medium needs to be taken into account even though it is on a much smaller scale than the probing wavelength [2]. In this method, the z-dependence of the wave amplitude is given by

$$\exp\left(i\eta^{\frac{1}{2}}kz\right) \tag{2.1}$$

The constant η is read as the square of the effective index for the periodic structures in the z direction and the given polarization. Then the periodic wave with the z-Dependence of Eq. (2.1), is used to satisfy the Maxwell's equations inside the periodic structure. Obviously such a solution is not correct, but it can be shown that at least for small period-to-wavelength ratios, it is possible to find a particular η value such that Maxwell's equations are satisfied. It is convenient to expand η in a power series of $\chi = \alpha^{-1} = \lambda_0/\Lambda$ (where Λ is the period of the grating in *x* or *z* directions and λ_0 is the wavelength in vacuum):

$$\eta = \eta_0 + \eta_1\alpha^{-1} + \eta_2\alpha^{-2} + \cdots \tag{2.2}$$

where η_0 is the square of the zero-th order (quasi-static or long wavelength limit) effective index and $\eta_i, i = 1, 2, \cdots$ is the *i*-th order coefficient of the series expansion.

Due to existence of the closed form equations for 1-D photonic crystals (as we have derived them in chapter 3), the effective medium theories that are developed for 1-D cases have limited advantages. Limited research has been carried out in the area of 2-D photonic crystals. The authors of [3] have derived upper and lower bounds for the zero-th order effective index of 2-D periodic structures only. Since these bounds are generally quite narrow when the two media have similar optical indices, their average represents a good approximation of the zero-th order effective index. The approximation is valid when the grating vector is normal to the direction of propagation [4].

For shallow grating, we cannot use the effective indices derived for the bulk. In our case, the depth of the slab photonic crystal layer must not be excessive in order to avoid the second order modes from propagating. Additionally, we are not interested in deep gratings that make the aspect ratio of the etching process unrealistic. For 1-D photonic crystal cases, by analytically solving Maxwell's equation in the small depth limit, it has been shown that effective refractive indices are strongly dependent on the grating depth. Moreover, the effective properties are shown to depend not only on the grating structure but also on the refractive indices of the surrounding media [5]. Considering these limitations, there has not been much benefit from this method and its simplicity in our analysis.

2.1.1.2 *Effective index and Weighted index methods*

Effective index methods are approximate, easy and common techniques for the first order modeling that reduces the 3-D modeling effectively into two 2-D models. In its simplest form it is based on the assumption that separable wave solution in the Cartesian coordinates is a good approximation and that the field is confined mainly in the high refractive index medium.

The weighted index method [6] belongs to the effective index methods family and is another simple method. It is based on the same assumption as the effective index method, but the accuracy of the method is enhanced by a variational formula. We have applied weighted index method to slab photonic crystals in Chapter 4.

2.1.2 *Numerical approximations*

There are three categories of numerical methods in the literature, which are capable of solving our problem. The plane wave expansion method, which comes from solid state theory, numerical techniques based on the time domain (mainly finite difference time domain method) and finally numerical techniques based on spectral domain, (finite element methods and the transfer matrix method are good examples of such a family). In the following we discuss each of them and try to explain its pros and cons briefly.

2.1.2.1 *Plane wave expansion method (Floquet-Bloch formalism)*

This is one of the standard methods in electronic band structure problems [7]. It is based on the Fourier series expansion of permittivity $\varepsilon(\mathbf{r})$ and expressing wave functions as Bloch theorem indicates. Substituting into Helmholtz equation and using the orthogonality of Floquet-Bloch modes leads to a system of homogenous linear equations. For a solution to exist the determinant of the linear system should be zero. The propagation constant can be found by truncating the linear system and find the solution of the resulting nonlinear equation of determinant equal zero [8].

The Floquet-Bloch approach was first applied to 1-D photonic crystals [9]. It is shown that by tracing the paths taken by the various components of group velocity, one can reach a detailed understanding of the field structure in all regions of the field [10]. Indeed, since it defines the main constant ray-direction of a Floquet-Bloch mode, the group velocity leads us to the conclusion that the Floquet-Bloch modes play the same role in a periodic medium as the plane waves in an isotropic medium. They may be reflected, refracted, focused, scattered, independently excited, will interfere with one another, and groups of them can be united to form finite beams. As a matter of fact, the propagation of light inside any dielectric grating can be qualitatively understood through the excitation, interference, refraction, and reflection (at discontinuities or boundaries) of the Floquet-Bloch modes. We have used this idea extensively through the next chapters. In addition (and in sharp contrast to the coupled waves), there exists an elegant and satisfying means of summarizing the characteristics of the Floquet-Bloch modes called the wave vector diagram[11;12]. In the reciprocal space, this diagram shows all the wave vectors permitted (at a fixed optical wavelength) in the periodic medium. This diagram has similarity to the dispersion surfaces in the dynamical theory of x-ray diffraction [13], and provides an elegant summary of the properties of Floquet-Bloch modes. We have used it in a normalized form in this thesis, resembling the index ellipsoid.

The plane wave expansion method is clearly an attractive method because of its simplicity and applicability, at least in principal to any type of $\varepsilon(\mathbf{r})$. In the case of our interest (slab photonic crystal, which the permittivity is constant in each section), the normal component of electric field to be discontinuous at the dielectric interfaces. Therefore, the electric field is a discontinuous field. On the other hand, the magnetic field is continuous, but its derivatives are not. The discontinuity behavior of the electromagnetic fields near the dielectric interfaces causes the plane wave expansion method to converge slowly. These discontinuities severely limit the accuracy of the method. Deviation of the truncated series from the actual one is large and the convergence is very slow. In fact it is well known that the convergence rate of a Fourier series depends strongly on the smoothness of the expansion functions. This problem will be more severe for high dielectric contrast and near close-packing ratios and for higher frequencies [14].

Ref [15] has reduced 3-D modeling of slab photonic crystal to a 2-D one by using an equivalent slab refractive index. This approach is highly skeptical in the case that refractive index contrast is high. We have shown that how this may lead to erroneous results in chapter 6. Ref [16] has presented some results for sinusoidally modulated slab waveguide. Ref [17] considers a slab photonic crystal as a 3-D periodic structure in the out of plane direction (the supercell method). It also considers the period in the third direction is large enough that the bound modes are not affected. The high number of plane waves in the non-periodic direction, and the replacing of the open boundary with a periodic one have consequences which are discussed in Chapter 5. In that chapter we also present a new method to remove these deficiencies.

2.1.2.2 *FDTD method for photonic crystals*

For the calculation of band diagrams of 2-D photonic crystal slabs, one period of the structure is mapped on the computational domain [18]. The Bloch boundary condition, which is defined by

$$\mathbf{E}(\mathbf{r}+\mathbf{a},t)=\mathbf{E}(\mathbf{r}+\mathbf{a},t)\exp(i\mathbf{k}\cdot\mathbf{a}) \tag{2.3a}$$

$$\mathbf{H}(\mathbf{r}+\mathbf{a},t)=\mathbf{H}(\mathbf{r}+\mathbf{a},t)\exp(i\mathbf{k}\cdot\mathbf{a}) \tag{2.3b}$$

where **a** is a primitive lattice vector and **k** is the wave vector, can be applied at the four lateral edges parallel to the y axis (see Figure 2.1.1) . For the top and bottom edges perpendicular to the y axis, the Mur's second-order absorbing boundary conditions [19] are applied to absorb the waves leaked from the slab. First, broad Gaussian pulses are used to excite the electromagnetic eigenmodes of the slab over a wide range of frequencies. The electromagnetic fields at observation points are recorded for every time step and then Fourier transformed to obtain frequency spectra. The spectra will contain peaks at frequency values of the eigenmodes corresponding to the wave vector **k** given by the Bloch boundary condition. Second, narrow Gaussian pulses are used to excite every single eigenmode individually and to obtain the field pattern of such modes. A variational expression has also been obtained for eigen frequencies of slab photonic crystals [20].

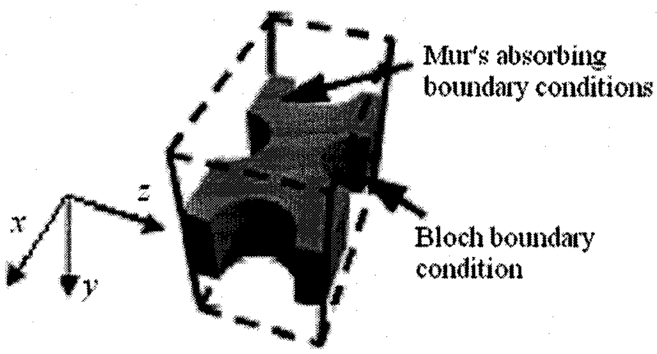

Figure 2.1.1. One Unit cell computational domain for the band calculation using 3-D FDTD method with Bloch and Mur's boundary conditions.

As is clear, FDTD assumes the wave vector in photonic crystal and obtains the corresponding frequency and fields thereafter. In practice, we usually seek to determine the propagation constant and field amplitudes for a given frequency (or wavelength in vacuum), and direction of propagation. So, one needs to perform a series of simulations in which the direction of **k** is fixed and propagation constant is changed over a given range. The corresponding frequencies (or wavelengths in vacuum) then can be used via interpolation to determine the unknown propagation constant corresponding to the desired wavelength in vacuum. The method is also not capable of tracing leaky modes due to the presence of absorbing boundaries.

2.1.2.3 Finite element spectral domain

The elegance and accuracy of time harmonic electromagnetic field numerical methods for photonic crystals shows itself in the finite element method in which periodic boundary conditions can be implemented easily [21]. Domain discretiziation of the unit cell is performed to produce meshes which are wrapped such that opposite boundary nodes meet. Knowing the frequency and the Bloch wave number, propagation constant and fields can be obtained by solving an eigenvalue equation. We have used this method as a benchmark for comparison of the accuracies in methods presented in chapters 3 and 4. The details of the method have been discussed in Appendix A.

The programming efforts needed to implement the finite element method and to generate meshes are considerably higher than other methods. It is the reason that such an accurate method has not found its deserved position in photonic crystal modeling yet.

2.2 Reflection from and Transmission through Photonic crystals

Although, a wave vector diagram can be used to get the transmission and reflection beam directions, anything beyond this, needs more accurate numerical modeling. Particularly important is the amplitude of the beam, which has commonly been calculated using FDTD techniques [22-24].

2.2.1 FDTD method

Although the robustness of FDTD method makes it a choice for analysis of wave propagation in many different structures, however FDTD implementation without considering the physics behind the model usually makes its computer resource consumption unacceptable. This is mostly the case for a full 3-D modeling of structures. Consider our case of interest, which is slab mode reflection and transmission from photonic crystals. The structure is periodic in only two directions or even one direction, the mode confinement in normal to the slab photonic crystal plane is achieved by proper refractive index contrast. The wavelength and direction of incident slab mode are known. The reflection and transmission coefficients and directions are to be determined. The accurate simulation needs 3-D simulation. Ignoring the periodicity of the media has a dramatic consequence regarding the computer resource consumption that makes 3-D simulations virtually impossible. Implementing periodic boundary conditions in time domain requires fields to be known a priori. Even for 2-D modeling when the structure is large, the FDTD simulations are often time consuming, and in many cases prohibitive. To study such an effect characterized by high wavelength and angular sensitivity, fine spatial and temporal grids and large simulation region are inevitable, which are frequently beyond the capability of commonly available computer facilities.

In the last two decades, there have been numerous attempts to improve computational efficiency of the FDTD method by using local space and time grid refinement strategies. The accuracy, and/or stability were the sacrifices of the grid refinement. Recently, a 3-D refinement scheme has been introduced that is stable for long time integration, and possesses the accuracy of the original FDTD. A tenfold improvement in computational time was obtained in computing the quality factor of photonic crystal micro-cavity [25]. This method can find potential application in our case of interest where the wave reflection at free space (with a large grid) from photonic crystal (with fine grid) is desired.

Parallelization of the FDTD method using distributed computing has been suggested by implementing rules and tolerances on a cluster of computers [26;27]. With the new generation of parallel machines that possess the connected parallel shared memory system (SMP nodes), a typical three weeks long computation period has been reduced to a less than a day (with 24 processors) [28].

Even with all these improvements, 3-D FDTD simulation of more than a few photonic crystal periods is not practical [29].

2.2.2 Coupled mode theory

The coupled-wave approach has tended in the past to be used in approximate analyses, however, a rigorous numerical coupled wave method, suitable for treating the diffraction of plane waves incident on parallel-slab-gratings, has also been introduced [30]. The theory can be simplified tremendously for the sub-wavelength grating. Therefore, it may be possible that due to their small period, all higher order diffracted waves are at cut off and only zero-order transmitted and reflected beams propagate outside the grating. The condition for such a simplified case is discussed further in Chapter 10.

The grating region is characterized by a permittivity, which can be represented by a Fourier expansion. Using Maxwell's equation, a set of coupled ordinary differential equations can be found. The number of coupled equation that must be solved depends on the number of spatial harmonics that one takes in the Fourier series expansion. As the number of spatial harmonics is increased, the solution will converge to the exact one. In the case that there is no higher order diffracted wave, the theory leads to replacing the layer with a biaxial thin film [31]. This method has been used as a bench mark for effective medium theories [32].

The coupled-wave approaches have been developed mainly for holographic and surface relief grating structures. They have been formulated to analyze transmission and reflection of an incident plane wave on the surface relief gratings, thick or thin volume index gratings, *etc.* The extension of the theory for slab 2-D photonic crystals has also been presented, but with limited accuracy for higher contrast system of materials [33]. It is a proper tool for analysis of multi-stack 1-D photonic crystals (cascaded volume grating) [34].

2.2.3 Transfer, Scattering and Impedance matrix method

The transfer matrix method is another heritage of solid state theory. In its original form, it is based on the electron wave equation (the Schrödinger equation) that ignores the polarization states of photons [35]. Including polarization, Pendry in 1992 was the pioneer in obtaining metrics relating the field components on a rectangular grid. Multiplying these transfer metrics and using Bloch condition over a unit cell, one can get an eigenvalue equation with the Bloch mode numbers as eigenvalues[36]. It can also be used for transmission spectra calculation. However, the method in its basic form has a convergence problem. It is suitable for small number of layers, and even for that it needs special treatments [36]. Assuming the field at the mesh points along a line or a plane (depending on the modeling complexity) a smooth function of position., one may use orthogonal functions for representing the field. Then the field at the mesh points can be replaced by the amplitude of the orthogonal functions. Rayleigh multi-poles [37], analytical modal functions [38], and plane waves [39] have been tried as the orthogonal set already. The transfer matrix then relates the amplitudes at a line (or plane) to the proceeding line (or plane). If the structure is periodic along this line (or plane), then problem can be simplified provided one uses the well developed theory for the field [37]. Changing the dependent variable to forward and backward field (instead of one of the field components), the method's convergence problem has a great improvement. Very accurate and stable results have been obtained by choosing the impedance matrix for connecting magnetic field at a line (or plane) to the electric field at the proceeding line (or plane) [38]. Although the method is used for 3-D photonic crystals [39], it has not been used for obtaining the band diagram and the transmission of the interested case of slab photonic crystal yet. The reason probably is behind the open boundaries and the convergence problem.

2.3 Mode matching techniques

The practicality of many photonic crystal devices relates to how effectively one can couple light into them or couple out the light to the free space (or in the planar technology, to the slab or the waveguide mode). Unfortunately this coupling is not satisfactory. Depending on the situation the mode matching techniques have different structures. In this thesis we are interested to couple light from homogenous medium into bulk photonic crystal.

The light coupling deficiency was recognized soon after the planar superprism was proposed[40]. The first successful idea for the 2-D photonic crystal was to play with the interface holes. Projected holes are able to reduce the coupling loss efficiently. The loss as small as 0.01dB through FDTD simulation [41], the direction of the hole and its corresponding shape is critical to achieve such a low coupling loss (see Figure 2.3.1).

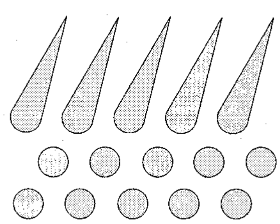

Figure 2.3.1 The projected hole as have been suggested by Baba *et.al.* [41]

Putting rectangular air-holes at the interface and aligning them in direction of the transmission has also been proposed. The 70% coupling efficiency has been reported using FDTD simulation [22]. The suppression of unwanted refracted modes has also been reported. Adiabatic tapering of the air holes at the interface has also been suggested. The 10-layer tapered air hole has been optimized to achieve wide band, wide angle coupling efficiency using a combination of plane-wave expansion method and mode matching technique. The loss could be negligible but unfortunately, the hole sizes as small as 0.05 of the bulk photonic crystal are needed [42]. For a typical example of a bulk silicon photonic crystal of square lattice with period 230nm, and hole size of 100nm, the minimum hole size would be as small as 5nm.

Composing the reflected wave component by cascaded diffracting gratings is a novel idea with limited applicability. A coupling efficiency of 84% has been achieved for un-slanted hexagonal lattice [43].

2.4 Multiplexing using photonic crystals (superprism effect)

The first observation of beam steering with wavelength (later called **S**-vector superprism effect) was observed in slab 1-D photonic crystal (and at TM polarization) in 1987 [16]. A two-channel demultiplexer with channel spacing of 3.9nm and cross talk of 12dB was reported using moderate refractive index material (Ta_2O_5 with refractive index of 2.10 over Tempax glass of refractive index of 1.47). The photonic crystal patterns were generated using fringes of He-Cd laser produced by an interferometer at wavelength of 441.6 nm. The wave vector diagram (also called equi-frequency contour) has been used to analyze the behavior of Bloch modes. Optics of Floquet-Bloch waves in photonic crystals was well described using wave vector diagram by Russell in 1986 too [44]. As we will show in later chapters, the normalized form of the wave vector diagram is more suitable for our applications.

However, it was not until 1998, that Kosaka et.al reported 500 times more dispersion than the conventional glasses (*i.e.*, 5°/nm compared to 10°/μm of a conventional glass) [45;46]. The phenomenon is caused by the apparent distortion from a circular shape of the wave vector diagram and also by multiplicity within the diagram of the second or the third band of photonic crystal. Later this beam steering phenomenon was called **S**-vector superprism dispersion. In planar technology, using GaAs-based heterostructure perforated by a triangular photonic crystal lattice, it was Wu, *et.al.*, in 2002 who reported 0.5°/nm dispersion [47].

The observation of 5°/nm beam steering dispersion in a pseudo-2-D auto-cloned photonic crystal (using high refractive index contrast of silicon and glass) was so promising that the authors claimed that the demultiplexer based on the superprism phenomenon can be four orders of magnitude smaller in area compared to other alternatives (say silica-based array waveguide grating, AWG, filter) [46]. However soon after, it was recognized that this type of dispersion does not lead necessarily to a high resolution. Using simple Gaussian wave assumption in photonic crystal Baba [48] showed that the resolution of **S**-vector superprism is not that great due to large beam divergence inside photonic crystal. This excessive beam divergence is originated from the curvature of the wave vector diagram near the bandedge where the dispersion is high. They have shown that a resolution of 0.4 nm for 56 channels needs photonic crystal size of 6.5 cm^2 (comparable to the conventional AWG).

Momeni *et.al.* developed a more rigorous theory for approximating light propagation in photonic crystals [49], and optimized the **S**-vector superprism structure using 2-D photonic crystal of air holes into bulk of silicon [50;51]. They have shown that 754 μm^2 device size (photonic crystal area) is sufficient to resolve 4 channels with 20 nm channel spacing. As we will show in chapter 6, even this device size is an over estimation of a real situation where one has to take into account the finite slab height.

The excessive beam expansion in **S**-vector superprism has been mitigated using a preconditioning technique. The idea is the using to the negative refraction observable at the bandedge of the second band to compensate the positively refracted incident beam [52;53].

Another issue regarding the observation of the huge dispersion is that it only occurs over narrow spectral range. Effective use of the dispersion needs to maintain the dispersion over relatively longer spectral range. Cascading the photonic crystals to make a relatively wide band demultiplexer is a new idea that has been introduced in chapter 7.

An alternative to the beam steering dispersion (the **S**-vector superprism), is to employ the angular dispersion that also occurs near the bandedge (the so called **k**-vector superprism). The high sensitivity of refraction angle with wavelength at the free space photonic crystal interface will add together if the photonic crystal interfaces cross each other with an angle (this makes photonic crystal a prism shape with the interface crossing angle as the apex angle). As a consequence, the enhanced type of spectral resolution, (similar to a traditional prism made for visual light) can be achieved [24;54;55]. Better resolution and scaling with channel count make it a suitable choice for fine resolutions and for the most DWDM applications. As we have shown in Chapter 8, the device size (prism area) of about 0.01 mm^2 is enough for resolving 32 channels with 100GHz (~0.8 nm) channel spacing.

The first experimental result of **k**-vector superprism has been carried out in millimeter wave range of spectrum. Lin, et.als. made a two dimensional photonic lattice consists of 10cm long cylindrical alumina-ceramic rods of diameter with permittivity of $\varepsilon_r = 8.9$. Using the conventional microwave setup, they excited the prism with an antenna radiating a beam at $v = 99$ GHz, and observed the high sensitivity of the deviation angle to the incident angle [56].

2.5 Waveguide focusing elements

Our proposal for **k**-vector demultiplexing consists of two focusing elements. The focusing elements for the high contrast material that we have used can be two mirrors. The mirrors can be made using the total internal reflection of light from silicon slab to air. Therefore a parabolic trench is the simplest solution. This is the approach we adopted for our layout as is explained in chapter 10. However, the case gets more challenging as the refractive index contrast becomes smaller. Waveguide lenses have been investigated by several researchers. We have reviewed them in the following section.

The curvature of the wave vector diagram also has been used to collimate light propagating inside a photonic crystal.

2.5.1 Mode-index lenses

Mode-index (also called homogenous refracting) waveguide lenses were proposed in the early days of integrated optics, but they were not so useful due to mode coupling loss [57]. In homogeneous thin-film lenses, guided light is refracted at the boundary between two regions of disparate waveguide. Having optimized the design of a homogeneous multi-element lens, the lens performance will in practice be limited by the efficiency of light transfer across that boundary. This is the coupling efficiency between the fundamental waveguide modes in the two waveguides. Light may be lost by scattering out into the substrate, or by coupling to modes other than the fundamental one in the second guide.

The coupling efficiency may be expressed as the overlap integral between the transverse electric field profiles E_l and E_h in the low and high index guiding regions, respectively. It is clear that in order to reduce light in unwanted modes (which would be refracted differently from the fundamental mode and hence would constitute a background noise signal around the focused spot) the low index waveguide at least should only support one mode. It is shown that the high index guide will inevitably be multimode for optimum coupling efficiency. However, any higher mode excited in the high index lens element by coupling from the fundamental mode of the low index waveguide region, at low efficiency, will be re-coupled at exit from the lens element at equally low efficiency to the fundamental guide mode, and although mis-focused, should not present significant background noise if coupling efficiency is high. Nevertheless, higher modes were supported in the guided region; there could be significant coupling of light to them from higher modes in the lens region.

Various refractive index profiles have been considered for the two guiding layers. Using step profiles the solution of the waveguide characteristic equation is straight forward and electric field profiles are easily calculated, and then closed form relation for coupling efficiency can be obtained. It can be shown that Snell's law is applicable if one uses the effective refractive index of the propagating mode instead of the refractive index of the guide material. It follows that the classical lens design techniques can also be used in the design of waveguide lenses. A bi-aspheric lens with focal length of 12mm, $f/\# = 4$ and field of view of $\theta = 6^\circ$ has been designed for $\Delta n \approx 0.12$, the reported insertion loss is 5 dB [58]. Clearly the loss is very high. Our investigation regarding mode-index waveguide lenses is on its first stage. The challenge is reducing the coupling loss as much as possible, while providing the required $f/\#$ and field of view.

2.5.2 *Photonic crystal focusing elements*

The light propagating inside a photonic crystal is governed by its wave vector diagram, which corresponds to the index ellipsoid in conventional optics. The optical beam shaping due to the curvature of different operating point in the wave vector diagram was first observed by Russell in 1986[12]. Self collimating was first reported in 3-D photonic crystal by Kosaka in 1999[59].

These types of lenses usually work at the second band of the photonic crystal, where the band curvature is higher, but they all suffer from the spherical aberration. A perfect lens needs a parabolic wave vector diagram and because of that all photonic crystal lenses are suffering from spherical aberration. Engineering of the photonic crystal to make given part of wave vector diagram as parabolic as possible has been done by deforming the triangular lattice [60]. Also the insertion loss has to be improved.

There is also other kind of lens that needs a region of wave vector diagram that looks like a circle (isotropic region), then the equivalent refractive index can de defined (which is usually smaller than the slab region). Then the conventional lens equations can be used to shape the front that back surface of the lens for making the desired beam shaping [61]. By the introduced angular periodicity, we have used a similar idea to propose a novel lens for integrated optics in chapter 9.

References

[1] J . D. Jackson, "Multipoles, Electrostatics of macroscopic media, dielectrics," in *Classical Electrodynamics,* 2 ed New York: John Wiely and Sons, eds., 1974, pp. 136-167.

[2] S . Datta, C. T. Chan, K. M. Ho, and C. M. Soukoulis, "Effective Dielectric-Constant of Periodic Composite Structures," *Physical Review B*, vol. 48, no. 20, pp. 14936-14943, Nov.1993.

[3] J . L. Jackson and S. R. Coriell, "Transport Coefficients of Composite Materials," *Journal of Applied Physics*, vol. 39, no. 5, p. 2349-&, 1968.

[4] F . T. Chen and H. G. Craighead, "Diffractive Phase Elements Based on 2-Dimensional Artificial Dielectrics," *Optics Letters*, vol. 20, no. 2, pp. 121-123, Jan.1995.

[5] P . Lalanne and D. LemercierLalanne, "Depth dependence of the effective properties of subwavelength gratings," *Journal of the Optical Society of America A-Optics Image Science and Vision*, vol. 14, no. 2, pp. 450-458, Feb.1997.

[6] P . C. Kendall, M. J. Adams, S. Ritchie, and M. J. Robertson, "Theory for Calculating Approximate Values for the Propagation Constants of An Optical Rib Wave-Guide by Weighting the Refractive-Indexes," *Iee Proceedings-A-Science Measurement and Technology*, vol. 134, no. 8, pp. 699-702, Sept.1987.

[7] M . L. Cohe and J. R. Chelkowsky, *Electronic structure and optical properties of semiconductors.* Berlin: Springer-Verlag, 1987.

[8] Z . Zhang and S. Satpathy, "Electromagnetic-Wave Propagation in Periodic Structures - Bloch Wave Solution of Maxwell Equations," *Physical Review Letters*, vol. 65, no. 21, pp. 2650-2653, Nov.1990.

[9] S . T. Peng, T. Tamir, and H. L. Bertoni, "Theory of Periodic Dielectric Waveguides," *Ieee Transactions on Microwave Theory and Techniques*, vol. MT23, no. 1, pp. 123-133, 1975.

[10] Y ariv Amnon and Yeh Pochi, "Electromagnetic propagation in periodic media," in *Optical Waves in Crystals : Propagation and Control of Laser Radiation* Wiley Series in Pure and Applied Optics, 2003, pp. 115-219.

[11] R . S. Chu and T. Tamir, "Wave-Propagation and Dispersion in Space-Time Periodic Media," *Proceedings of the Institution of Electrical Engineers-London*, vol. 119, no. 7, pp. 797-806, 1972.

[12] P . S. J. Russell, "Interference of Integrated Floquet-Bloch Waves," *Physical Review A*, vol. 33, no. 5, pp. 3232-3242, May1986.

[13] Z . Pinsker, *Dynamical Scatering of X-rays in Crystals.* Berlin, Heidelberg: Springer-verlag, 1978.

[14] H . S. Sozuer, J. W. Haus, and R. Inguva, "Photonic Bands - Convergence Problems with the Plane-Wave Method," *Physical Review B*, vol. 45, no. 24, pp. 13962-13972, June1992.

[15] L . J. Wu, M. Mazilu, and T. F. Krauss, "Beam steering in planar-photonic crystals: From superprism to supercollimator," *Journal of Lightwave Technology*, vol. 21, no. 2, pp. 561-566, Feb.2003.

[16] Z engerle R., "Light propagation in single and doubly periodic planar waveguides," *Journal of Modern Optics*, vol. 34, no. 12, pp. 1589-1610, 1987.

[17] S . G. Johnson, S. H. Fan, P. R. Villeneuve, J. D. Joannopoulos, and L. A. Kolodziejski, "Guided modes in photonic crystal slabs," *Physical Review B*, vol. 60, no. 8, pp. 5751-5758, Aug.1999.

[18] A . Chutinan and S. Noda, "Waveguides and waveguide bends in two-dimensional photonic crystal slabs," *Physical Review B*, vol. 62, no. 7, pp. 4488-4492, Aug.2000.

[19] A . Taflove and S. C. Hagness, "Analytical Absorbing Boundary Conditions," in *Computational Electromagnetics: the finite-difference time domain method,* 3 ed Artech House, 2005, pp. 229-272.

[20] Y . Ohtera, K. Kurokawa, and S. Kawakami, "Variational expression for the analysis of photonic crystal devices," *Ieee Journal of Quantum Electronics*, vol. 38, no. 7, pp. 919-926, July2002.

[21] B . P. Hiett, J. M. Generowicz, S. J. Cox, M. Molinari, D. H. Beckett, and K. S. Thomas, "Application of finite element methods to photonic crystal modeling," *Iee Proceedings-Science Measurement and Technology*, vol. 149, no. 5, pp. 293-296, Sept.2002.

[22] T . Baba and M. Nakamura, "Photonic crystal light deflection devices using the superprism effect," *Ieee Journal of Quantum Electronics*, vol. 38, no. 7, pp. 909-914, July2002.

[23] K . B. Chung and S. W. Hong, "Wavelength demultiplexers based on the superprism phenomena in photonic crystals," *Applied Physics Letters*, vol. 81, no. 9, pp. 1549-1551, Aug.2002.

[24] C . Y. Luo, M. Soljacic, and J. D. Joannopoulos, "Superprism effect based on phase velocities," *Optics Letters*, vol. 29, no. 7, pp. 745-747, Apr.2004.

[25] A . R. Zakharian, M. Brio, C. Dineen, and J. V. Moloney, "Second-order accurate FDTD space and time grid refinement method in three space dimensions," *Ieee Photonics Technology Letters*, vol. 18, no. 9-12, pp. 1237-1239, May2006.

[26] V . Varadarajan and R. Mittra, "Finite-Difference Time-Domain (Fdtd) Analysis Using Distributed Computing," *Ieee Microwave and Guided Wave Letters*, vol. 4, no. 5, pp. 144-145, May1994.

[27] W . H. Yu, Y. J. Liu, T. Su, N. T. Hunag, and R. Mittra, "A robust parallel conformal finite-difference time-domain processing package using the MPI library," *Ieee Antennas and Propagation Magazine*, vol. 47, no. 3, pp. 39-59, June2005.

[28] D . Takahashi, T. Boku, and M. Sato, "An implementation of parallel 3-D FFT using short vector SIMD instructions on clusters of PCs," *Applied Parallel Computing: State of the Art in Scientific Computing*, vol. 3732, pp. 1159-1167, 2006.

[29] J . B. Cai, G. P. Nordin, S. H. Kim, and J. H. Jiang, "Three-dimensional analysis of a hybrid photonic crystal-conventional waveguide 90 degrees bend," *Applied Optics*, vol. 43, no. 21, pp. 4244-4249, July2004.

[30] M . G. Moharam, E. B. Grann, D. A. Pommet, and T. K. Gaylord, "Formulation for Stable and Efficient Implementation of the Rigorous Coupled-Wave Analysis of Binary Gratings," *Journal of the Optical Society of America A-Optics Image Science and Vision*, vol. 12, no. 5, pp. 1068-1076, May1995.

[31] E . B. Grann, M. G. Moharam, and D. A. Pommet, "Artificial Uniaxial and Biaxial Dielectrics with Use of 2-Dimensional Subwavelength Binary Gratings," *Journal of the Optical Society of America A-Optics Image Science and Vision*, vol. 11, no. 10, pp. 2695-2703, Oct.1994.

[32] P . Lalanne and D. LemercierLalanne, "On the effective medium theory of subwavelength periodic structures," *Journal of Modern Optics*, vol. 43, no. 10, pp. 2063-2085, Oct.1996.

[33] P . Paddon and J. F. Young, "Two-dimensional vector-coupled-mode theory for textured planar waveguides," *Physical Review B*, vol. 61, no. 3, pp. 2090-2101, Jan.2000.

[34] E . N. Glytsis and T. K. Gaylord, "Rigorous 3-Dimensional Coupled-Wave Diffraction Analysis of Single and Cascaded Anisotropic Gratings," *Journal of the Optical Society of America A-Optics Image Science and Vision*, vol. 4, no. 11, pp. 2061-2080, Nov.1987.

[35] H . Jones, "Electron-Energy Spectrum in Long Period Superlattices," *Journal of Physics F-Metal Physics*, vol. 3, no. 12, pp. 2075-2081, 1973.

[36] J . B. Pendry and A. Mackinnon, "Calculation of Photon Dispersion-Relations," *Physical Review Letters*, vol. 69, no. 19, pp. 2772-2775, Nov.1992.

[37] L . C. Botten, N. A. Nicorovici, R. C. McPhedran, C. M. de Sterke, and A. A. Asatryan, "Photonic band structure calculations using scattering matrices," *Physical Review e*, vol. 6404, no. 4, p. Art. No. 046603 Part 2, Oct.2001.

[38] B . Gralak, S. Enoch, and G. Tayeb, "From scattering or impedance matrices to Bloch modes of photonic crystals," *Journal of the Optical Society of America A-Optics Image Science and Vision*, vol. 19, no. 8, pp. 1547-1554, Aug.2002.

[39] Z . Y. Li and L. L. Lin, "Photonic band structures solved by a plane-wave-based transfer-matrix method," *Physical Review e*, vol. 67, no. 4, p. Art. No. 046607 Part 2, Apr.2003.

[40] T . Baba and D. Ohsaki, "Interfaces of photonic crystals for high efficiency light transmission," *Japanese Journal of Applied Physics Part 1-Regular Papers Short Notes & Review Papers*, vol. 40, no. 10, pp. 5920-5924, Oct.2001.

[41] T . Baba, T. Matsumoto, and M. Echizen, "Finite difference time domain study of high efficiency photonic crystal superprisms," *Optics Express*, vol. 12, no. 19, pp. 4608-4613, Sept.2004.

[42] B . Momeni and A. Adibi, "Adiabatic matching stage for coupling of light to extended Bloch modes of photonic crystals," *Applied Physics Letters*, vol. 87, no. 17, p. Art. No. 171104, Oct.2005.

[43] J . Witzens, M. Hochberg, T. Baehr-Jones, and A. Scherer, "Mode matching interface for efficient coupling of light into planar photonic crystals," *Physical Review e*, vol. 69, no. 4, p. Art. No. 046609 Part 2, Apr.2004.

[44] P . St. Russell, "Optics of Floquet-Bloch Waves in Dielectric Gratings," *Applied Physics B-Photophysics and Laser Chemistry*, vol. 39, no. 4, pp. 231-246, Apr.1986.

[45] H . Kosaka, T. Kawashima, A. Tomita, M. Notomi, T. Tamamura, T. Sato, and S. Kawakami, "Superprism phenomena in photonic crystals," *Physical Review B*, vol. 58, no. 16, pp. 10096-10099, Oct.1998.

[46] H . Kosaka, T. Kawashima, A. Tomita, M. Notomi, T. Tamamura, T. Sato, and S. Kawakami, "Superprism phenomena in photonic crystals: Toward microscale lightwave circuits," *Journal of Lightwave Technology*, vol. 17, no. 11, pp. 2032-2038, Nov.1999.

[47] L . J. Wu, M. Mazilu, T. Karle, and T. F. Krauss, "Superprism phenomena in planar photonic crystals," *Ieee Journal of Quantum Electronics*, vol. 38, no. 7, pp. 915-918, July2002.

[48] T . Baba and T. Matsumoto, "Resolution of photonic crystal superprism," *Applied Physics Letters*, vol. 81, no. 13, pp. 2325-2327, Sept.2002.

[49] B . Momeni and A. Adibi, "An approximate effective index model for efficient analysis and control of beam propagation effects in photonic crystals," *Journal of Lightwave Technology*, vol. 23, no. 3, pp. 1522-1532, Mar.2005.

[50] B . Momeni and A. Adibi, "Optimization of photonic crystal demultiplexers based on the superprism effect," *Applied Physics B-Lasers and Optics*, vol. 77, no. 6-7, pp. 555-560, Nov.2003.

[51] B . Momeni and A. Adibi, "Systematic design of superprism-based photonic crystal demultiplexers," *Ieee Journal on Selected Areas in Communications*, vol. 23, no. 7, pp. 1355-1364, July2005.

[52] B . Momeni, J. D. Huang, M. Soltani, M. Askari, S. Mohammadi, M. Rakhshandehroo, and A. Adibi, "Compact wavelength demultiplexing using focusing negative index photonic crystal superprisms," *Optics Express*, vol. 14, no. 6, pp. 2413-2422, Mar.2006.

[53] J . Witzens, T. Baehr-Jones, and A. Scherer, "Hybrid superprism with low insertion losses and suppressed cross-talk (vol E 71, art no 026604, 2005)," *Physical Review e*, vol. 71, no. 3 Mar.2005.

[54] A . Bakhtazad and A. G. Kirk, "Superprism effect with planar 1-D photonic crystal," *Proceedings of the SPIE*, vol. 5360, pp. 364-372, June2004.

[55] T . Matsumoto and T. Baba, "Photonic crystal **k**-vector superprism," *Journal of Lightwave Technology*, vol. 22, no. 3, pp. 917-922, Mar.2004.

[56] S . Y. Lin, V. M. Hietala, L. Wang, and E. D. Jones, "Highly dispersive photonic band-gap prism," *Optics Letters*, vol. 21, no. 21, pp. 1771-1773, Nov.1996.

[57] P . J. R. Laybourn, G. Molesini, and G. C. Righini, "Homogeneous Refracting Lenses for Integrated Optical Circuits," *Journal of Modern Optics*, vol. 35, no. 6, pp. 1029-1048, June1988.

[58] K . Tatsumi, T. Nakaguchi, and S. Ito, "Wide Field Angle Bi-Aspherical Wave-Guide Lens in Linbo3 Fabricated by Proton-Exchange," *Electronics Letters*, vol. 24, no. 9, pp. 546-548, Apr.1988.

[59] H . Kosaka, T. Kawashima, A. Tomita, M. Notomi, T. Tamamura, T. Sato, and S. Kawakami, "Self-collimating phenomena in photonic crystals," *Applied Physics Letters*, vol. 74, no. 9, pp. 1212-1214, Mar.1999.

[60] T . Matsumoto, S. Fujita, and T. Baba, "Wavelength demultiplexer consisting of Photonic crystal superprism and superlens," *Optics Express*, vol. 13, no. 26, pp. 10768-10776, Dec.2005.

[61] S . Enoch, G. Tayeb, and B. Gralak, "The richness of the dispersion relation of electromagnetic bandgap materials," *Ieee Transactions on Antennas and Propagation*, vol. 51, no. 10, pp. 2659-2666, Oct.2003.

Chapter 3

1-D PHOTONIC CRYSTALS

In this chapter, we start with the matrix formulation of dielectric stratified media, and then we obtain the dispersion equation of the slanted 1-D photonic crystal. The normalized wave vector diagram, which is the diagram of choice for our next step of exploration, is obtained for slanted and un-slanted cases. Based on the normalized wave vector diagram we explain and explore the basis of k-vector and S-vector dispersion. The zero order diffraction condition is derived for 1-D photonic crystals. Finally a model for FDTD analysis is explained. An excellent agreement between our wave vector analysis and results of FDTD is observed. Transmission and reflection coefficients to and from 1-D photonic crystal have been obtained using the FDTD analysis.

3.1 Maxwell's equation for dielectric media

The spatial relationship between electric field $\mathbf{E}(x,y,z)$ and the magnetic field $\mathbf{H}(x,y,z)$ of an optical medium are determined by Maxwell's equations. If we assume that the medium is isotropic, then the dielectric constant $\varepsilon(x,y,z)$ can be related to the refractive index $n(x,y,z)$ by $\varepsilon = n^2\varepsilon_0$, where ε_0 is the permittivity of free space. On the other hand, for non-magnetic materials, which normally constitute an optical materials, the magnetic permeability μ is almost equal to the free space value μ_0. Under these conditions, the source free Maxwell's equations will be as below[1]

$$\nabla \times \mathbf{E} = i \left(\frac{\mu_0}{\varepsilon_0} \right)^{1/2} k_0 \mathbf{H} \tag{3.1}$$

$$\nabla \times \mathbf{H} = -i \left(\frac{\varepsilon_0}{\mu_0} \right)^{1/2} k_0 n^2 \mathbf{E} \tag{3.2}$$

$$\nabla \cdot \left(n^2 \mathbf{E} \right) = 0 \tag{3.3}$$

$$\nabla \cdot \mathbf{H} = 0 \tag{3.4}$$

where the waves are assumed to be monochromatic with angular frequency ω, $k_0 = 2\pi/\lambda_0$ is the free space wave number and is equal to $\left(\omega^2 \varepsilon_0 \mu_0\right)^{1/2}$, and an implicit time dependence $\exp(-i\omega t)$ is suppressed throughout.

The boundary conditions across an interface between two media of different refractive indices are:

(i) Continuity of the tangential components of magnetic and electric fields across the interface,

(ii) Continuity of the normal component of the displacement vector, $\varepsilon_0 n^2 \mathbf{E}$ across the interface.

If a medium has a refractive index profile, which dose not vary with distance along z axis, *i.e.*, $n = n(x, y)$, then the media is translationally (axially) invariant. In other words, the electric and magnetic fields in the medium are separable as below

$$\mathbf{E}(x, y, z) = \mathbf{E}(x, y) \exp(i k_z z) \tag{3.5}$$

$$\mathbf{H}(x, y, z) = \mathbf{H}(x, y) \exp(i k_z z) \tag{3.6}$$

where k_z is the propagation constant along the optical axis. We decompose these fields into longitudinal and transverse components, parallel and perpendicular to the optical axis respectively, and denoting by subscripts z and **t**, where

$$\mathbf{E}(x, y) = \mathbf{E}_t(x, y) + E_z(x, y)\, \hat{\mathbf{a}}_z \tag{3.7}$$

$$\mathbf{H}(x, y) = \mathbf{H}_t(x, y) + H_z(x, y)\hat{\mathbf{a}}_z \tag{3.8}$$

where $\hat{\mathbf{a}}_z$ is the unit vector parallel to the longitudinal axis.

If we substitute the field representation of Eqs.(3.7) and (3.8) into the source free Maxwell's equations (Eqs.(3.1) and (3.2)) and compare the longitudinal and the transverse components, we will obtain

$$\mathbf{E}_t = -\left(\frac{\mu_0}{\varepsilon_0}\right)^{1/2} \frac{1}{k_0\, n^2} \hat{\mathbf{a}}_z \times \left(k_z \mathbf{H}_t + i \nabla_t H_z \right) \tag{3.9}$$

$$\mathbf{H}_t = -\left(\frac{\varepsilon_0}{\mu_0}\right)^{1/2} \frac{1}{k_0} \hat{\mathbf{a}}_z \times \left(k_z \mathbf{E}_t + i \nabla_t E_z \right) \tag{3.10}$$

$$E_z = i \left(\frac{\mu_0}{\varepsilon_0}\right) \frac{1}{k_0\, n^2} \hat{\mathbf{a}}_z \cdot \nabla_t \times \mathbf{H}_t = \frac{i}{k_z} \left(\nabla_t \cdot \mathbf{E}_t + \mathbf{E}_t \cdot \nabla_t \ln n^2 \right) \tag{3.11}$$

$$H_z = -i \left(\frac{\varepsilon_0}{\mu_0}\right)^{1/2} \frac{1}{k_0} \hat{\mathbf{a}}_z \cdot \nabla_t \times \mathbf{E}_t = \frac{i}{k_z} \nabla_t \cdot \mathbf{H}_t \tag{3.12}$$

If we eliminate $\mathbf{H}_t$ or $\mathbf{E}_t$ from Eqs.(3.9) and (3.10), then we can express the transverse fields in terms of the longitudinal fields as below

$$\mathbf{E}_t = \frac{i}{k_0^2\, n^2 - k_z^2} \left[k_z \nabla_t E_z - \left(\frac{\mu_0}{\varepsilon_0}\right)^{1/2} k_0\, \hat{\mathbf{a}}_z \times \nabla_t H_z \right] \tag{3.13}$$

$$\mathbf{H}_t = \frac{i}{k_0^2\, n^2 - k_z^2} \left[k_z \nabla_t H_z + \left(\frac{\varepsilon_0}{\mu_0}\right)^{1/2} k_0\, n^2\, \hat{\mathbf{a}}_z \times \nabla_t E_z \right] \tag{3.14}$$

The electric and magnetic fields can be normalized arbitrarily, so that in general $\mathbf{E}(x, y)$ and $\mathbf{H}(x, y)$ are complex vectors. However, in a non-absorbing or non-active media, the refractive index n is a real number, and Eqs.(3.9)-(3.12) show that we can choose the components of $\mathbf{E}$ and $\mathbf{H}$ such that the transverse components are real, and the longitudinal components are imaginary. Thus,

$$\mathbf{E}_t,\ \mathbf{H}_t \text{ real, and } E_z,\ H_z \text{ imaginary} \tag{3.15}$$

The backward-propagating fields are simply related to the forward-propagating fields, by transforming k_z to $-k_z$. We can deduce from Eqs (3.9)-(3.12) that there are two possibilities, either

$$\mathbf{E}^- = -\mathbf{E}_t^+ + E_z^+\,\hat{a}_z; \qquad \mathbf{H}^- = \mathbf{H}_t^+ - H_z^+\,\hat{a}_z \tag{3.16}$$

or

$$\mathbf{E}^- = \mathbf{E}_t^+ - E_z^+\,\hat{a}_z; \qquad \mathbf{H}^- = -\mathbf{H}_t^+ + H_z^+\,\hat{a}_z \tag{3.17}$$

We adopt the last convention throughout this chapter. The relationships (3.15) and (3.17) both hold for non-absorbing or non-active media, then by combining them, we will have

$$\mathbf{E}^- = \left(\mathbf{E}^+\right)^*; \qquad \mathbf{H}^- = \left(-\mathbf{H}^+\right)^* \tag{3.18}$$

If we eliminate either the electric field or magnetic field components from Maxwell's equations (Eqs.(3.1) and (3.2)) assuming fields are separable (as Eqs.(3.5)-(3.8)), we obtain the homogeneous vector wave equations

$$\left(\nabla_t^2 + n^2 k_0^2 - k_z^2\right)\mathbf{E} = -\left(\nabla_t + i\,k_z\hat{\mathbf{a}}_z\right)\mathbf{E}_t \cdot \nabla_t \ln n^2 \tag{3.19}$$

$$\left(\nabla_t^2 + n^2 k_0^2 - k_z^2\right)\mathbf{H} = \left[\left(\nabla_t + i\,k_z\hat{\mathbf{a}}_z\right)\times\mathbf{H}\right]\times\nabla_t \ln n^2 \tag{3.20}$$

The above equations can be reduced to a set of homogeneous vector wave equations for transverse and longitudinal components given by

$$\left(\nabla_t^2 + n^2 k_0^2 - k_z^2\right)\mathbf{E}_t = -\nabla_t\left(\mathbf{E}_t \cdot \nabla_t \ln n^2\right) \tag{3.21}$$

$$\left(\nabla_t^2 + n^2 k_0^2 - k_z^2\right)E_z = -i\,k_z\,\mathbf{E}_t \cdot \nabla_t \ln n^2 \tag{3.22}$$

$$\left(\nabla_t^2 + n^2 k_0^2 - k_z^2\right)\mathbf{H}_t = \left(\nabla_t \times \mathbf{H}_t\right)\times\nabla_t \ln n^2 \tag{3.23}$$

$$\left(\nabla_t^2 + n^2 k_0^2 - k_z^2\right)H_z = \left(\nabla_t H_z - i\,k_z\mathbf{H}_t\right)\cdot\nabla_t\ \ln\ n^2 \tag{3.24}$$

The longitudinal components E_z and H_z in Eqs.(3.22) and (3.24), depend on the transverse fields $\mathbf{E}_t$ and $\mathbf{H}_t$. If we use Eqs.(3.13) and (3.14) to express $\mathbf{E}_t$ and $\mathbf{H}_t$ in terms of E_z and H_z, we will obtain the following coupled equations

$$\left(\nabla_t^2 + p\right)E_z - \frac{k_z^2}{p}\nabla_t E_z \cdot \nabla_t \ln n^2 = \left(\frac{\mu_0}{\varepsilon_0}\right)^{1/2} \frac{k_0\, k_z^2}{p}\, \hat{\mathbf{a}}_z \cdot \left(\nabla_t H_z \times \nabla_t \ln n^2\right) \quad (3.25)$$

$$\left(\nabla_t^2 + p\right)H_z - \frac{n^2 k_0^2}{p}\nabla_t H_z \cdot \nabla_t \ln n^2 = \left(\frac{\varepsilon_0}{\mu_0}\right)^{1/2} \frac{k_0\, k_z\, n^2}{p}\hat{\mathbf{a}}_z \cdot \left(\nabla_t E_z \times \nabla_t \ln n^2\right) \quad (3.26)$$

where $p = k_0^2\, n^2 - k_z^2$. As it can be seen, the nonzero $\nabla_t \ln n^2$ terms relate E_z and H_z together; so the equations cannot in general be decoupled. Therefore, in general TE and TM modes are not appropriate solely, since neither $E_z = 0$ nor $H_z = 0$ are accepted solutions. Accordingly, the modes of optical media are in general hybrid having both E_z and H_z components.

The transverse components $\mathbf{E}_t$ and $\mathbf{H}_t$ are related to each other. If we eliminate E_z from Eq.(3.10) by using Eq. (3.11) and after substitution from Eq.(3.21), we will have

$$\mathbf{H}_t = \left(\frac{\varepsilon_0}{\mu_0}\right)^{1/2} \frac{1}{k_0\, \beta_z}\, \hat{\mathbf{a}}_z \times \left[n^2\, k_0^2\, \mathbf{E}_t - \nabla_t \times \left(\nabla_t \times \mathbf{E}_t\right)\right] \quad (3.27)$$

and similarly for $\mathbf{E}_t$

$$\mathbf{E}_t = \left(\frac{\mu_0}{\varepsilon_0}\right)^{1/2} \frac{1}{k_0\, n^2}\, \hat{\mathbf{a}}_z \times \left[k_z\, \mathbf{H}_t - \frac{1}{k_z}\nabla_t \cdot \left(\nabla_t \cdot \mathbf{H}_t\right)\right] \quad (3.28)$$

3.2 Wave equation in one dimensional stratified media

Consider a dielectric medium, which is uniform in y and z directions. The z axis is assumed to be the direction of wave propagation. (see Figure 3.2.1) In this planar structure the refractive index profile is $n(x)$, and the field components given by Eqs. (3.21)-(3.24) reduces to the following equations

$$\frac{d^2 E_x}{dx^2}+\frac{d}{dx}\left(E_x\frac{d\ln n^2}{dx}\right)+\left(n^2k_0^2-k_z^2\right)E_x=0 \tag{3.29}$$

$$\frac{d^2 E_y}{dx^2}+\left(n^2k_0^2-k_z^2\right)E_y=0 \tag{3.30}$$

$$\frac{d^2 E_z}{dx^2}+ik_z\left(\frac{d\ln n^2}{dx}\right)E_z+\left(n^2k_0^2-k_z^2\right)E_z=0 \tag{3.31}$$

$$\frac{d^2 H_x}{dx^2}+\left(n^2k_0^2-k_z^2\right)H_x=0 \tag{3.32}$$

$$\frac{d^2 H_y}{dx^2}-\frac{d\ln n^2}{dx}\cdot\frac{dH_y}{dx}+\left(n^2k_0^2-k_z^2\right)H_y=0 \tag{3.33}$$

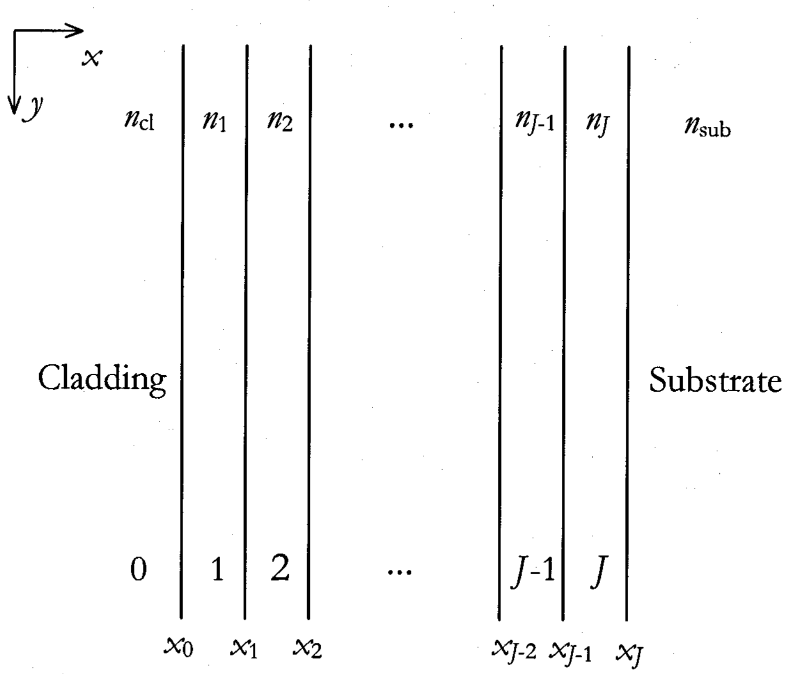

Figure 3.2.1 The J+2 layers dielectric stack, lying between the semi-infinite cladding and substrate media.

$$\frac{d^2 H_z}{d x^2}+\frac{d \ln n^2}{d x}\left(i k_z H_z-\frac{d H_z}{d x}\right)+\left(n^2 k_0^2-k_z^2\right) H_z=0 \tag{3.34}$$

Field components are related to each other via the following equations:

$$E_x=\frac{i \beta_z}{n^2 k_0^2-k_z^2} \cdot \frac{d E_z}{d x} \tag{3.35}$$

$$H_y=\left(\frac{\varepsilon_0}{\mu_0}\right)^{1/2} \frac{i k_0 n^2}{n^2 k_0^2-k_z^2} \cdot \frac{d E_z}{d x} \tag{3.36}$$

$$E_y=\left(\frac{\mu_0}{\varepsilon_0}\right)^{1/2} \frac{i k_0}{n^2 k_0^2-k_z^2} \cdot \frac{d H_z}{d x} \tag{3.37}$$

$$H_x=\frac{i k_z}{n^2 k_0^2-k_z^2} \cdot \frac{d H_z}{d x} \tag{3.38}$$

Equations (3.35) and (3.36) are independent of H_z , thus if we assume $E_z=0$ (for TE mode) we will immediately have $E_x=H_y=0$. If we express other field components in term of E_y, we will have the following relationships for nonzero field components,

$$H_x=\frac{-k_z}{k_0}\left(\frac{\varepsilon_0}{\mu_0}\right)^{1/2} E_y \tag{3.39}$$

$$H_z=\frac{-i}{k_0}\left(\frac{\varepsilon_0}{\mu_0}\right)^{1/2} \frac{dE_y}{d x} \tag{3.40}$$

where Eq. (3.12) is used and E_y satisfies the scalar wave equation (3.30). Similarly Eqs.(3.37) and (3.38) are independent of E_z . By assuming $H_z=0$ (for TM mode), we have $H_x=E_y=0$. Using Eq. (3.11), other nonzero field components in term of H_y are written as

$$E_x=\frac{k_z}{k_0 n^2}\left(\frac{\mu_0}{\varepsilon_0}\right)^{1/2} H_y \tag{3.41}$$

$$E_z = \frac{i}{k_0 n^2}\left(\frac{\mu_0}{\varepsilon_0}\right)^{1/2}\frac{dH_y}{dx} \tag{3.42}$$

where H_y does not satisfy the scalar wave equation, but Eq. (3.33).

A set of polarization-dependent parameters γ , U, V and W can be defined, so that all equations can be applied to both polarizations [2]. For each polarization, three field components are zero, and we assign U, V and W to the amplitudes of the nonzero components according to Table 3.1. The signs are chosen to coincide with the positive direction of the traveling wave propagation in the positive x and z axes.

Table 3.1 Polarization-dependent parameters

Parameters / Polarization	γ	U	V	W	Remaining field components
TE	$\frac{-i\alpha}{k_0}\left(\frac{\varepsilon_0}{\mu_0}\right)^{1/2}$	E_y	$-H_z$	H_x	$H_y = E_x = E_z = 0$
TM	$\frac{-i\alpha}{k_0 n^2}\left(\frac{\mu_0}{\varepsilon_0}\right)^{1/2}$	H_y	E_z	$-E_x$	$E_y = H_x = H_z = 0$

The power flow is given by the time averaged Poynting vector **S,** so the components can be written as:

$$S_x = \frac{1}{2}\mathrm{Re}\left(UV^*\right)\exp\left[i\left(k_z - k_z^*\right)z\right] \tag{3.43}$$

$$S_y = 0 \tag{3.44}$$

$$S_z = \frac{1}{2}\mathrm{Re}\left(UW^*\right)\exp\left[i\left(k_z - k_z^*\right)z\right] \tag{3.45}$$

where we consider the possibility of $\mathrm{Im}(k_z) \neq 0$. The total power is found by integrating **S** over an infinite cross sectional area A_∞

According to Eqs.(3.39)-(3.42) we have:

$$V = \frac{\gamma}{\alpha} \cdot \frac{dU}{dx} \tag{3.46}$$

$$W = i k_z \frac{\gamma}{\alpha} U \tag{3.47}$$

$$U = \frac{1}{\gamma\alpha} \cdot \frac{dV}{dx} \tag{3.48}$$

where

$$\gamma = \begin{cases} \dfrac{-i\alpha}{k_0}\left(\dfrac{\varepsilon_0}{\mu_0}\right)^{1/2} & \text{for TE mode} \\ \dfrac{-i\alpha}{k_0 n^2}\left(\dfrac{\mu_0}{\varepsilon_0}\right)^{1/2} & \text{for TM mode} \end{cases} \tag{3.49}$$

and

$$\alpha = \sqrt{k_z^2 - k_0^2 n^2} \tag{3.50}$$

The tangential field components U and V are continuous across the interfaces. Meanwhile W is the amplitude of the component normal to the interfaces and is proportional to U. Therefore, a total field is adequately specified by the vector $[U \quad V]^T$. Combining Eqs.(3.46) and (3.48), we have the following coupled equations

$$\frac{d}{dx}\begin{bmatrix} U \\ V \end{bmatrix} = \begin{bmatrix} 0 & \alpha\gamma^{-1} \\ \alpha\gamma & 0 \end{bmatrix} \cdot \begin{bmatrix} U \\ V \end{bmatrix} \tag{3.51}$$

3.3 Field Transfer Matrix Formulation

There are various ways to solve Eq. (3.51) for arbitrary $n(x)$ profile. However, we consider only a general approximate method that uses multiplication of 2×2 matrices. Unfortunately, this is not a very efficient method for complicated structures. If we approximate $n^2(x)$ stepwise (see Figure 3.3.1), then we will have

$$n^2(x)=\begin{cases} n_c^2 & x>0 \\ \sum_{j=1}^{J} n_j^2 \prod_{\Delta_j}(x-x_j) & x_J<x<0 \\ n_s^2 & x<x_J \end{cases} \tag{3.52}$$

where $\Delta_j = x_j - x_{j-1}$ is the width of j^{th} interval approximated with constant refractive index n_j^2. This technique is known as stratification method, which consists of replacing the arbitrary $n(x)$ by a multilayer structure, where the index value and width of each step is chosen to yield a good approximation of the original profile. It can be shown that this method is formally equivalent to the Euler discretization method, but it involves substantially greater computation. Although it is not a very efficient method, it is shown to be easy and versatile.

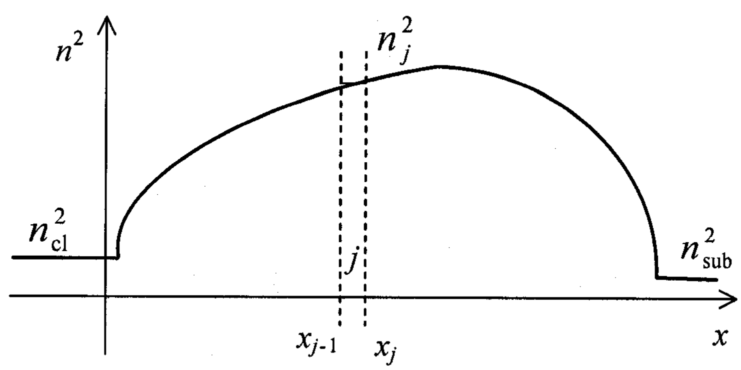

Figure 3.3.1 The refractive index profile of non-dissipative or non-active medium

The following field transfer matrix $\mathbf{M}_j$, relates the field amplitudes U_j and V_j at x_j to the corresponding amplitudes at the point x_{j-1} as follow

$$\begin{bmatrix} U_{j-1} \\ V_{j-1} \end{bmatrix} = \mathbf{M}_j \begin{bmatrix} U_j \\ V_j \end{bmatrix} \tag{3.53}$$

The total transfer matrix for a stack, consisting of J films is given by the product of the respective transfer matrices for individual layers

$$\mathbf{M} = \prod_{j=1}^{J} \mathbf{M}_j \tag{3.54}$$

It can be shown that the transfer matrix for non dissipative or non active medium (real refractive indices) are unimodular *i.e.*, its diagonal elements m_{11} and m_{22} are real, whereas its off-diagonal elements m_{12} and m_{21} are imaginary.

The total field transfer matrix $\mathbf{M}$ characterizing the stack must yield the correct field at the cladding interface, when it is applied to the field at the substrate interface, *i.e.*,

$$\begin{bmatrix} U_{\text{cl}} \\ V_{\text{cl}} \end{bmatrix} = \mathbf{M} \begin{bmatrix} U_{\text{sub}} \\ V_{\text{sub}} \end{bmatrix} \tag{3.55}$$

The propagation constant k_z must be found in such a way that the above equation remains valid. Using the above procedure, the dispersion relation can usually be obtained.

The field transfer matrix $\mathbf{M}_j$ accounting for the wave propagation through the bulk of each layer, is considered in next sections.

3.4 The field transfer matrix for a uniform layer

Consider the j^{th} layer whose dielectric profile is constant, as n_j^2 . Taking Laplace transform of Eq.(3.51), we obtain

$$\begin{bmatrix} s\,u_j \\ s\,v_j \end{bmatrix} - \begin{bmatrix} U_{j-1} \\ V_{j-1} \end{bmatrix} = \begin{bmatrix} 0 & \gamma_j^{-1}\alpha_j \\ \gamma_j \alpha_j & 0 \end{bmatrix} . \begin{bmatrix} u_j \\ v_j \end{bmatrix} \tag{3.56}$$

where $u_j = \mathcal{L}(U_j)$, $v_j = \mathcal{L}(V_j)$ and s is the variable of the Laplace transform. By solving Eq.(3.56) we have

$$\begin{bmatrix} u_j \\ v_j \end{bmatrix} = \frac{1}{s^2 - \alpha_j^2} \begin{bmatrix} s & \gamma_j^{-1}\alpha_j \\ \gamma_j \alpha_j & s \end{bmatrix} \cdot \begin{bmatrix} U_{j-1} \\ V_{j-1} \end{bmatrix} \tag{3.57}$$

Thus $\mathbf{M}_j$ equals to [2]

$$\mathbf{M}_j = \begin{bmatrix} \cosh(\alpha_j \Delta_j) & -\gamma_j^{-1} \sinh(\alpha_j \Delta_j) \\ -\gamma_j \sinh(\alpha_j \Delta_j) & \cosh(\alpha_j \Delta_j) \end{bmatrix} \tag{3.58}$$

Note that $\mathbf{M}_j$ is unimodular (real diagonal and imaginary off-diagonal elements).

3.5 The field transfer matrix for 1-D photonic crystal

A unit cell of a binary stratified media (1-D photonic crystal) consists of two layers of different refractive index n_1 and n_2 or

$$n(x) = \begin{cases} n_1 & 0 < x < \tau\Lambda \\ n_2 & \tau\Lambda < x < \Lambda \end{cases} \tag{3.59}$$

where Λ is the period of the layered media, and τ is the duty factor. Using Eq.(3.58), the transfer matrix of the cell can be obtained as:

$$\mathbf{T} = \mathbf{M}_{1,2} = \begin{bmatrix} \cosh(\alpha_1 a)\cosh(\alpha_2 b) + \gamma_1^{-1}\gamma_2 \sinh(\alpha_1 a)\sinh(\alpha_2 b) & -\gamma_2^{-1}\cosh(\alpha_1 a)\sinh(\alpha_2 b) - \gamma_1^{-1}\sinh(\alpha_1 a)\cosh(\alpha_2 b) \\ -\gamma_2 \cosh(\alpha_1 a)\sinh(\alpha_2 b) - \gamma_1 \sinh(\alpha_1 a)\cosh(\alpha_2 b) & \cosh(\alpha_1 a)\cosh(\alpha_2 b) + \gamma_1\gamma_2^{-1}\sinh(\alpha_1 a)\sinh(\alpha_2 b) \end{bmatrix} \tag{3.60}$$

Where $a = \tau\Lambda$, and $b = (1-\tau)\Lambda$. Note also that matrix $\mathbf{T}$ is unimodular.

3.6 Dispersion relation for a 1-D photonic crystal

If the media is periodic, *i.e.*, $n(x) = n(x + \Lambda)$, then according to Floquet theorem, wave components are of the form

$$U(x) = U_{k_x}(x)\exp(ik_x x) \tag{3.61}$$

where $U_{k_x}(x)$ is periodic with a period of Λ, *i.e.*,

$$U_{k_x}(x + \Lambda) = U_{k_x}(x) \tag{3.62}$$

and k_x is Bloch wave number. Using transfer matrix of Eq.(3.60), we have

$$\begin{bmatrix} U_1 \\ V_1 \end{bmatrix} = \mathbf{T}\begin{bmatrix} U_n \\ V_n \end{bmatrix} = \exp(-i\,k_x\Lambda)\begin{bmatrix} U_n \\ V_n \end{bmatrix} \tag{3.63}$$

The phase factor $\exp(-i\,k_x\Lambda)$ is thus the eigenvalue of the translation matrix $\mathbf{T}$ which can be given by

$$\exp(-i\,k_x\Lambda) = \frac{1}{2}(t_{11} + t_{22}) \pm \left\{\left[\frac{1}{2}(t_{11} + t_{22})\right]^2 - 1\right\}^{\frac{1}{2}} \tag{3.64}$$

where t_{11}, t_{12}, t_{21} and t_{22} are matrix components of transfer matrix $\mathbf{T}$. Since matrix $\mathbf{T}$ is uni-modular, its eigenvalues are inverse of each other. Eq.(3.64) gives the dispersion relation between ω, k_z and k_x. Rewriting Eq. (3.64) as [3]

$$k_x\Lambda = \cos^{-1}\left[\frac{1}{2}(t_{11} + t_{22})\right] \tag{3.65}$$

Regimes $\left|(t_{11} + t_{22})/2\right| < 1$ corresponds to real k_xa nd thus propagating Bloch waves. In this case wave vector finds component in x direction (in addition of the component in z direction), *i.e.*,

$$\mathbf{k} = k_z \hat{a}_z + k_x \hat{a}_x \tag{3.66}$$

However when $\left|(t_{11}+t_{22})/2\right|>1$ then $k_x = m\pi/\Lambda + i\,k_{xi}$ which has an imaginary part k_{xi}, so the Bloch wave is evanescent. The regime in which $\left|(t_{11}+t_{22})/2\right|=1$, corresponds to the wave propagation in z direction ($k_x = m\pi/\Lambda$, corresponding to band edges). In this case Eq.(3.65) can be written as:

$$\cosh(\alpha_1 a)\cosh(\alpha_2 b)+\frac{1}{2}\left(\frac{\gamma_1}{\gamma_2}+\frac{\gamma_2}{\gamma_1}\right)\sinh(\alpha_1 a)\sinh(\alpha_2 b)=1 \tag{3.67}$$

Introducing more conventional variable k (transversal wave number instead of α)

$$k = i\alpha = \sqrt{n^2 k_0^2 - k_z^2} \tag{3.68}$$

in Eq. (3.67) and using Eq. (3.49), we have [4]

$$\begin{cases} \cos(k_1 a)\cos(k_2 b)-\dfrac{1}{2}\left(\dfrac{k_2}{k_1}+\dfrac{k_1}{k_2}\right)\sin(k_1 a)\sin(k_2 b)=1 & \text{for TE modes} \\ \cos(k_1 a)\cos(k_2 b)-\dfrac{1}{2}\left(\dfrac{n_1^2 k_2}{n_2^1 k_1}+\dfrac{n_2^2 k_1}{n_1^2 k_2}\right)\sin(k_1 a)\sin(k_2 b)=1 & \text{for TM modes} \end{cases} \tag{3.69}$$

The eigenvectors corresponding to the eigenvalues of Eq.(3.64) are obtained from Eq.(3.63) as

$$\begin{bmatrix} U_0 \\ V_0 \end{bmatrix} = \begin{bmatrix} t_{12} \\ \exp(-ik_x\Lambda)-t_{11} \end{bmatrix} \tag{3.70}$$

The diagram showing the relation between k_x and k_z at specific wavelength is called the wave vector diagram (or equi-frequency contour) [5]. Usually we normalize wave vectors versus k_0 (the wave number in vacuum) as below

$$n_x \equiv k_x/k_0, \qquad n_z \equiv k_z/k_0 \tag{3.71}$$

The analogy of this diagram and index ellipse is obvious [6]. This type of normalization also makes implementing of wave vector interface boundary condition easy (see Eq.(3.79)). The diagram can be made only on the first quadrant; the other parts of the diagram can be obtained easily using the group symmetry of the lattice, namely there are mirror symmetries around n_z and n_x.

3.7 Snell's law in photonic crystals

Consider a time harmonic plane wave from a homogenous and isotropic medium of refractive index n_0 with a wave-number $k_1 = n_0 k_0$ is incident to another homogenous and isotropic medium of refractive index n_0' where the incident angle is φ_1. A schematic diagram of the structure is depicted in Figure 3.7.1. The tangential component of the wave vector of at the planar interface of two different media must be conserved. This is the equivalent way of expressing the Snell's refraction in the conventional optics. This law is originated from the translational symmetry of the system in the direction of interface [7]. Any wave solutions have to follow this symmetry, or

$$k_1 \sin\varphi_1 = k_1' \sin\varphi_2 \tag{3.72}$$

Normalize it versus k_0, we have

$$n_0 \sin\varphi_1 = n_0' \sin\varphi_2 \tag{3.73}$$

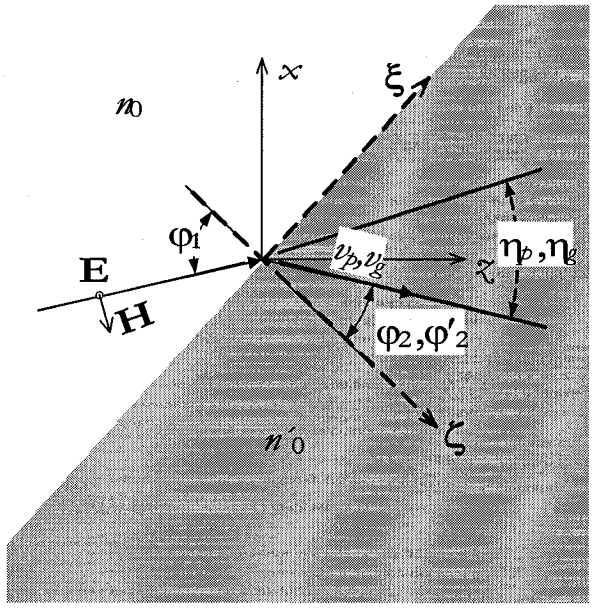

Glossary

n_0: Refractive index of homogenous medium

n'_0: Higher refractive index of 1D photonic crystal

φ_1: Incident angle

φ_2: Refracted phase velocity angle

φ'_2 : Refracted group velocity angle

v_p : Phase velocity

v_g : Group velocity

η_p: Phase velocity deviation angle

η_g : Group velocity deviation angle

Figure 3.7.1 The interface of the two homogenous, isotropic media

Now consider a time harmonic plane wave from a homogenous and isotropic medium of refractive index n_0 with a wave-number $k_1 = n_0 k_0$ is incident to a 1-D photonic crystal slanted by θ_1, where again the incident angle is φ_1 (see Figure 3.7.2). Snell's law now reads

$$k_0 n_0 \sin\varphi_1 = k_\xi \tag{3.74}$$

where k_ξ is the wave vector component of the photonic crystal parallel to the interface. Eq.(3.74) in a normalized form can be expressed as

$$n_0 \sin\varphi_1 = n_\xi \tag{3.75}$$

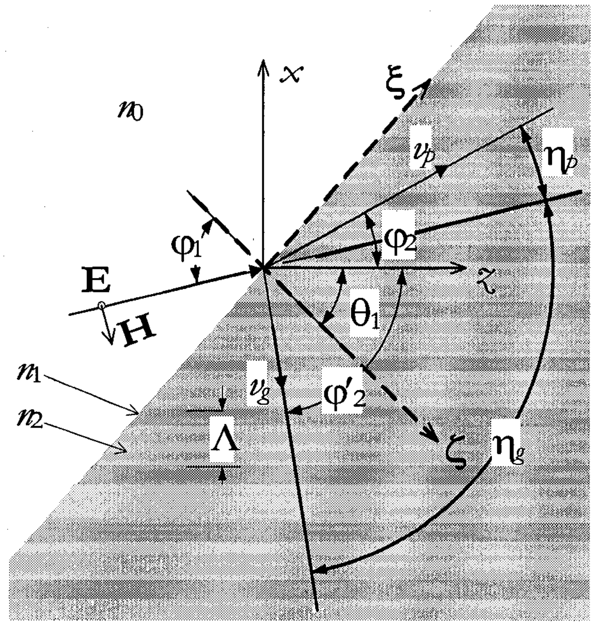

Glossary

n_0: Refractive index of homogenous medium
n_1: Higher refractive index of 1D photonic crystal
n_2: Lower refractive index of 1D photonic crystal
Λ: 1D photonic crystal period
θ_1: 1D photonic crystal slant angle
φ_1: Incident angle
φ_2: Refracted phase velocity angle
φ'_2 : Refracted group velocity angle
v_p : Phase velocity
v_g : Group velocity
η_p : Phase velocity deviation angle
η_g : Group velocity deviation angle

Figure 3.7.2 The interface of the 1-D photonic crystal and the homogenous medium

Figure 3.7.3 shows how Eq.(3.75) can be implemented on the wave vector diagram to obtain the quiescent point (operating point). From the quiescent point one can fond the refracted Bloch mode direction, and (as we show in the proceeding sections) the corresponding group and phase velocities.

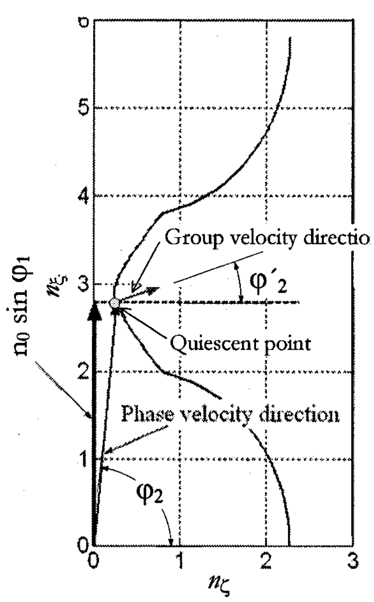

Figure 3.7.3 A normalized wave vector diagram and the quiescent point

The slanted 1-D photonic crystal can be assumed as a 2-D rectangular lattice with the following lattice constants

$$\Lambda_{\xi} = \Lambda/\cos\theta_1, \qquad \Lambda_{\zeta} = \Lambda/|\sin\theta_1| \tag{3.76}$$

The unit cell is depicted Figure 3.7.4. The wave vector diagram of the slanted 1-D photonic crystal can be obtained either by considering it as a 2-D square lattice with the unit cell depicted in Figure 3.7.4 (and analyzing the 2-D lattice accordingly), or by rotating the wave vector diagram of 1-D photonic crystal by the slant angle θ_1. Obviously the later case seems easier to implement, as we adopt it in the following sections.

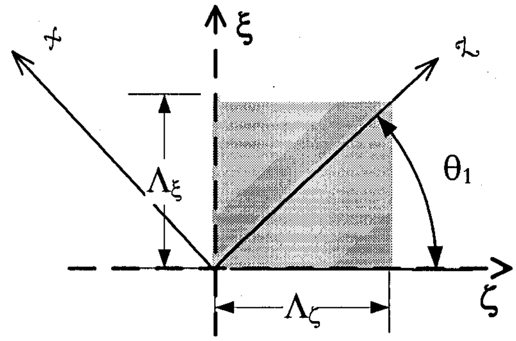

Figure 3.7.4 The unit cell of the slanted slab 1-D photonic crystal

3.8 The Quiescent point of an slanted wave vector diagram

For TM modes, we choose E_y as the expanding field and the incident wave can be expressed as

$$\mathbf{E}_i = \Phi \exp\left[i\left(k_{\xi}\xi + k_{\zeta}\zeta\right)\right]\hat{\mathbf{a}}_y \tag{3.77}$$

where

$$k_{1\xi} = k_1 \sin\varphi_1, \quad k_{1\zeta} = k_1 \cos\varphi_1 \tag{3.78}$$

and $k_1 = n_0 k_0$ is the wave vector in the free space (k_0 is the wave vector in vacuum). Applying the Snell's law of Eq.(3.74) we have

$$k_{1\xi} = k_x \cos\theta_1 + k_z \sin\theta_1 \tag{3.79}$$

Combining Eqs.(3.79) and (3.65) we can obtain the dispersion equation, from which the transmission phase vector can de obtained as below

$$\Lambda\left(k_{1\xi} \sec\theta_1 - k_z \tan\theta_1\right) = \cos^{-1}\left[\frac{1}{2}\left(t_{11} + t_{22}\right)\right] \tag{3.80}$$

It is interesting to note that the slanted 1-D photonic crystal can be assumed periodic in both x and z directions, so the wave inside photonic crystal can be expressed as

$$\Phi(\zeta,\xi) = \Psi_{k_\xi,k_\zeta}(\zeta,\xi)\exp\left(ik_\zeta\zeta + ik_\xi\xi\right) \tag{3.81}$$

Where $\Psi_{k_\zeta,k_\xi}(\zeta,\xi)$ is a periodic function as below

$$\Psi_{k_\xi,k_\zeta}(\zeta,\xi) = \Psi_{k_\zeta,k_\xi}\left(\zeta + \Lambda/\sin\theta_1, \xi + \Lambda/\cos\theta_1\right) \tag{3.82}$$

and k_ξ and k_ζ are the Bloch wave numbers of the slanted photonic crystal. They are related to the Bloch wave number of the un-slanted photonic crystal by

$$\begin{bmatrix} k_\zeta \\ k_\xi \end{bmatrix} = \begin{bmatrix} \cos\theta_1 & -\sin\theta_1 \\ \sin\theta_1 & \cos\theta_1 \end{bmatrix} \begin{bmatrix} k_z \\ k_x \end{bmatrix} \tag{3.83}$$

Then the condition (3.79) can be expressed as

$$k_\xi = k_{1\xi} \tag{3.84}$$

Knowing k_ξ from Eq.(3.84), and by solving Eq. (3.80) for k_z, one can obtain k_ζ from

$$k_\zeta = k_z \sec\theta_1 - k_{1\xi} \tan\theta_1 \tag{3.85}$$

3.9 A typical wave vector diagram for 1-D photonic crystal and form birefringence

By solving Eq. (3.80) at a particular wavelength, we can obtain the diagram showing the relation between k_x and k_z at that specific wavelength. For illustration purposes consider the following case,

$$\begin{aligned}
&\lambda = 1545.3 \text{ nm} \\
&\tau = 0.5 \\
&\theta_1 = 0 \\
&n_1 = \begin{cases} 3.1294 & \text{for TE mode} \\ 3.2565 & \text{for TM mode} \end{cases} \\
&n_2 = 1
\end{aligned} \tag{3.86}$$

Figure 3.9.1 and Figure 3.9.2 shows the normalized wave vector diagram for TE and TM modes. Note the small period regime where the form birefringence can be observed.

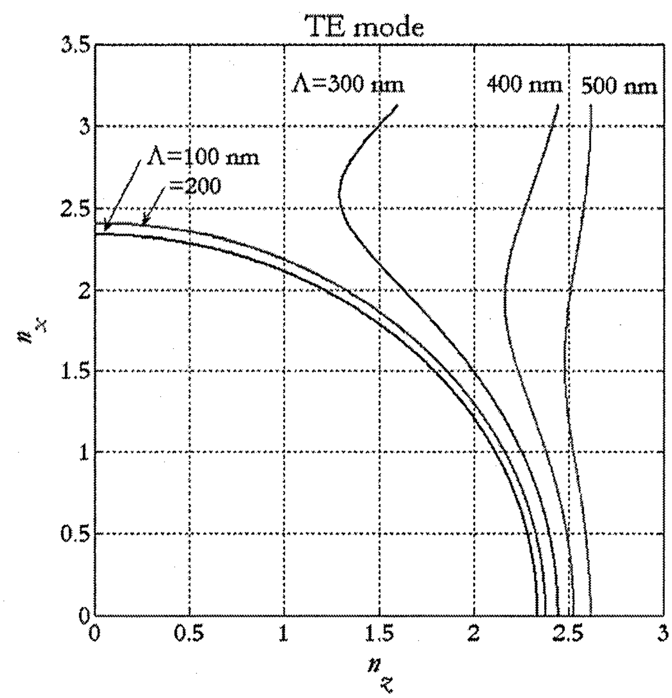

Figure 3.9.1 The normalized wave vector diagram for TE mode (E_y is dominant) at $\lambda = 1.54982$ μm for different periods

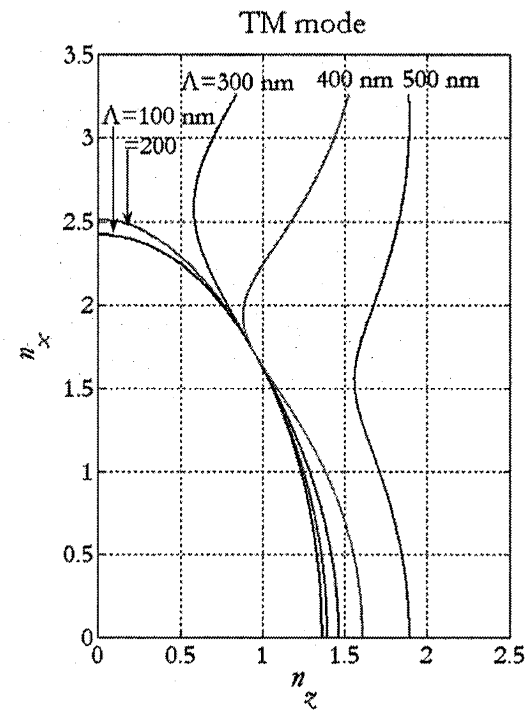

Figure 3.9.2 The normalized wave vector diagram for TM mode (E_x is dominant) at $\lambda = 1.54982$ μm for different periods.

The birefringence property of a periodic layered medium will now be discussed. The long wavelength (or short period) regime is worthy of attention. If the period Λ is sufficiently small compared to the wavelength, then the whole structure behaves as if it is homogeneous and uniaxially anisotropic. The wave thus behaves as if it is a plane wave. In the long-wavelength regime ($\lambda \gg \Lambda$), these are similar to the dispersion curves of electromagnetic waves in a negative uniaxial crystal. To demonstrate the analogy we take the limit of $\alpha_1 a \ll 1$, $\alpha_2 b \ll 1$ and $k_0\Lambda \ll 1$ and expand all the transcendental functions in Eq.(3.69). After neglecting higher-order terms, we obtain [8]:

$$\begin{aligned} \frac{n_x^2}{n_o^2} + \frac{n_z^2}{n_o^2} &= 1 \quad \text{for TE mode} \\ \frac{n_x^2}{n_o^2} + \frac{n_z^2}{n_e^2} &= 1 \quad \text{for TM mode} \end{aligned} \tag{3.87}$$

with

$$
\begin{aligned}
n_o^2 &= \tau n_1^2 + (1-\tau) n_2^2 \\
\frac{1}{n_e^2} &= \tau \frac{1}{n_1^2} + (1-\tau)\frac{1}{n_2^2}
\end{aligned}
\tag{3.88}
$$

where $\tau = a/\Lambda$. Equations (3.87) represent the two shells of the normal surface in the $n_z n_x$ plane. One surface of Eqs.(3.87), which applies to the a TE wave is a sphere, while the TM normal surface is an ellipsoid of revolution. TE waves thus are formally similar to the so-called ordinary waves in a uniaxial crystal, while TM waves are the extraordinary waves. The normal surface becomes more complicated at higher periods. It consists of two oval surfaces osculating each other at the intersections with the n_x axis as long as the wavelength is higher than the first forbidden gap. For wavelengths higher than the forbidden gap, the oval surfaces break into several sections. The break points occur at

$$
n_x = m\frac{\lambda}{2\Lambda} \tag{3.89}
$$

which is the Bragg condition. For the wavelengths lower than the forbidden gap and before the second band emerges, there is no propagating wave through photonic crystal.

The ordinary and extraordinary refractive indices according to Eq.(3.88) are 2.323 and 1.352, respectively. These values are matched well by the values obtained from Figure 3.9.1 and Figure 3.9.2.

The scaling law of electromagnetics can be used to relate period to the wavelength, so one can normalize period versus wave number in vacuum, and find a transcendental wave vector diagram. In other words, if we multiply period by $\Lambda \rightarrow \alpha\Lambda$, the wave vector diagram is the same as when the wavelength is divided by the same factor, *i.e.*, $\lambda \rightarrow \lambda/\alpha$. For practical reasons, Figure 3.9.3 shows a typical normalized wave vector diagram at different wavelengths (fixed period), which is obtained using Eq.(3.80) and the following parameters

$$
\begin{aligned}
&\Lambda = 273.8\,\text{nm} \\
&\lambda = 1545.3\ \text{nm} \\
&\tau = 0.5 \\
&\theta_1 = 0 \\
&n_1 = 3.1294 \\
&n_2 = 1 \\
&\text{Polarization TE, Electric field in } y \text{ direction}
\end{aligned}
\tag{3.90}
$$

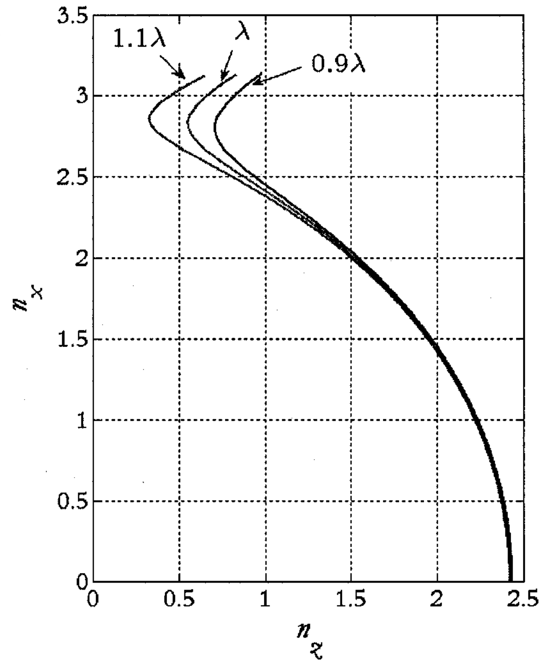

Figure 3.9.3 A typical normalized wave vector diagram for 1-D photonic crystal at different wavelength

The wave vector diagram evolution with wavelength is the basis of dispersion. This dispersion as it is shown in Figure 3.9.3 is at the highest value near the band-edge, where the transmission is poor. There are separate sections devoted to the two different types of **k** and ***S*** vectors dispersion, but before that we will talk about the Snell's law and how the quiescent point can be obtained.

3.10 k-vector dispersion

The variation of the phase front direction (or direction of phase velocity, or wave vector) with wavelength is called **k**-vector dispersion [9-12]. Figure 3.7.2 shows the interface between free space and a 1-D photonic crystal. The angle between phase velocity vector and the horizon is defined as φ_2. The incident and slant angles are φ_1 and θ_1 respectively. The phase velocity deviation angle (η_p) is defined as

$$\eta_p = \varphi_1 - \varphi_2 \tag{3.91}$$

Then the phase velocity dispersion of a single junction can be defined as

$$\frac{\partial \eta_p}{\partial \lambda} = \frac{\eta_p(\lambda_2) - \eta_p(\lambda_1)}{\lambda_2 - \lambda_1} = \frac{\varphi_2(\lambda_2) - \varphi_2(\lambda_1)}{\lambda_2 - \lambda_1} \tag{3.92}$$

The interface condition (Eq. (3.79)) is crucial determining how the wave front is refracted at the photonic crystal. Assuming the refractive index of the homogenous region is constant with wavelength, the quiescent point at each wavelength is the cross section of the horizontal line $n_x = n_0 \sin\varphi_1$, and the normalized wave vector diagram (which may be rotated by the slant angle too) at any specific wavelength (see Figure 3.10.1). The normalized phase vector ($\bar{k}_p = k_p / k_0$) is the vector from the origin to the quiescent point. The angle between the phase vector and the horizontal direction (ζ axis) is φ_2 (see Figure 3.7.2).

Figure 3.10.1 shows the same wave vector diagram as in Figure 3.9.3, but we have shown a typical quiescent points, normalized phase vectors, and so on.

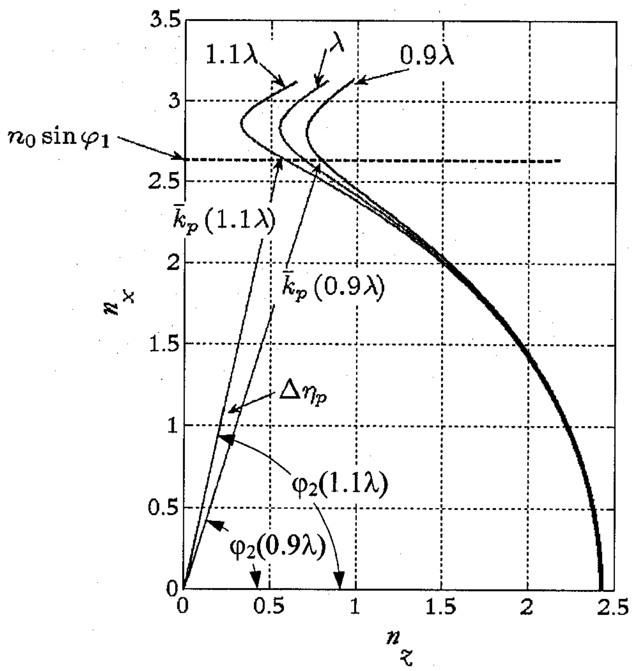

Figure 3.10.1 The normalized wave vector diagram and quiescent points at different wavelength. The slant angle is zero.

Figure 3.10.2 depicts the phase velocity direction versus incident angle for various wavelengths. The free space refractive index is assumed $n_0 = n_1$ in (3.90). It is interesting that the deviation angle is maximized at the band-edge. As we will show later, this is the case only when the slant angle is zero.

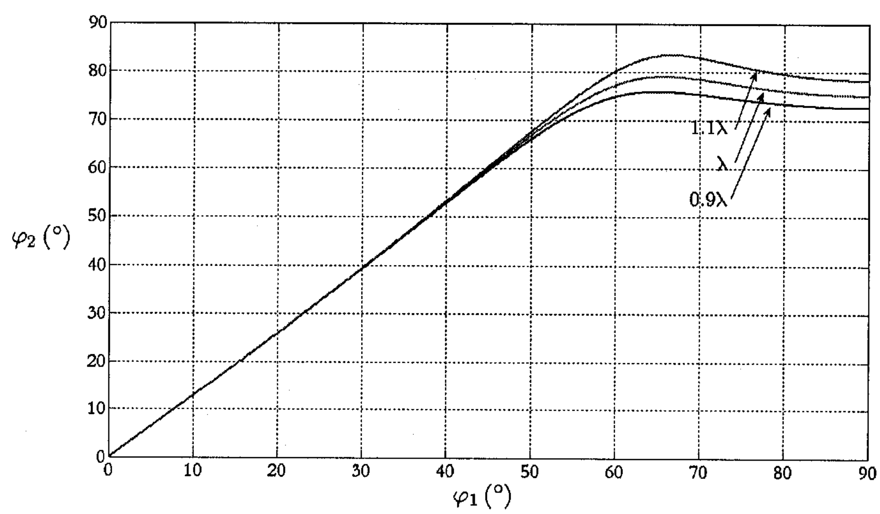

Figure 3.10.2 Phase velocity angle versus incident angle when slant angle is zero.

Figure 3.10.3 shows the phase velocity dispersion of a single junction versus incident angle. The dispersion is maximum at the band-edge $0.24\ °/\mathrm{nm}$. The dispersion decreases fast away from the band edge at the first Brillouin zone (toward $\varphi_1 = 0$), but it declines slower from the band edge at the second Brillouin zone (toward $\varphi_1 = 90°$).

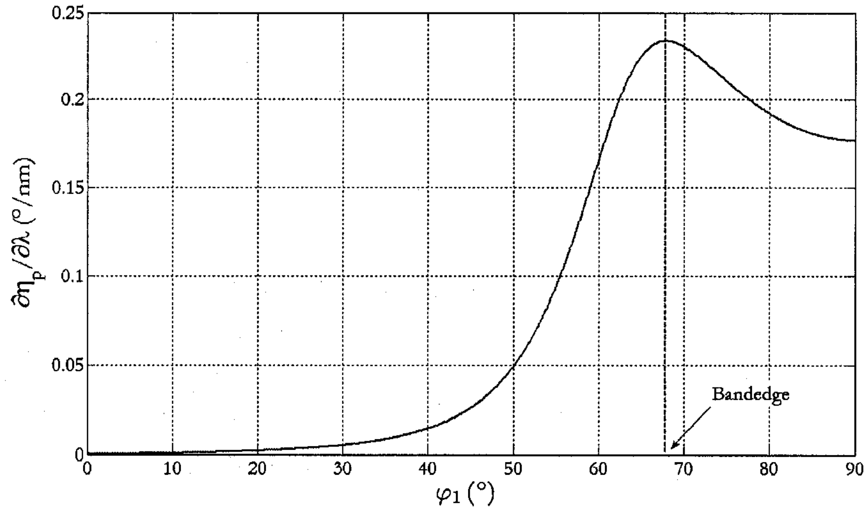

Figure 3.10.3 The phase velocity dispersion of a single junction versus the incident angle when slant angle is zero.

Our focus has been on untitled 1-D photonic crystal so far. Slanting the photonic crystal is another degree of freedom that has a great effect on dispersion and transmission. Let us slant the photonic crystal by $\theta_1 = -15°$. Using Eq.(3.80), the normalized wave vector diagram with the parameters of (3.90) is plotted in Figure 3.10.4. The quiescent points are located at the second Brillouin zone. This is the case that we are especially interested in chapter 8, where we try to optimize the superprism based on the phase velocity dispersion.

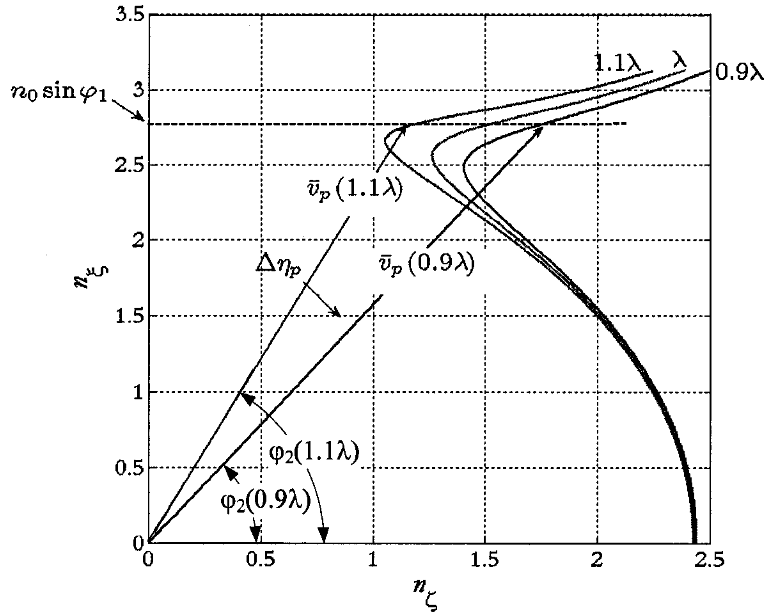

Figure 3.10.4 The normalized wave vector diagram and quiescent points at different wavelengths. The slant angle is -15°.

Figure 3.10.5 and Figure 3.10.6 show phase velocity angle and dispersion versus incident angle. As is shown in Figure 3.10.6, while the maximum dispersion is increased (from 0.24 °/nm for untitled to 0.29 °/nm for -15° of slant), it is possible to avoid the band-edge when the maximum dispersion is chosen.

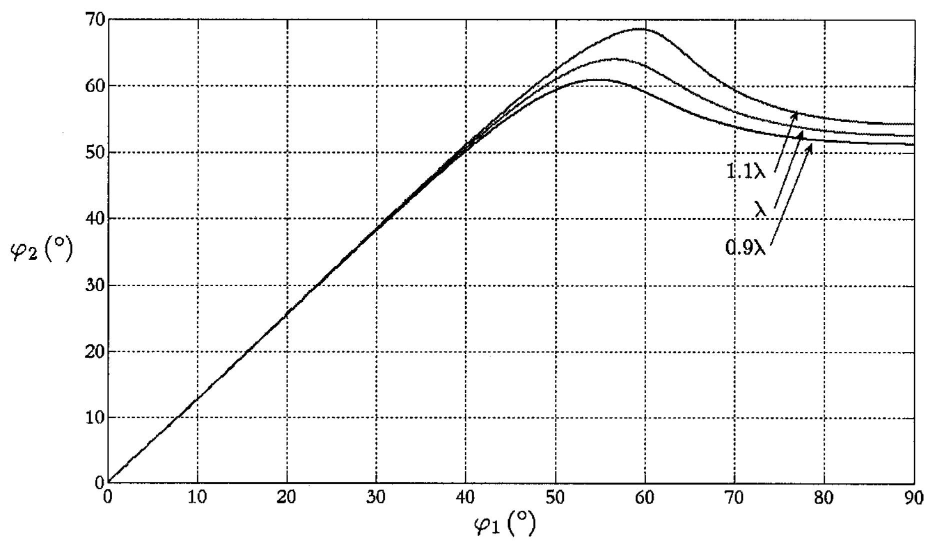

Figure 3.10.5 Phase velocity angle versus incident angle when slant angle is -15°.

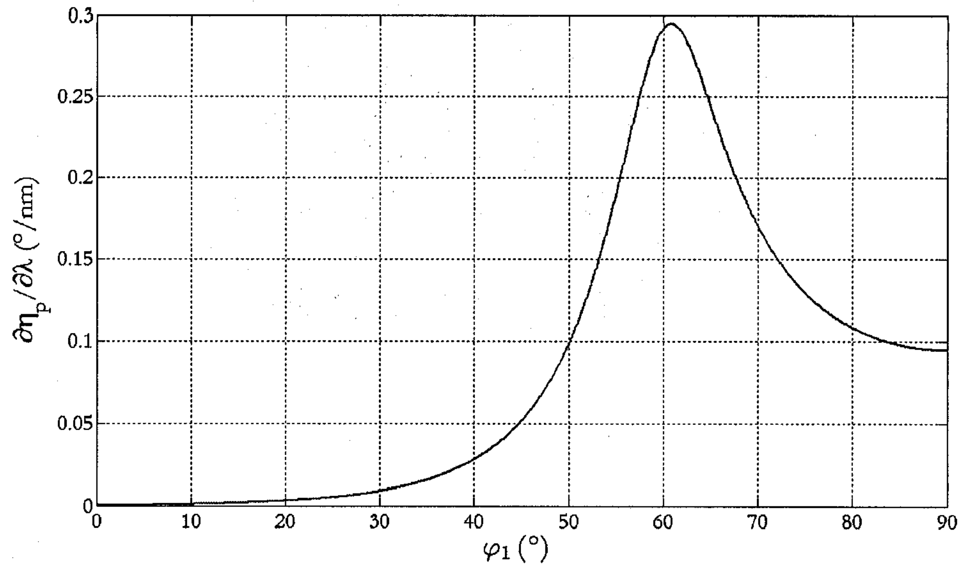

Figure 3.10.6 The phase velocity dispersion of a single junction versus the incident angle when slant angle is -15°.

The optimization of the 1-D photonic crystal for obtaining the best dispersion will be discussed in chapter 8. We will show that it is not always desirable to maximize the phase velocity dispersion.

3.11 *S*-vector dispersion

The energy velocity integrated over a unit cell is identical with the group velocity [13-15], so the direction of the group velocity in an infinite photonic crystal coincides with the energy flow (or the beam direction) [16]. The group velocity can be obtained from

$$\mathbf{v}_g = \nabla_k \omega(k) = c\frac{-\nabla_k \lambda(k)}{2\pi\lambda^2} \tag{3.93}$$

Where c is the speed of light in vacuum. The group velocity vector at the quiescent point is perpendicular to the wave vector diagrams and is directed toward the lower wavelength contours as it is indicated in Eq.(3.93) and shown in Figure 3.11.1.

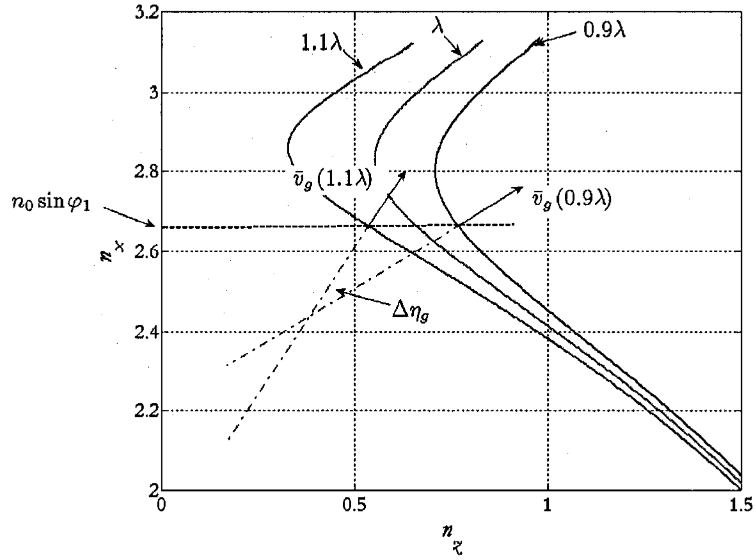

Figure 3.11.1 The typical wave vector diagram and the group velocity at the quiescent points, the slant angle is zero.

The beam deviation angle (or group velocity deviation angle) is the difference between incident angle (φ_1 group velocity direction outside the photonic crystal) and the group velocity direction inside the photonic crystal φ_2' (see Figure 3.7.2) , i.e,.

$$\eta_g = \varphi_2' - \varphi_1 \tag{3.94}$$

The group velocity dispersion is defined as the relative change of group velocity deviation angle with respect to the wavelength, *i.e.*,

$$\frac{\partial \eta_g}{\partial \lambda} = \frac{\eta_g(\lambda_2) - \eta_g(\lambda_1)}{\lambda_2 - \lambda_1} = \frac{\varphi_2'(\lambda_2) - \varphi_2'(\lambda_1)}{\lambda_2 - \lambda_1} \tag{3.95}$$

Figure 3.11.2 and Figure 3.11.3 show the beam direction angle and group velocity direction versus the incident beam direction. It is interesting that after the band-edge and at the second Brillouin zone, the refraction and group velocity dispersion are negative. The group velocity dispersion (as it is expected and shown in Figure 3.11.3) is zero at the band edge [17]. The maximum dispersion is about 1.3°/nm.

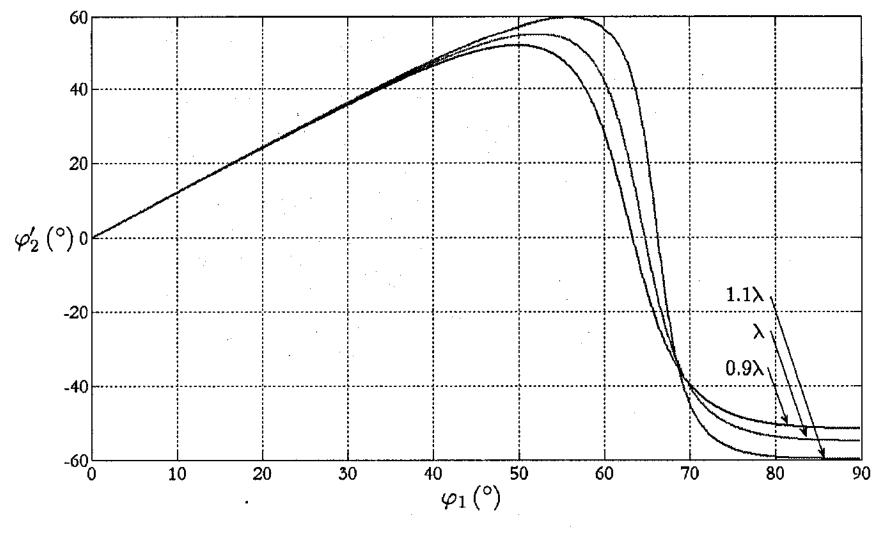

Figure 3.11.2 The beam direction versus incident beam direction at various wavelength. The slant angle is zero.

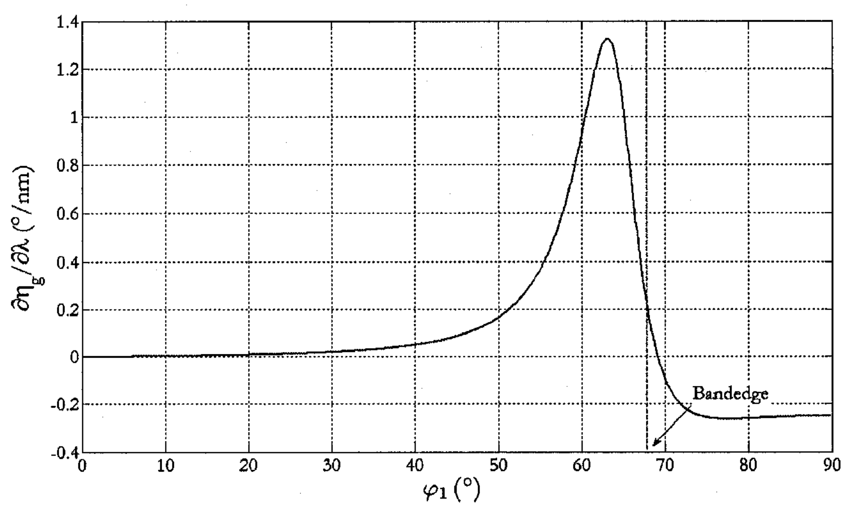

Figure 3.11.3 The group velocity dispersion versus incident beam direction, the slant angle is zero.

Figure 3.11.4 shows the part of slanted wave vector diagram (by -15°), which is relevant to the quiescent points and the corresponding beam direction.

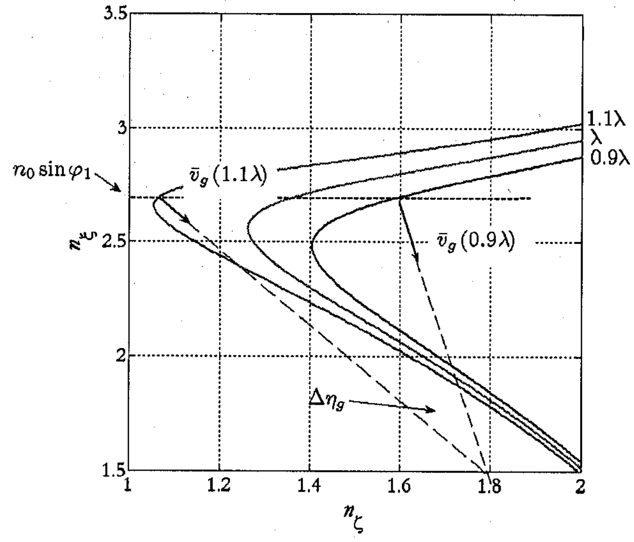

Figure 3.11.4 The wave vector diagram of typical 1-D photonic crystal, the slant angle is -15°. The group velocity directions are also shown at the quiescent points.

Figure 3.11.5 and Figure 3.10.6 show the beam direction and group velocity dispersion versus incident angle. As is shown in Figure 3.11.6, the maximum group velocity is increased from 1.3°/nm of the un-slanted photonic crystal (see Figure 3.11.3) to 2.6°/nm of -15° slanted case. Maximizing the dispersion and its effect on the superprism area is an important issue, which will be discussed thoroughly in chapter 6.

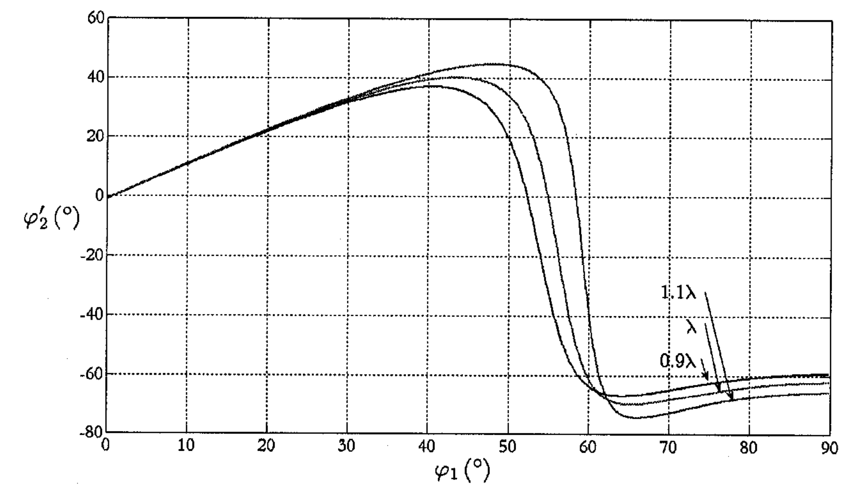

Figure 3.11.5 The beam angle inside photonic crystal versus incident angle at different wavelengths.

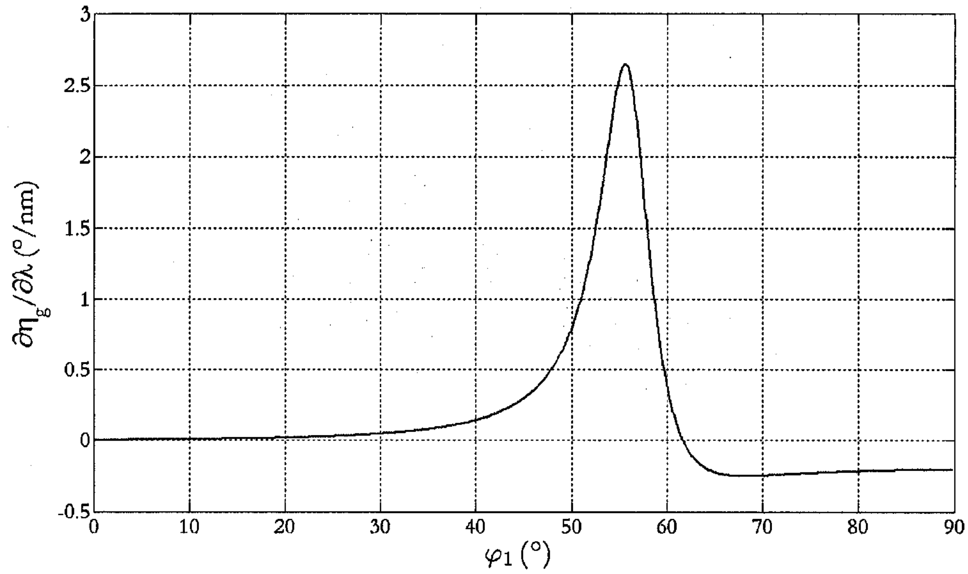

Figure 3.11.6 The group velocity dispersion versus incident angle for the slanted 1-D photonic crystal.

3.12 Refraction and transmission wave vector from 1-D photonic crystal, the condition of having only one diffraction order

The transmission and reflection at the interface of a bulk 2-D (un-slanted) photonic crystal is analyzed and documented in [18]. In general, when the interface is not aligned with a special crystal direction, the dielectric structure (including both the crystal and the interface) is not periodic [19]. However, in 1-D photonic crystal, for any slant angle the structure remains periodic.

The reflected waves in Figure 3.7.2 (from the different diffraction orders) have two wave vector components. One of them can be written as

$$k_{r,\xi}^{m} = k_{\xi} + \frac{2m\pi}{\Lambda_{\xi}} \tag{3.96}$$

The other reflected wave vector component can be written as

$$k_{r,\zeta}^{m} = \left(k_1^2 - \left|k_{r,\xi}^{m}\right|^2\right)^{\frac{1}{2}} \tag{3.97}$$

The square root sign in Eq. (3.97) has to be selected to guarantee the reflection of a propagating wave or a decaying wave from the interface. The reflected wave then can be expressed as

$$\mathbf{E}_r = \sum_m \mathrm{R}_m^E \exp\left[i\left(\xi k_{r,\xi}^{m} + \zeta k_{r,\zeta}^{m}\right)\right]\hat{\mathbf{a}}_y \tag{3.98}$$

or

$$\mathbf{E}_r = \sum_m \mathrm{R}_m^E \exp\left\{i\xi\left(k_\xi + 2m\pi/\Lambda_\xi\right) + i\zeta\left[k_1^2 - \left(k_\xi + 2m\pi/\Lambda_\xi\right)^2\right]^{\frac{1}{2}}\right\}\hat{\mathbf{a}}_y \tag{3.99}$$

The reflected wave is not evanescent if (see Eq.(3.97))

$$k_1 > k_{r,\xi}^{m} \tag{3.100}$$

All reflected wave except the main one ($m = 0$) are evanescent, provided

$$\Lambda_\xi < \frac{\lambda_{\min}}{\left(1 + \left|\sin\varphi_1\right|\right) n_0} \tag{3.101}$$

where $\lambda_{\min}$ is the minimum wavelength of interest. Or using Eq.(3.76), we have

$$\Lambda < \frac{\lambda_{\min}\cos\theta_1}{\left(1 + \left|\sin\varphi_1\right|\right) n_0} \tag{3.102}$$

The above equation is also valid for the other type of polarization. Figure 3.12.1 shows the condition that all reflections due to different diffraction orders except zero are evanescent. The homogenous medium refractive index is assumed $n_0 = 3.104$ at $\lambda_{\min} = 1537.40\ \mathrm{nm}$.

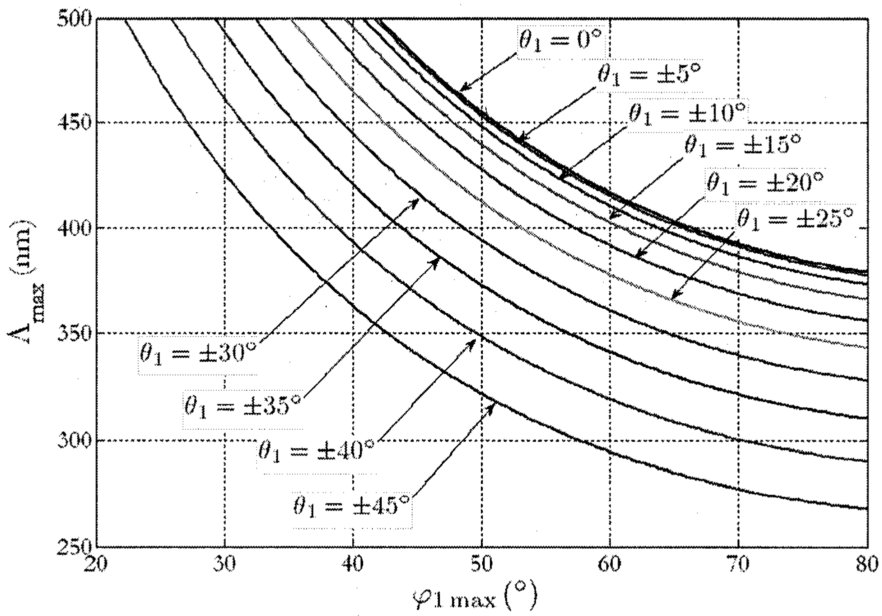

Figure 3.12.1 The condition for reflection due to higher order diffraction being evanescent

Normally, we would like to work near the band-edge where the dispersion is high; so we are not interested to let this region be unavailable by slanting the photonic crystal too much. The maximum and minimum allowable rotation is the angle that brings the band-edge to the n_x and/or n_z axis. Considering that, n_{z0} (known as the band-edge after slanting by θ_1) moves to the new location of

$$\begin{bmatrix} n_z \\ n_x \end{bmatrix} = \begin{bmatrix} \cos\theta_1 & -\sin\theta_1 \\ \sin\theta_1 & \cos\theta_1 \end{bmatrix} \begin{bmatrix} n_{z0} \\ \lambda_{max}/2\Lambda \end{bmatrix} \tag{3.103}$$

If we assume φ_{1d} as the incident angle at which the incident beam hit the un-slanted 1-D photonic crystal band-edge, then applying the Snell's law (Eq.(3.75)) we have

$$n_0 \sin\varphi_{1d} = \lambda_{max}/2\Lambda \tag{3.104}$$

Then the slant angle must be in the following window

$$\theta_1 = \left[-\tan^{-1}\left(\frac{n_0 \sin\varphi_{1d}}{n_{z0}} \right), \tan^{-1}\left(\frac{n_{z0}}{n_0 \sin\varphi_{1d}} \right) \right] \tag{3.105}$$

As we will show in chapter 8, sometimes we are interested to work in the second Brillouin zone, then the incident angle φ_1 must be greater than

$$\sin\varphi_1 > \sin\varphi_{1d}\cos\theta_1 + \frac{n_{z0}}{n_0}\sin\theta_1 \tag{3.106}$$

Or the period Λ must be greater than

$$\Lambda > \frac{\lambda_{max}}{2n_0\sec\theta_1\sin\varphi_1 - 2\tan\theta_1 n_{z0}} \tag{3.107}$$

For the operating point being in the second Brillouin zone and for the homogenous medium of refractive index $n_0 = 3.124$ at λ_{max}=1562.23 nm, Figure 3.12.2 shows the minimum period versus incident angle for different refractive index at the bandedge n_{z0}.

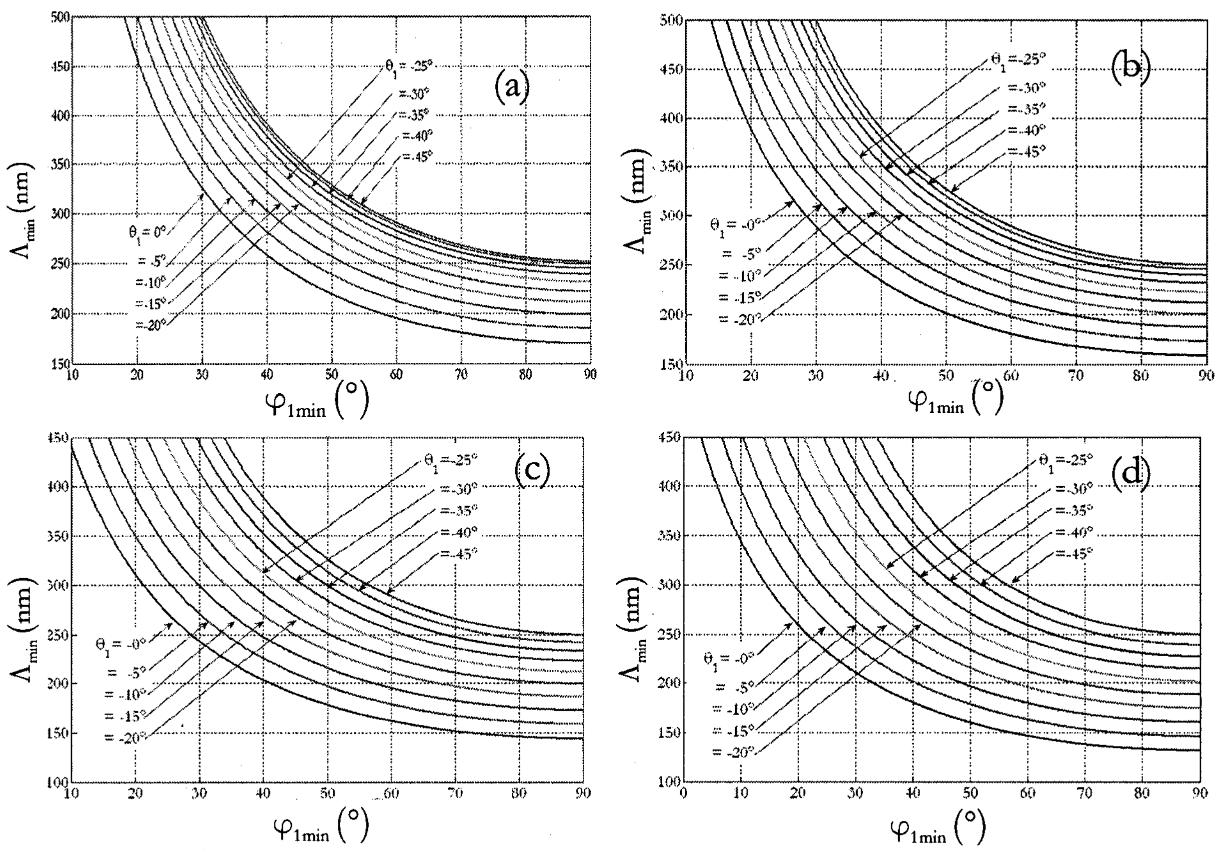

Figure 3.12.2, The minimum period condition for being at the second Brillouin zone, versus the incident angle and the slant angle is a parameter, where the effective index at the bandedge is at (a) $n_{z0} = 0.2$, (b) $n_{z0} = 0.5$, (c) $n_{z0} = 1$ and (d) $n_{z0} = 2$.

The period has to satisfy both Eqs.(3.107) and (3.102) in order to have only one diffraction order and being at the second Brillouin zone. Assuming $n_{z0} = 0.2$, Table 3.2 shows a typical data.

Table 3.2 Typical data for $n_{z0} = 0.2$

$\theta_1\,(^\circ)$	$\varphi_1\,(^\circ)$	$\Lambda(\mathrm{nm})$
0	45	237
-5	45	258
-10	45	278
-15	45	295

Note that, as the period gets close to the condition of (3.107), nearer to the band-edge, the higher dispersion will be achieved.

3.13 Refraction and transmission wave vector from 1-D photonic crystal, the FDTD Bloch boundary condition

Expressing the transmitted wave inside photonic crystals by a summation of Bloch modes, enable us to apply electric and magnetic fields boundary conditions based on Eqs.(3.99) and (3.77). The trial field expression inside photonic crystal must satisfy the Helmholtz equation. We expand the periodic dielectric constant and the Bloch modes by Fourier series. Using orthogonality of Fourier components (plane waves), we will achieve a set of equations for the Fourier series coefficients. The resulting set of equations after truncation is a finite set of equation with reflection coefficient of each diffraction order among the unknowns [20;21]. This method like other plane wave expansion method has a convergence difficulty for high contrast systems [7]. .Utilization of this method in the slab photonic crystal also seems impossible due to presence of continuum of radiation modes inside and outside the photonic crystal.

Analysis of the 1-D photonic crystal (thick hologram) has a vast history in literature. Several methods have been proposed; of them due to its advantages, rigorous coupled wave analysis (RCWA) is the most widely used [22;23]. It uses Maxwell's equations along with Floquet theorem to solve the field distribution in spatially modulated media. It should be noted that the method is an approximation and is not suited for very high modulation depths and very thick layers. But the method is well applicable to the problems involving wave propagation through cascaded 1-D photonic crystal (specifically, to slanted periodic structures).

Here we choose a different approach which is adapted to the slanted 1-D photonic crystal. Basically, this method is capable of handling the 3-D modeling of the slab 1-D photonic crystal, but the computational burden is exhausting for our computers at the moment.

When the structure under study is periodic along the interface, then the plane wave excitation, reflection and transmission can be obtained by analyzing only a unit cell using the Finite Difference Time Domain (FDTD) method. Consider the structure of Figure 3.7.2, the structure remains periodic in the direction of interface (ξ direction) even after slanting. Figure 3.13.1 demonstrates such a region. The unit cell can be confined on the other direction (ζ direction) by implementing sufficient Perfectly Matched Layers (PML). The length of the unit cell must be large enough that the transmission and reflection at the free space and 1-D photonic crystal ends are not affected by the boundary conditions (PML layers). In other words, reflection of structure at the far ends of the unit cell which is replaced by PML layers has little effect on transmission and reflection. This restriction can be satisfied by increasing the length of the unit cell inside the photonic crystal. The PML width must be wide enough and its reflection must be small enough that it suits steep wave directions.

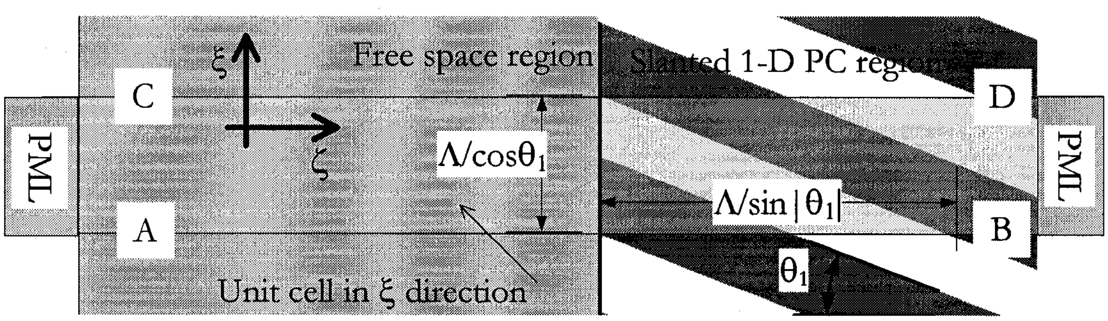

Figure 3.13.1 The Bloch Boundary condition between free space and the slanted 1-D Photonic crystal.

The fields at the boundary marked as D in Figure 3.13.1 are the same as the corresponding points at boundary B except for the Bloch phase factor of $\exp\left(i\beta_\xi \Lambda/\cos\theta_1\right)$ (see Eq.(3.82))

$$\Phi\left(\zeta,\xi+\Lambda/\cos\theta_1\right)\Big|_D = \Phi\left(\zeta,\xi\right)\Big|_B \exp\left(i\beta_\xi \Lambda/\cos\theta_1\right) \tag{3.108}$$

The plane wave excitation as it is expressed by Eq.(3.77) satisfies the Bloch boundary condition, i.e,

$$\begin{aligned} \Phi\Big|_C &= \Phi_0 \exp\left[i\left(k_\xi\xi + k_\zeta\zeta\right)\right]\Big\|_C = \Phi_0 \exp\left[i\left(k_\xi \Lambda/\cos\theta_1 + k_\zeta\zeta\right)\right]\Big\|_C \\ &= \Phi\Big\|_A \exp\left(ik_\xi \Lambda/\cos\theta_1\right) \end{aligned} \tag{3.109}$$

This result is not surprising because we can assume the free space is periodic with the period of $\Lambda/\cos\theta_1$. In conclusion both Bloch wave in photonic crystal and plane wave in free space satisfy the Bloch boundary condition. This conclusion originates from the boundary condition expressed in Eq.(3.84).

Consider the cases represented in Figure 3.13.2, which are un-slanted and -15° slanted 1-D photonic crystal with the parameters depicted in (3.90). Five micron of PML is added to the top and the bottom of the structure and its reflection is kept very small at 10^{-20}. The grid size is chosen as 10 nm on both directions, and the computational domain is restricted to a unit cell with Bloch periodic boundary conditions. The time grid is chosen at the Courant stability limit (about $c\Delta t \le 7.11$ nm), and simulation has continued up to $ct = 300\,\mu\text{m}$. The continuous wave type of excitation and TE polarization is chosen.

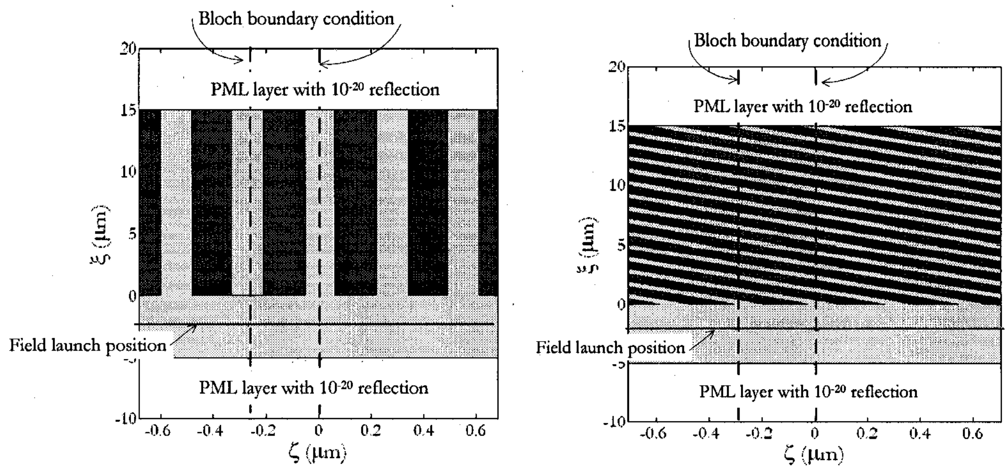

Figure 3.13.2 The un-slanted and slanted 1-D photonic crystal with appropriate boundary conditions.

Considering the incident angle of

$$\varphi_1 = 60^\circ \tag{3.110}$$

the quiescent points shown in Figure 3.10.1 and Figure 3.11.1 for un-slanted and Figure 3.10.4 and Figure 3.11.4 for slanted cases is achieved. The simulation result after stacking five unit cells together is depicted in Figure 3.13.3 for un-slanted and in Figure 3.13.4 for the slanted case. As is shown in Figure 3.10.1 (and more clearly in Figure 3.10.2), for this incident angle, the phase velocity direction is about 78° above the horizontal direction (ζ direction in Figure 3.7.2). As is seen from Figure 3.13.3, it is pretty much on the same direction as perpendicular to the wave front inside photonic crystal.

Similarly for the slanted case, as is shown in Figure 3.10.4 (and more clearly in Figure 3.10.5) Figure 3.10.1, for this incident angle, the phase velocity direction is about 62° above the horizontal direction (ζ direction in Figure 3.7.2). A good agreement is seen in Figure 3.13.4.

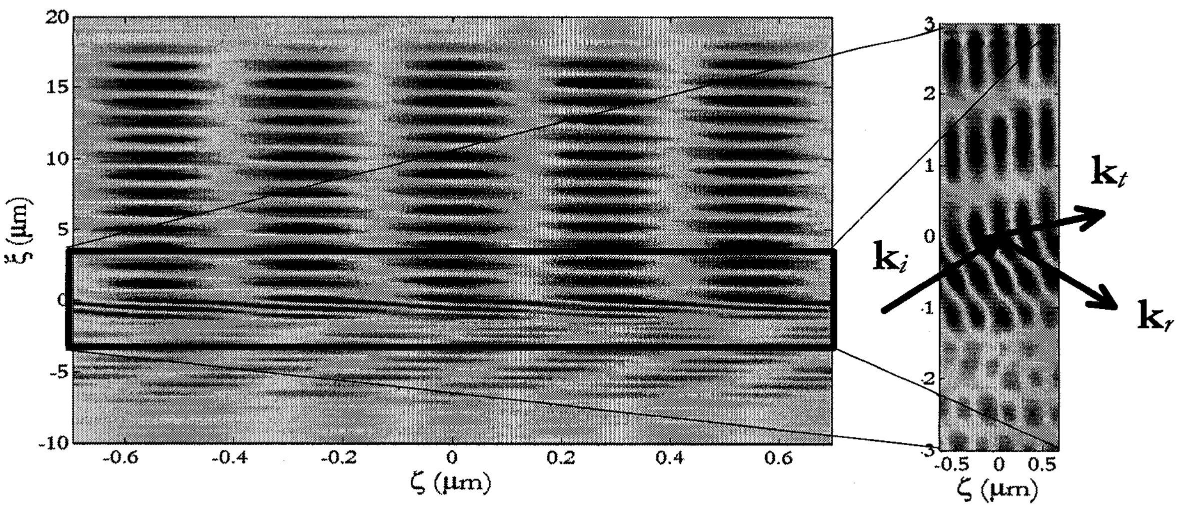

Figure 3.13.3 Stacking E_y profile for five unit cells when $\varphi_1 = 60°$, $\theta_1 = 0$.

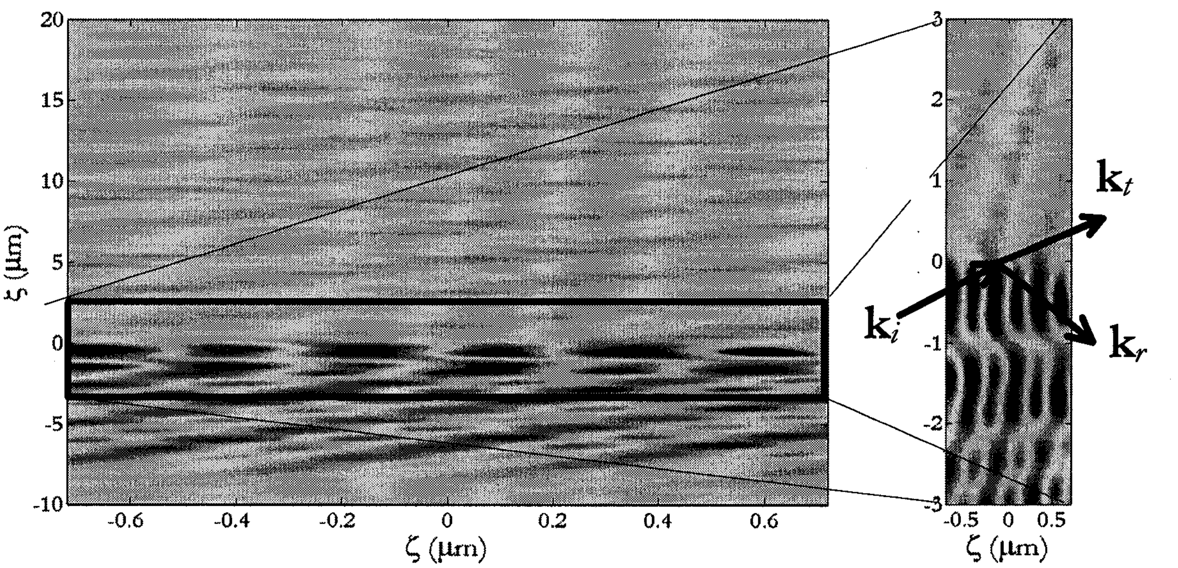

Figure 3.13.4 Stacking E_y profile for five unit cells when $\varphi_1 = 60°$, $\theta_1 = -15°$.

Direction of power flow, or the group velocity can be found using Eqs. (3.43) and (3.45). If we calculate the average power by integrating the Poynting vector along x axis and choose integration interval as Λ, and similarly along the z axis, then the power flow direction with respect to ζ direction can be found as

$$\varphi_2' = \theta_1 + \tan^{-1}\left(p_x / p_z\right) \tag{3.111}$$

And the total transmitted power can be obtained as below

$$\overline{S}_t = \frac{\sqrt{p_x^2 + p_z^2}}{\Lambda} \tag{3.112}$$

where $\overline{S}_t$ is the average power density. The reflected power density ($\overline{S}_r$) considering only zero order diffraction, can be obtained by averaging the Poynting vector along $\pi + \varphi_1$ direction. Finally, provided the electric field excitation with amplitude of A, the incident power density is obtained as below

$$S_i = \frac{n_0 Z_0}{2} A^2 \tag{3.113}$$

where $Z_0 = 376.730\ \Omega$ is the characteristic impedance of the vacuum. Then the reflection and transmission coefficients can be obtained as:

$$T = \frac{\overline{S}_t}{S_i} \text{ and } \Gamma = \frac{\overline{S}_r}{S_i} \tag{3.114}$$

Note that basically because there is no radiation loss

$$T + \Gamma = 1 \tag{3.115}$$

The results of FDTD analysis for both cases have been summarized in Table 3.3.

Table 3.3 The result of FDTD analysis

	$\theta_1 = 0$	$\theta_1 = -15°$
p_x	0.1495	0.0260
p_z	0.2873	-0.1320
$\overline{S}_t$	1.1829	0.4915
$\overline{S}_r$	0.0539	2.9399
S_i	1.2368	3.4314
$\varphi_2^t\ (°)$	42.48	-63.85
T	0.9564	0.1432
Γ	0.0436	0.8568

The group velocity directions in both cases are in a very good agreement with the results shown in Figure 3.11.2 and Figure 3.11.5 (which are obtained using the wave vector diagrams). The negative refraction on the second Brillouin zone of the slanted case [24] is accompanied by low transmission coefficient.

References

[1] S nyder A.W.and J.D.Love, in *Optical waveguide theory* Chapman and Hall, 1983.

[2] J . Chilwell and I. Hodgkinson, "Thin-Films Field-Transfer Matrix-Theory of Planar Multilayer Waveguides and Reflection from Prism-Loaded Waveguides," *Journal of the Optical Society of America A-Optics Image Science and Vision*, vol. 1, no. 7, pp. 742-753, 1984.

[3] P . Yeh, A. Yariv, and C. S. Hong, "Electromagnetic Propagation in Periodic Stratified Media .1. General Theory," *Journal of the Optical Society of America*, vol. 67, no. 4, pp. 423-438, 1977.

[4] H . Kikuta, Y. Ohira, and K. Iwata, "Achromatic quarter-wave plates using the dispersion of form birefringence," *Applied Optics*, vol. 36, no. 7, pp. 1566-1572, Mar.1997.

[5] P . St. Russell, "Optics of Floquet-Bloch Waves in Dielectric Gratings," *Applied Physics B-Photophysics and Laser Chemistry*, vol. 39, no. 4, pp. 231-246, Apr.1986.

[6] M ax Born and Emil Wolf, "Optics of crystals," in *Principles of Optics: Electromagnetic Theory of Propagation, Interference and Diffraction of Light,* 7th ed 1999, pp. 790-849.

[7] K .Sakoda, "Transmision spectra," in *Optical Properties of Photonic Crystals,* 1st ed Springer, Berlin, 2001, p. 90.

[8] P . Y. Amnon Yariv, "Electromagnetic propagtaion in periodic media," in *Optical Waves in Crystals : Propagation and Control of Laser Radiation* Wiley Series in Pure and Applied Optics, 2003, pp. 115-219.

[9] A . Bakhtazad and A. G. Kirk, "Superprism effect with planar 1-D photonic crystal," *Proceedings of the SPIE*, vol. 5360, pp. 364-372, June2004.

[10] A . Bakhtazad and A. G. Kirk, "slab 1-D photonic crystal **k**-vector superprism demultiplexer: analysis, and design," *Optics Express*, vol. 13, no. 14, pp. 5472-5482, July2005.

[11] C . Y. Luo, M. Soljacic, and J. D. Joannopoulos, "Superprism effect based on phase velocities," *Optics Letters*, vol. 29, no. 7, pp. 745-747, Apr.2004.

[12] T . Matsumoto and T. Baba, "Photonic crystal **k**-vector superprism," *Journal of Lightwave Technology*, vol. 22, no. 3, pp. 917-922, Mar.2004.

[13] H . Kosaka, T. Kawashima, A. Tomita, M. Notomi, T. Tamamura, T. Sato, and S. Kawakami, "Superprism phenomena in photonic crystals," *Physical Review B*, vol. 58, no. 16, pp. 10096-10099, Oct.1998.

[14] T . Baba and D. Ohsaki, "Interfaces of photonic crystals for high efficiency light transmission," *Japanese Journal of Applied Physics Part 1-Regular Papers Short Notes & Review Papers*, vol. 40, no. 10, pp. 5920-5924, Oct.2001.

[15] S . Y. Lin, V. M. Hietala, L. Wang, and E. D. Jones, "Highly dispersive photonic band-gap prism," *Optics Letters*, vol. 21, no. 21, pp. 1771-1773, Nov.1996.

[16] R . S. Chu and T. Tamir, "Group Velocity in Space-Time Periodic Media," *Electronics Letters*, vol. 7, no. 14, p. 410-&, 1971.

[17] M . J. Steel, R. Zoli, C. Grillet, R. C. McPhedran, C. M. de Sterke, A. Norton, P. Bassi, and B. J. Eggleton, "Analytic properties of photonic crystal superprism parameters," *Physical Review e*, vol. 71, no. 5 May2005.

[18] E . Istrate, A. A. Green, and E. H. Sargent, "Behavior of light at photonic crystal interfaces," *Physical Review B*, vol. 71, no. 19 May2005.

[19] X . F. Yu and S. H. Fan, "Anomalous reflections at photonic crystal surfaces," *Physical Review e*, vol. 70, no. 5 Nov.2004.

[20] E . Istrate, A. A. Green, and E. H. Sargent, "Behavior of light at photonic crystal interfaces," *Physical Review B*, vol. 71, no. 19 May2005.

[21] X . F. Yu and S. H. Fan, "Anomalous reflections at photonic crystal surfaces," *Physical Review e*, vol. 70, no. 5 Nov.2004.

[22] M . G. Moharam, E. B. Grann, D. A. Pommet, and T. K. Gaylord, "Formulation for Stable and Efficient Implementation of the Rigorous Coupled-Wave Analysis of Binary Gratings," *Journal of the Optical Society of America A-Optics Image Science and Vision*, vol. 12, no. 5, pp. 1068-1076, May1995.

[23] M . G. Moharam, D. A. Pommet, E. B. Grann, and T. K. Gaylord, "Stable Implementation of the Rigorous Coupled-Wave Analysis for Surface-Relief Gratings -

Enhanced Transmittance Matrix Approach," *Journal of the Optical Society of America A-Optics Image Science and Vision*, vol. 12, no. 5, pp. 1077-1086, May1995.

[24] S . L. He, Z. C. Ruan, L. Chen, and J. Q. Shen, "Focusing properties of a photonic crystal slab with negative refraction," *Physical Review B*, vol. 70, no. 11 Sept.2004.

Chapter 4

WEIGHTED INDEX METHOD FOR SLAB 1-D PHOTONIC CRYSTALS

An analytical approximate method is introduced to obtain wave vector diagrams for slab 1-D photonic crystals. Based on the best separable wave solution, a variational formula provides the best estimate for propagation constant. The wave vector diagram and the wave profile are obtained for a typical PECVD technology (with a medium refractive index contrast $\Delta n \approx 0.5$). Excellent agreement with an accurate finite element method is achieved. Due to iterative nature of the method, any wave amplitude nonlinearity can be modeled easily. By applying this method we also evaluate the wavelength tuneability of 1-D photonic crystal k-vector superprisms.

4.1 Introduction

All the potential applications of slab 1-D photonic crystals rely on the understanding of the wave behavior in the structure. Analytical approximate techniques which require low computer resources to solve the wave equation in slab 1-D photonic crystals are attractive tools for first order analysis (specially when the refractive index is high). Such techniques are well-suited to design optimization tasks that need many simulations to find the best results. One may check the final design with a more accurate and time consuming method such as the plane wave expansion method, or the finite element method. We have chosen the finite element method results as a benchmark to check the accuracy of the proposed method. The details of the benchmark method are outlined in appendix A.

Effective index methods are approximate, easy and common techniques for a first order model that reduces the 2-D waveguide model effectively into two 1-D models. In its simplest form it is based on the assumption that the separable wave solution in Cartesian coordinates is a good approximation and that the field is confined mainly in the high refractive index medium. The weighted index method [6] belonging to the effective index method family is another simple method, which is based on a same assumptions as simple as the effective index method. A variational formula is then used to get to the best propagation constant based on the best separable modal field profile. In order to get to the best separable solution the perturbation feedback method has been adopted [7]. In this chapter, we show how weighted index method can be applied to slab 1-D photonic crystal. In the next section, we will discuss the nonlinear weighted index method as applied to slab 1-D photonic crystal for obtaining wave-vector diagrams for various input power levels.

The band gap shift due to Kerr type nonlinearity in photonic crystals is well known phenomenon [5]. This phenomenon can be used to make a tunable photonic crystal multiplexer. Two kinds of tunability are recognized. The dispersion can be adjusted by using an external pump beam, or by the signal power itself. The latter needs less power and leads to the self-induced superprism effect, if the input power level reaches the amount necessary to bring the quiescent point near the band-edge where the dispersion is the highest. The huge dispersion reported in 3-D and 2-D slab [1] makes a high channel multiplexer a reality. The certain amount of power than many input channels brings into the multiplexer when adds together would be a large amount of power. The multiplexer then must operate linearly at high power or measure must be taken into account to address the nonlinearity. As we will show, the deviation angle sensitivity of the prism is much larger than the angular dispersion sensitivity. In other words, superprism can be a multilevel switch and a multiplexer together if it operates at multilevel input power (or control can be imposed by multilevel pump signal). The device also can be tuned by controlling the optical power to compensate all of the process-related uncertainties that may exist due to the fabrication of the fine periodic structure. So it is important to understand the behavior of the device at high power.

Dispersion management via the nonlinear regime of slab 1-D photonic crystals is another interesting area of research [3]. Varying input power, self focusing and defocusing have been observed within the same medium, structure and wavelength [4].

4.2 Weighted effective index method for slab 1-D photonic crystals

The weighted index method was first developed for rectangular dielectric waveguides [6]. The main idea of the method is in finding the best separable solution based on a variational formula. The variational formula plays a dual role. It gets the best propagation constant based on the approximate field profile and on the other hand it provides a gauge for convergence. Weighting the real refractive index, it searches for the nearest structure with true separable solution. The convergence gauge will guarantee that the result is the nearest to reality which poses the separable solution.

While the theory could be developed for the most general case (*i.e.*, 3-D cubic photonic crystal, for this chapter we restrict ourselves to slab 1-D photonic crystal. We assume the structure is periodic in one dimension (say x direction) and it is uniform in z direction, that is:

$$n(x, y) = n(x + \Lambda, y) \tag{4.1}$$

Figure 4.2.1 shows a simple slab 1-D photonic crystal. Real structures usually are more complicated than this simple one; however the theory can be extended easily.

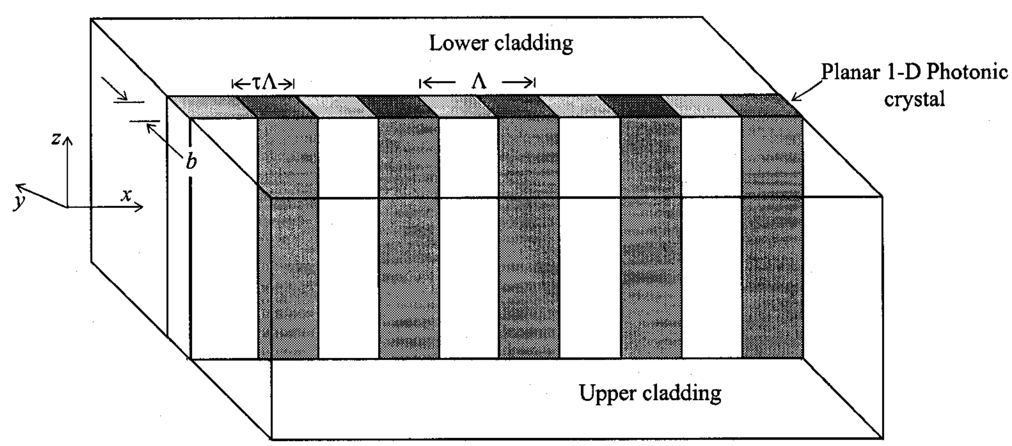

Figure 4.2.1 A typical slab 1-D photonic crystal

Using Floquet's theorem, the wave solution can be expressed as:

$$\Psi(x, y) = \Phi(x, y)\exp(ik_x x) \tag{4.2}$$

where $\exp\left(k_z z - i\omega t\right)$ has been suppressed. $\Phi(x, y)$ is a periodic function in the x direction, *i.e.*,

$$\Phi(x, y) = \Phi(x + \Lambda, y) \tag{4.3}$$

and k_x is the Bloch wave number. Our analysis is based on solving Helmholtz equation approximately and has a variational nature. It seeks a separable solution for $\Phi(x, y)$ in order to minimize a variational equation. Let us start with establishing a variational equation for this case.

4.2.1 *Variational equation for slab 1-D photonic crystal*

The scalar Helmholtz equation can be expressed as a generalized eigenvalue problem:

$$\left(\nabla^2 + k_0^2 n^2\right)\Psi = k_z^2 \Psi \tag{4.4}$$

The eigenvalue k_z^2 is a scalar constant. Defining a scalar dot product of Ω and Ψ over the unit cell volume of V as:

$$\langle \Omega | \Psi \rangle = \int_V \Omega \Psi dv \tag{4.5}$$

Since ∇^2 is a Hermitian operator and n^2 is real, the following variational equation in the form of Rayleigh's quotient is valid [8]:

$$\left[k_z^2\right] = \frac{\langle \Psi | \nabla^2 + k_0^2 n^2 | \Psi \rangle}{\langle \Psi | n^2 | \Psi \rangle} \tag{4.6}$$

Inserting Eq.(4.2) into Eq.(4.6), it is not difficult to show that:

$$\left[k_z^2\right] = \frac{-k_x^2 + \left\langle \Phi \middle| \nabla^2 + k_0^2 n^2 \middle| \Phi \right\rangle}{\left\langle \Phi \middle| \Phi \right\rangle} \tag{4.7}$$

and note that due to periodic nature of Φ, $\left\langle \Phi \middle| \partial_x \middle| \Phi \right\rangle = 0$.

4.2.2 *Basic assumptions*

Let us assume that separable solution is a good approximation, *i.e.*,

$$\Phi(x, y) = F(x)G(y) \tag{4.8}$$

Also assume that there is a photonic crystal with refractive index $\tilde{n}(x, y)$ (perturbation of real $n(x, y)$) such that its exact solution is separable. If we define Δp proportional to the difference between the wave number squared of real and perturbed photonic crystals as:

$$\Delta p = k^2 - \tilde{k}^2 \tag{4.9}$$

where $k^2 = k_x^2 + k_z^2$. Note that $\tilde{k}^2$ is satisfied in Eq.(4.7), *i.e.*,

$$\tilde{k}^2 = \left\langle F \middle| F'' \right\rangle + \left\langle G \middle| G'' \right\rangle + k_0^2 \left\langle FG \middle| \tilde{n}^2 \middle| FG \right\rangle \tag{4.10}$$

where we have normalized field components over periods:

$$\left\langle F \middle| F \right\rangle = \left\langle G \middle| G \right\rangle = 1 \tag{4.11}$$

Initially, we take the actual field as $\Phi = FG$ of the perturbed waveguide, then using Eqs.(4.7) and (4.10), we have:

$$\Delta p = \left\langle FG \middle| \delta n^2 \middle| FG \right\rangle \tag{4.12}$$

where

$$\delta n^2 = n^2(x,y) - \tilde{n}^2(x,y) \tag{4.13}$$

The method converges when Δp converges to its minimum.

4.2.3 *Separating Helmholtz equation*

Inserting the separable solution of (4.8) into Helmholtz equation, we have:

$$|F''G\rangle + |FG''\rangle + 2ik_x|F'G\rangle + \left(k_0^2 n^2 - k^2\right)|FG\rangle = 0 \tag{4.14}$$

Multiplying Eq.(4.14) with $\langle G|$ we have:

$$|F''\rangle + 2ik_x|F'\rangle + \left(k_0^2 n_e^2(x) - k^2\right)|F\rangle = 0 \tag{4.15a}$$

where

$$n_e^2(x) = \langle G|n^2|G\rangle + \frac{\langle G|G''\rangle}{k_0^2} \tag{4.15b}$$

Eq.(4.15a) can be considered as the equation of horizontal slab waveguide with a periodic refractive index of $n_e(x) = n_e(x+\Lambda)$. Similarly multiply Eq.(4.14) with $\langle F|$, we have:

$$|G''\rangle + \left(k_0^2 n_e^2(y) - k^2\right)|G\rangle = 0 \tag{4.16a}$$

where

$$n_e^2(y) = \langle F|n^2|F\rangle + \frac{\langle F|F''\rangle}{k_0^2} \tag{4.16b}$$

Eq.(4.16a) can be considered as the equation of a vertical slab waveguide with a periodic refractive index of $n_e(y)$. Multiplying Eq.(4.15a) with $|G\rangle$ and Eq.(4.16a) with $|F\rangle$ and adding them together, we have:

$$|F''G\rangle+|FG''\rangle+2ik_x|F'G\rangle+\left(k_0^2\tilde{n}^2-k^2\right)|FG\rangle=0 \tag{4.17a}$$

where

$$\tilde{n}^2(x,y)=n_e^2(x)+n_e^2(y)-\frac{k^2}{k_0^2} \tag{4.17b}$$

4.2.4 The method

We adopt a perturbation feedback method which has an iterative nature [7]. In each iteration, we solve Eqs.(4.15a),(4.16a), then check the convergence gauge (4.12) . In the beginning of i^{th} iteration, knowing F_{i-1} and G_{i-1} of the last step, we solve Eq.(4.15a), with the refractive index of (4.15b) (however we ignore the second term), *i.e.*,

$$n_{e,i}^2(y)=\langle F_{i-1}|n^2|F_{i-1}\rangle \tag{4.18}$$

to obtain $k_{b,i}$ and $G_i(y)$. Now in order to take the second term of Eq.(4.15b) into account which was previously assumed zero, we proceed as follows:

We multiply both sides of Eq.(4.18) by $|G_i(y)|^2$ and integrate with respect to y, we have:

$$\langle G_i|n_{e,i}^2(y)|G_i\rangle=\langle F_{i-1}G_i|n^2|F_{i-1}G_i\rangle \tag{4.19}$$

Multiplying both side of Eq.(4.15a) by $\langle F_{i-1}|$, we have:

$$\langle F_{i-1}|F''_{i-1}\rangle=k_{v,i-1}^2-k_0^2\langle F_{i-1}|n_{e,i-1}^2(x)|F_{i-1}\rangle \tag{4.20}$$

Adding Eqs.(4.19) and (4.20), we have:

$$\begin{aligned}\left\langle F_{i-1} \middle| F''_{i-1} \right\rangle &= k^2_{v,i-1} - k_0^2 \left\langle F_{i-1} \middle| n^2_{e,i-1}(x) \middle| F_{i-1} \right\rangle \\ &- k_0^2 \left\langle G_i \middle| n^2_{e,i}(y) \middle| G_i \right\rangle + k_0^2 \left\langle F_{i-1} G_i \middle| n^2 \middle| F_{i-1} G_i \right\rangle\end{aligned} \tag{4.21}$$

Defining $\tilde{n}_i^2$ as :

$$\tilde{n}_i^2(x,y) = n^2_{e,i-1}(x) + n^2_{e,i}(y) - \frac{k^2_{v,i-1}}{k_0^2} \tag{4.22}$$

then from Eqs.(4.15b), and (4.12) we have:

$$\left\langle F_{i-1} \middle| F''_{i-1} \right\rangle = \Delta p_i \tag{4.23}$$

where the subscript i has been added to Δp to emphasize that this error belongs to the ith iteration. $n^2_{e,i}(y)$ will be is corrected at the end of this iteration as:

$$n^2_{e,i}(y) = \left\langle F_i \middle| n^2 \middle| F_i \right\rangle - \Delta p_i \tag{4.24}$$

and $\beta_{b,i}$ and $G_i(y)$ are also updated. The next iteration begins by solving Eq.(4.15a), ignoring the first term of refractive index in Eq.(4.15b), *i.e.*:

$$n^2_{e,i+1}(x) = \left\langle G_i \middle| n^2 \middle| G_i \right\rangle \tag{4.25}$$

with $n^2_{e,i+1}(x)$ calculated from the above equation. To consider the effect of the second term, by a similar procedure, we obtain:

$$\begin{aligned}\left\langle G_i \middle| G''_i \right\rangle &= k^2_{b,i} - k_0^2 \left\langle G_i \middle| n^2_{e,i}(y) \middle| G_i \right\rangle \\ &- k_0^2 \left\langle F_{i+1} \middle| n^2_{e,i+1}(x) \middle| F_{i+1} \right\rangle + k_0^2 \left\langle F_{i+1} G_i \middle| F_{i+1} G_i \right\rangle\end{aligned} \tag{4.26}$$

Now defining $\tilde{n}^2_{i+1}$ as:

$$\tilde{n}_{i+1}^2(x,y)=n_{e,i+1}^2(x)+n_{e,i}^2(y)-\frac{k_{b,i}^2}{k_0^2} \tag{4.27}$$

we can write:

$$\langle G_i | G_i'' \rangle = \Delta p_{i+1} \tag{4.28}$$

Including this correction in Eq.(4.25) we have:

$$n_{e,i+1}^2(x) = \langle G_i | n^2 | G_i \rangle - \Delta p_{i+1} \tag{4.29}$$

This completes the iteration procedure, which must be repeated until Δp becomes negligible. For the first iteration we need to choose initial guesses for $F(x)$ and $G(y)$, as follows

$$F_0(x)=\begin{cases} 1/\sqrt{\Lambda\tau} & \text{for } |x|<\Lambda\tau/2 \\ 0 & \text{elsewhere} \end{cases} \tag{4.30}$$

$$G_0(y)=\begin{cases} 1/\sqrt{b} & \text{for } |y|<b/2 \\ 0 & \text{elsewhere} \end{cases} \tag{4.31}$$

With the initial guess of Eq.(4.30), Eq. (4.16a) will be the wave equation of a three layer vertical dielectric waveguide, while the initial guess of Eq.(4.31) makes Eq.(4.15a) the wave equation for horizontal stratified dielectric waveguide. (see Figure 4.2.2)

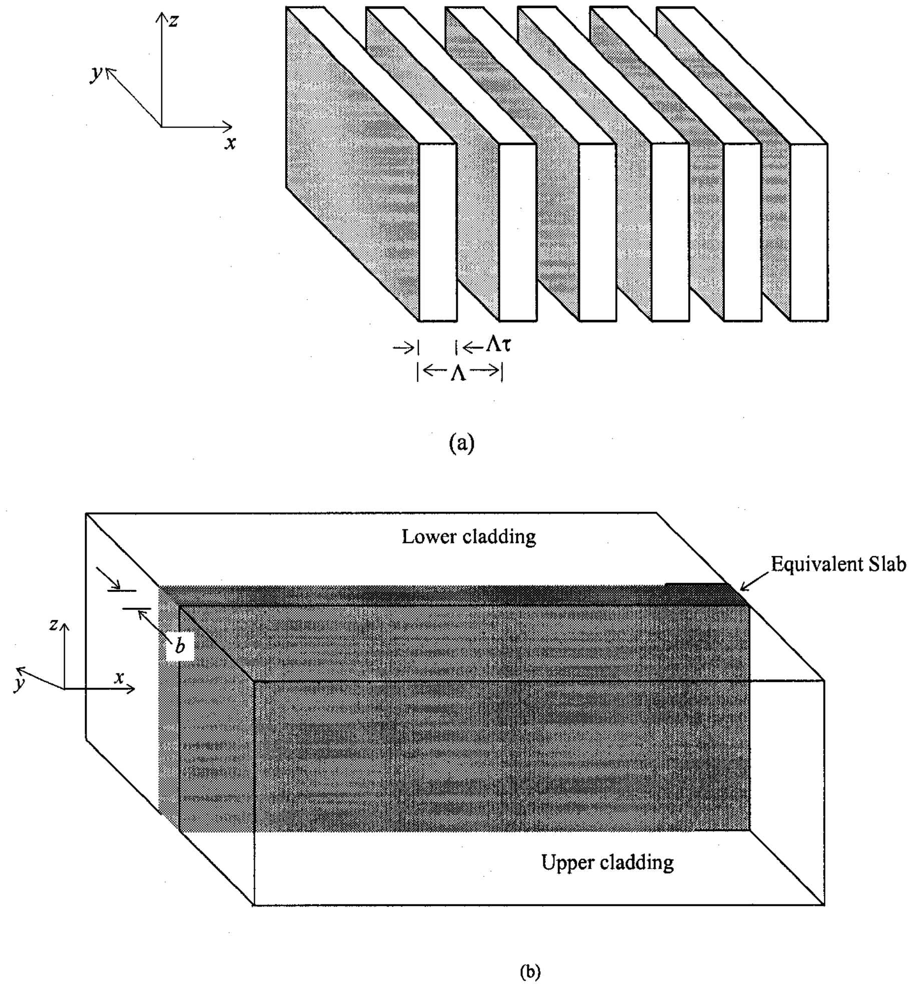

Figure 4.2.2 Equivalent vertical (a) and horizontal (b) waveguide corresponding to initial guesses of Eq.(4.30) and (4.31) respectively.

Numerical illustration based on this formulation will be presented in the following sections after we discuss the method in handling a nonlinear 1-D photonic crystal.

4.3 Nonlinear weighted index method

Nonlinear wave propagation in photonic crystals involving Kerr type nonlinearity leads to interesting phenomena. Positive Kerr type nonlinearity can lead to spatial gap solutions [4;5], while negative Kerr type nonlinearity can cause bi-stability [9]. Optical switches and limiters have also been suggested recently using alternative layers of positive and negative Kerr type nonlinearity [10]. The main analytical approach to the analysis of nonlinear propagation in 1-D photonic crystal has been coupled mode theory [11-13], however recently FDTD analysis has been applied [14]. The main drawback of coupled mode theory is the lack of modal understanding of the structure, while the proposed FDTD analysis cannot be applied to large structures and is unable to provide a thorough understanding of the photonic crystals. The numerical spectral domain method is the best alternative in this case. Nonlinearity can be implemented in the original Helmholtz equation or can be applied if the host method is iterative. Those rigorous methods that solve for modes must be based on self-consistency and must take the vectorial nature of the problem into account which would be very time and memory consuming. The effective index method is a well-known simple method for analyzing dielectric waveguides [15]. It can analyze virtually any linear dielectric waveguide with rectangular cross section. The method has been extended to take the guide nonlinearity into account [16;17]. Another simple, but more accurate method is the weighted index method [6]. Here we extend it for analyzing of slab 1-D photonic crystal with intensity dependent refractive index nonlinearity.

Any nonlinear guiding system can be analyzed with an iterative procedure using a suitable linear analysis tool as a basis. Indeed it is not necessary to directly solve the governing nonlinear differential equation. Rather it is possible to construct solutions from modal solutions of linear waveguides through an elementary self-consistency relation. It can be shown that any solution of a nonlinear problem can be associated to a linear solution of an equivalent structure[18]. Indeed the problem can be reduced to only determining the equivalent linear model, and then analyzing it by a reliable linear routine. The equivalent linear model and the original nonlinear structure are related to each other by an elementary self consistency relation. The self consistency relation is one that indicates the relation between the nonlinear refractive index and the modal pattern [18]. As an example, for Kerr type nonlinearity it can be expressed as: $n = n_0 \pm \alpha |\mathbf{E}|^2$. On the other hand, it is reasonable to claim that the modes of any linear waveguide correspond to the modes of some nonlinear waveguide with a particular type of nonlinearity. This type of nonlinearity is revealed by the inversion of the self consistency relation.

The equivalent linear model can be obtained by the following iterative procedure. At initial step of each iteration, the nonlinearity is not considered while the system is analyzed. At the end of the step the nonlinearity is taken into account, *i.e.*, by evaluating the field distribution in the linear model and using the self consistency relation, the refractive index of the equivalent linear model is corrected accordingly. This is an approximation of the equivalent linear model. The next iteration begins by analyzing the approximate equivalent model of the previous step, and ends up by obtaining the next approximation of linear equivalent model. This procedure can be repeated until convergence is achieved. The outputs of iterations are the equivalent linear model together with the propagation constant and the modal pattern corresponding to the original nonlinear waveguide. The flowchart of the above procedure is shown in Fig. 3a. In this flowchart it is assumed that the basis linear analyzing routine has an iterative nature.

The nonlinear iteration loop and the linear analysis loop could be merged, if the basis linear analyzing routine has an iterative nature. In this way a new algorithm will emerge. The flowchart of this method is shown in Fig. 3b. Note that the convergence blocks are also merged. In this way, all the analysis capability of the previous routine is transferred naturally to the new nonlinear one. Furthermore it is evident that, the new routine is much faster than the previous one.

We select the weighted index method as the basis routine. Figure 4.3.2 depicts one period of the slab 1-D photonic crystal. This algorithm assigns vertical and horizontal equivalent slab

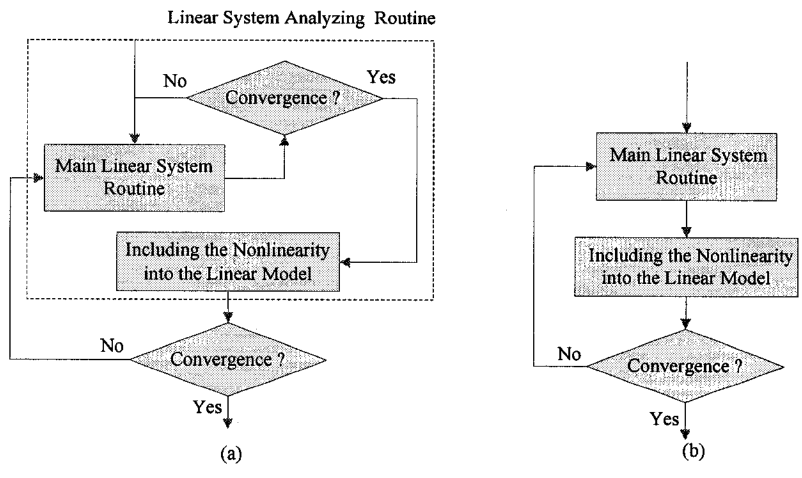

Figure 4.3.1 The flowcharts of two nonlinear system analyzers based on an iterative linear system analyzing routine, (a) the simple but inefficient routine, and (b) the modified one.

waveguides to the original slab 1-D photonic crystal in each computational step. The equivalent horizontal waveguide is a slab waveguide with non-uniform periodic refractive index. The equivalent vertical one is ordinary slab waveguide with non-uniform refractive index. There are various ways to analyze such waveguides. One such method, (which is the most reliable and the simplest one, but with the lowest efficiency) is stratification [19]. Our analysis employs the stratification technique.

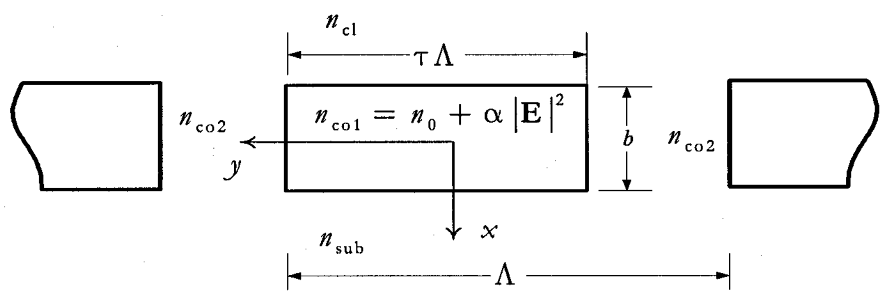

Figure 4.3.2 The schematic representation of a slab 1-D photonic crystal with nonlinear Kerr type nonlinearity.

4.4 Numerical illustrations

For the sake of demonstrating the methods, we have selected two structures, one with relatively low refractive index contrast, and the other with higher refractive index contrast with Kerr type non-linearity. The cross section of the 1-D photonic crystal of lower refractive index contrast is depicted in Figure 4.4.1.

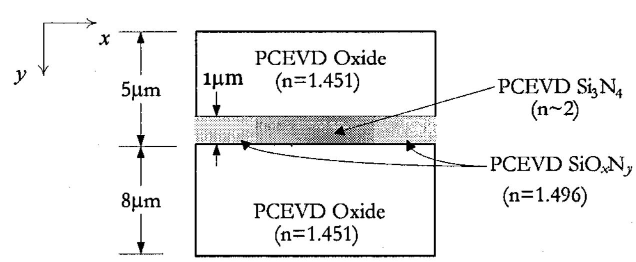

Figure 4.4.1 Schematic of the low refractive index contrast slab 1-D photonic crystal.

Using the structure illustrated in Figure 4.4.1 and with grating period of $\Lambda = 0.5$ μm and duty factor of $\tau = 0.5$, Figure 4.4.2 shows the normalized wave vector diagram

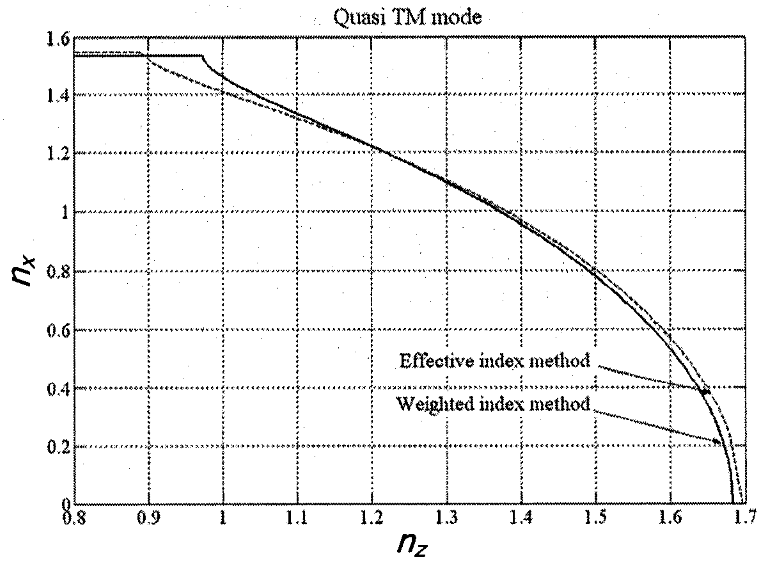

Figure 4.4.2. Wave vector diagram obtained using effective index method (dashed) and weighted index method (solid).

Table 4.1 shows the comparison with the finite element method (which we take as a benchmark). There is a good agreement between these two methods which is an indication that our method is accurate in this range of refractive index contrast. The maximum error happens again at the bandedge and it is 2.5%. Note that the computational domain for finite element method can be reduced by 50% by considering the structural symmetry along the *y* direction (see Figure 4.4.1)

Table 4.1 The comparison of our method with the finite element method results in low refractive index contrast regime

	$n_x = 0$	$n_x = 1$	$n_x = 1.4$	$n_x = \lambda/2\Lambda = 1.55$
Weighted index method	1.681	1.377	1.018	0.965
Finite element method	1.688	1.369	1.011	0.941
% error	0.4	0.6	0.7	2.5

In Figure 4.4.3 and Figure 4.4.4 the deviation of the refractive indices of equivalent horizontal and vertical waveguides are plotted compared to the corresponding effective index method ones versus normalized Bloch wave number. The best separable field solution is obtained by these refractive index adjustments. As expected the deviation is higher near the band edge.

In Figure 4.4.3 and Figure 4.4.4 the deviation of the refractive indices of equivalent horizontal and vertical waveguides are plotted compared to the corresponding effective index method ones versus normalized Bloch wave number. The best separable field solution is obtained by these refractive index adjustments. As expected the deviation is higher near the band edge.

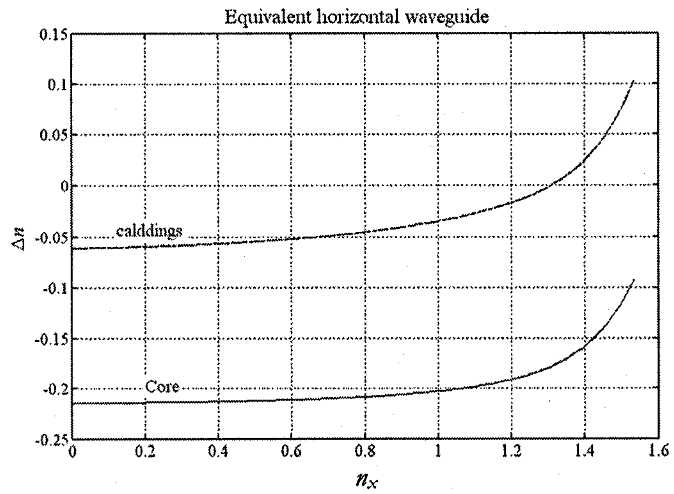

Figure 4.4.3. Refractive index deviation of the equivalent horizontal waveguide compared the corresponding effective index method versus normalized Bloch wave number. Due to symmetry the upper and lower cladding refractive indices are always the same.

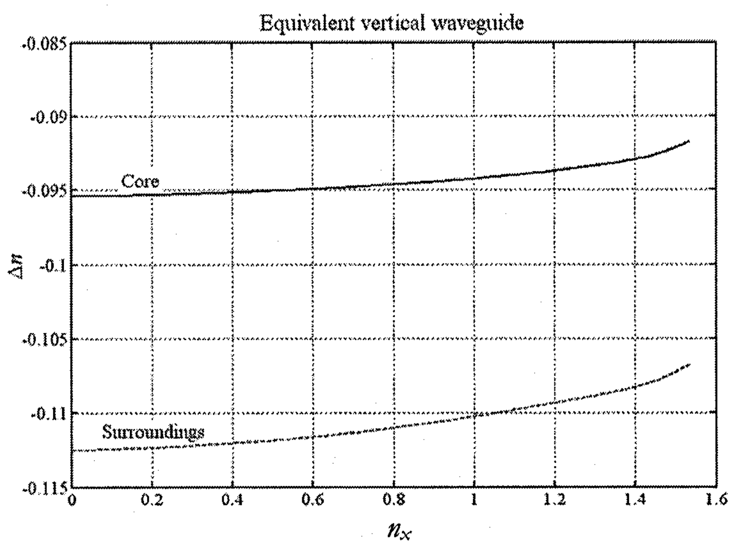

Figure 4.4.4 Refractive index deviation of equivalent vertical waveguide comparing to the corresponding effective index method one versus normalized Bloch wave number. Due to symmetry upper and lower cladding refractive indices are always the same.

Finally in Figure 4.4.5 and Figure 4.4.6 we plot the mode profile (E_x) in x and y directions at a fixed Bloch wave number $n_x = 1.24$. As Figure 4.4.6 shows there is a field discontinuity at the core interface. This kind of discontinuity cannot be observed by solving the scalar Helmholtz equation.

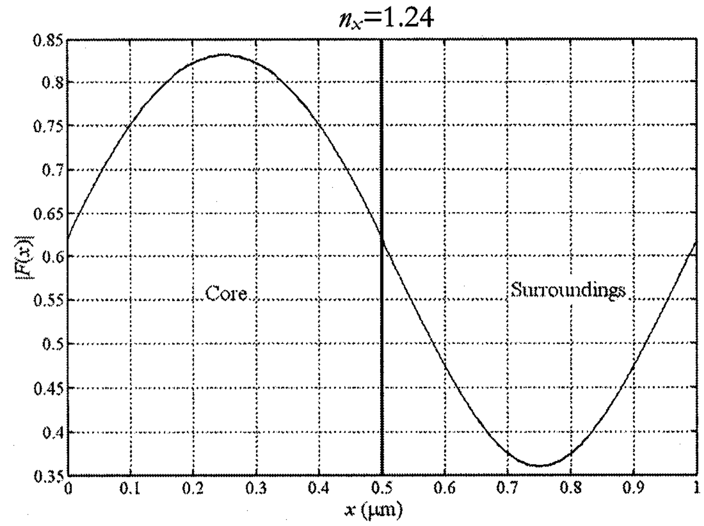

Figure 4.4.5. Field distribution in x direction for quasi TM mode at a fixed Bloch wave number.

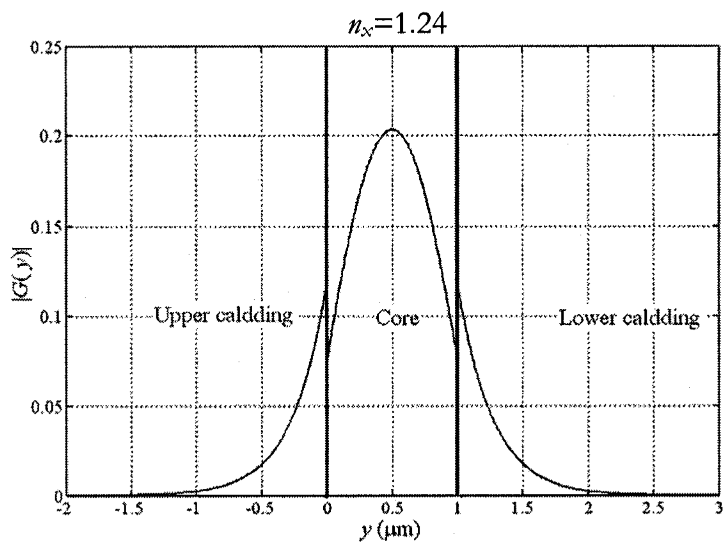

Figure 4.4.6. Field distribution in y direction for quasi TM mode at a fixed Bloch wave number.

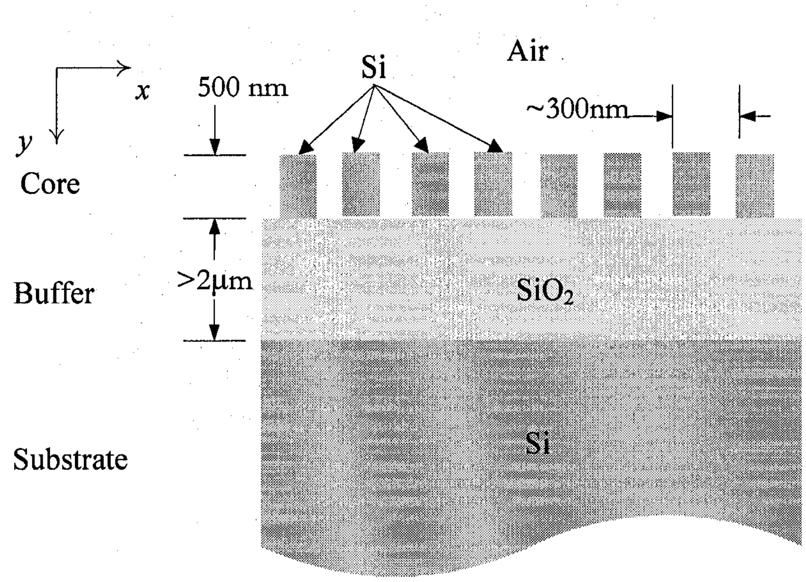

Figure 4.4.7 Cross section of the silicon on insulator slab 1-D photonic crystal.

Table 4.2 shows the results of the comparison. As can be seen, the accuracy is acceptable except near the bandedge.

Table 4.2 The comparison of our method with Finite element results in high refractive index contrast regime

	$n_x = 0$	$n_x = \lambda/2\Lambda = 2.583$
Weighted index method	2.11	0.38
Finite element method	2.14	0.45
% error	1.4	15

The second example that we have chosen is a slab 1-D photonic crystal of nonlinear rectangular cores (Si) on a linear substrate (SiO_2). The cladding is also linear (Air). The third order nonlinearity of Si is taken into account $n_2 = 4.1\times10^{-12}\ (\mathrm{m}^2/\mathrm{V}^2)$ [20]. The nonlinearity of the silica is ignored. We have also ignored losses and assume a constant temperature throughout the device. We choose the model of Figure 4.3.2 with the following constants: $b = 0.5\mu m$, $\Lambda = 300\ \mu\mathrm{m}$, $\tau = 0.5$, $\lambda_0 = 1.55\mu\mathrm{m}$, $n_{\mathrm{co1}} = 3.26 + 4.1\times10^{-12}|E|^2$, $n_{\mathrm{sub}} = 1.45$ and $n_{\mathrm{co2}} = n_d = 1$. In Figure 4.4.8 w e have shown the normalized wave vector diagram ($n_{x,z} \equiv \beta_{x,z}/k_0$), with maximum electric field ($E_{\max}$) as a parameter. The routine is fast and

$b = 0.5\mu m$, $\Lambda = 300\ \mu\text{m}$, $\tau = 0.5$, $\lambda_0 = 1.55\mu\text{m}$, $n_{co1} = 3.26 + 4.1\times10^{-12}|E|^2$, $n_{sub} = 1.45$ and $n_{co2} = n_d = 1$. In Figure 4.4.8 w e have shown the normalized wave vector diagram ($n_{x,z} \equiv \beta_{x,z}/k_0$), with maximum electric field (E_{max}) as a parameter. The routine is fast and

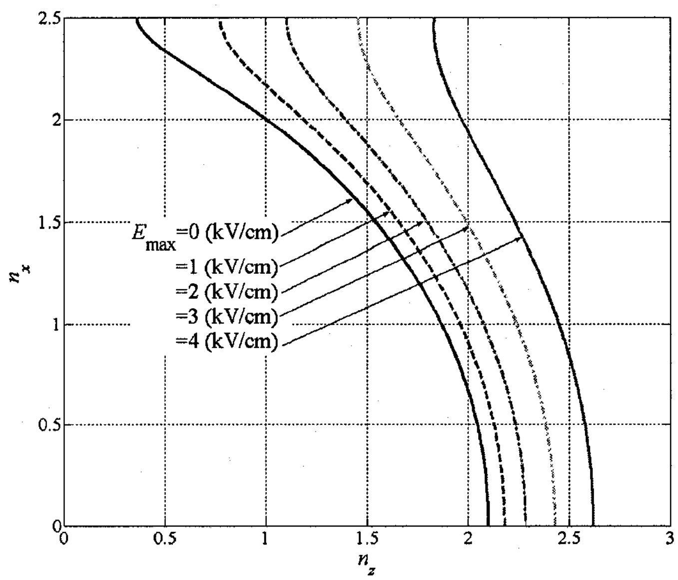

Figure 4.4.8 Normalized wave vector diagram with various maximum electric field as a parameter.

converges within 4 - 8 iterations. Note that the conventional Floquet theory is not valid in the nonlinear case, however due to periodicity; the wave vector diagram repeats itself as is the case for linear systems.

Figure 4.4.9 demonstrates the refractive index perturbation in the core region of the equivalent linear model at $E_{max} = 3\text{kV/m}$ and $n_x = 0$, $n_x = 1.5$ and $n_x = 2.5$. The field nonlinearity causes the increase of the core refractive index, but it smoothes out the refractive index contrast. This smoothing increases the accuracy of the method. In other words, the results would be more accurate than the linear case (or when $|E| << 1$). The accuracy of linear case has been listed in Table 4.2. Note that the refractive index is periodic in each case, but the refractive index profile changes with the propagation direction. More field confinement at near the bandedge also causes larger refractive index gradient at the core region.

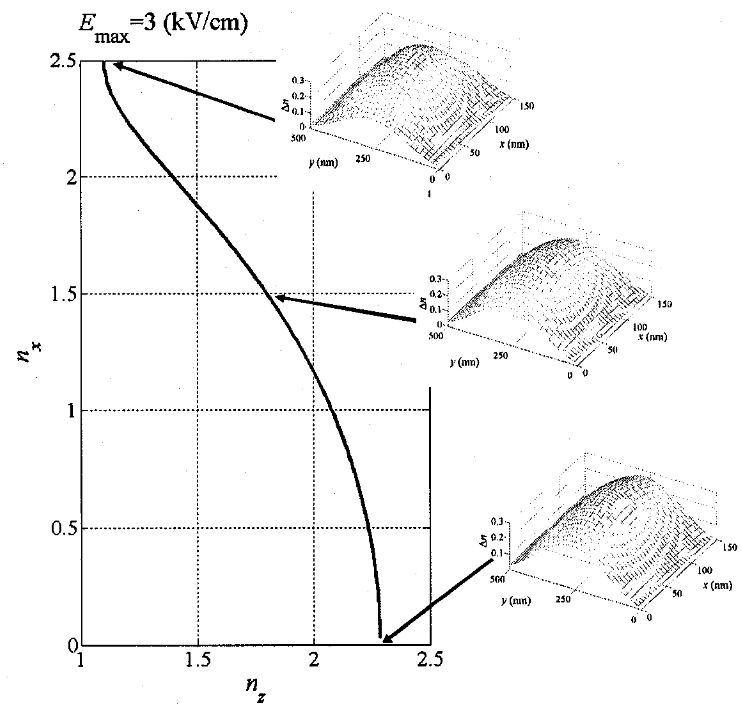

Figure 4.4.9 Refractive index perturbation for different Bloch wave number.

In Figure 4.4.10 the superprism geometry with various defined parameters is illustrated. We have assumed that the left and the right sides of the prism are air and any reflections at the boundaries have been ignored.

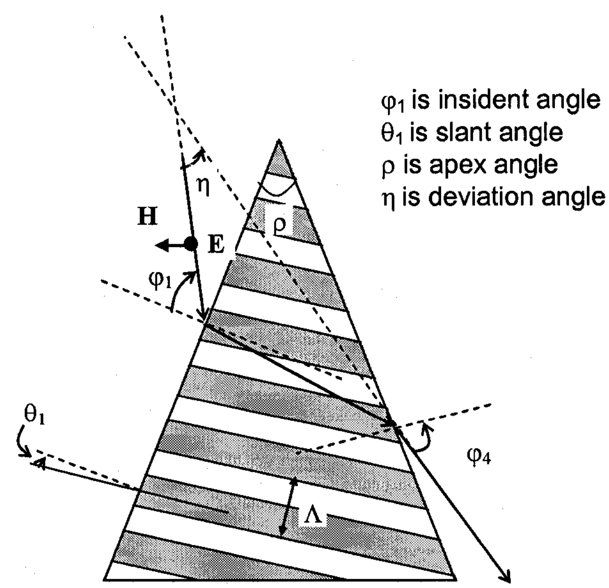

Figure 4.4.10. Superprism geometry based on slab 1-D photonic crystal.

Figure 4.4.11 shows the deviation angle versus maximum electric field at fixed incident angle $\varphi_1 = -55°$, apex angle of $\rho = 60°$ and slant angle of $\theta_1 = -20°$. Figure 4.4.11 also shows angular dispersion versus maximum electric field under

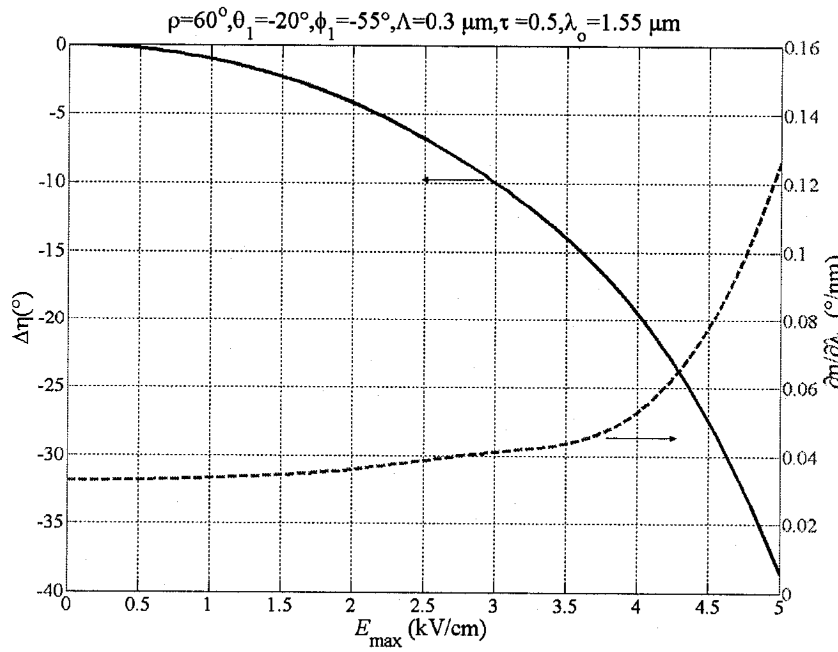

Figure 4.4.11. Change of deviation angle and angular dispersion versus maximum electric field in the core region.

the similar conditions. As can be seen, at lower power levels the dispersion is nearly constant whilst the deviation angle change starts even at lower power levels. This feature is helpful for tuning the device versus any process related imperfections. The sensitivity to optical power is high enough that at higher power levels, the device can divert all output channels many degrees by increasing input power. This effect could be used to make a multilevel optical switch.

4.5 Conclusion

An approximate analytical method for the analysis of slab 1-D photonic crystal has been introduced. The method is an extension of the known weighted index method for rectangular dielectric waveguides. Based on a variational equation developed for this case, the best separable wave solution is sought. Due to the variational nature of the method, the wave vector diagram will have a second order accuracy if the wave profile has only first order accuracy. The wave vector diagram plays a vital role determining refraction and reflection direction of the slab waveguide modes of the slab 1-D photonic crystal.

Based on the modal behavior of rectangular dielectric waveguides, the accuracy of this method is much better than the effective index method especially near bandedge, while the accuracy of effective index method is comparable to the solution of scalar Helmholtz equation. Compared to the accurate finite element methods results, the the weighted index method is accurate in the low refractive index contrast systems ($\Delta n \approx 0.5$), but it deteriorates as the refractive index contrast becomes higher ($\Delta n \approx 2$).

The weighted index method has also been extended to handle the nonlinear slab 1-D photonic crystal. Merging the loop of the weighted index method with the loop of the nonlinear routine will speed up the method considerably. The resultant method is simpler, and converges virtually as fast as the conventional perturbation feedback method (through 4 to 8 iterations). A wave vector diagram versus the input power can be obtained using the results shown in Figure 4.4.8 (the maximum electric field in Figure 4.4.8 can be replaced with the transmitted power). Furthermore, since we have not considered the refractive index saturation effects, there is a one to one correspondence between maximum electric field at the core center and the transmitted power [21].

References

[1] H . Kosaka, T. Kawashima, A. Tomita, M. Notomi, T. Tamamura, T. Sato, and S. Kawakami, "Superprism phenomena in photonic crystals: Toward microscale lightwave circuits," Journal of Lightwave Technology, vol. 17, no. 11, pp. 2032-2038, Nov.1999.

[2] L . J. Wu, M. Mazilu, T. Karle, and T. F. Krauss, "Superprism phenomena in planar photonic crystals," Ieee Journal of Quantum Electronics, vol. 38, no. 7, pp. 915-918, July2002.

[3] H . S. Eisenberg, Y. Silberberg, R. Morandotti, and J. S. Aitchison, "Diffraction management," Physical Review Letters, vol. 85, no. 9, pp. 1863-1866, Aug.2000.

[4] R . Morandotti, H. S. Eisenberg, Y. Silberberg, M. Sorel, and J. S. Aitchison, "Self-focusing and defocusing in waveguide arrays," Physical Review Letters, vol. 86, no. 15, pp. 3296-3299, Apr.2001.

[5] N . C. Panoiu, M. Bahl, and R. M. Osgood, "Optically tunable superprism effect in nonlinear photonic crystals," Optics Letters, vol. 28, no. 24, pp. 2503-2505, Dec.2003.

[6] P . C. Kendall, M. J. Adams, S. Ritchie, and M. J. Robertson, "Theory for Calculating Approximate Values for the Propagation Constants of An Optical Rib Wave-Guide by Weighting the Refractive-Indexes," Iee Proceedings-A-Science Measurement and Technology, vol. 134, no. 8, pp. 699-702, Sept.1987.

[7] Y . M. Cai, T. Mizumoto, and Y. Naito, "Improved Perturbation Feedback Method for the Analysis of Rectangular Dielectric Wave-Guides," Journal of Lightwave Technology, vol. 9, no. 10, pp. 1231-1237, Oct.1991.

[8] E . Gerjuoy, A. R. P. Rau, and L. Spruch, "A Unified Formulation of the Construction of Variational-Principles," Reviews of Modern Physics, vol. 55, no. 3, pp. 725-774, 1983.

[9] J . Danckaert, K. Fobelets, I. Veretennicoff, G. Vitrant, and R. Reinisch, "Dispersive Optical Bistability in Stratified Structures," Physical Review B, vol. 44, no. 15, pp. 8214-8225, Oct.1991.

[10] W . N. Ye, L. Brzozowski, E. H. Sargent, and D. Pelinovsky, "Stable all-optical limiting in nonlinear periodic structures. III. Nonsolitonic pulse propagation," Journal of the Optical Society of America B-Optical Physics, vol. 20, no. 4, pp. 695-705, Apr.2003.

[11] J . W. Haus, B. Y. Soon, M. Scalora, C. Sibilia, and I. V. Mel'nikov, "Coupled-mode equations for Kerr media with periodically modulated linear and nonlinear coefficients," Journal of the Optical Society of America B-Optical Physics, vol. 19, no. 9, pp. 2282-2291, Sept.2002.

[12] Q . M. Li, C. T. Chan, K. M. Ho, and C. M. Soukoulis, "Wave propagation in nonlinear photonic band-gap materials," Physical Review B, vol. 53, no. 23, pp. 15577-15585, June1996.

[13] J . H. Feng and F. K. Kneubuhl, "Solitons in A Periodic Structure with Kerr Nonlinearity," Ieee Journal of Quantum Electronics, vol. 29, no. 2, pp. 590-597, Feb.1993.

[14] E. P. Kosmidou and T. D. Tsiboukis, "An FDTD analysis of photonic crystal waveguides comprising third-order nonlinear materials," Optical and Quantum Electronics, vol. 35, no. 10, pp. 931-946, Aug.2003.

[15] S. Ramo, J. R. Whinnery, and T. V. Duzer, "Optics," in Fields and Waves in Communication Electronics, 3 ed John Wiley and Sons Inc., 1994, pp. 742-801.

[16] G. J. M. Krijnen, H. J. W. M. Hoekstra, and P. V. Lambeck, "A New Method for the Calculation of Propagation Constants and Field Profiles of Guided Modes of Nonlinear Channel Wave-Guides Based on the Effective-Index Method," Journal of Lightwave Technology, vol. 12, no. 9, pp. 1550-1559, Sept.1994.

[17] K. S. Chiang and R. A. Sammut, "Effective-Index Method for Spatial Solitons in Planar Wave-Guides with Kerr-Type Nonlinearity," Journal of the Optical Society of America B-Optical Physics, vol. 10, no. 4, pp. 704-708, Apr.1993.

[18] A. W. Snyder, D. J. Mitchell, and B. Lutherdavies, "Dark Spatial Solitons Constructed from Modes of Linear Wave-Guides," Journal of the Optical Society of America B-Optical Physics, vol. 10, no. 12, pp. 2341-2352, Dec.1993.

[19] E. Anemogiannis and E. N. Glytsis, "Multilayer Wave-Guides - Efficient Numerical-Analysis of General Structures," Journal of Lightwave Technology, vol. 10, no. 10, pp. 1344-1351, Oct.1992.

[20] M. Dinu, F. Quochi, and H. Garcia, "Third-order nonlinearities in silicon at telecom wavelengths," Applied Physics Letters, vol. 82, no. 18, pp. 2954-2956, May2003.

[21] S. J. Albader and H. A. Jamid, "Guided-Waves in Nonlinear Saturable Self-Focusing Thin-Films," Ieee Journal of Quantum Electronics, vol. 23, no. 11, pp. 1947-1955, Nov.1987.

Chapter 5

A NEW PLANE WAVE EXPANSION METHOD FOR SLAB 1-D PHOTONIC CRYSTALS

The conventional plane wave expansion method is extended for slab photonic crystal. The open boundary condition is applied instead of the conventional supercell scheme. The implicitly restarted Arnoldi method is also modified to solve a nonlinear eigenvalue equation. Fewer Fourier components are necessary for convergence than are required for the conventional plane wave expansion method with supercell definition. The open boundary condition makes analysis of leaky mode a feasible task.

5.1 Introduction

Modeling of slab mode reflections from and transmission into the slab photonic crystal is crucial for any practical designs using slab photonic crystal. Every accurate model should encompass the vertical field confinement and also out of slab radiation losses. The mode matching method is a powerful technique for analysis of waveguide discontinuities such as junctions and facets. Existence of discrete and finite orthogonal modes at both sides of the junction is a key factor that makes the mode matching method an efficient tool. However, for open waveguides commonly used in photonic integrated circuits, the mode-matching method is limited to applications in which the modal solutions are known analytically such as one-dimensional (1-D) multilayer waveguides [1;2]. The plane wave expansion method also can be applied to the modeling of 1-D photonic crystal structure, where the vertical field confinement and out of slab radiation have no place in the adopted model. In this respect, the inclusion of the continuum of radiation modes in the field expansion constitutes a significant challenge. In order to avoid this problem, one may enclose the structure with applying artificial periodicity in vertical direction, so that all modes become discrete. It also makes the implementation of the traditional plane-wave expansion method possible. Then the modes can be divided into two categories: the guided modes, which are confined to the slab and the supercell modes (or above the light line modes), which are related to the imposed artificial periodicity. If the supercell is sufficiently large, then the original problem can be accurately simulated by the artificial model. On the other hand, the plane wave spectral spacing is inversely proportional to the size of the supercell, so a large number of plane waves need to be included in the field expansion to ensure adequate accuracy. Mathematically, the field expansion method in terms of the guided and supercell modes is not very effective, especially for accurate representation of the radiation fields.

A solution for guidance along an open structure is called spectral if it satisfies all the boundary conditions, including the one at infinity (in the transverse direction). Certain "nonspectral" complex solutions (so called leaky modes), which do not satisfy the boundary condition at infinity (in the transverse direction), may nevertheless be physically valid in a restricted region of space. They are very useful due to highly convergent representations of a major portion of the continuum of radiating spectrum. The imaginary parts of the propagation constants for the leaky modes represent for the leakage loss and the modal-field distributions within the critical points represent the radiation fields[3]. Therefore, the radiation field in a slab photonic crystal can be approximated by the summation of leaky modes too.

In this chapter, the plane wave expansion method has been modified for the slab 1-D photonic crystal. Although the formulation is presented for slab 1-D photonic crystals, it can be easily adapted for 2-D cases. The modified implicitly restarted Arnoldi method is introduced to solve the nonlinear eigenvalue equation, which are obtained in the next section. Numerical results are compared with the conventional plane wave expansion method and supercell definition. The capability of the method for obtaining the leaky modes is also demonstrated. We conclude the chapter with some final comments on this method.

5.2 The method

Full vector wave calculation of photonic band structure has been carried out using the plane wave expansion method [4]. Given the desired Bloch wave number (usually along the irreducible Brillouin zone) the band structure can be obtained, *i.e.*, the method provides the wavelength corresponding to that wave number. If L and M reciprocal lattice points (Fourier components) are included in the calculation in each periodic directions, then the resulting eigenvalue equation will be of the order of $2L \times 2M$. The eigenvalue matrix will be Hamiltonian with real eigenvalues (wavelength). There was a poor convergence of Fourier transform especially in high contrast material system [5], which has been mitigated by interpolating the dielectric constant over discontinues. The Hamiltonian nature of the Helmholtz equation is reflected to the Hamiltonian matrix eigenvalue equation (which is sparse too). To calculate the real eigenvalues of a sparse Hamiltonian matrix, there are very effective computational technique [6]. Employment of a basis of $\sim 10^6$ plane waves can be processed with 10^4 times less computer resources, if one uses a proper variational approach [7]. With all these improvements, now the plane wave expansion method is a viable technique to obtain the band diagram of photonic crystal. Nonetheless, the method has some disadvantages. First it is necessary to start with Bloch wave numbers and then the wavelength (corresponding to that Bloch wave number) can be obtained. However, if the wavelength is known and the permitted Bloch wave numbers are sought (for the so called wave vector diagram), then we have to scan the whole Brillouin zone very finely. Secondly, the method cannot handle mixed periodic, non-periodic structures, *i.e.* the structure is periodic in at least one direction but it is not on the others. The supercell technique replaces the unit cell with a more complicated unit cell while retaining the periodicity. For a known case of slab photonic crystal, periodicity is preserved in the vertical direction by assuming periodicity at that direction, but the period is assumed too large that the filed at the periodic boundary is negligible [8]. In addition to the need to model a large unnecessary area (requiring the incorporation of a large number of plane waves), more importantly, the leaky modes cannot be traced.

The structure to be analyzed is depicted in Figure 5.2.1. There are many forms of Helmholtz equation and choices of wave vector components, which are literally equivalent. The best selection of components and the corresponding form of Helmholtz equation, however

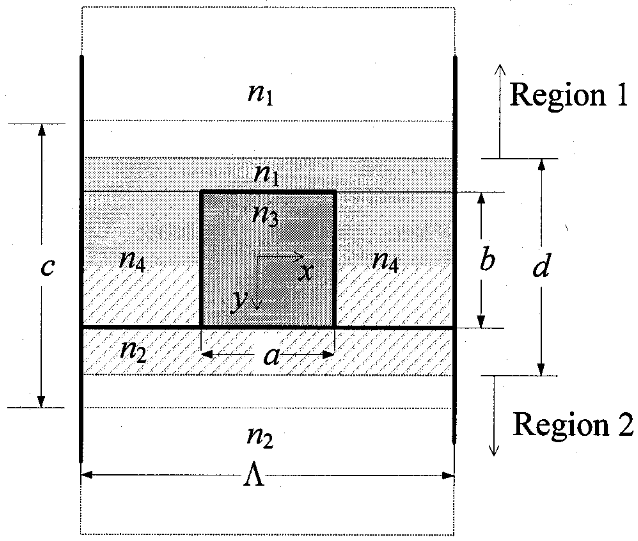

Figure 5.2.1. A simplified slab 1-D photonic crystal cross section, suitable for modeling.

depends on the nature of the problem in hand. As the structure is periodic, Fourier series are used to expand field and refractive index profiles. Due to nonmagnetic nature of the structure, transverse magnetic fields are continuous, so their Fourier series converge more rapidly than the Fourier transform of transverse electric fields, which are not continuous. Whilst traditionally, researchers prefer modeling using electric field components, however for the speed of convergence it is better to choose the magnetic field as a set of independent field components. Electric field components if they are required can be calculated easily using the transverse magnetic field eigenvectors. In this case, in which two open boundaries (in the y directions) exist, and we do not desire to consider any forms of absorbing boundary conditions (in order to keep sufficient accuracy near cutoffs) we will need to apply open boundary conditions. Implementing these conditions will transform the final eigenvalue problem to a complex, nonsymmetrical and nonlinear one. Considering this fact, we can eliminate H_z from the homogenous Helmholtz equation (see Eq. (3.20)) to achieve

$$\left\{\nabla_t + n^2 k_0^2 - k_z^2\right\}\mathbf{H}_t = (\nabla_t \times \mathbf{H}_t) \times \nabla_t \ln n^2 \tag{5.1}$$

where k_z is the propagation constant in z direction. By this elimination we reduce the size of the eigenmatrix by one third, but unfortunately it also reduces the sparsity of the final eigen matrix. Considering the circumstances, the simulation is based on Eq.(5.1), and of course we expect to have a complex and non-symmetrical eigenmatrix (with less sparsity).

The transverse magnetic field is approximated by a limited summation of Bloch modes, as

$$\mathbf{H}_t = \sum_{l=-L}^{L} h_{xl}(y)\exp\left[i\left(2l\pi/\Lambda + k_x\right)x\right]\hat{\mathbf{a}}_x + \sum_{l=-L}^{L} h_{yl}(y)\exp\left[i\left(2l\pi/\Lambda + k_x\right)x\right]\hat{\mathbf{a}}_y \quad (5.2)$$

where k_x is the Bloch wave number, and Λ is the period in x direction. Note that there is no refractive index change outside hatched regions so we can write Eq.(5.1) as a homogenous Maxwell's equation, and implement boundary conditions at the interfaces. Therefore, outside the hatched regions, we have

$$\left\{\nabla_t + n^2k_0^2 - k_z^2\right\}\mathbf{H}_t = 0 \quad (5.3)$$

Inserting Eq.(5.2) in Eq.(5.3), we have

$$\sum_l \left\{\ddot{h}_{xl} - \left[\left(2l\pi/\Lambda + k_x\right)^2 + k_z^2 - n^2k_0^2\right]h_{xl}\right\}\exp\left(i\,2l\pi x/\Lambda\right) = 0 \quad (5.4)$$

where the dot stands for derivative with respect to y . A similar equation can be obtained for h_{yl}. Then we can use the orthogonality of exponential functions to achieve

$$\ddot{h}_{xl} - \left[\left(2l\pi/\Lambda + k_x\right)^2 + k_z^2 - n^2k_0^2\right]h_{xl} = 0 \qquad \forall l = -L,\cdots,L \quad (5.5)$$

Assuming zero boundary conditions at infinities in the y direction (or no wave coming from there), the solution will be as follows

$$h_{xl}(y) = \begin{cases} a_{xl}\exp\left[k_{1l}\left(y + d/2\right)\right] & y \le -d/2 \\ c_{xl}\exp\left[-k_{2l}\left(y - d/2\right)\right] & y \ge d/2 \end{cases} \quad (5.6)$$

where

$$k_{jl}=\sqrt{\left(2l\pi/\Lambda+k_x\right)^2+k_z^2-n_j^2k_0^2} \quad , \; j=1,2 \tag{5.7}$$

and a_{xl}, c_{xl} are constants to be determined. The square root branch cut has to be selected properly to satisfy the boundary conditions at infinity. For h_{yl}, similarly we have

$$h_{yl}(y)=\begin{cases} a_{yl}\exp\left[k_{1l}\left(y+d/2\right)\right] & y\le -d/2 \\ c_{yl}\exp\left[-k_{2l}\left(y-d/2\right)\right] & y\ge d/2 \end{cases} \tag{5.8}$$

For the central region ($-c/2\le y\le c/2$ including the hatched region and two small top and bottom strips), we expand the refractive index squared as a two dimensional Fourier series

$$n^2=\sum_{m=-M}^{M}\sum_{l=-L}^{L}\nu_{lm}\exp\left(i2\pi lx/\Lambda\right)\exp\left(i2\pi my/c\right), \qquad -c/2\le y\le c/2 \tag{5.9}$$

And truncate it to $m=-M,\cdots,M$ $l=-L,\cdots,L$ and similarly,

$$\nabla_t \ln n^2=\sum_{m=-M}^{M}\sum_{l=-L}^{L}\left(\nu'_{xlm}\hat{\mathbf{a}}_x+\nu'_{ylm}\hat{\mathbf{a}}_y\right)\exp\left(i2\pi lx/\Lambda\right)\exp\left(i2\pi my/c\right), \; -c/2\le y\le c/2 \tag{5.10}$$

In addition, we expand h_{xl} and h_{yl} as:

$$\begin{aligned} h_{xl}(y)&=\sum_{m=-M}^{M}b_{xlm}\exp\left(i2\pi my/c\right), & -c/2\le y\le c/2 \\ h_{yl}(y)&=\sum_{m=-M}^{M}b_{ylm}\exp\left(i2\pi my/c\right), & -c/2\le y\le c/2 \end{aligned} \tag{5.11}$$

which we have limited the number of elements in the summation to $2M+1$. By inserting Eqs. (5.2), (5.9), (5.10), and (5.11) into Eq. (5.1), and arranging terms, we will have:

$$
\begin{cases}
-\left[\left(2l\pi/\Lambda+k_x\right)^2+\left(2m\pi/c\right)^2\right]b_{x,l,m}+\sum_{l'=-L}^{L}\sum_{m'=-M}^{M}\left\{i\nu'_{y,l-l',m-m'}\right. \\
\qquad \left.\left[\left(2\pi l'/\Lambda+k_x\right)b_{y,l',m'}-b_{x,l',m'}2\pi m'/c\right]+\nu_{l-l',m-m'}k_0^2 b_{x,l',m'}\right\}=k_z^2 b_{x,l,m} \\
-\left[\left(2l\pi/\Lambda+k_x\right)^2+\left(2m\pi/c\right)^2\right]b_{y,l,m}-\sum_{l'=-L}^{L}\sum_{m'=-M}^{M}\left\{i\nu'_{x,l-l',m-m'}\right. \\
\qquad \left.\left[\left(2\pi l'/\Lambda+k_x\right)b_{y,l',m'}-b_{x,l',m'}2\pi m'/c\right]-\nu_{l-l',m-m'}k_0^2 b_{y,l',m'}\right\}=k_z^2 b_{y,l,m}
\end{cases}
\tag{5.12}
$$

where $l=-L,\cdots,L,\ m=-M+1,\cdots,M-1$. If we apply boundary conditions (continuity of tangential magnetic and normal electric field) at $y=\pm d/2$, see Figure 5.2.1., we will have

$$
\begin{cases}
\sum_{m=-M}^{M} b_{x,l,m}\left(k_{1l}-2i\pi m/c\right)\exp\left(-i\pi md/c\right)=0 \\
\sum_{m=-M}^{M} b_{x,l,m}\left(k_{2l}+2i\pi m/c\right)\exp\left(i\pi md/c\right)=0
\end{cases}
\tag{5.13}
$$

where $l=-L,\cdots,L$, and Eqs. (5.11), (5.6) and (5.8), have been involved. For $b_{y,l,m}$ the same equations are valid.

From Eqs. (5.13), we can solve $b_{x,l,-M}, b_{x,l,M}$ as follow

$$
b_{x,l,-M}=\sum_{m=-M+1}^{M-1} d_{l,m}b_{x,l,m},\qquad b_{x,l,M}=\sum_{m=-M+1}^{M-1} e_{l,m}b_{x,l,m}
\tag{5.14}
$$

Where

$$
\begin{aligned}
d_{l,m}=\frac{-1}{D_l}\Bigg[&\left(k_{1l}k_{2l}+4\frac{mM\pi^2}{c^2}\right)\sin\left(\frac{\pi d(M-m)}{c}\right)+\exp\left(\frac{i\pi d(M-m)}{c}\right)\left(\frac{M\pi}{c}k_{1l}-\frac{m\pi}{c}k_{2l}\right) \\
&+\exp\left(\frac{-i\pi d(M-m)}{c}\right)\left(\frac{M\pi}{c}k_{2l}-\frac{m\pi}{c}k_{1l}\right)\Bigg]
\end{aligned}
\tag{5.15}
$$

$$
\begin{aligned}
e_{l,m}=\frac{-1}{D_l}\Bigg[&\left(k_{1l}k_{2l}-4\frac{mM\pi^2}{c^2}\right)\sin\left(\frac{\pi d(M+m)}{c}\right)+\exp\left(\frac{i\pi d(M+m)}{c}\right)\left(\frac{m\pi}{c}k_{1l}+\frac{M\pi}{c}k_{2l}\right) \\
&+\exp\left(\frac{-i\pi d(M+m)}{c}\right)\left(\frac{m\pi}{c}k_{2l}+\frac{M\pi}{c}k_{1l}\right)\Bigg]
\end{aligned}
\tag{5.16}
$$

and D_l is defined as

$$D_l = \left(k_{1l}k_{2l} - 4\pi^2 M^2/c^2\right)\sin\left(2\pi Md/c\right) + \frac{2M\pi}{c}\left(k_{1l} + k_{2l}\right)\cos\left(2\pi Md/c\right) \tag{5.17}$$

By inserting Eqs. (5.14), and similar equations for $b_{y,l,-M}$ and $b_{y,l,M}$ back into Eqs. (5.12), we will have

$$\begin{cases} t_0 b_{x,l,m} + \sum\limits_{m'=-M+1}^{M-1} \sum\limits_{l'=-L}^{L} \left\{ b_{x,l',m'}\left(t_1 + t_3\right) + b_{y,l',m'} t_4 \right\} = k_z^2 b_{x,l,m} \\ t_0 b_{y,l,m} + \sum\limits_{m'=-M+1}^{M-1} \sum\limits_{l'=-L}^{L} \left\{ b_{y,l',m'}\left(t_5 + t_3\right) + b_{x,l',m'} t_2 \right\} = k_z^2 b_{y,l,m} \end{cases} \tag{5.18}$$

where

$$\begin{aligned} t_0(l,m) &= -\left[\left(2l\pi/\Lambda + k_x\right)^2 + \left(2m\pi/c\right)^2\right] \\ t_1(l,m,l',m') &= 2i\pi/c\left(-m'\nu'_{y,l-l',m-m'} + Md_{l',m'}\nu'_{y,l-l',m+M} - Me_{l',m'}\nu'_{y,l-l',m-M}\right) \\ t_2(l,m,l',m') &= -2i\pi/c\left(-m'\nu'_{x,l-l',m-m'} + Md_{l',m'}\nu'_{x,l-l',m+M} - Me_{l',m'}\nu'_{x,l-l',m-M}\right) \\ t_3(l,m,l',m') &= k_0^2\left(\nu_{l-l',m-m'} + d_{l',m'}\nu_{l-l',m+M} + e_{l',m'}\nu_{l-l',m-M}\right) \\ t_4(l,m,l',m') &= i\left(2\pi l'/\Lambda + k_x\right)\left(\nu'_{y,l-l',m-m'} + d_{l',m'}\nu'_{y,l-l',m+M} + e_{l',m'}\nu'_{y,l-l',m-M}\right) \\ t_5(l,m,l',m') &= -i\left(2\pi l'/\Lambda + k_x\right)\left(\nu'_{x,l-l',m-m'} + d_{l',m'}\nu'_{x,l-l',m+M} + e_{l',m'}\nu'_{x,l-l',m-M}\right) \end{aligned} \tag{5.19}$$

With these modifications, Eqs.(5.18) are $2(2L+1)\times(2M-1)$ complex nonlinear eigenvalue equations. Eqs.(5.18) are about two times larger than the eigenvalue matrix of the conventional plane wave expansion method, which is due to the complex nature of the plane wave amplitude (compared to the real ones in conventional plane wave expansion method [9]).

5.3 Fourier transform coefficients of Eqs. (5.9) and (5.10)

$\nu_{m,l}$ of Eq. (5.9) can be expressed as

$$\nu_{l,m} = n_1^2 I_{l,m} + n_2^2 J_{l,m} + n_3^2 K_{l,m} + n_4^2 L_{l,m} \tag{5.20}$$

where

$$I_{l,m} = \frac{1}{c\Lambda}\int_{b/2}^{c/2}\int_{-\Lambda/2}^{\Lambda/2} \exp(-i2\pi lx/\Lambda)\exp(-i2\pi my/c)\,dxdy \tag{5.21}$$

$$J_{l,m} = \frac{1}{c\Lambda}\int_{-c/2}^{-b/2}\int_{-\Lambda/2}^{\Lambda/2} \exp(-i2\pi lx/\Lambda)\exp(-i2\pi my/c)\,dxdy \tag{5.22}$$

$$K_{l,m} = \frac{1}{c\Lambda}\int_{-b/2}^{b/2}\int_{-\tau\Lambda/2}^{\tau\Lambda/2} \exp(-i\,2\pi lx/\Lambda)\exp(-i\,2\pi my/c)\,dxdy \tag{5.23}$$

$$L_{l,m} = \frac{1}{c\Lambda}\left[\int_{-b/2}^{b/2}\int_{-\Lambda/2}^{-\tau\Lambda/2} + \int_{-b/2}^{b/2}\int_{\tau\Lambda/2}^{\Lambda/2}\right]\exp(-i\,2\pi lx/\Lambda)\exp(-i\,2\pi my/c)\,dxdy \tag{5.24}$$

or

$$I_{l,m} = \frac{(1-\tau')}{2}\operatorname{sinc}(l)\operatorname{sinc}\left[m/2(1-\tau')\right]\exp\left[-i\,m\pi/2(1+\tau')\right] \tag{5.25}$$

$$J_{l,m} = \frac{(1-\tau')}{2}\operatorname{sinc}(l)\operatorname{sinc}\left[m/2(1-\tau')\right]\exp\left[im\pi/2(1+\tau')\right] \tag{5.26}$$

$$K_{l,m} = \tau\tau'\operatorname{sinc}(m\tau')\operatorname{sinc}(l\tau) \tag{5.27}$$

$$L_{l,m} = \tau'\operatorname{sinc}(m\tau')\left[\operatorname{sinc}(l) - \tau\operatorname{sinc}(l\tau)\right] \tag{5.28}$$

where $\tau' \equiv b/c$, and $\operatorname{sinc} x \equiv \sin \pi x/\pi x$. If we take derivative of the Fourier series of $\ln n^2$, then by using the above expansion, $\nu'_{xl,m}$ and $\nu'_{yl,m}$ in Eq. (5.10) can be calculated as below

$$\begin{aligned} \nu'_{x,l,m} &= i2\pi l/\Lambda\left(\ln n_1^2 I_{l,m} + \ln n_2^2 J_{l,m} + \ln n_3^2 K_{l,m} + \ln n_4^2 L_{l,m}\right) \\ \nu'_{y,l,m} &= i2\pi m/c\left(\ln n_1^2 I_{l,m} + \ln n_2^2 J_{l,m} + \ln n_3^2 K_{l,m} + \ln n_4^2 L_{l,m}\right) \end{aligned} \tag{5.29}$$

The Hamming window of

$$w_{l,m} = \begin{cases} [0.54+0.46\cos(2\pi m/M)][0.54+0.46\cos(2\pi l/L)], & \begin{array}{l} -M \le m \le M, \\ -L \le l \le L \end{array} \\ 0 & \text{otherwise} \end{cases} \tag{5.30}$$

has also been applied to moderate the Gibbs phenomenon due to truncation of elements in the series [10].

5.4 Iterative nonlinear Arnoldi method

Eqs (5.18) represents a nonlinear eigenvalue problem. It can be re-written in matrix form as

$$\mathbf{B}\left(k_z^2\right)\mathbf{b} = k_z^2\mathbf{b} \tag{5.31}$$

where $\mathbf{B}$ is a complex large sparse matrix and a function of the sought eigenvalue k_z^2 $\mathbf{b}$ represents the collection of eigenvectors.

The implicitly restarted Arnoldi method is an efficient iterative technique to determine the few eigenvalues and eigenvectors of a large linear sparse matrix[11]. To explain the method, first consider a linear case, in which $\mathbf{B}$ is a constant square matrix. The method in its basic form is the most suitable technique for finding a specific eigenvalue and eigenvector, based on an initial eigenvector guess. The Ritz pair (the eigenvector and eigenvalue) at the end of each iteration also provide the best eigenvalue and a better eigenvector guess for the next step. However, the results are too sensitive to the initial guess. The implicitly restarted Arnoldi method sorts a few eigenvalues according to the desired criteria (e.g., maximum real value) that one can choose between, and then adapt the Ritz pairs according to that selection. The simplified flow chart of linear implicitly restarted Arnoldi method is depicted in Figure 5.4.1.

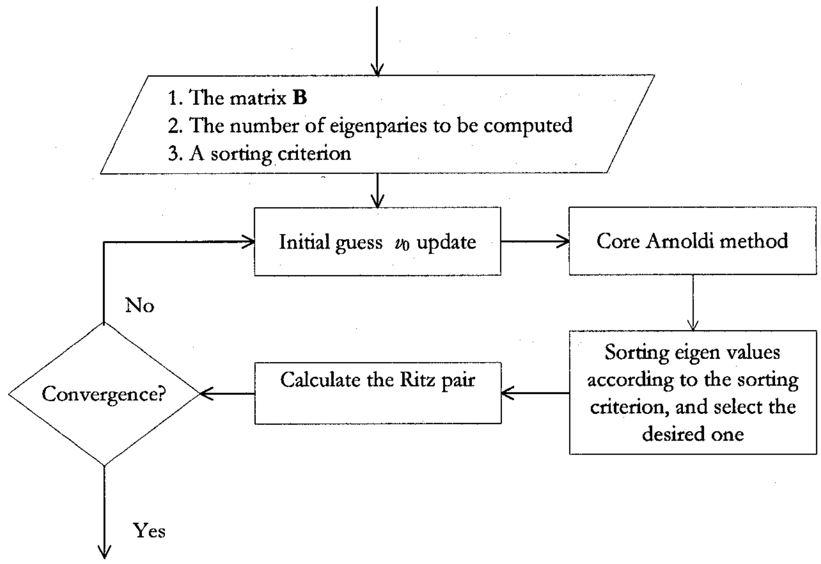

Figure 5.4.1 The flow chart of linear Arnoldi method

Now consider the nonlinear case in which the matrix **B** is a function of the sought eigenvalue. The proposed flowchart of nonlinear Arnoldi method is depicted in Figure 5.4.2 . Note that we have to update the nonlinear matrix **B** based on the desired eigenvalue. For example to achieve the bound mode, one can sort the eigenvalues according to the magnitude of their real parts, and then select the largest one for updating matrix **B**.

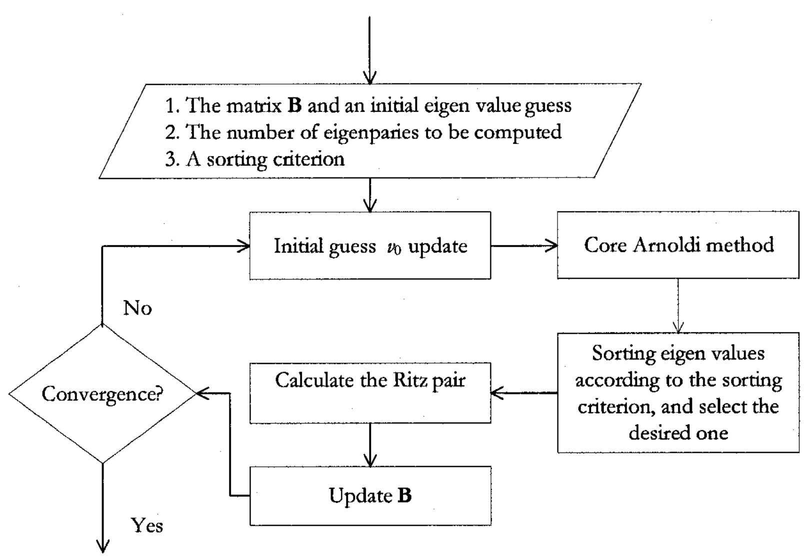

Figure 5.4.2 The flow chart of nonlinear Arnoldi method

If the method converges, then the output of this technique will be the desired eigenvalue satisfying Eq.(5.31) .

5.5 Mode characterization

Since the Bloch wave number is the phase of a periodic Bloch wave, so all wave numbers beyond the first Brillouin zone can be shifted into the first Brillouin zone. All discussion in this chapter is based on this assumption.

A bound mode is a mode with an amplitude that neither decreases nor increases by propagating through the photonic crystal. Also all of the wave components have to be decaying outside the photonic crystal. The transverse propagation constant of the field components outside photonic crystal (Eqs.(5.7)) can be written as

$$k_{jl} = \sqrt{4l\pi k_x/\Lambda + \left(2l\pi/\Lambda\right)^2 + k^2 - n_j^2 k_0^2} \quad , \ j = 1,2 \tag{5.32}$$

Where

$$k^2 = k_x^2 + k_z^2 \tag{5.33}$$

So for the bound mode, all k_{jl} must be real, *i.e.*,

$$k/k_0 > n_j \quad , j = 1,2 \tag{5.34}$$

Otherwise, some field components outside photonic crystal will have imaginary transverse wave numbers. In other words, they will be radiative. Figure 5.5.1 shows the complex $n_{pc} \equiv k/k_0$ plane in terms of various solutions for slab 1-D photonic crystals. Additionally, we have assumed $n_{clad} < n_{sub}$; and for symmetrical structure in which $n_{clad} = n_{sub}$, the "substrate leaky" region ceases to exist.

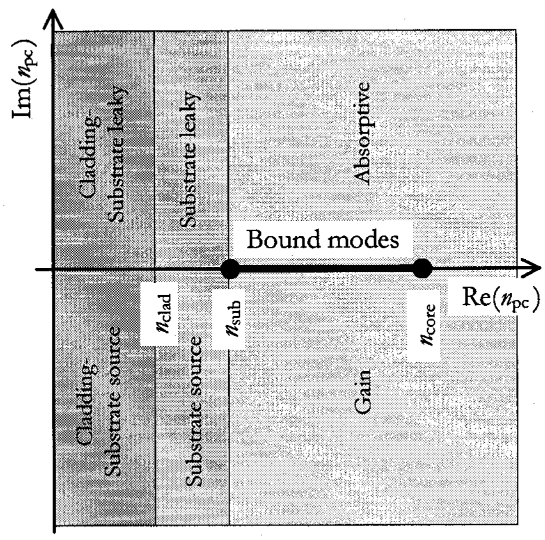

Figure 5.5.1 The complex n_{pc} plane in terms of various solutions

5.6 Numerical demonstration

Consider the SOI wafer with top silicon layer of 0.5 μm thickness. The grating period of 256nm, and the grating duty factor of $\tau = 0.5$. The wavelength of interest is $\lambda = 1537.4\,\text{nm}$ and the polarization is TM like (Electric field normal to the slab surface). For the sake of modeling the permittivity of the silicon and silica are assumed 12 and 2, respectively. The parameters of Figure 5.2.1 are chosen as

$$\begin{aligned}
&n_1 = 1,\ n_2 = \sqrt{2},\ n_3 = \sqrt{12},\ n_4 = 1 \\
&\Lambda = 265\,\text{nm},\quad a = \Lambda/2 = 132.5\,\text{nm},\ b = 500\text{nm} \\
&c = 1000\ \text{nm},\ d = 800\text{nm},\ L = M = 20
\end{aligned} \tag{5.35}$$

Figure 5.6.1 shows near the band edge versus the number of plane waves in normal direction to the slab, using the conventional plane wave expansion method with the supercell of 6 times of the height of slab[9]. Neither refractive index over sampling nor tensor averaging is applied. The number of modes in the periodic direction is assumed to be $L = 32$. As is seen, at the band edge, there is about 10% error, when $M = L = 32$ (total number of participating plane waves is 1024). Accurate results are only achievable after $M = 256$, or total number of modes of 4096. Then the eigenmatrix dimension is 32768.

Figure 5.6.2 shows the convergence pattern of the adopted Arnoldi method when it is initiated with randomly generated eigenvector. One hundred twenty iterations are enough to get to four

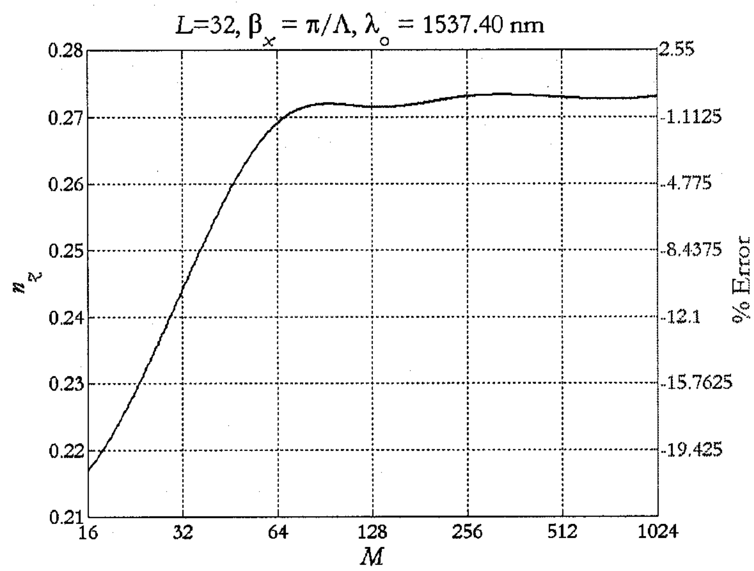

Figure 5.6.1 Normalized band edge versus plane wave components in the vertical direction.

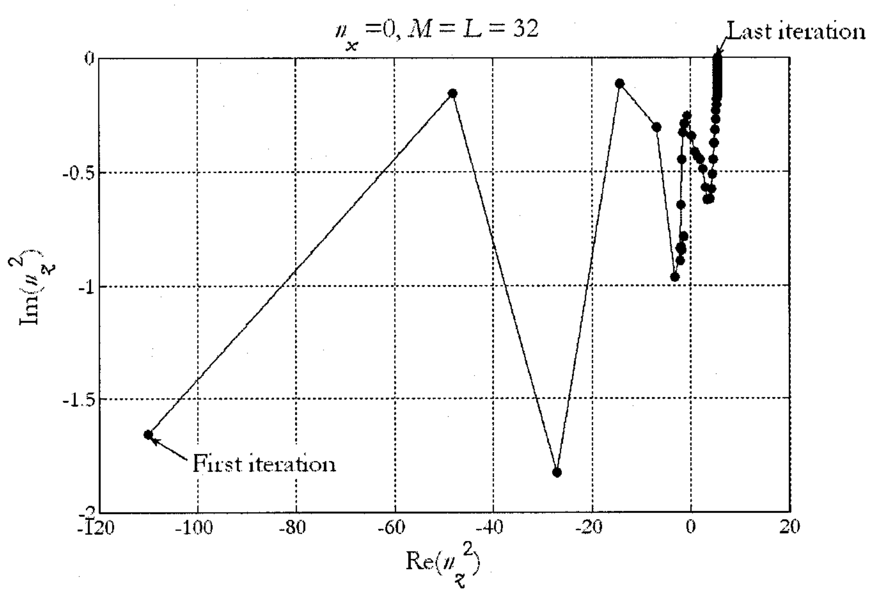

Figure 5.6.2 A typical convergence pattern of the nonlinear Arnoldi method for the dominant eigenvalue

meaningful decimal points accuracy for the real main eigenvalue. If one starts from an appropriate initial guess (e.g. the eigenvector of the previous step in the procedure of obtaining the full wave vector diagram), the convergence will be faster and it will be achievable in about thirty iterations. All intermediate values have a zero imaginary parts too (the convergence path lay on the real axis). Considering the number of components that we have chosen, $L = M = 32$, the dimension of eigen matrix is $2(2L+1)(2M-1) = 8190$.

Figure 5.6.3 shows the results of our method compared to the traditional plane wave expansion method with a variational formula, and the exact finite element method. The parameters of (5.35) are selected. Assuming the results of the finite elements as a benchmark, our results are very well matched with the accurate results. More specifically, the error is less than 0.3% in the ranges that the graph has been plotted. The method provides better agreement with the exact finite element method than the conventional plane wave extension method [9] when $L = 128$ and $M = 32$ modes have been employed. The size of the corresponding eigenvalue matrix is 16384. The benchmark method is explained in appendix A.

Figure 5.7.1 shows the movement of the six first modes in the complex n_{pc}^2 plane with n_x (at a constant wavelength of $\lambda_{41} = 1537.40$ nm). As is seen, each mode has a unique trajectory.

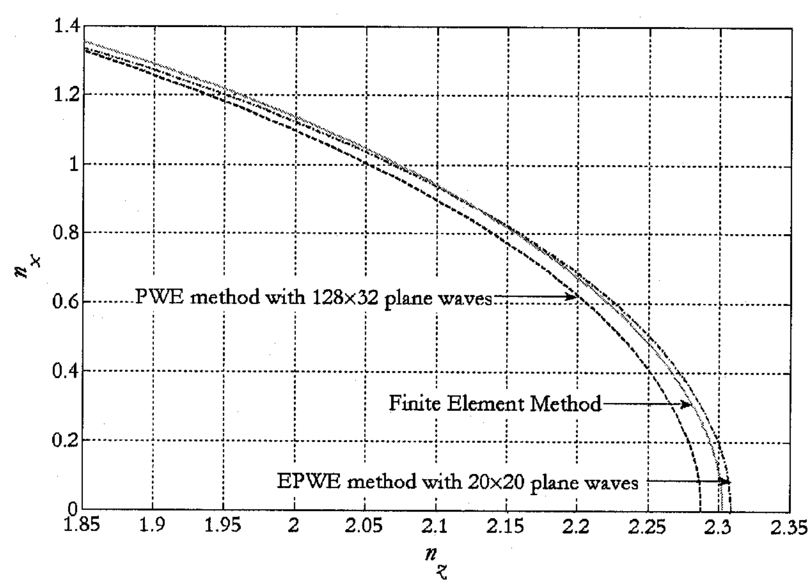

Figure 5.6.3 The results of various methods

Bound modes are basically those with no imaginary parts and their real parts lie between $\min\left(n_{\text{sub}}^2, n_{\text{clad}}^2\right) = 2$, and $n_{\text{core}}^2 = 12$. Figure 5.5.1 depicts how the proper set of modes can be selected to match a particular setup.

5.7 Conclusion

Eqs. (5.12) can be reduced to the conventional plane wave expansion method with supercell definition, provided we choose a sufficiently large expansion window $c/2 \geq y \geq -c/2$ and choosing $l = -L, \cdots, L$, $m = -M, \cdots, M$. This selection by default implies that the field repeats itself along the vertical direction. The convergence of this form of the plane wave

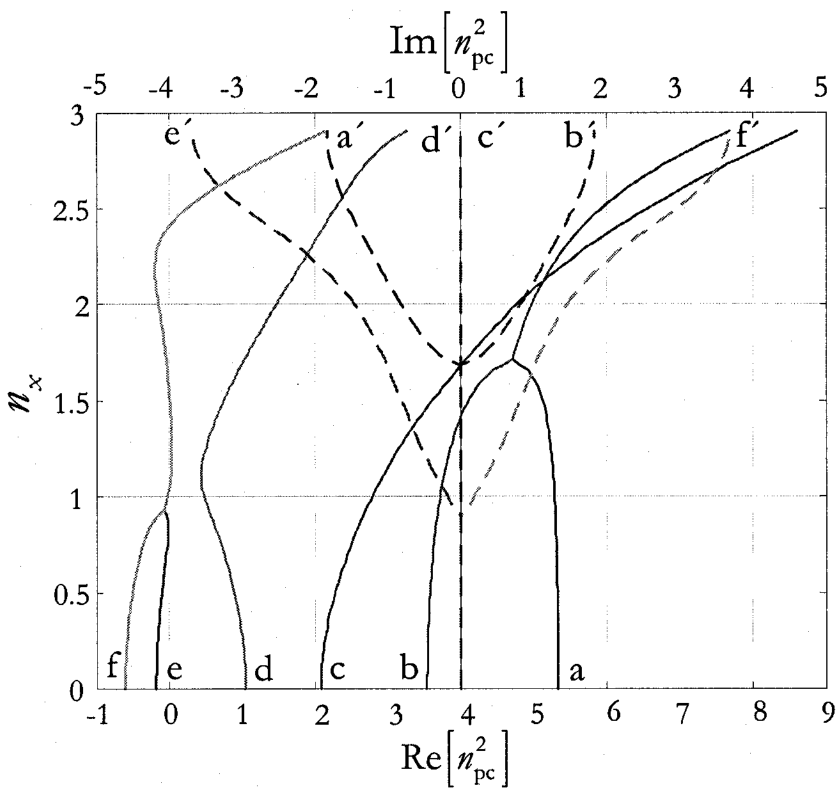

Figure 5.7.1 The real and imaginary part of n_{pc}^2 versus n_x at fixed wavelength of $\lambda_{41} = 1537.40\ \text{nm}$. The bottom scale is for the real part (bold lines) modes characterized sequentially by the English alphabet. The top scale is for the imaginary part (dashed lines) modes characterized sequentially by the English alphabet and a prime.

expansion method remains the same compared with the method when it was initially introduced [4]. However, the method as presented here is computationally more intensive than the state of art plane wave expansion method. Although we have to execute the plane wave expansion program numerous times, thanks to the Bloch variational iterative formula[9], the method is relatively fast. Finally, the capability of our method to trace the leaky modes and the fact that it needs fewer Fourier components in the non-periodic direction make it attractive.

References

[1] T. E. Rozzi, "Rigorous Analysis of Step Discontinuity in A Planar Dielectric Waveguide," *Ieee Transactions on Microwave Theory and Techniques*, vol. 26, no. 10, pp. 738-746, 1978.

[2] H. Shigesawa and M. Tsuji, "Mode Propagation Through A Step Discontinuity in Dielectric Planar Wave-Guide," *Ieee Transactions on Microwave Theory and Techniques*, vol. 34, no. 2, pp. 205-212, Feb.1986.

[3] Snyder A.W. and Love J.D., in *Optical waveguide theory* Chapman and Hall, 1983.

[4] K. M. Leung and Y. F. Liu, "Full Vector Wave Calculation of Photonic Band Structures in Face-Centered-Cubic Dielectric Media," *Physical Review Letters*, vol. 65, no. 21, pp. 2646-2649, Nov.1990.

[5] H. S. Sozuer, J. W. Haus, and R. Inguva, "Photonic Bands - Convergence Problems with the Plane-Wave Method," *Physical Review B*, vol. 45, no. 24, pp. 13962-13972, June1992.

[6] S. G. Johnson and J. D. Joannopoulos, "Block-iterative frequency-domain methods for Maxwell's equations in a planewave basis," *Optics Express*, vol. 8, no. 3, pp. 173-190, Jan.2001.

[7] R . D. Meade, A. M. Rappe, K. D. Brommer, J. D. Joannopoulos, and O. L. Alerhand, "Accurate Theoretical-Analysis of Photonic Band-Gap Materials," *Physical Review B*, vol. 48, no. 11, pp. 8434-8437, Sept.1993.

[8] J ohnson S.G. and Joannopoulos J.D., *Photonic Crystals: The Road from Theory to Practice* Boston, MA: Kluwer Academic Publishers, 2002.

[9] S . G. Johnson and J. D. Joannopoulos, "Block-iterative frequency-domain methods for Maxwell's equations in a planewave basis," *Optics Express*, vol. 8, no. 3, pp. 173-190, Jan.2001.

[10] O ppenheim Alan V and Schafer Ronald W., "Filter design techniques," in *Discrete-time signal processing* Prentice-Hall, 1998, pp. 403-513.

[11] R . B. Lehoucq, D. C. Sorensen, and C. Yang, "ARPACK Users' Guide: Solution of Large-Scale Eigenvalue Problems with Implicitly Restarted Arnoldi Methods," SIAM, Rice University, Department of Computational and Applied Mathematics,1996.

Chapter 6

FIRST BAND S-VECTOR PHOTONIC CRYSTAL SUPERPRISM DEMULTIPLEXER DESIGN AND OPTIMIZATION

We present a complete approach to the design of a wavelength demultiplexer based on the S-vector superprism photonic crystal phenomenon. We make use of a full 3-D modeling approach based on the plane wave expansion method which allows the full dynamics of beam propagation to be considered. This reveals significant non-uniformities in beam divergence and dispersion as a function of wavelength which has been neglected in previous 2-D models and which reduces the scalability of these devices. We examine 1-D and 2-D photonic crystal lattices and show that the 1-D lattice results in the smallest superprism area as a function of channel count. This is due to its lower band curvature relative to 2-D square and hexagonal lattices, even though it has much lower angular dispersion. We also modify the previous S-vector superprism design so that for each channel the prism region extends only as far as necessary for channel resolution at a specified crosstalk level. Based on Silicon-On-Insulator technology, with a top silicon layer of 260 nm and minimum feature size of 75nm, we present the design of a 4-channel Coarse Wavelength Division Multiplexing (CWDM) demultiplexer with theoretical crosstalk of 20dB, which has a superprism area of 1367μm^2.

6.1 Introduction

Although the first motivation for the development of photonic crystals was the prohibition of light propagation in specified directions at wavelengths inside the bandgap, wave propagation through photonic crystals at wavelengths below the band edge has more recently been of great interest. One of the most widely investigated phenomena is that of beam steering which was first observed in slab 1-D photonic crystals about 20 years ago [1], but it was not until 1998 that the observation of 5°/nm beam steering dispersion in a pseudo-2-D auto-cloned photonic crystal [2] gathered a great deal of attention. This phenomenon has become known as the superprism effect, despite the fact that it arises from anomalous refraction near the band edge, (which is based on group velocity dispersion) rather than phase velocity dispersion which is the origin of wavelength separation in a conventional isotropic prism. This distinction recently has been made clearer by referring to devices of this type as **S**-vector superprisms. In contrast, photonic crystal superprisms that make use of phase velocity dispersion are referred to as **k**-vector superprisms [3-6]. When the large beam steering effect in the **S**-vector superprism was first observed it was thought that it would be a promising alternative for DWDM demultiplexers (requiring 100 GHz channel spacing) or even beyond. However, it has been shown recently that the demultiplexer resolution of the **S**-vector superprism is not only a function of dispersion, but is also a function of the beam divergence within the photonic crystals [6]. Unfortunately, the beam divergence is a function of band curvature which is not small near the band edge where the dispersion is high [7]. The beam divergence is indeed the main factor limiting the resolution. Using the negative refraction observable at the bandedge of the second band to compensate the positively refracted incident beam (the so called preconditioning) is a novel idea that has been suggested for mitigating this issue [8;9]. But this cancellation is achievable only over relatively narrow bandwidth (only 32 nm), and the loss of working too near the band edge is considerable[8]. Adiabatic tapering of the lattice has also been introduced to reduce the loss[9;10], but of course the fabrication would be challenging. The resolution can also be improved by increasing the aperture size, this requires large photonic crystal regions that means the devices are no longer small compared to other demultiplexer technologies. However for Coarse Wavelength Division Multiplexing (CWDM) applications which require a 20 nm channel spacing the **S**-vector superprism has been shown to be competitive [6]. However, as we will show in this chapter previous studies of superprism scalability have been based on a set of assumptions that may lead to overly optimistic results.

Figure 6.1.1 shows the well known **S**-vector superprism configuration where the output waveguides are located on the circumference of a circle and directed radially (in direction of the beam inside the photonic crystal) and the input waveguide is at the centre of the circle [11;12].

Although this configuration makes the physical path inside photonic crystal the same for all channels, it suffers from the fact that channels with large divergence angles and high angular dispersion occupy unnecessarily a large slice of photonic crystal to reach the output circumference. This will result in excessive loss and output beam width, in addition to requiring a larger photonic crystal area, although it simplifies the design process. Noting that the conservation of the tangential component of the wave vector across the bulk photonic crystal and the output facets is the key factor in determining the output beam direction, the output beam direction outside photonic crystal is not always the same as the one inside. Therefore, either the output waveguide direction needs correction or the output facet direction with the bulk photonic crystal must be modified.

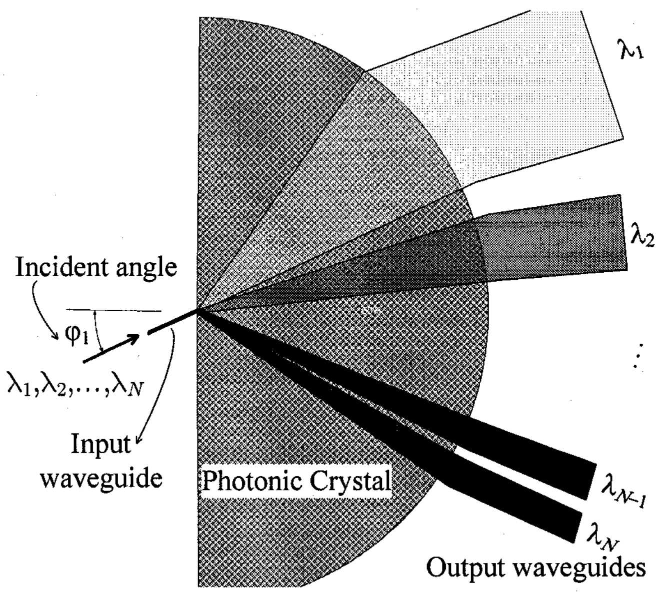

Figure 6.1.1. The conventional S-vector demultiplexer configuration.

The S-vector superprism phenomenon can be observed either in the first or the second photonic crystal bands. For the second band the effect is caused by the apparent distortion from a circular shape of the wave vector diagram (equi-frequency band diagram) and also by multiplicity within the diagram [2] Clearly when there is no multiplicity (as in 1-D photonic crystals), there will be less dispersion, and when there is high multiplicity (as in hexagonal lattice), there will be more [11]. Fabrication is simplified since for the second band the period is about twice that of the first band, but the presence of the first band may cause bands to overlap. Then multiple refractions at the input interface are unavoidable due to the overlapping of the bands. This multiple refraction will increase the coupling loss (all the power which has been coupled to the modes in the first band is lost). Furthermore, there may be many diffracted waves at the output facet of the photonic crystal with various diffraction angles [13] which is due to many reciprocal lattice vectors of small amplitude (due to the size of the photonic crystal period). Considering the fact that each diffracted beam carries a portion of the initial power and the design is based only on one particular beam, the loss would be large.

The dispersion observed in the first band of photonic crystal has been also exploited for **S**-vector superprisms[12]. The source of dispersion in this case is the evolution of the band with wavelength. The first band diagram evolves with decreasing wavelength from a closed curve (resembling the photonic crystal type in the reciprocal space), to having the band gap perpendicular to the main symmetry axes of the lattice. The maximum dispersion happens at the transition of the band where it evolves from a closed curve around the origin to having bandgaps. The period is usually small enough and the reciprocal lattice vectors are too large to allow many diffracted waves at the output interface to be generated. The wave refraction at the interface of photonic crystal can be described by the wave vector diagram which represents the wave propagation constant for a given wavelength and direction of propagation (also known as the equi-frequency contour diagram). Figure 6.1.2 shows wave vector diagram of a superprism where input and output interfaces are parallel and the incident angle is normal. The lattice is a 2-D square which has been rotated by 15°. The circle is the slab free-space wave vector diagram. As is shown on the diagram, double refraction (points A and B in Figure 6.1.2) are possible at the output interface. Aligning the output waveguide with either direction will capture the wave deflected only in that direction (subject to the low acceptance angle of the output waveguides, and/or deflection beam angles that are not too close to each other).

However, the great dispersion that has been observed and reported [2;5;14] usually happens within a narrow bandwidth, which fades quickly for other wavelengths. Furthermore and as we will show, the divergence angle of the beam is also highly non-uniform with respect to wavelength. Under these circumstances, the wavelength resolution is not related in any simple way to dispersion and beam divergence. Also, although the design equations usually are not affected if one chooses 2-D photonic crystal modeling the omission of the third dimension will cause the results obtained to be unrealistic. However this has been the approach followed in most previous analyses of these devices [3;6;15].

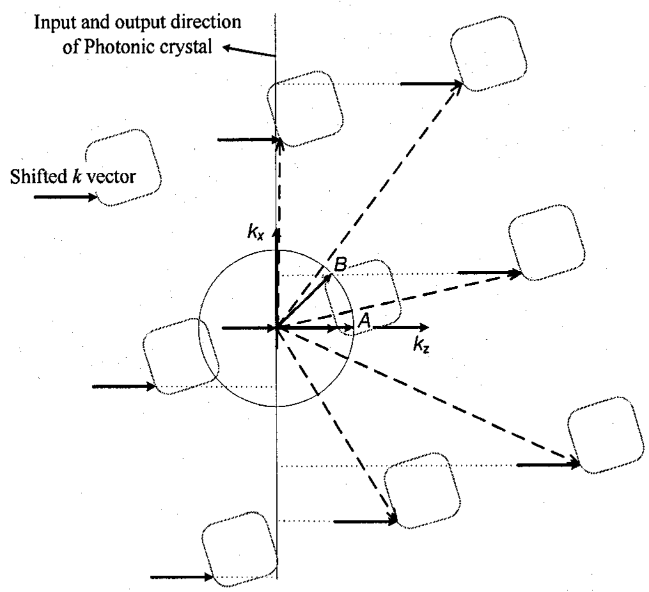

Figure 6.1.2. Input and output light deflection including all Brillouin zones.

We will show in this chapter that an attempt to determine which photonic crystal type and configuration renders maximum dispersion and minimum beam divergence at a single wavelength using linear analysis (*i.e.* assuming equal dispersion and beam divergence for all channels) is not adequate for real applications. Therefore there is a need for a general modeling and design tool that can properly predict and take into account the non-uniformities of these devices.

This chapter attempts to find the best photonic crystal type, configuration and geometry for an *N*-channel demultiplexer using the first band **S**-vector superprism. Making use of full 3-D modeling of the slab photonic crystal, the general modeling and design equations are developed which include all the non-uniformities of the **S**-vector superprism. We will then use this model to demonstrate the limitations of 2-D modeling in this context and the importance of a full 3-D model when realistic results are required. Independently of this more rigorous modeling approach, we also introduce a novel method for finding the best configuration for each lattice type. The chapter is organized as follows. In section 2 we introduce the dispersion gauge concept and apply it to three slab lattice photonic crystal types including the 1-D lattice, a 2-D square lattice, and a 2-D hexagonal lattice on the first band. Based on this gauge, we maximize dispersion in order to obtain the best lattice configurations for each lattice type. The superprism design equations are developed in section 3. This uniform design approach enables us to make a comparison between lattice types based on the criteria of minimum prism area for a given channel count, spacing and crosstalk level. Being mature enough to provide a feature size of 50 nm or less with an aspect ratio of more than 10, we have selected the Silicon-on-insulator (SOI) technology for our demonstration. The wafer we have chosen has 260 nm top silicon layer. The design equations have been used by applying them to the design of a 4-channel CWDM demultiplexer with theoretical cross talk level of 20dB, using various slab photonic crystal types in section 4. We compare these lattice types with respect to superprism area. In section 5 we discuss our results and compare them with other design data. A discussion of the importance of full 3-D modeling and difficulty of the 2-D equivalent models are presented in section 6. Section 7 concludes the chapter.

6.2 Maximum available dispersion, average group velocity

Figure 6.2.1 shows the unit cell of 1-D lattice, 2-D square lattice and 2-D hexagonal lattice photonic crystals. The lattices are rotated to ensure that there will be a band-gap for a wave traveling in the z direction. For later reference, the first Brillouin zone in each case is also shown in Figure 6.2.2. The photonic crystals are made by etching groves (for the 1-D case) or holes (for the 2-D cases) on a slab of silicon, the substrate is silicon oxide.

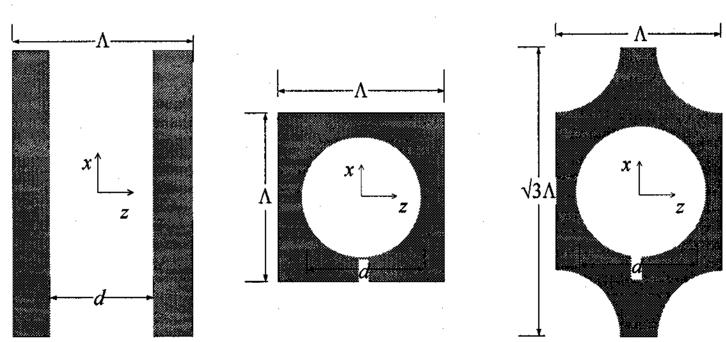

Figure 6.2.1. 1-D lattice, 2-D square lattice, and 2-D hexagonal lattice photonic crystal unit cells

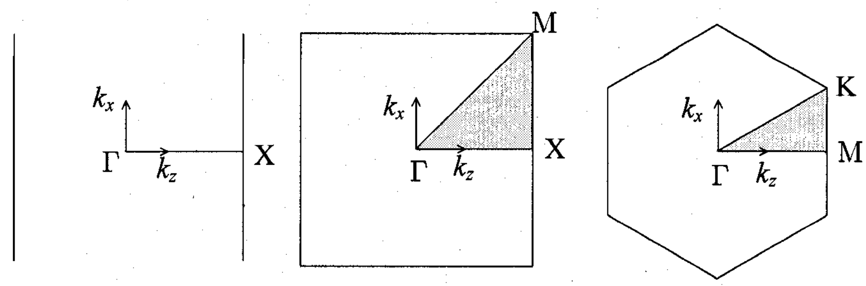

Figure 6.2.2. 1-D lattice, 2-D square lattice, and 2-D hexagonal lattice photonic crystal Brillouin zones together with irreducible zones.

Wave-front refraction at the photonic crystal boundaries can be determined by imposing the conservation of the tangential component of the phase velocity (or **k**-vector) across the interface. However, the beam direction follows the group velocity direction (S-vector) and it is directed along the gradient of the wave vector diagram at the operating point[16].

The beam divergence inside the photonic crystal, which has a dominant effect in limiting the resolution of the demultiplexer, can be obtained by using the curvature of the wave vector diagram again at the operating point [7]. We find that using the normalized wave vector diagram (wave vector components divided by the wave number in vacuum ($k_0 = 2\pi/\lambda$), *i.e.* $n_x \equiv k_x/k_0$, $n_z \equiv k_z/k_0$) simplifies the implementation of the wave vector boundary conditions [4;17-19]. This is because the effective index of the slab ($n_{\text{eff}} \equiv \beta/k_0$) is only a weak function of the wavelength and so we can treat it as a constant. In contrast to this, the tangential component of wave vector is obviously a strong function of wavelength, and thus different boundary conditions are required for each wavelength. It is also interesting to note that at longer wavelengths (or at the smaller photonic crystal periods), as the Bloch modes approach plane waves, the normalized wave vector diagram approaches the index ellipsoid. For the 2-D photonic crystals that we investigate here, due to symmetry, the normalized wave vector diagram approaches a circle (the photonic crystal behaves as an isotropic material), while for the 1-D case, it approaches to an ellipse and the birefringence is well-known as form birefringence[20].

Keeping the tangential component of the phase velocity continuous across the interface, *i.e.*,

$$n_x = n_{\text{eff}} \sin \varphi_1 \tag{6.1}$$

where φ_1 is the incident angle (see Figure 6.1.1), one can find the direction of phase velocity in the photonic crystal as

$$\mathbf{v}_p = c\left(n_x \hat{\mathbf{a}}_x + n_z \hat{\mathbf{a}}_z\right) \Big/ \left(n_x^2 + n_z^2\right) \tag{6.2}$$

where c is the velocity of light in vacuum and n_z corresponds to n_x obtained from Eq.(6.1) at the specified wavelength. The group velocity is defined by

$$\mathbf{v}_g = \nabla_k \omega(k) \tag{6.3}$$

and it is perpendicular to the wave vector diagram [16] at the operating point. For our analysis it is easier to work with a normalized group velocity given by:

$$\begin{aligned} \overline{\mathbf{v}}_g = \frac{\mathbf{v}_g}{c} &= \frac{\hat{\mathbf{a}}_x}{\omega\left(\partial n_x / \partial \omega\right)} + \frac{\hat{\mathbf{a}}_z}{\omega\left(\partial n_z / \partial \omega\right)} \\ &= \frac{\hat{\mathbf{a}}_x}{-\lambda\left(\partial n_x / \partial \lambda\right)} + \frac{\hat{\mathbf{a}}_z}{-\lambda\left(\partial n_z / \partial \lambda\right)} \end{aligned} \tag{6.4}$$

The wave refraction at the interface of the input waveguide and the photonic crystal can be described by the wave vector diagram too. In this case the effective index of the slab can be replaced by the effective index of the input waveguide at the interface.

It has been shown recently that the amount of dispersion is related to the stored energy in the photonic crystal [21]. Therefore more dispersive photonic crystals have lower energy velocities. For the spatially modulated medium, the group velocity represents the velocity of energy transfer averaged over the period [21]. We monitor the variation of the normalized wave vector n_x along the band edge (where $k_z = \pi/\Lambda$ at point X, $k_z = \pi/\Lambda$ along XM and $k_z = 2\pi/\sqrt{3}\Lambda$ along KM directions for 1-D, 2-D square and 2-D hexagonal lattice types respectively, see Figure 6.2.2) within the desired spectral window $\left[\lambda_1, \lambda_N\right]$. Figure 6.2.3 depicts a typical 2-D hexagonal wave vector diagram at 8 different wavelengths. It shows clearly the normalized wave vector components at the

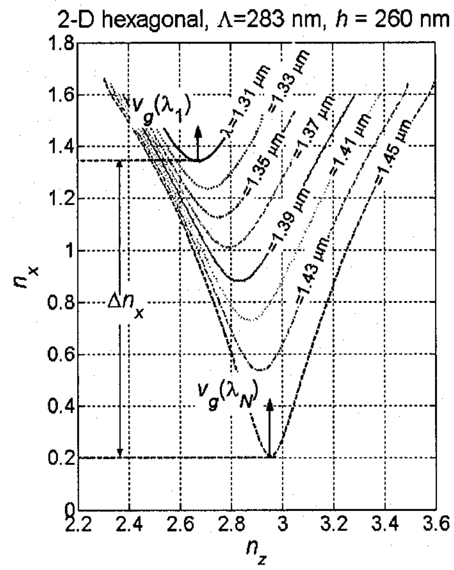

Figure 6.2.3. A typical normalized wave vector diagram of a 2-D hexagonal lattice slab photonic crystal at eight different wavelengths.

band edge. The average gradient of n_x along the band edge (first Brillouin zone edge) can be written as:

$$\left.\frac{\Delta n_x}{\Delta \lambda}\right|_{\text{bandedge}} = \left.\frac{n_x(\lambda_1) - n_x(\lambda_N)}{\lambda_1 - \lambda_N}\right|_{\text{bandedge}} \tag{6.5}$$

Then the average normalized group velocity at the band edge, using Eq.(6.5), can be expressed as:

$$\langle \overline{\mathbf{v}}_g \rangle = \frac{\hat{\mathbf{a}}_x}{-\left(\dfrac{\lambda_1 + \lambda_N}{2}\right) \times \left.\left(\dfrac{n_x(\lambda_1) - n_x(\lambda_N)}{\lambda_1 - \lambda_N}\right)\right|_{\text{bandedge}}} \tag{6.6}$$

Because the maximum dispersion usually happens at the band edge (and the lower the group velocity, the higher the dispersion) the above parameter can be taken as an indicator for the maximum available dispersion. In other words, a lattice type with a configuration that provides lower $\langle \overline{\mathbf{v}}_g \rangle$ over the desired spectral window has higher available dispersion and would be a better choice for making a superprism.

The wave vector diagrams are obtained by using the plane wave expansion method over the 3-D structure. The mesh size is 64×64 on the lattice surface (*x*-*z* plane) and also 64 points in the vertical direction (*y* axis), on which we impose an artificial periodicity (the so called super-cell) of 6 times the slab height. Figure 6.2.4 shows the super-cell of a 2-D hexagonal slab photonic crystal. The dielectric constant is sampled 6 times finer than the imposed mesh size. For an accurate complete wave vector diagram the reduced Brillouin zone has been sampled into 10^4 partitions. The polarization is assumed to be TM (electric field normal to the slab surface).

Within our model, we assume that the silicon slab and silica substrate have a refractive index of $\sqrt{12}$ and $\sqrt{2}$ respectively. We ensure that we are working above the light line cone by checking that the effective index of the photonic crystal defined as $n_{\text{eff}}(\text{PC}) \equiv \sqrt{n_x^2 + n_z^2}$ is less than the refractive index of the cladding (which is air) and the substrate (which is silica).

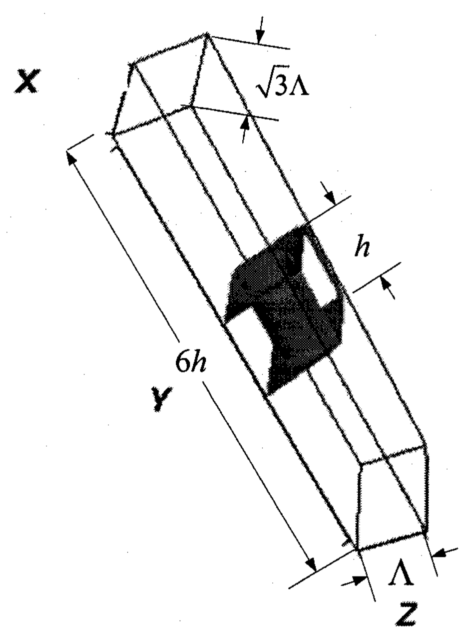

Figure 6.2.4. The supercell of slab 2-D hexagonal photonic crystal.

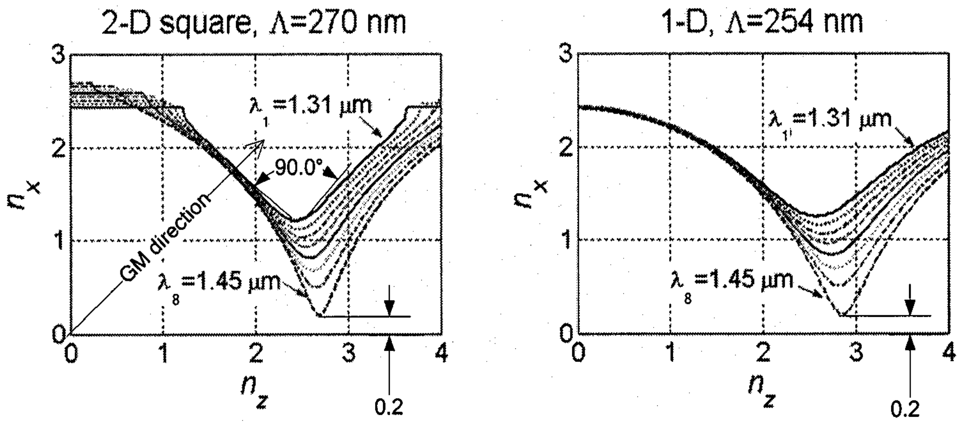

Figure 6.2.5 The normalized wave vector diagram for 2-D square lattice and 1-D lattice photonic crystal.

Figure 6.2.5 shows a typical normalized wave vector diagram for the first band of the 2-D square lattice and the 1-D lattice photonic crystal. There are some differences and similarities among the wave vector diagrams of different lattice types. The first band of the 1-D photonic crystal is an open curve (provided there is a bandgap), but the 2-D square and 2-D hexagonal first band wave vector diagrams resemble square and equilateral triangles with an asymptotic internal angle of 90 and 60 degrees respectively. In other words, the wave vector diagrams resemble the lattice type in reciprocal space (as is shown in Figure 6.2.5) and they inherit the photonic crystal symmetries along the edges of the irreducible Brillouin zone (*i.e.*, along k_x, ΓM and ΓK directions for 1-D, square and hexagonal lattices respectively), Therefore, one can conclude that the higher the symmetry order (*i.e.* higher n in the symmetry operation C_n), the more pronounced the curvature of the wave vector diagram will be. Comparing lattice types with this respect, 1-D has the least curvature whilst hexagonal has the most. (see Figure 6.2.5).

As we mentioned before, the maximum dispersion happens when the band diagram evolves from the closed curve around the origin to the onset of the bandgap. However, in order to reduce sensitivity to fabrication imperfections we choose the lattice parameters such that the bandgap size is less sensitive to the lattice dimensions (*i.e.*, we do not want too small the bandgap). However this represents a trade-off between improved dispersion and more challenging fabrication. This implies that (for practical reasons) it is preferable to have a small band gap at the long wavelength end of the desired spectrum, (for example, in Figure 6.2.4 the wave vector diagram shows a small band gap $n_x = 0.2$ for a wavelength of $\lambda_8 = 1.45\mu\text{m}$), *i.e.*, we keep $n_x(\lambda_N)\big|_{\text{bandedge}} = 0.2$. Note that in photonic crystals, the dispersion is usually negative, *i.e.*, $n_x(\lambda_1)\big|_{\text{bandedge}} \geq n_x(\lambda_N)\big|_{\text{bandedge}}$, as a result, there will be a well established band edge along the whole spectrum. Also since the smaller the bandgap, the more dispersion is achievable, by fixing $n_x(\lambda_N)\big|_{\text{bandedge}} = 0.2$ we impose a reasonable restriction for lattice types, which makes comparison more meaningful.

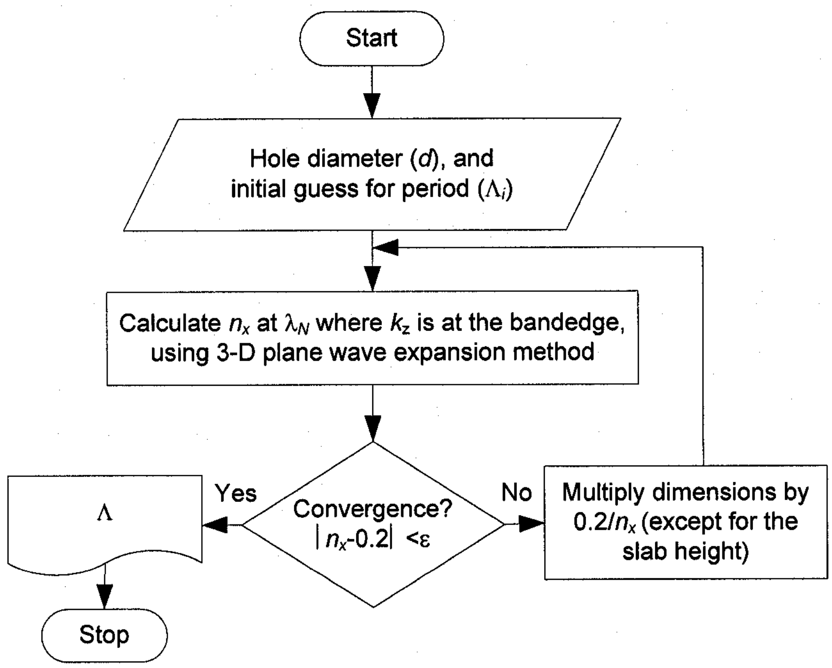

Figure 6.2.6. The flow chart for obtaining the period for each hole diameter, keeping $n_x(\lambda_N) = 0.2$ at the bandedge.

Imposing the above restriction on photonic crystals with fixed slab height, we propose the following procedure (See Figure 6.2.6 for the flow chart). This iterative procedure finds proper period for each hole diameter maintaining the restriction $n_x(\lambda_N)\big|_{\text{bandedge}} = 0.2$. The scaling law of photonic crystals (ignoring its effect of the slab height) was used to correct the initial guess and to link iterations. Five iterations were almost always enough for convergence.

Figure 6.2.7 shows the average normalized group velocity versus the hole diameter d for 1-D, 2-D square and 2-D hexagonal lattice slab photonic crystals maintaining the restriction of

$n_x(\lambda_N)\big|_{\text{bandedge}} = 0.2$. The average has been taken over the wavelength span of $\lambda_1 = 1.39\,\mu\text{m}$ to $\lambda_4 = 1.45\,\mu\text{m}$. As can be seen, the lowest group velocity is found for the 2-D hexagonal lattice slab photonic crystal whilst the largest is found for the slab 1-D photonic crystal. It is notable that the extent of the hexagonal lattice band diagram shrinks dramatically for larger hole diameters (or at lower wavelengths), making it less appropriate for practical applications.

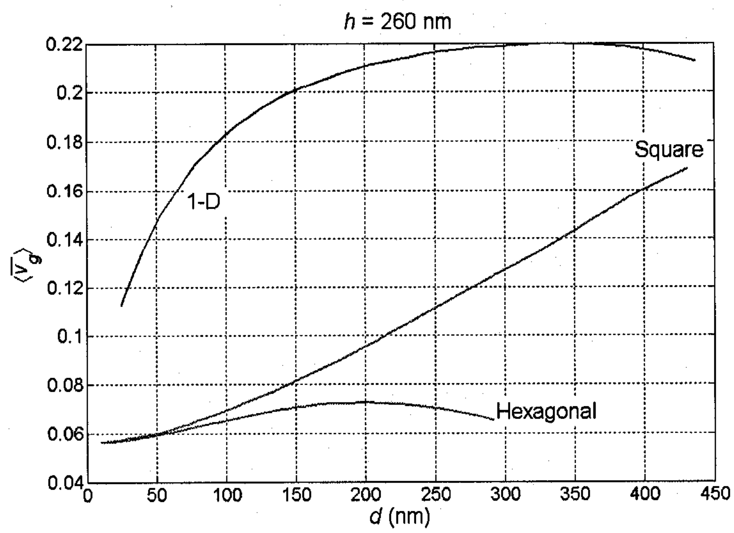

Figure 6.2.7. Averaged normalized group velocity at the band-edge for various lattice types versus hole diameter.

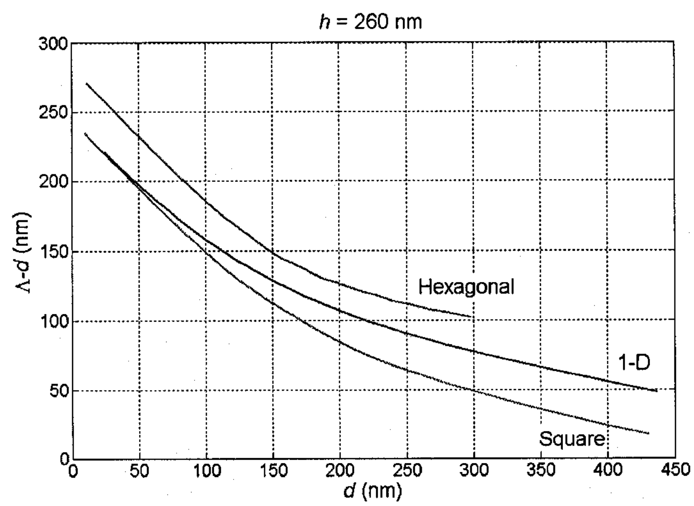

Figure 6.2.8. The inner-hole spacing versus hole diameter corresponds to Figure 6.2.7.

Figure 6.2.8 shows the inter-hole size ($\Lambda - d$) versus hole diameter d with the same conditions as considered in Figure 6.2.7. The hole size and inter-hole size must be greater than the minimum feature size of the fabrication process.

Using Figure 6.2.8 and with the minimum feature size of 75 nm, the results for the best parameter of various lattice types (which maximize the dispersion at the bandedge whilst respecting the restriction of $n_x(\lambda_N)\big|_{\text{bandedge}} = 0.2$) are summarized in Table 6.1.

Table 6.1 Period, fill factor and maximum available dispersion for various lattice types based on a 75 nm hole diameter

Slab Lattice types	Inter-hole size(nm)	Period\ (nm)	Fill factor (%)	Average normalized group velocity
1-D	176.7	251.7	30	0.169
2-D square	171.1	246.1	7	0.064
2-D hex	208.4	283.4	6	0.062

Table 6.1 also records the fill factor. It is interesting to observe in Table 6.1 that the minimum group velocity and the fill factor are monotonically related. Having the lowest fill factor, the hexagonal lattice provides the lowest group velocity at the band edge, whilst the 1-D photonic crystal gives the highest fill factor with the highest group velocity. Keep in mind that the average group velocity and dispersion are inversely related.

6.3 S-vector demultiplexer design equations

The goal is to design an N-channel demultiplexer, which resolves N wavelengths at $\lambda = \lambda_1, \cdots, \lambda_N$ within a specified crosstalk level. The channel spacing is fixed at $\Delta\lambda$. Figure 6.3.1a shows a typical first band diagram near the band edge in a suitable operating region for the **S**-vector superprism. To be sure that tangential component of the wave vectors inside photonic crystal are greater than or equal to the tangential component of the incident beam wave vector (in other words to avoid band-gap), the bulk photonic crystal structure has to be wavelength, see Figure 6.3.1a) in the line with the tangential component of incident beam wave vector, *i.e.*,

$$n_{\text{eff}} \sin\varphi_1 > \left(n_x(\lambda_1)\cos\theta_1 - n_z(\lambda_1)\sin\theta_1\right)\Big|_{\text{bandedge}} \tag{6.7}$$

where φ_1 is the input waveguide angle with respect to the normal to the interface, and θ_1 is the slant angle defined as the angle between the z axis of the lattice (as defined in Figure 6.2.2) and the normal to the interface). Figure 6.3.1b demonstrates how the band gap is avoided by choosing the slant angle greater than $\theta_{1\min}$. When incident angle is zero ($\varphi_1 = 0$) Eq.(6.7) will be reduced to [22]

$$\theta_{1\min} = \tan^{-1}\left(n_z / n_x\right)\Big|_{\text{bandedge}} \tag{6.8}$$

The schematic of the proposed demultiplexer is shown in Figure 6.3.2, in which the beam propagation length is truncated to the minimum value necessary to resolve a channel from its neighbors (we will explain how this length is determined later), and also we extend the demultiplexer area to exactly accommodate the beam expansion inside the photonic crystal.

The minimum propagation length $R_{m,m+1}$ to resolve the m^{th} channel (at the wavelength λ_m with the main propagation direction of $\varphi'_{2,m}$) from the $(m+1)^{\text{th}}$ channel (at λ_{m+1} with the main propagation direction of $\varphi_{2,m+1}$) within a specified photonic crystal, since each plane-wave component is expanded into Bloch waves and they will then be affected by the complex dispersion characteristics of the photonic crystal. The light intensity envelope can be approximated by a Gaussian profile when the beam divergence angle is sufficiently small [7]. Modeling Gaussian beam propagation in the photonic crystal therefore requires calculation of the propagation characteristics of the plane wave components (with the full spectral width at e^{-2} intensity of θ_0). The divergence angle of the beam can be approximated as follows [7].

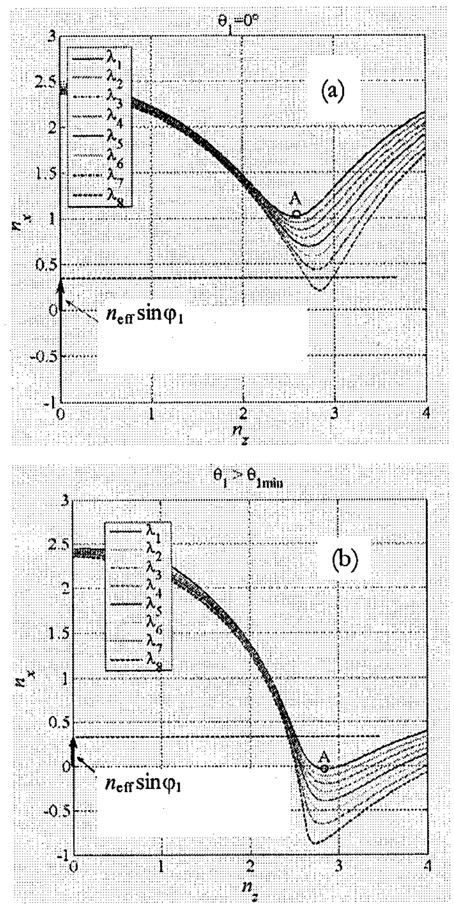

Figure 6.3.1. Normalized wave vector diagram near the band edge (a) without rotation (b) with a rotation of $\theta_1 > \theta_{1\min}$.

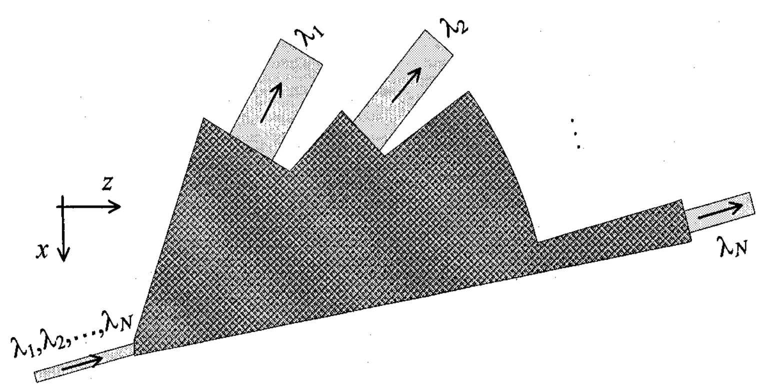

Figure 6.3.2. The proposed S-vector superprism demultiplexer.

The input waveguide mode can be approximated by a Gaussian beam[23]. However, this beam is no longer Gaussian when it propagates through the photonic crystal, since each plane-wave component is expanded into Bloch waves and they will then be affected by the complex dispersion characteristics of the photonic crystal. The light intensity envelope can be approximated by a Gaussian profile when the beam divergence angle is sufficiently small [7].

$$\theta_c(R) = p\theta_0(R) = \lambda p\sqrt{1+(R_0/R)^2}\Big/\left(\pi n_{\mathrm{eff}} w_{\mathrm{eff}}\right) \tag{6.9}$$

where w_{eff} is the effective input beam width Modeling Gaussian beam propagation in the photonic crystal therefore requires calculation of the propagation characteristics of the plane wave components (with the full spectral width at e^{-2} intensity of θ_0). The divergence angle of the beam can be approximated as follows [7]

$$w_{\mathrm{eff}} = w_0 \cos\varphi_2' \big/ \cos\varphi_1 \tag{6.10}$$

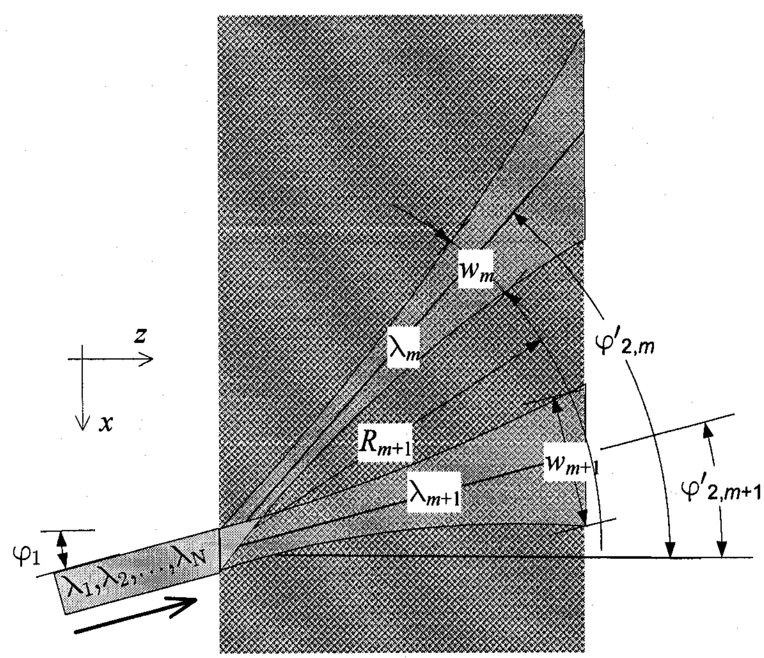

Figure 6.3.3. A Schematic of the demultiplexer showing the defined parameters.

and w_0 is the effective input waveguide width[23], n_{eff} is the effective refractive index of the slab region and p is the beam divergence multiplication factor (representing the beam divergence property of the photonic crystal) which is defined as [7]

$$p \equiv \partial\varphi_2'/\partial\varphi_1 \tag{6.11}$$

where φ_1 and φ_2' are the incident and the steering angle of the beam. R_0 is the Rayleigh range defined as

$$R_0 = n_{\text{eff}}\pi w_{\text{eff}}^2/\lambda p \tag{6.12}$$

λ is the wavelength of the incident light. Thus, the optical power density in the slab region (to first order approximation) can be written as

$$I = \frac{2I_0}{\pi h_0\theta_c R}\exp\left(-2\theta^2/\theta_c^2\right)\exp\left(-2y^2/h_0^2\right)\exp\left(-\alpha_m R\right) \tag{6.13}$$

where θ is measured versus propagation direction, h_0 is the effective photonic crystal slab height, the y axis is perpendicular to the slab direction. α_m is the total propagation loss. Theoretical cross talk of two neighboring channel can be defined as the normalized overlapping integral of the two propagating Gaussian beam at the fixed R corresponds to these channels, *i.e.*,

$$\xi = \sqrt{2/(\pi\rho)}\int_{-\infty}^{+\infty}\exp\left(-\theta^2/\theta_c^2\right)\exp\left[-(\theta-\eta\theta_c)^2/(\rho\theta_c)^2\right]d\theta \tag{6.14}$$

where ρ (divergence angle ratio) is the ratio of beam divergence angle of the two neighboring channels, and η (deviation angle ratio) is the ratio of the difference in the beam deviation angle and the beam divergence angle ($\Delta\varphi_2' \equiv \eta\theta_c$). Using Eq.(6.14), the maximum theoretical cross talk can be expressed as

$$\xi = \sqrt{2/(\rho+1/\rho)}\exp\left[-2\eta^2/\left(\max(\rho,1/\rho)^2+1\right)\right] \tag{6.15}$$

Figure 6.3.4 shows the deviation angle ratio η versus the beam divergence angle ratio ρ for various theoretical cross talk levels. The divergence angle of the Gaussian beam reduces from infinity at the waist to its minimum value at the far field. However, it is not necessary to let it expand that far to be ableto resolve it from neighboring channels. The minimum propagation length to resolve the m^{th} channel from $(m+1)^{th}$ one within a specified crosstalk level $R_{m,m+1}$ (see Figure 6.3.4) can be found solving Eq. (6.15)using Eq. (6.9), and noting that

$$\eta \min\left(\theta_{c,\lambda_m}, \theta_{c,\lambda_{m+1}}\right) = \left|\varphi'_{2,\lambda_m} - \varphi'_{2,\lambda_{m+1}}\right| \tag{6.16}$$

Obviously, the propagation length obtained in this way is not in the Fraunhofer zone. The demultiplexer length for m^{th} channel (R_m) is the maximum of $R_{m,m+1}$ and $R_{m,m-1}$.

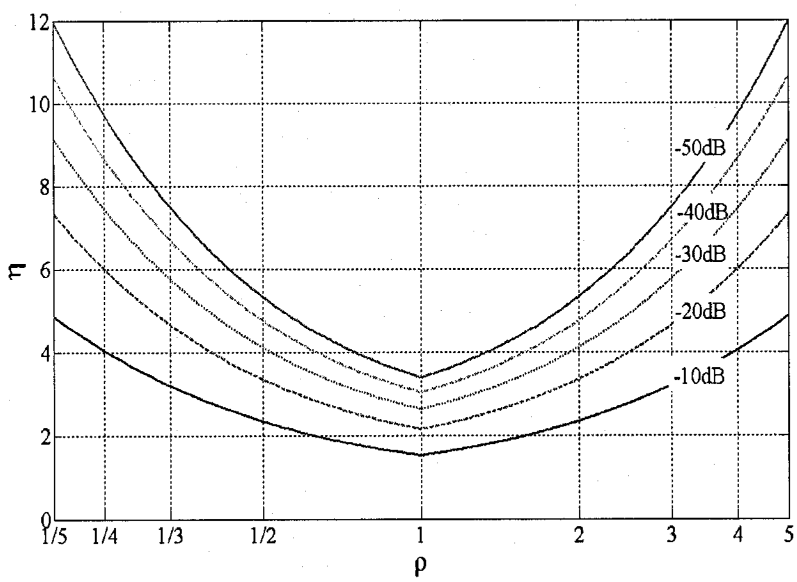

Figure 6.3.4. The deviation angle ratio η versus beam divergence ratio ρ for various maximum theoretical crosstalk levels.

We will now show that our analysis (Eq.(6.15)) is an extension of previous models [6] and it will reduce to the previous results if the device size is large compared to the Rayleigh range, and if the wavelength increment is small (or non-uniformity is negligible), Let us assume that beam divergence is equal for all channels so that $\rho \approx 1$, then using Eq.(6.15) cross-talk can be approximated as

$$\xi = \exp\left(-\eta^2\right) \tag{6.17}$$

Using Eq.(6.9) and in the Fraunhofer range (or when the Rayleigh range is small compared to the device size), we have

$$\xi = \exp\left[-\left(r\pi n_{\text{eff}} w_{\text{eff}}\, \Delta\lambda/\lambda^2\right)^2\right] \tag{6.18}$$

Where r is the resolution parameter defined as

$$r \equiv p/q \tag{6.19}$$

And q is the normalized angular dispersion defined as

$$q \equiv \lambda\, \partial\varphi_2' / \partial\lambda \tag{6.20}$$

Thus the resolution can be written as

$$\Delta\lambda/\lambda = \lambda\sqrt{-\ln\xi} / \left(r\pi n_{\text{eff}} w_{\text{eff}}\right) \tag{6.21}$$

This is essentially the same expression (for a theoretical cross talk level of 17.4dB, or $\sqrt{-\ln\xi} = 2$) as the one obtained previously [6]. As will be explained in the next section, we can neither ignore the non-uniformity nor treat the device as large compared to the Rayleigh range, so we have to use the general Eq.(6.15) in our case.

6.4 Numerical illustration

To obtain specific results, we design a 4-chanel CWDM demultiplexer ($\Delta\lambda = 20\text{nm}$) with a desired theoretical crosstalk level of 20dB. The desired spectral window is from $\lambda_1 = 1.39\mu\text{m}$ to $\lambda_4 = 1.45\mu\text{m}$. The polarization is TM with the electric field normal to the slab surface. The design has been carried out for the three lattice types that we optimized in section 2 (with the results summarized in Table 6.1). The direction of the input waveguide (incident angle φ_1), the angle θ_1 can be used to minimize the superprism area (S). There is a trade-off between being near the band edge (*i.e.*, higher dispersion) and having the required output beam width (i.e, higher band curvature or beam divergence). Whilst getting too close to the band edge makes the output beam too large, operating far from the band edge will reduce the dispersion. The gauge for the trade off is the minimization of the superprism area. We performed a downhill search on the three parameters (φ_1, θ_1 and w_0), scanning the values of each until no further reduction in prism area was found.

Table 6.2, shows the result of such an optimization for various lattice types. The lattice parameters are taken from Table 6.1. As is seen from Table 6.2, the optimum 1-D superprism is about one order of magnitude smaller than the 2-D lattice counterparts. From this finding, one can conclude that the dominant factor determining the size of multiplexer is the band curvature. Although the 1-D case has the lowest dispersion (see Table 6.1), it provides the smallest demultiplexer size due to its low wave vector diagram curvature near the band-edge.

Table 6.2 4-channel CWDM demultiplexer design specification with various lattice types

Lattice type	θ_{1opt} $(°)$	φ_{1opt} $(°)$	w_{0opt} (μm)	w_{max} (μm)	w_{min} (μm)	Surface (μm^2)
1-D	15.8	32.56	3.06	1.48	1.12	1,367
2-D squ	22.2	-2.04	6.85	17.58	6.85	19,062
2-D hex	21.2	-1.36	6.33	19.18	7.31	22,284

Comparing square and hexagonal lattices which have similar dispersion at the band edge (see Table 6.1) is also interesting. The hexagonal demultiplexer size is greater than the square one due to higher curvature of the hexagonal wave vector diagram. In conclusion, the slab 1-D photonic crystal, by providing modest dispersion but smallest wave vector diagram curvature, is the best choice for demultiplexers based on the **S**-vector superprism phenomena.

As is shown in Table 6.2, the best operating point (which is determined by the slant angle and incident angles) of the superprism for the 1-D lattice differs significantly from the two other cases. This emphasizes the fact that beam divergence is more important than the dispersion if the superprism wavelength resolution is a concern. Our optimization procedure puts the optimum operating point of the 1-D photonic crystal (with open wave vector diagram) far away from the bandedge where both the dispersion and the beam divergence are low. However by working that far from the bandedge in 2-D photonic crystals (with closed wave vector diagram), we only sacrifice the dispersion without reducing the divergence that much, so the trade-off operating point for 2-D phonic crystals are very near the bandedge. Being far from the bandedge is also advantageous because it promises better transmission.

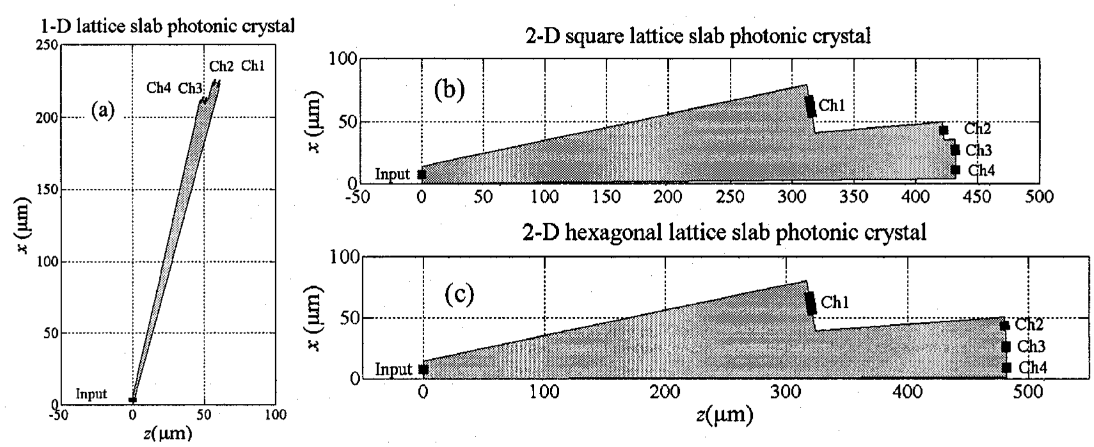

Figure 6.4.1, A Schematic of the demultiplexer using a) slab 1-D photonic crystal, b) 2-D square lattice photonic crystal and c) 2-D hexagonal lattice photonic crystal.

It is also interesting to note that the input and output beam widths of the 1-D case are compatible with the use of ordinary waveguides, whereas in the other cases a more complex optical system (*i.e.*, focusing lenses, mirrors or long tapered waveguides, *etc.*) must be added to the demultiplexer output to reduce the output beam to a manageable size for integrated optics applications.

Note that this conclusion is based on the first band of the above-mentioned lattice types. Note also that the second band of 1-D photonic crystal is not located around the origin and also there is no multiplicity in the wave vector diagram; therefore it is not a proper choice for this kind of application.

The superprism layouts of the three demultiplexer photonic crystals are shown in Figure 6.4.1. Input and output channel locations and sizes are marked too. Note that the output beam direction can be adjusted by changing the output facet direction with respect to the bulk photonic crystal.

As we mentioned before, and as is clear from Figure 6.4.1, neighboring channels may have quite different beam widths (see specifically channels 1 and 2 in Figure 6.4.1b, and c) depicting the output beam width for all channels at the exit points for three lattice types. To be more specific, Figure 6.4.2 shows the output beam width for different channels for the designs depicted in Figure 6.4.1. As is seen, for 2-D lattice types, the output beam width varies considerably from channel to channel, and usually it is higher where the dispersion is higher (or the divergence factor is higher, see Eq.(6.11), and (6.15)). If the designs are going to have any integrated applications, the variation of the output beam width has to be addressed (especially in 2-D lattice types). Considering the high refractive index contrast material that we have used in our design, a curved mirror seems to be the easiest way to focus the output beams to more practical values. Also one always can compromise the output power, by selecting an output waveguide width which is smaller than the beam width.

Figure 6.4.3 shows the deviation angle $\eta = \varphi_2' - \varphi_1$ (see Figure 6.3.3 for clarification of the parameters) for all channels and for three lattice types. By using this data, together with the channel spacing (20 nm), we can calculate the angular dispersion as a function of wavelength. For the 2-D square lattice, although the angular dispersion is high (0.25°/nm) for the first channel (at 1390nm), it is low (0.09°/nm) at the last channel (at 1450nm). This is a 2.7-fold dispersion reduction over 60 nm. The 2-D hexagonal lattice follows a similar pattern. Considering the fact that the conventional demultiplexer design is usually governed by the worst channel dispersion [11], this significant non-uniformity is troublesome (especially for higher channel count demultiplexers where dispersion non-uniformity is much higher). However, the situation will be more complicated if one takes the non-uniformity of p into account (see Eq.(6.11)).

Figure 6.4.4 shows the beam divergence multiplication factor p for various channels for the three lattice types. The non-uniformity of p, especially for 2-D lattice types is significant, particularly when dispersion is high (compare Figure 6.4.4 and Figure 6.4.3). This is the main factor limiting the scalability of the **S**-vector superprism as has already been pointed out by Baba [3].

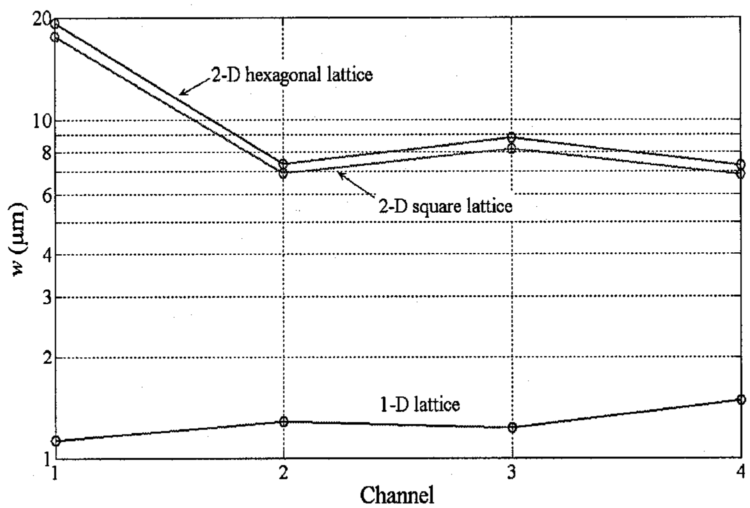

Figure 6.4.2. The output beam width at the exit point for various channels.

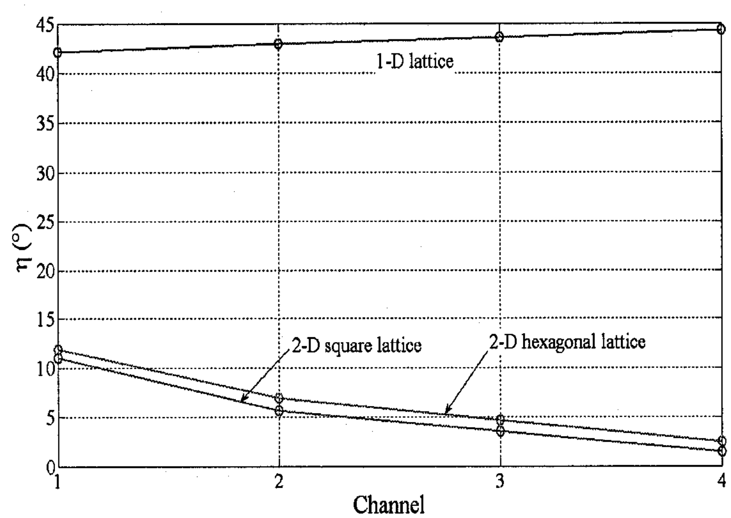

Figure 6.4.3. Beam steering angle for each channel.

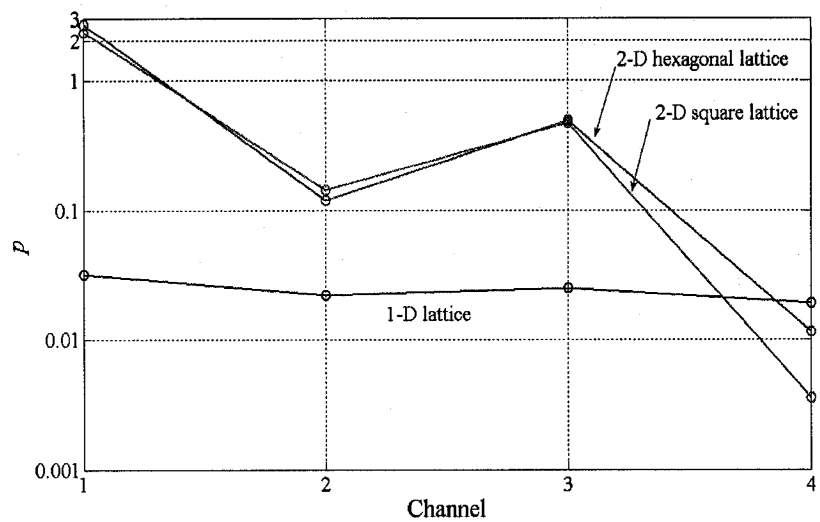

Figure 6.4.4. Beam divergence multiplication factor for each channel

Also note the sign of angular dispersion in 1-D and 2-D cases (in the 1-D case it is positive; in 2-D cases it is negative). This fact however is not general; a search over the design space yields regions of positive and negative dispersion. However, the dispersion in 1-D lattices is always more uniform, also p values are lower and more uniform than the 2-D lattices. We emphasize once again that the main reason that 1-D lattice type allows the smallest prism area is its low band curvature. Despite having the lowest dispersion (see Figure 6.4.3), its low p value (see Figure 6.4.4) more dominant as long as demultiplexer area is the main concern.

6.5 Discussion and comparison with previous work

Once the resolution of the S-vector superprism had been formulated, and it was understood that the resolution was less than had been previously hoped [3] (and to achieve even a modest resolution impractical photonic crystal sizes have to be utilized[3]) there were many attempts to push the limits to find the smallest device [3;6;11;14;15]. The second band of various lattice types were examined. Using the 2-D plane wave expansion method and making use of the photonic crystal scaling laws these researchers obtained designs which are wavelength independent. The linearized model using p, q and r parameters (see Eqs. (6.11), (6.19) and (6.18)) has been used to maximize dispersion and minimize divergence angle [6;11;15]. The design equations which have been developed are based on the conventional **S**-vector superprism depicted in Figure 6.1.1, assuming a nearly normal angle of incidence, equal dispersion for all channels, and the Fraunhofer Gaussian field approximation [2;6]. The propagation mechanism of the beam inside photonic crystal has been partially taken into account recently (we will refer to it as the semi-linear model to distinguishing it from the simple linear method) [11]. The design equations in this case are based on the assumption of an equal divergence angle of neighboring channels which as we have shown is not always the case if the channel spacing is not very small [11]. The assumption that at the maximum resolution length (*i.e.* the maximum propagation distance required to resolve the worst channels), all channels have smaller or equal beam-widths than the worst channels was also implied [11]. However, as we have shown in Figure 6.3.3 this may not always be the case (this is also illustrated in Figure 6.1.1, where the resolution length might be sufficient to resolve channel N from channel $N-1$, but it is the first two channels that have the greatest beam widths). In addition, the beam direction outside the photonic crystal in the conventional **S**-vector superprism photonic crystal will not remain radial, so that radially directed output waveguides will result in excessive channel non-uniformity. Theoretical analysis based on the plane wave expansion and mode matching methods show 10dB channel non-uniformity in a 4-Channel demultiplexer [11].

The fact that these models neglect non-uniformity might be acceptable for sufficiently narrow bandwidths, but unfortunately, their resolutions are too low to justify the narrow bandwidth assumption. In other words, the **S**-vector superprism can only resolve wide channel spacings where the non-uniformity can no longer be ignored (particularly beam divergence non-uniformity as shown in Figure 6.4.2). Therefore, when designing such a wideband **S**-vector superprism, we need a model such as the one presented here that takes the full non-uniformity into account.

We can compare our design results with those of other researchers who used these more approximate models. One recent study which is based on the semi-linear model and made use of the 2-D plane wave expansion method on the second band (which uses real refractive indices for the 2-D model), concluded that the best lattice type is the hexagonal lattice in the ΓM direction with TE polarization [11]. For the similar CWDM demultiplexer, the minimum photonic crystal size was then found to be 754 μm^2 (which is about half the size of our minimum case). However the validity of this conclusion is limited by the validity of the semi-linear model used and the fact that they have used the 2-D model with real refractive indices. As we will show in the next section, it overestimates the dispersion.

6.6 2-D versus 3-D modeling of slab photonic crystals

Considering the efficiency of plane wave expansion method, it is relatively simple to employ 3-D modeling. However this requires a fixed slab height, which sacrifices the scaling properties of 2-D modeling. In other words, our results will be specific, rather than general. This may explain why many superprism designers have tended to make use of 2-D models. Another reason why designers tend to avoid using the full 3-D model for obtaining the wave vector diagram may be the lack of a viable 3-D model for calculating the transmission spectrum from a slab photonic crystal, whereas a 2-D transmission model is available. However, as we have shown, we do not need a transmission modeling for designing a multiplexer.

It is also true that 2-D models that assume geometrical uniformity in one direction and periodicity in the other two exhibit all the fundamental phenomena of the slab photonic crystal where the field is not uniform in non-periodic direction. However finding the proper 2-D modeling parameters for each application is not very obvious. Although one can use the slab guiding layer refractive index for the background, and the air refractive index for the holes, the band edge and the dispersion so obtained are far from the real 3-D model, especially when the confinement is low in the non-periodic direction. Using the effective index of the slab region for the background of the 2-D model and air for the holes has been used already [6;12;14] but the band edge is not still the same as the 3-D model and furthermore there is no physical basis for such an assumption.

Thanks to the efficiency of the plane wave expansion methods, the band diagram using the 3-D model can be found easily by imposing virtual periodicity in the third direction. Figure 6.6.1 shows the average group velocity of the 2-D square lattice of Table 6.1 versus slab height using 3-D model and 2-D model using the effective index of the slab for the background and refractive index of air for the holes (SOI technology has been assumed). The two methods converge for slab heights greater than 5μm. It means that if one uses 2-D model with real refractive index of the guiding layer and air for the holes, it shows similar dispersion only if the slab heights is greater than 5μm. There is also another cross point where two models give similar dispersion (at $h \approx 0.48\mu m$) and some authors [6;14] have chosen this one as the effective index of their model. As it is clear for our case of $h = 260\,\text{nm}$ the 2-D model using effective index [12] underestimates the dispersion, whilst using the slab index [11], or the middle cross point [6;14] overestimates the dispersion. By decreasing the background refractive index and increasing the holes' the location of the band edges for the 2-D model may closely approach those of the real 3-D band diagram [22]. The best 2-D model parameters (basically the best refractive indices for the background and the holes) can be obtained by matching the band edge of 3-D and 2-D band diagrams over the desired wavelength span [22]. Whilst the band diagrams of 2-D and the 3-D cases now look much the same, the band curvatures are not, thus making beam divergence modeling inside photonic crystal unrealistic.

Furthermore there is no guarantee that the transmission spectra would be the same if the band diagrams are much the same. It remains an open question as to which 2-D model provides the most realistic transmission spectra. These problems show the importance of the full 3-D modeling in calculating either band diagrams or transmission spectra. We have therefore used a full 3-D model band diagram in our design procedure.

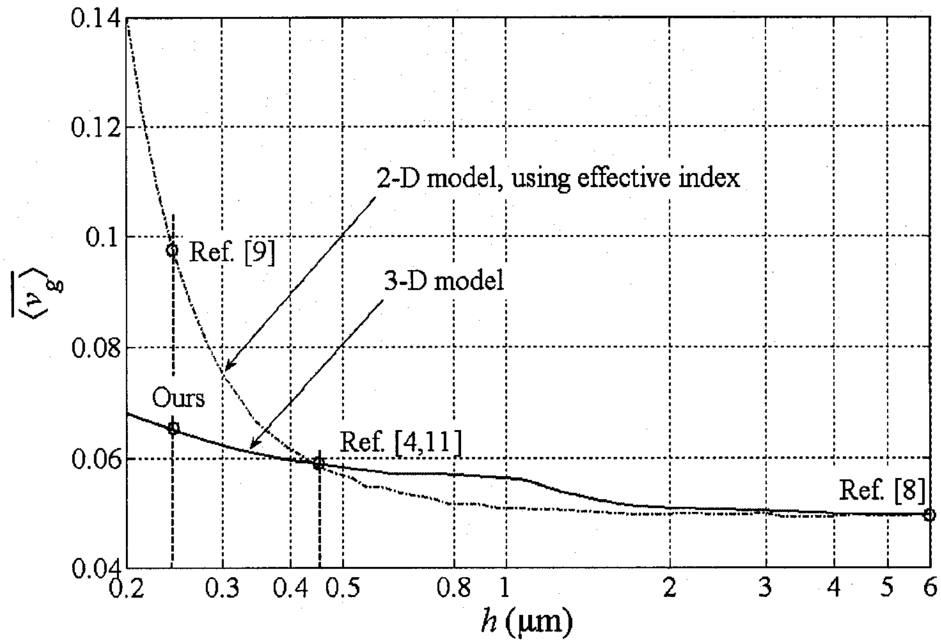

Figure 6.6.1. The average group velocity versus slab height, calculated either by 3-D modeling or 2-D which employs effective index of the slab with the same width for the background refractive index.

6.7 Summary and conclusions

We have developed general design equations for designing a demultiplexer using **S**-vector superprism phenomena based on the first band of photonic crystals. We have examined three lattice types: 1-D, 2-D square and 2-D hexagonal. A typical SOI wafer technology with a top silicon layer thickness of 260 nm has been used for our simulation. We have shown that the average group velocity over the band edge is a suitable indicator for the maximum available dispersion. The hexagonal lattice, followed by the square lattice, shows the maximum available dispersion. The slab 1-D photonic crystal provides the lowest dispersion available at the band edge. Based on the Gaussian field approximation in photonic crystals, the minimum resolution length for each channel has been calculated. The superprism area is then adjusted to provide enough area for the beam expansion and to allow each channel be resolved from neighboring channels. We have shown that the resolution is more critically dependent on the beam divergence inside the photonic crystal than on angular dispersion. As result the 1-D photonic crystal provides the best resolution, despite the fact that the hexagonal lattice displays an order of magnitude larger angular dispersion.

We have shown that a 4-channel CWDM demultiplexer with a theoretical cross talk level of 20 dB can be made with a the prism area of $1367\mu m^2$. The lattice type is slab 1-D photonic crystal and it is based on a typical SOI technology with a minimum feature size of 75μm. The input beam width is about 1.5 μm and the maximum output beam width is about 3 μm. Utilizing the full 3-D plane wave expansion method, the design parameters are much more realistic than those obtained by 2-D models. Our investigation also shows that it is not easy to design higher channel count demultiplexers based on the **S**-vector superprism phenomenon due to the high non-uniformity of the band diagram as it evolves with the wavelength.

REFERENCES

[1] Zengerle R., "Light propagation in single and doubly periodic planar waveguides," *Journal of Modern Optics*, vol. 34, no. 12, pp. 1589-1610, 1987.

[2] H. Kosaka, T. Kawashima, A. Tomita, M. Notomi, T. Tamamura, T. Sato, and S. Kawakami, "Superprism phenomena in photonic crystals," *Physical Review B*, vol. 58, no. 16, pp. 10096-10099, Oct.1998.

[3] T. Baba and T. Matsumoto, "Resolution of photonic crystal superprism," *Applied Physics Letters*, vol. 81, no. 13, pp. 2325-2327, Sept.2002.

[4] A. G. Kirk and A. Bakhtazad, "Dispersion optimization of a 1-D superprism based on phase velocities," *LEOS 2004*, pp. 879-880, 2004.

[5] S. Y. Lin, V. M. Hietala, L. Wang, and E. D. Jones, "Highly dispersive photonic band-gap prism," *Optics Letters*, vol. 21, no. 21, pp. 1771-1773, Nov.1996.

[6] T. Matsumoto and T. Baba, "Photonic crystal **k**-vector superprism," *Journal of Lightwave Technology*, vol. 22, no. 3, pp. 917-922, Mar.2004.

[7] B. Momeni and A. Adibi, "An approximate effective index model for efficient analysis and control of beam propagation effects in photonic crystals," *Journal of Lightwave Technology*, vol. 23, no. 3, pp. 1522-1532, Mar.2005.

[8] B. Momeni, J. D. Huang, M. Soltani, M. Askari, S. Mohammadi, M. Rakhshandehroo, and A. Adibi, "Compact wavelength demultiplexing using focusing negative index photonic crystal superprisms," *Optics Express*, vol. 14, no. 6, pp. 2413-2422, Mar.2006.

[9] J. Witzens, T. Baehr-Jones, and A. Scherer, "Hybrid superprism with low insertion losses and suppressed cross-talk (vol E 71, art no 026604, 2005)," *Physical Review e*, vol. 71, no. 3 Mar.2005.

[10] J. Witzens, M. Hochberg, T. Baehr-Jones, and A. Scherer, "Mode matching interface for efficient coupling of light into planar photonic crystals," *Physical Review e*, vol. 69, no. 4 Apr.2004.

[11] B. Momeni and A. Adibi, "Systematic design of superprism-based photonic crystal demultiplexers," *Ieee Journal on Selected Areas in Communications*, vol. 23, no. 7, pp. 1355-1364, July2005.

[12] L. J. Wu, M. Mazilu, and T. F. Krauss, "Beam steering in planar-photonic crystals: From superprism to supercollimator," *Journal of Lightwave Technology*, vol. 21, no. 2, pp. 561-566, Feb.2003.

[13] T. Baba and M. Nakamura, "Photonic crystal light deflection devices using the superprism effect," *Ieee Journal of Quantum Electronics*, vol. 38, no. 7, pp. 909-914, July2002.

[14] M. J. Steel, R. Zoli, C. Grillet, R. C. McPhedran, C. M. de Sterke, A. Norton, P. Bassi, and B. J. Eggleton, "Analytic properties of photonic crystal superprism parameters," *Physical Review e*, vol. 71, no. 5 May2005.

[15] B. Momeni and A. Adibi, "Optimization of photonic crystal demultiplexers based on the superprism effect," *Applied Physics B-Lasers and Optics*, vol. 77, no. 6-7, pp. 555-560, Nov.2003.

[16] Russell P.St., Birks T.A., and Lloyd-Lucas F.D., *Confined Electrons and Photons.* New York: NATO, Plenum, 1995.

[17] A. Bakhtazad and A. G. Kirk, "Superprism effect with planar 1-D photonic crystal," *Proceedings of the SPIE*, vol. 5360, pp. 364-372, June2004.

[18] A. Bakhtazad and A. G. Kirk, "1-D slab photonic crystal **k**-vector superprism demultiplexer: analysis, and design," *Optics Express*, vol. 13, no. 14, pp. 5472-5482, July2005.

[19] A. G. Kirk and A. Bakhtazad, "Wave-front engineering with photonic crystal structures in slab waveguides," *Proc. SPIE*, vol. 5970, pp. 602-610, 2005.

[20] Yariv Amnon and Yeh Pochi, "Electromagnetic propagtaion in periodic media," in *Optical Waves in Crystals : Propagation and Control of Laser Radiation* Wiley Series in Pure and Applied Optics, 2003, pp. 115-219.

[21] M. Gerken and D. A. B. Miller, "Relationship between the superprism effect in one-dimensional photonic crystals and spatial dispersion in nonperiodic thin-film stacks," *Optics Letters*, vol. 30, no. 18, pp. 2475-2477, Sept.2005.

[22] A. S. Jugessur, A. Bakhtazad, A. G. Kirk, L. Wu, T. F. Krauss, and R. M. De la Rue, "Compact and integrated 2-D photonic crystal super-prism filter-device for wavelength demultiplexing applications," *Optics Express*, vol. 14, no. 4, pp. 1632-1642, Feb.2006.

[23] Unger H.G., *Planar Optical Waveguides and fibers* Oxford, UK, Clarendon Press, 1977.

Chapter 7

STRATIFIED PHOTONIC CRYSTAL DEMULTIPLEXER

A new wide-band CWDM demultiplexer using cascaded photonic crystals is proposed. Five-fold superprism size reduction is achieved. The new demultiplexer is compared with the conventional S-vector superprism. The output channel beam sizes are found to be more uniform.

7.1 Introduction

In the previous chapter we showed that **S**-vector device has some limitations that make them more suitable for CWDM applications. In this chapter, we introduce a new approach to improve the scalability of the **S**-vector superprism.

While in the previous chapter, we modified the conventional **S**-vector superprism a little bit to minimize the area, in this chapter we compare the results of our proposed structure with the conventional **S**-vector demultiplexer. For the sake of simplicity, we assume that the input waveguide is normal to the photonic crystal interface. Then the tangential component of the **k** vector will be zero at the input interface and stays zero up to the output interface. The output waveguide similarly needs to be aligned perpendicular to the photonic crystal interface [9]. If we start with the familiar square lattice photonic crystal, and restrict ourselves to the first band, then it is not difficult to demonstrate that the beam reflection angles could be all positive provided the lattice rotation angle is positive. Based on this observation, the schematic of the demultiplexer for a planar fabrication technology is shown in Figure 7.1.1

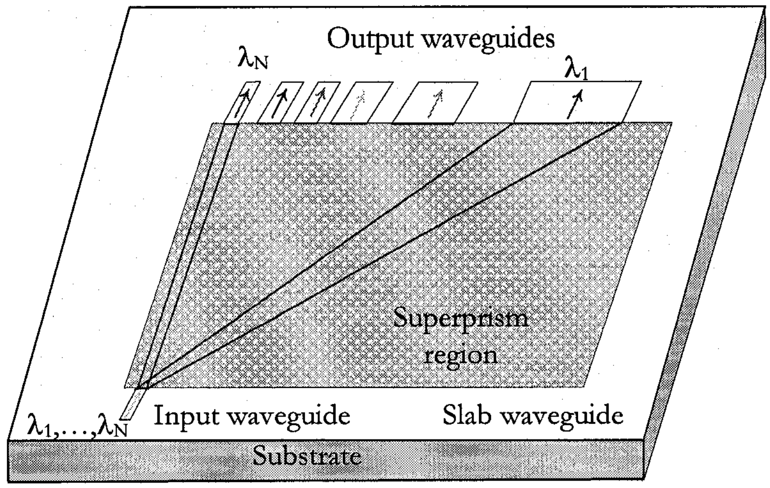

Figure 7.1.1 The conventional S-vector superprism demultiplexer

As we have previously explained, the wave refraction behavior at the interface of the input waveguide and the photonic crystal can be described by the wave vector diagram. The direction of phase velocity in the photonic crystal can be determined by keeping the tangential component of the phase velocities constant on both sides of the interface (in the normalized form $n_{\text{eff}} \sin \varphi_1 = n_x$, where n_{eff} is the effective index of the slab region and φ_1 is the incident angle). The phase velocity can then be found from $\mathbf{v}_p = c\left(n_x \hat{\mathbf{a}}_x + n_z \hat{\mathbf{a}}_z\right) / \left(n_x^2 + n_z^2\right)$ where c is the velocity of light in vacuum. The group velocity $\mathbf{v}_g = \nabla_k \omega(k)$, however is perpendicular to the wave vector diagram at the intersection point [10].

This chapter is arranged as follows. In the next section, the optimization of the conventional **S**-vector superprism is discussed. Our proposed photonic crystal demultiplexer is introduced in section 3. We compare the results and conclude the chapter in sections 4.

7.2 The conventional S-vector superprism

To be more specific, let us follow the design of a conventional demultiplexer based on **S**-vector superprism. It also provides us with the necessary framework for our proposal. The goal is to design an 8-channel CWDM demultiplexer working at $\lambda = 1310, \cdots, 1450$ nm. The channel spacing is assumed to be 20 nm. The Gaussian beam propagation in the photonic crystal involves different propagation characteristic of its plane wave components (with the full spectral width at $\exp(-2)$ intensity of θ_0). However, the envelop of the light intensity profile can be approximated by a Gaussian when θ_0 is sufficiently small. The divergence angle of the beam can be approximated by [11;12]

$$\theta_c = p\theta_0 = \frac{\lambda_0}{\pi n_{\mathrm{eff}} w_0} p \tag{7.1}$$

where w_0 is the effective input waveguide width [13], n is the effective refractive index of the incident beam media, λ_0 is the wavelength of the incident light and p is the beam divergence multiplication factor (which represents the beam divergence property of the photonic crystal) and defined as

$$p = \partial\varphi_1^+ / \partial\varphi_0 \tag{7.2}$$

where φ_0 and φ_1^+ are the incident and the refraction angle of the beam. The far field beam width can be approximated by

$$w = w_0 + 2L\sec\varphi_1^+ \tan\theta_c^+ \tag{7.3}$$

where L is the distance from input end. i^{th} channel has the following beam width and the lateral shift at the output interface

$$w_i = w_0 + 2L\sec\varphi_{1,\lambda_i}^+ \tan\theta_{1,\lambda_i}^+ \tag{7.4}$$

$$D_i = L\tan\varphi_{1,\lambda_i}^+ \tag{7.5}$$

The minimum length to resolve i^{th} channel from $(i\text{-}1)^{\text{th}}$ one with a modest crosstalk can be determined from the following equation.

$$D_i - D_{i-1} = w_i + w_{i-1} \tag{7.6}$$

or

$$L_i = \frac{2w_0}{\tan\varphi_{1,\lambda_{i-1}}^+ - \tan\varphi_{1,\lambda_i}^+ - 2\sec\varphi_{1,\lambda_i}^+ \tan\theta_{c,\lambda_i}^+ - 2\sec\varphi_{1,\lambda_{i-1}}^+ \tan\theta_{c,\lambda_{i-1}}^+} \tag{7.7}$$

where L_i is the resolution length (minimum length from the input end to resolve channel i from the proceeding one). The demultiplexer length is the maximum of L_i. The demultiplexer photonic crystal area (assuming it is in rectangular shape) can be found from

$$S = L \times \left(L \tan \varphi^{+}_{1,\lambda_1} + w_1 + w_0 \right) \tag{7.8}$$

A feature size of 50 nm with aspect ratio of grater than 10 is chosen. We have selected the silicon on insulator technology. The wafer has 260 nm top silicon layer thickness, the hole diameter is 190 nm and the polarization is TM (electric field parallel to the air hole). The period of 280 nm on square lattice provides us a broad enough band diagram. The wave vector diagram (equi-frequency band diagram) is obtained using the plane wave expansion method. The mesh size is 64×64 in the lattice surface and also 64 points in the vertical direction, which we impose periodicity of 6 times grater than the slab height. The dielectric constant is sampled 6 times finer that the imposed mesh. The whole first Brillion zone has been scanned 4×10^4 times for a complete wave vector diagram.

The minimum rotational angle of the lattice which ensures that no channel launches at the band gap can be found from [14]

$$\theta_{\min} = \tan^{-1}\left(n_x(\lambda_1) / n_z(\lambda_1) \Big|_{\text{bandedge}} \right) \tag{7.9}$$

where the wavelength of the first channel is $\lambda_1 = 1310$ nm. In our case, $\theta_{\min} = 22.9°$. It is not difficult to show the minimum demultiplexer surface area occurs at $\theta = 23.4°$. Figure 7.2.1 illustrates part of normalized wave diagrams relevant to our design. Directions of group velocity (beam directions) are also indicated.

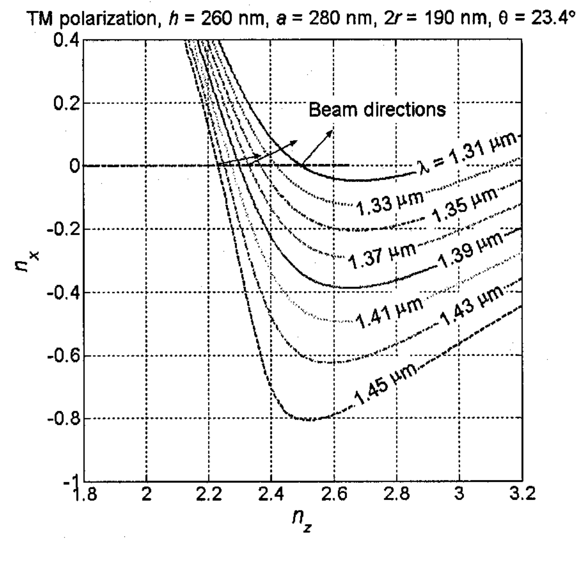

Figure 7.2.1 The normalized wave vector diagram

Figure 7.2.2 demonstrates the angular deviation profile for an 8-channel demultiplexer based on the band diagram of Figure 7.2.1. As is seen, whilst the theoretical dispersion is significant at the first channel (at 1310nm) 0.9 °/nm, it is not that large at the last channel (at 1450nm) 0.087 °/nm. This large non-uniformity is troublesome, considering the fact that demultiplexer design is usually governed by the worst dispersion. However, the situation gets more complicated, if one takes the non-uniformity of p (see Eq. (7.1)) into account. We will discuss this issue later.

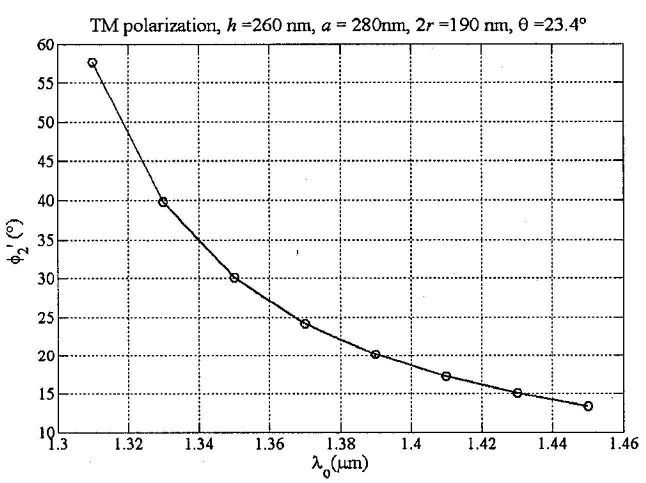

Figure 7.2.2 The beam deviation angle versus wavelength of a typical demultiplexer

Figure 7.2.3 depicts the demultiplexer length versus input waveguide width. As is clear, at low waveguide width, the dispersion of the photonic crystal can only overcome the spatial divergence of the beam inside the photonic crystal at large distances. Since, the spatial divergence of the beam reduces by increasing the input waveguide width, the required distance to achieve the desired spectral resolution will decrease. However, this distance increases again as we need more length to separate wide beams. The minimum multiplexer length of $L_{\min} = 754\ \mu\text{m}$ is achievable at the input waveguide width of $w_0 = 9.1\mu\text{m}$. Then the photonic crystal area will be 1.38 mm^2.

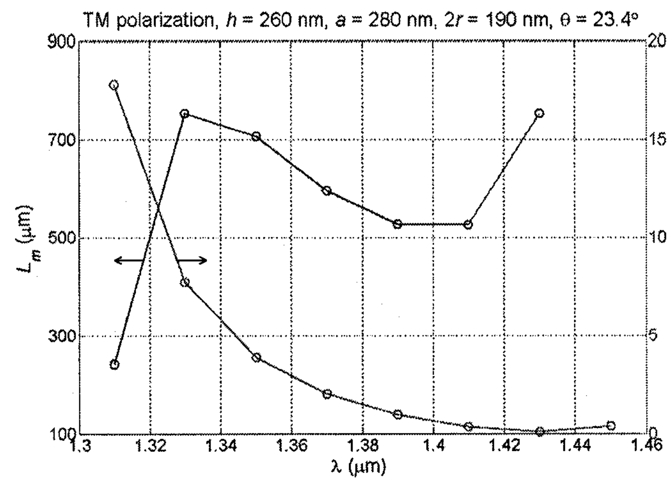

Figure 7.2.3 Resolution length and beam divergence multiplication factor versus channel wavelength.

Figure 7.2.3 shows the beam divergence multiplication factor p (see Eq.(7.1)) at the input wavelength for $w_0 = 9.1\ \mu\text{m}$. The first point from the large non-uniformity of dispersion observed in Figure 7.2.2 is that the low dispersion of the last channel has caused the demultiplexer length to be large. It is interesting to mention that the large dispersion of the first channel is negated by the large divergence factor, whereas the dispersion near the band edge (at the first channel) is high enough that needs a quarter of the distance required at the last channels. Putting the first channel in the same line as the last channel causes the first channel to expand excessively. Figure 7.2.4 shows the output channel width of the multiplexer. The output channel width reduces 300 fold from the first channel to the last one. In other words, we need to increase the demultiplexer width to cover the entire expanded beam. In previous chapter, by bringing forward the exit of the first channel, we tried to reduce the prism area. Here we introduce a new idea; the next section is devoted to this new idea.

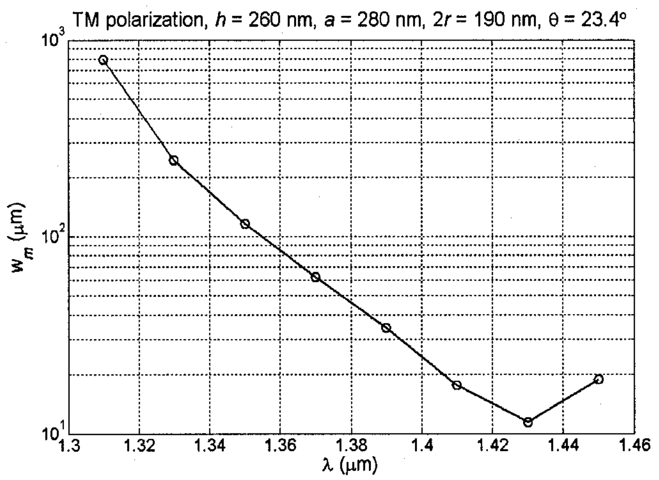

Figure 7.2.4 Output channel widths versus channel wavelength

7.3 Our proposal

In order to bring the band edge in line with the normal incident angle beam, the lattice rotational angle must be θ_{min} (see Eq.(7.9)). The signal will propagate through the lattice provided the rotational angle is greater than θ_{min}, otherwise the beam will be reflected back after encountering the lattice band gap. There is no barrier to experiencing high dispersion at the last channel, but the type of structure that demonstrates high dispersion probably does not allow the beam to propagate at the first channel. The beams, which are prohibited from propagation through the band gap usually reflect back. This intuitive observation brings us to the following design idea. Consider a stack of photonic crystals where each layer is designed to maximize the dispersion for specific channel; however it puts the entire proceeding channels into the band gap (reflect them back). Figure 7.3.1 illustrates the schematic of our proposal.

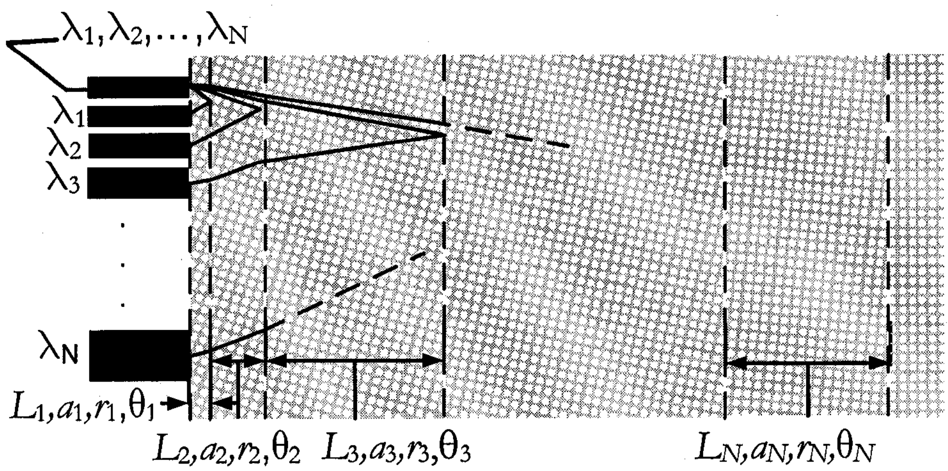

Figure 7.3.1 The schematic of the stratified photonic crystal for N channel demultiplexing

By setting the incident beam angle normal to the interfaces, the tangential phase velocity components will remain zero along the layers, which makes the design much simpler. The lattice type is assumed to be square and because of its axial symmetry the beam encounters similar lattice geometry in propagating forward or backward. Each section has four parameters to be chosen: length L, period a, hole diameter $2r$ and lattice rotational angle (slant angle) θ. The set of parameters, $\{L_1, a_1, r_1, \theta_1\}$, $\{L_2, a_2, r_2, \theta_2\}$, $\ldots$,$\{L_N, a_N, r_N, \theta_N\}$, can be selected in order to make the multiplexer response uniform (*i.e.*, grid wavelengths be reflected back at the desired location). Arbitrarily, we select

$$a_1 = a_2 = \cdots = a_N = \Lambda, \text{ and } r_1 = r_2 = \cdots = r_N = r \tag{7.10}$$

In order to avoid low reflection at the boundaries, we select the slant angle θ of the each layer in such a way to make $n_x = 0$ half way between two successive wave vector diagram (corresponding to the channel in the band gap, which is supposed to be reflected and the one with maximum dispersion which is supposed to pass through). For this purpose, the only remaining degree of freedom is the length of each layer, which must be chosen together with the input waveguide width appropriately, in order to make photonic crystal area as small as possible.

Furthermore we define refraction angle matrices which contain the refraction angles at each wavelength through each layer for the forward traveling waves as

$$\boldsymbol{\varphi}^{+}=\begin{bmatrix}\varphi_{1,\lambda_1}^{+} & & & \\ \varphi_{1,\lambda_2}^{+} & \varphi_{2,\lambda_2}^{+} & & \\ \vdots & \vdots & & \\ \varphi_{1,\lambda_N}^{+} & \varphi_{2,\lambda_N}^{+} & \cdots & \varphi_{N,\lambda_N}^{+}\end{bmatrix} \tag{7.11}$$

And similarly for the backward traveling waves, as

$$\boldsymbol{\varphi}^{-}=\begin{bmatrix}\varphi_{1,\lambda_1}^{-} & & & \\ \varphi_{1,\lambda_2}^{-} & \varphi_{2,\lambda_2}^{-} & & \\ \vdots & \vdots & & \\ \varphi_{1,\lambda_N}^{-} & \varphi_{2,\lambda_N}^{-} & \cdots & \varphi_{N,\lambda_N}^{-}\end{bmatrix} \tag{7.12}$$

Also we define the divergence factor matrices that contain the beam divergence multiplication factor can also be determined (using Eq.(7.2)) for the forward traveling waves as

$$\mathbf{p}^{+}=\begin{bmatrix}p_{1,\lambda_1}^{+} & & & \\ p_{1,\lambda_2}^{+} & p_{2,\lambda_2}^{+} & & \\ \vdots & \vdots & & \\ p_{1,\lambda_N}^{+} & p_{2,\lambda_N}^{+} & \cdots & p_{N,\lambda_N}^{+}\end{bmatrix} \tag{7.13}$$

For the backward traveling waves we have

$$\mathbf{p}^{-}=\begin{bmatrix}p_{1,\lambda_1}^{-} & & & \\ p_{1,\lambda_2}^{-} & p_{2,\lambda_2}^{-} & & \\ \vdots & \vdots & & \\ p_{1,\lambda_N}^{-} & p_{2,\lambda_N}^{-} & \cdots & p_{N,\lambda_N}^{-}\end{bmatrix} \tag{7.14}$$

The beam divergence angle can be calculated using Eq.(7.1) subsequently. The beam width of the first channel at the input interface is

$$w_1 = 2L_1 \sec\varphi_{1,\lambda_1}^{+} \tan\theta_{1,\lambda_1}^{+} + 2L_1 \sec\varphi_{1,\lambda_1}^{-} \tan\theta_{1,\lambda_1}^{-} + w_0 \tag{7.15}$$

In order to avoid excessive cross talk we have to separate the output channels for at least $2\theta_0$ apart from each other. Then the first channel has to be separated from the input channel by (see Figure 7.3.2):

$$D_1 = w_1 + w_0 \tag{7.16}$$

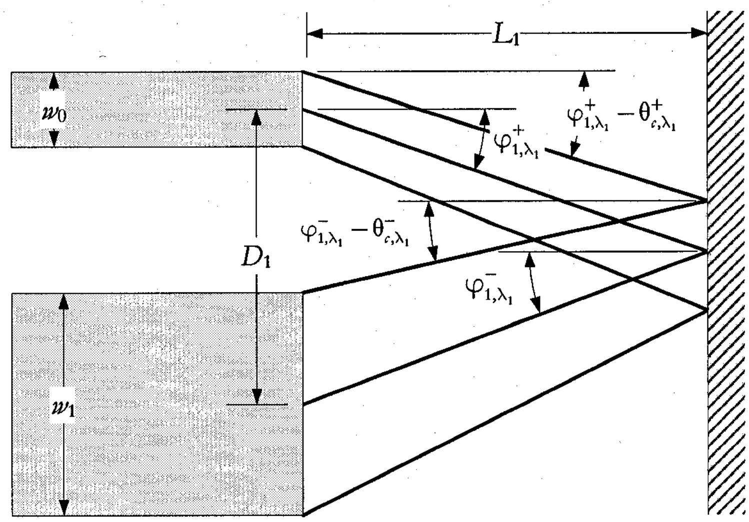

Figure 7.3.2 The input/output waveguide geometry.

The first layer must be wide enough to provide the lateral beam shift D_1, or

$$D_1 = L_1\left(\tan\varphi^{+}_{1,\lambda_1} + \tan\varphi^{-}_{1,\lambda_1}\right) \tag{7.17}$$

Solving Eqs(7.16) and (7.17) together (using Eq. (7.15)) we will have

$$L_1 = \frac{w_0}{0.5\left(\tan\varphi^{+}_{1,\lambda_1} + 0.5\tan\varphi^{-}_{1,\lambda_1}\right) - \tan\theta^{+}_{1,\lambda_1}\sec\varphi^{+}_{1,\lambda_1} - \tan\theta^{-}_{1,\lambda_1}\sec\varphi^{-}_{1,\lambda_1}} \tag{7.18}$$

if $L_1 > 0$ the layer will fulfill the requirements properly. The next channel beam width at the input interface is

$$\begin{aligned} w_2 = {} & 2L_1\left(\sec\varphi^{+}_{1,\lambda_2}\tan\theta^{+}_{1,\lambda_2} + \sec\varphi^{-}_{1,\lambda_2}\tan\theta^{-}_{1,\lambda_2}\right) + \\ & 2L_2\left(\sec\varphi^{+}_{2,\lambda_2}\tan\theta^{+}_{2,\lambda_2} + \sec\varphi^{-}_{2,\lambda_2}\tan\theta^{-}_{2,\lambda_2}\right) + w_0 \end{aligned} \tag{7.19}$$

The channel spatial shift and the layer width can be determined by finding the common solution to the both following equations

$$D_2 - D_1 = w_2 + w_1 \tag{7.20}$$

$$D_2 = L_1\left(\tan\varphi_{1,\lambda_2}^{+} + \tan\varphi_{1,\lambda_2}^{-}\right) + L_2\left(\tan\varphi_{2,\lambda_2}^{+} + \tan\varphi_{2,\lambda_2}^{-}\right) \tag{7.21}$$

Solving Eqs.(7.20) and (7.21) (using Eqs. (7.17)and (7.19) for L_2, we will have:

$$L_2 = \frac{w_0 + w_1 + D_1 - \left(\tan\varphi_{1,\lambda_2}^{+} + \tan\varphi_{1,\lambda_2}^{-} - 2\sec\varphi_{1,\lambda_2}^{+}\tan\theta_{1,\lambda_2}^{+} - 2\sec\varphi_{1,\lambda_2}^{-}\tan\theta_{1,\lambda_2}^{-}\right)L_1}{\tan\varphi_{2,\lambda_2}^{+} + \tan\varphi_{2,\lambda_2}^{-} - 2\sec\varphi_{2,\lambda_2}^{+}\tan\theta_{2,\lambda_2}^{+} - 2\sec\varphi_{2,\lambda_2}^{-}\tan\theta_{2,\lambda_2}^{-}} \tag{7.22}$$

Similarly if $L_2 > 0$ the layer will satisfy the needs properly. The beam width of i^{th} channel can be obtained as

$$w_i = \sum_{m=1}^{i} 2L_m\left(\cos\varphi_{m,\lambda_i}^{+}\tan\theta_{m,\lambda_i}^{+} + \cos\varphi_{m,\lambda_i}^{-}\tan\theta_{m,\lambda_i}^{-}\right) + w_0 \tag{7.23}$$

Similarly D_i and L_i can be found by solving the both following equations

$$D_i - D_{i-1} = w_i + w_{i-1} \tag{7.24}$$

$$D_i = \sum_{m=1}^{i} L_m\left(\tan\varphi_{m,\lambda_i}^{+} + \tan\varphi_{m,\lambda_i}^{-}\right) \tag{7.25}$$

Eqs.(7.24) and (7.25) are used to calculate L_i as follow

$$L_i = \frac{w_0 + w_{i-1} + D_{i-1} - \sum_{m=1}^{i-1}\left(\tan\varphi_{m,\lambda_i}^{+} + \tan\varphi_{m,\lambda_i}^{-} - 2\sec\varphi_{m,\lambda_i}^{+}\tan\theta_{m,\lambda_i}^{+} - 2\sec\varphi_{m,\lambda_i}^{-}\tan\theta_{m,\lambda_i}^{-}\right)L_m}{\tan\varphi_{i,\lambda_i}^{+} + \tan\varphi_{i,\lambda_i}^{-} - 2\sec\varphi_{i,\lambda_i}^{+}\tan\theta_{i,\lambda_i}^{+} - 2\sec\varphi_{i,\lambda_i}^{-}\tan\theta_{i,\lambda_i}^{-}} \tag{7.26}$$

If all $L_i > 0$ the design will be feasible. The photonic crystal area can be found from

$$S = \left(D_8 + w_8 + w_0\right) \times \sum_i L_i \tag{7.27}$$

The lattice rotational angle in order to bring the band edge in line with the normal incident beam angle is given by Eq(7.9). The beam will propagate through the lattice provided the rotational angle is greater than θ, otherwise the beam will be reflected back encountering the lattice band gap. Figure 7.3.3 demonstrates the band edge rotational angle versus the wavelength λ.

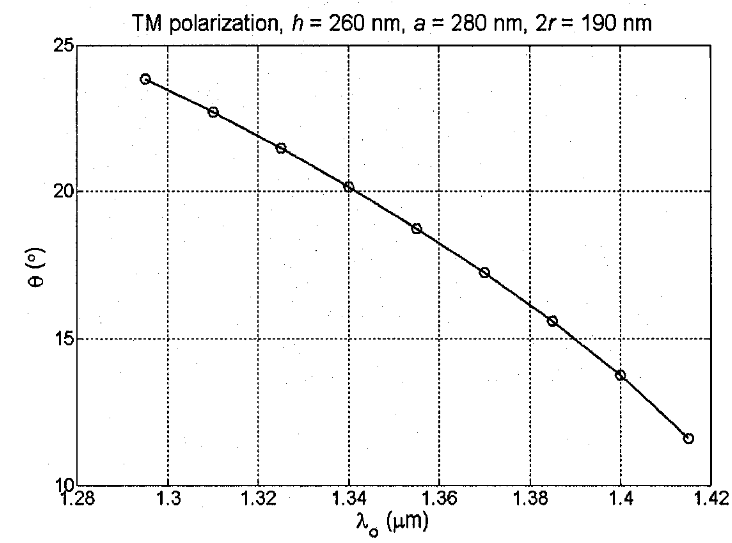

Figure 7.3.3 Band edge rotational angle versus the wavelength λ, vertical grid lines are plotted at the mid channel wavelengths for the design purposes.

If we select the rotational angle of each layer (the slant angle) to be the same as the band edge rotational angle of the mid wavelength grid points, we will ensure that while the dispersion is high, the reflection of the proceeding channels remains adequate. The results are shown in Table 7.1.

Table 7.1 Slant angle for each layer

θ_1 (°)	θ_2 (°)	θ_3 (°)	θ_4 (°)	θ_5 (°)	θ_6 (°)	θ_7 (°)	θ_8 (°)	θ_9 (°)
23.85	**22.68**	**21.45**	**20.15**	**18.75**	**17.24**	**15.59**	**13.73**	**11.58**

Figure 7.3.4 depicts the superprism area versus input waveguide width. Clearly the optimum input beam width is 18.6μm, and the minimum prism area will be 0.26 mm^2. Compared to the size of conventional superprism, we have achieved about five fold area reduction.

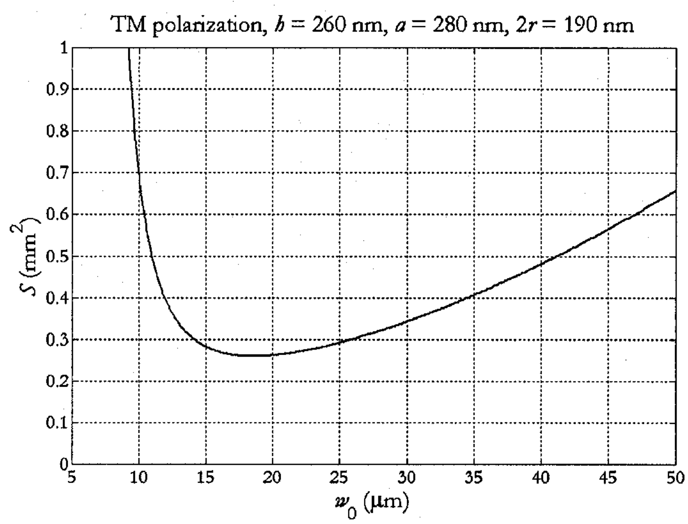

Figure 7.3.4 Superprism area versus input beam width for structure of Figure 7.3.1

Figure 7.3.5 shows the output beam width of the optimum stratified photonic crystal. As can be seen, much better output channel uniformity is achieved (2.2 times versus 300 times for the conventional one).

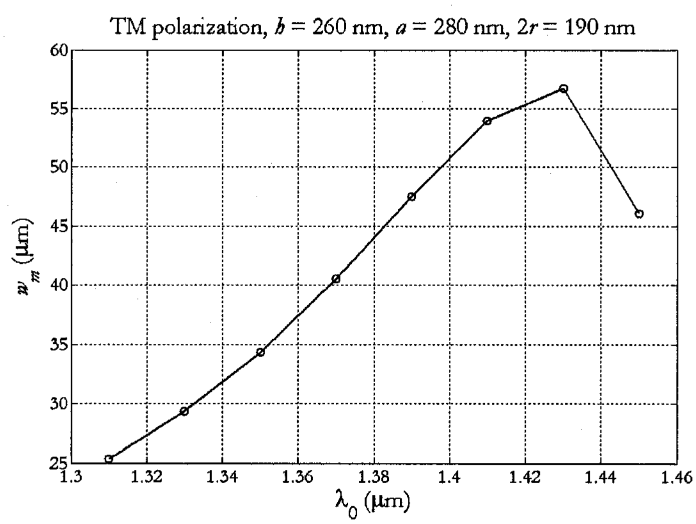

Figure 7.3.5 Output channel beam widths versus wavelength for structure of Figure 7.3.1

7.4 Conclusions

We have proposed a novel stratified photonic crystal, which is five times smaller than the conventional **S**-vector superprism. In particular we have designed an 8-channel standard CWDM demultiplexer (160nm bandwidth) with a 0.26 mm^2 photonic crystal area. The non-uniformity of the output channel width also shows tremendous improvement over the conventional superprism. It is also interesting to note that the fabrication challenges of the proposed demultiplexer would be the same as the conventional one (since we only use from the rotation of the base photonic crystal).

References

[1] T . Baba and T. Matsumoto, "Resolution of photonic crystal superprism," *Applied Physics Letters*, vol. 81, no. 13, pp. 2325-2327, Sept.2002.

[2] A . Bakhtazad and A. G. Kirk, "1-D slab photonic crystal **k**-vector superprism demultiplexer: analysis, and design," *Optics Express*, vol. 13, no. 14, pp. 5472-5482, July2005.

[3] H . Kosaka, T. Kawashima, A. Tomita, M. Notomi, T. Tamamura, T. Sato, and S. Kawakami, "Superprism phenomena in photonic crystals," *Physical Review B*, vol. 58, no. 16, pp. 10096-10099, Oct.1998.

[4] T . Matsumoto and T. Baba, "Photonic crystal **k**-vector superprism," *Journal of Lightwave Technology*, vol. 22, no. 3, pp. 917-922, Mar.2004.

[5] L . J. Wu, M. Mazilu, and T. F. Krauss, "Beam steering in planar-photonic crystals: From superprism to supercollimator," *Journal of Lightwave Technology*, vol. 21, no. 2, pp. 561-566, Feb.2003.

[6] H . Kosaka, T. Kawashima, A. Tomita, M. Notomi, T. Tamamura, T. Sato, and S. Kawakami, "Superprism phenomena in photonic crystals," *Physical Review B*, vol. 58, no. 16, pp. 10096-10099, Oct.1998.

[7] L . J. Wu, M. Mazilu, and T. F. Krauss, "Beam steering in planar-photonic crystals: From superprism to supercollimator," *Journal of Lightwave Technology*, vol. 21, no. 2, pp. 561-566, Feb.2003.

[8] T . Baba and T. Matsumoto, "Resolution of photonic crystal superprism," *Applied Physics Letters*, vol. 81, no. 13, pp. 2325-2327, Sept.2002.

[9] T . Baba and M. Nakamura, "Photonic crystal light deflection devices using the superprism effect," *Ieee Journal of Quantum Electronics*, vol. 38, no. 7, pp. 909-914, July2002.

[10] R ussell P.St., Birks T.A., and Lloyd-Lucas F.D., *Confined Electrons and Photons.* New York: NATO, Plenum, 1995.

[11] T . Baba and T. Matsumoto, "Resolution of photonic crystal superprism," *Applied Physics Letters*, vol. 81, no. 13, pp. 2325-2327, Sept.2002.

[12] B . Momeni and A. Adibi, "An approximate effective index model for efficient analysis and control of beam propagation effects in photonic crystals," *Journal of Lightwave Technology*, vol. 23, no. 3, pp. 1522-1532, Mar.2005.

[13] U nger H.G., *Planar Optical Waveguides and fibers* Oxford, UK, Clarendon Press, 1977.

[14] A . S. Jugessur, A. Bakhtazad, A. G. Kirk, L. Wu, T. F. Krauss, and R. M. De la Rue, "Compact and integrated 2-D photonic crystal super-prism filter-device for wavelength demultiplexing applications," *Optics Express*, vol. 14, no. 4, pp. 1632-1642, Feb.2006.

Chapter 8

FIRST BAND **K**-VECTOR SUPERPRISM PHOTONIC CRYSTAL DESIGN AND OPTIMIZATION

Design rules for a complete demultiplexer based on the k-vector superprism in a slab photonic crystal are presented. Based on these rules, we select parameters for three types of lattices of interest, *i.e.*, 1-D, 2-D square and 2-D hexagonal and compare the performance. The plane wave expansion method is used to obtain the wave vector diagram and from this we develop design equations based on conventional ray tracing. We then present an optimization approach which minimizes the prism area independent of lattice types. We show that the 1-D superprism photonic crystal shows a minimum prism area when compared to the other photonic crystal cases. Using typical silicon-on-insulator technology, a photonic crystal area of 0.099 mm^2 is sufficient to resolve 32 channels spaced by 0.8 nm (100 GHz) in the *C* band for a dense wavelength division multiplexing system. In order to achieve this, the angular dispersion of the slab photonic crystals are enhanced considerably by expanding the input beam through the superprism region and employing etched mirrors to collimate and focus the light into and out of the superprism. We have shown that the superprism area approximately increases by square of the channel count. Finally the non-uniformity of phase velocity dispersion across the desired spectral window is addressed. The 1-D photonic crystal is superior in this regard too.

8.1 Introduction

k-vector superprism is based on the angular dispersion of the light at each of the free space/photonic crystal interfaces. So long as the two interfaces are non-parallel, the different wavelengths will continue to diverge in the free-space region beyond the photonic crystal.

This implies that the photonic crystal is a prism shapes with the interface crossing angle equal to the apex angle. As a consequence, an enhanced spectral resolution, similar to that of a traditional prism made of dispersive glass can be achieved. Interestingly, the attainable resolution could be more than enough for resolving channels in the conventional DWDM applications. Peripheral optics usually is required to collimate input light and focus the output light to the output waveguides (or detectors). By careful selection of the photonic crystal parameters and prism geometry, we will show that it is possible to design a small photonic crystal to resolve narrow wavelengths of DWDM. Figure 8.1.1 shows a schematic of **k**-vector superprism in the planar technology [1]. In this example beam collimation and focusing is accomplished with etched mirrors (other approaches such as tapers or waveguide lenses may also be feasible).

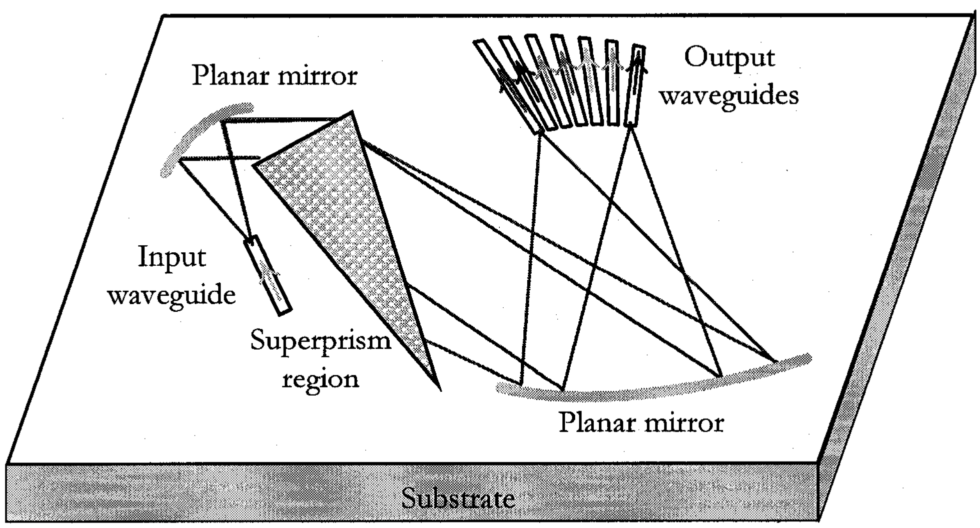

Figure 8.1.1 Schematic representation of **k**-vector superprism

The purpose of an input collimating mirror is to convert the input beam wavefront into a planar one with a small range of spatial frequencies. This avoids the need for the flat dispersive band diagram that would be required for narrow incident beams [2]. Note that the output beam width after the prism has to be sufficiently large to provide the required wavelength resolution through the Rayleigh criterion. So the resolution of the demultiplexer can be enhanced if the prism expands the incident beamwidth considerably. Using the fact that rays follow the group velocity direction but the wavefront refraction will be in the direction of the phase velocity, the photonic crystal can be rotated in such a way that there is a large deflection angle between the incident beam and the refracted beam inside the photonic crystal. By proper selection of the apex angle, this results in an expanded beam width which amplifies the resolution of the demultiplexer.

Whilst the input facet must be large enough to cover the incident beam, the output facet of the prism has to be of sufficient size to capture all beams in all wavelengths over the desired window of operation. Considering the group velocity dispersion of the prism near the band gap edge, the output side of the prism will usually be larger than the local beam width. The output mirror will collect the transmitted rays from the prism and focus them toward the output waveguides. The displacement of the output beam with wavelength due to the group velocity dispersion will only cause extra coma in the output waveguides, which can be mitigated by a proper mirror design.

The dispersion behavior of the Bloch modes can best be understood through the wave vector diagram, which is the contour of the components of propagation constant of the Bloch modes at a specific wavelength (also known as equi-frequency contour) [3]. We have also recognized that normalizing the wave vector components versus wave number in vacuum makes superprism design much easier.

The wave vector diagram shows as many degrees of symmetry as the corresponding photonic crystal type. Confining ourselves to the slab photonic crystal, there are three types of photonic crystal that have mainly been used. Figure 8.1.2 shows the three well known photonic crystal lattices. The lattices are rotated so we have always bandgap at the x direction. The rotational angle of the photonic crystal with respect of the interface (the slant angle θ_1 has also been defined).

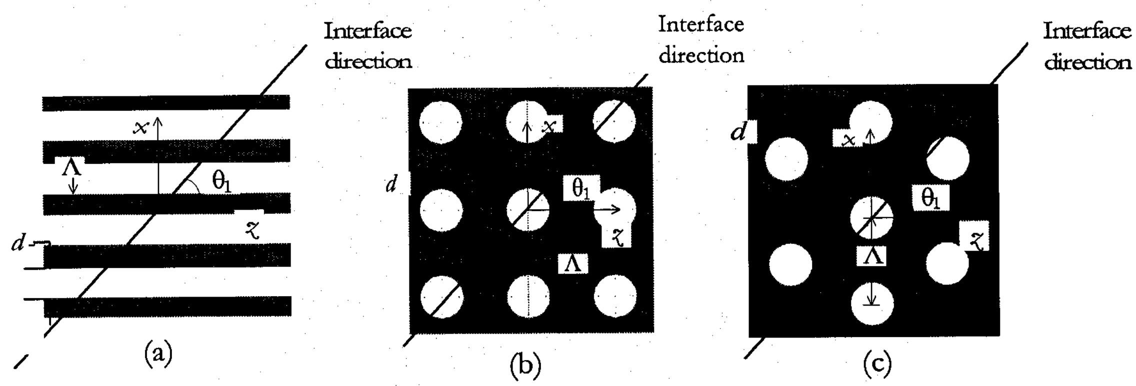

Figure 8.1.2 Three well known different photonic crystal lattices with the slant angle (θ_1) definition in each case.

For the superprism purpose, we need the wave that propagates through the photonic crystal, *i.e.*, we have to choose wavelengths below the band edge. The wave vector diagram of the 1-D photonic crystal is an open curve (which is the consequence of having band edge at only one direction), it also has the smoothest wave vector diagram (which is the consequence of having the lowest crystal symmetry) and provides the longest rang of operations. By providing a modest band gap and a modest lattice symmetry groups, the 2-D square lattice on the other hand provides modest range of operation. However, the hexagonal lattice by having large band gap and large lattice symmetry groups provides the smallest range of operation. Beside the difficulty of working with hexagonal lattice, it remains unclear which photonic crystal is better for making **k**-vector superprism. As a basis for comparison in this chapter, we have chosen superprism area as a figure of merit.

In the next section we describe a basis for photonic crystal comparison. Based on that basis, we select photonic crystal parameters for the three photonic crystals for which we are going to make a comparison. In section three, we will show how **k**-vector dispersion is higher at the second Brillouin zone. In section four we derive the unifying equations for the design of **k**-vector superprism. Our scheme for minimizing the superprism area which consists of working in second Brillouin zone and selecting the proper prism apex angles are presented in section five. The selections of the remaining parameters for minimizing the superprism area are taken care of in the next section. The typical results for designing a 32 DWDM channels in *C* band are presented for three photonic crystals of interest in section six. A discussion on the results followed by a conclusion terminates the chapter

8.2 Lattice parameter selection for k-vector superprism

The first band wave vector diagram of all photonic crystals evolves with the wavelength (or equivalently with the period) more or less the same way. They start as closed curves around the origin with a shape that resembles the crystallographical symmetry of the corresponding photonic crystal. Increasing the wavelength, the closed curves grow bigger and bigger until they touch the first Brillouin zone edges, then they break down (in direction normal to symmetry directions of photonic crystal) and the band gaps emerge. Both kinds of dispersion are basically related to how fast this evolution occurs with the wavelength (or period). This is usually slow when there is no bandgap, but it is fast when the bandgap is small and it settles at a minimum as the bandwidth grows larger. To show this fact analytically, we define a parameter to measure the speed of evolution. We define the slope of wave vector change at the bandedge (after it appears) versus wavelength as

$$\left.\frac{\partial n_x}{\partial \lambda}\right|_{\text{bandedge}} = \left.\frac{n_x(\lambda) - n_x(\lambda + \Delta\lambda)}{\Delta\lambda}\right|_{\text{bandedge}} \tag{8.1}$$

The slope is proportional to the slope of the conventional photonic crystal band diagram at the desired wavelength along the main symmetrical directions (*i.e.*, ΓX for 1-D and 2-D square and ΓM for 2-D hexagonal lattices). The slope defined by Eq.(8.1) can also be related to the normalized group velocity at the band edge as:

$$\bar{\mathbf{v}}_g = \frac{\hat{\mathbf{a}}_x}{-\lambda \left.\dfrac{\partial n_x}{\partial \lambda}\right|_{\text{bandedge}}} \tag{8.2}$$

It is well-known that both high phase and group velocity dispersion occur near the band edge [2]. Because the maximum dispersion usually happens at the band edge and the lower the group velocity, the higher the dispersion [4]; the above parameter can be adopted as a gauge for the maximum available dispersion. In other words, the lattice type with a configuration that provides lower $\bar{\mathbf{v}}_g$ at the central wavelength of interest has higher available dispersion at its band-edge and it would be a better choice for making a superprism.

Figure 8.2.1 shows n_z and its slope versus wavelength as a function of lattice constant for a typical 1-D photonic crystal. Note that the bandgap emerging point is where $n_z = 0$. As is clear near this point, where the bandgap is small and the wave vector diagram evolves fast, the dispersion is maximal. The dispersion falls rapidly with period and it settles at a minimum around $\Lambda = 300\,\text{nm}$ in this typical case.

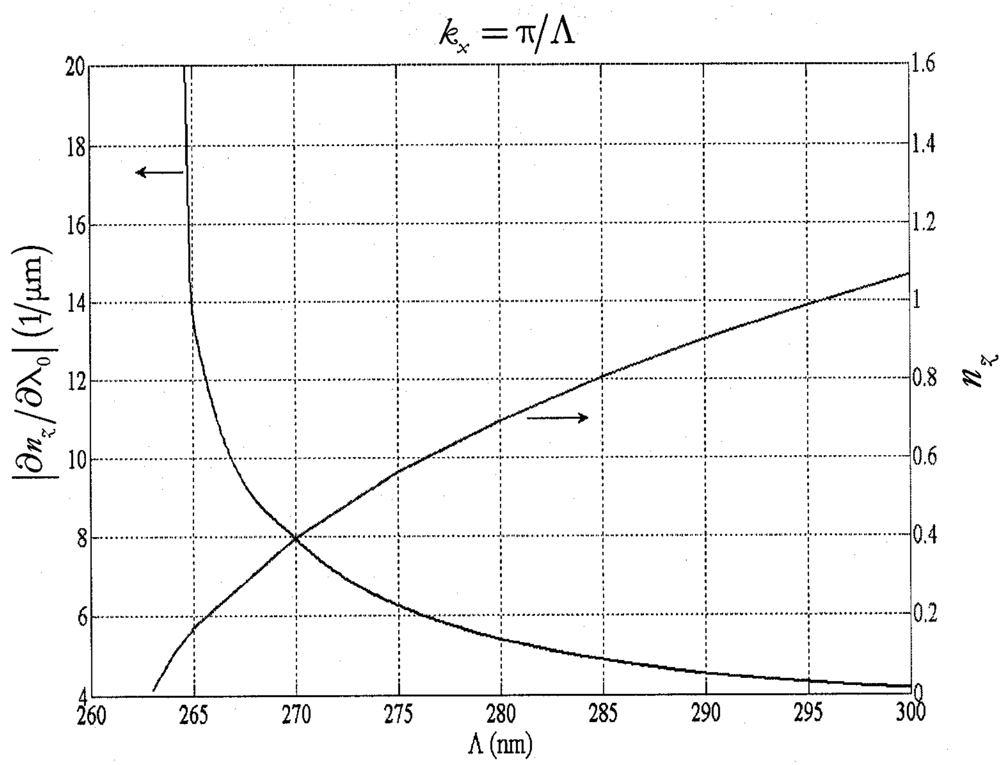

Figure 8.2.1 A typical n_z and its slope versus wavelength as a function of lattice constant for 1-D photonic crystal

Working very near the bandgap emerging point, we could enjoy higher dispersion as has been depicted in Figure 8.2.1. But being too near to this point has it own drawback. Sensitivity to the wavelength reflects the sensitivity to the photonic crystal dimensions (this is inferred from the scaling law of photonic crystals). Therefore for a practical device, we cannot choose an operating point too near to this point. Arbitrarily, we have chosen the margin of $n_z \geq n_{z0}$. Since by increasing the wavelength the bandgap decreases, so the only thing that we have to do is to fix bandedge at the highest wavelength of interest at n_{z0}.

Figure 8.2.2 shows a typical wave vector diagram near the bandedge. ρ' is the asymptotic angle of the wave vector diagram (which is determined by the lattice type). The operating point is determined by the continuity of tangential component of the wave vector at the interface. Consider the interface of the slab waveguide with the slab photonic crystal, and assume the effective index of the slab waveguide at the wavelength of interest as $n_{\text{eff}}(\text{slab})$, then for the slab mode incident angle of φ_1, the continuity of the tangential components of wave vectors at the interface (in the normalized form) can be expressed as

$$n_x = n_{\text{eff}}(\text{slab})\sin\varphi_1 \tag{8.3}$$

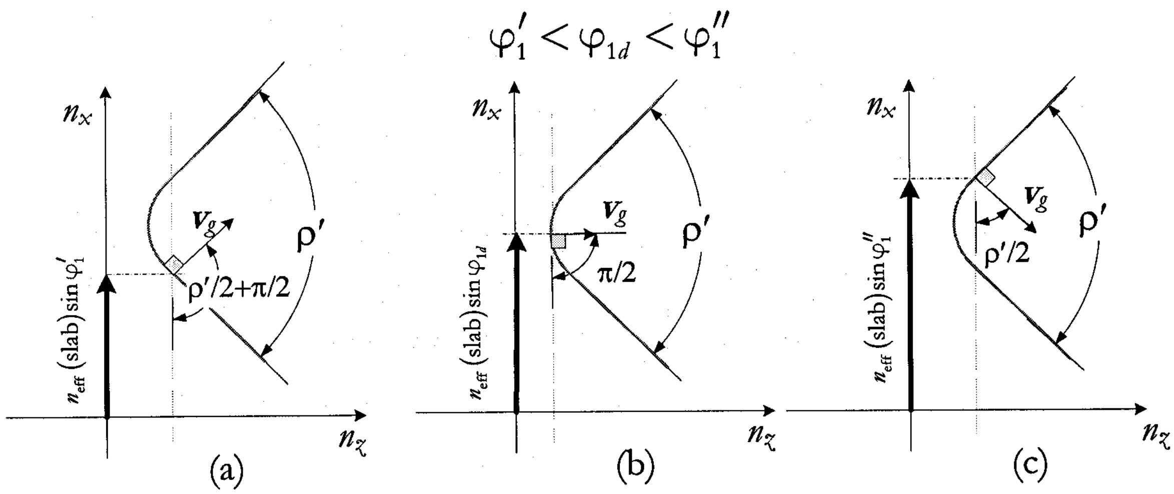

Figure 8.2.2 The operating point of un-slanted wave vector diagram with operating point a) in the first Brillouin zone, b) at the bandedge and c) in the second Brillouin zone.

It can be shown easily that the effective index of the slab waveguide is higher than the normalized Bloch wave number at the bandedge of the first Brillouin zone. It indicates that the operating point in the second Brillouin zone is feasible if one chooses a sufficient steep incident angle. If we define the φ_{1d} as the angle that causes the operating point to be at the bandedge (see Figure 8.2.2b), then if $\varphi_1 < \varphi_{1d}$, the operating point is the first Brillouin zone (see Figure 8.2.2a) and if $\varphi_1 > \varphi_{1d}$ then it is at the second Brillouin zone (see Figure 8.2.2c). As we will show later, for the sake of higher dispersion, we are in favor of working at the second Brillouin zone. Note also that the direction of the group velocity $\mathbf{v}_g$ is normal to the wave vector diagram at the operating point and directed toward the lower wavelength contours.

Let us fix the bandedge for all three photonic crystals (at the highest wavelength of interest) at

$$\begin{cases} n_z = n_{z0} \\ n_x = n_{\text{eff}}(\text{slab})\sin\varphi_{1d} \end{cases} \tag{8.4}$$

Given φ_{1d} , the photonic crystal period can be found from

$$\Lambda = \begin{cases} \dfrac{\lambda_{\text{max}}}{2\sin\varphi_{1d} n_{\text{eff}}(\text{slab})} & \text{for 1D} \\ \dfrac{\lambda_{\text{max}}}{2\sin\varphi_{1d} n_{\text{eff}}(\text{slab})} & \text{for 2D square} \\ \dfrac{\lambda_{\text{max}}}{\sqrt{3}\sin\varphi_{1d} n_{\text{eff}}(\text{slab})} & \text{for 2D hex} \end{cases} \tag{8.5}$$

Note that $n_{\text{eff}}(\text{slab})$ is a function of the slab height and wavelength. The functionality of $n_{\text{eff}}(\text{slab})$ for the Silicon On Insulator (SOI) wafer with permittivity of 12 and 2 at the wavelength of $\lambda_{10} = 1562.23$ nm is plotted in Figure 8.2.3.

At each period given by Eq.(8.5), the hole sizes can be obtained by adjusting n_z at the bandedge to n_{z0}. Figure 8.2.4 shows hole separations $(\Lambda - d)$ and the hole size d versus slab height for the three photonic crystals of interest where

$$n_{z0} = 0.2, \quad \varphi_{1d} = 60° \tag{8.6}$$

and TM polarization (electric field normal to the slab) have been assumed.

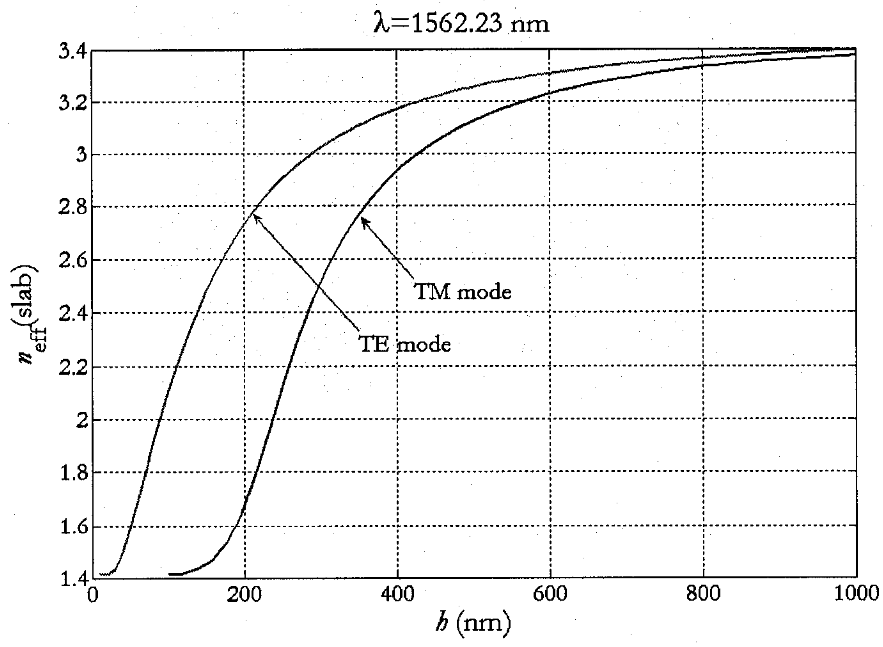

Figure 8.2.3 The slab waveguide effective index versus slab height for both polarizations. Electric field at TE and TM modes are directed parallel and normal to the slab surface respectively.

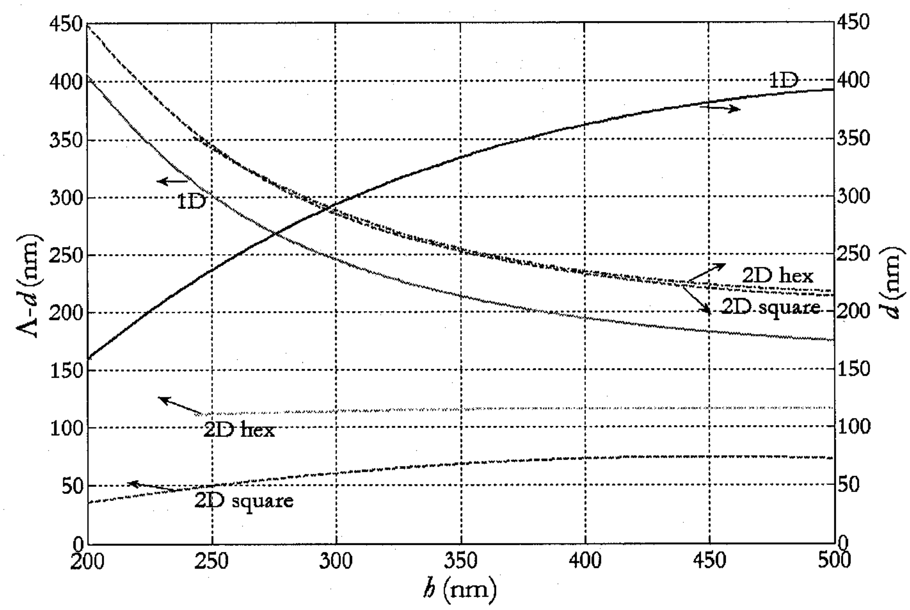

Figure 8.2.4 Distance between holes $(\Lambda - d)$, and hole size d versus slab height for a) 1-D photonic crystal, bold line, b) 2-D square, dashed line, and c) 2-D hexagonal, dot-dashed line when $n_{z0} = 0.2$ and $\varphi_{1d} = 60°$.

Using the parameters of Figure 8.2.4, the normalized group velocity versus the slab height for the photonic crystals of interest has been plotted in Figure 8.2.5. It is interesting to note that the 2-D hexagonal lattice has the highest dispersion at the bandedge while the 1-D lattice has the least. As we will show later, dispersion is not the only parameter determining the size of the prism.

The plane wave expansion method has been used to obtain the wave vectors. In order to apply the plane wave expansion method, the super cell technique has been employed, *i.e.*, the structure is assumed to be artificially periodic normal to the slab. But the period is large enough that the artificial periodicity can be ignored. We have observed that an artificial periodicity of 6 times of the slab width is enough to obtain convergence. The tolerance for eigenvalue calculation is 10^{-12}. The mesh size is 64×64 on the lattice surface (*x*-*z* plane) and also 64 points in the vertical direction (*y* axis), on which we impose an artificial periodicity. The dielectric constant is sampled 6 times finer than the imposed mesh size. For an accurate complete wave vector diagram the reduced Brillouin zone has been sampled into 10^4 partitions.

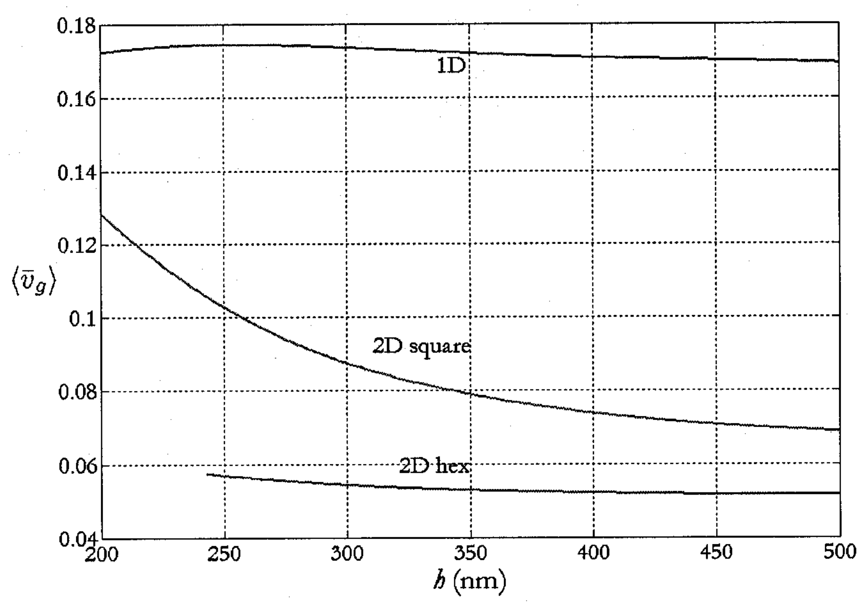

Figure 8.2.5 Normalized group velocity versus slab height for the photonic crystal of Figure 8.2.4.

Limiting the feature size to about 70nm, the three wave vector diagrams will look alike (*i.e.*, their band-edge at the specific wavelength pass through the specific point), provided that we choose their parameters according to the following table. Note that for TM polarization and at wavelength of $\lambda_{10} = 1562.23\ \text{nm}$, the slab effective index is $n_{\text{eff}}(\text{slab}) = 2.9087$ (see also Figure 8.2.3).

Table 8.1 The lattice parameters that makes comparison possible

	1-D	2-D square	2-D hexagonal
Slab width $b(nm)$	380	380	380
Period $a(nm)$	310	310	358
Hole width $d(nm)$	201	238	211

Figure 8.2.6 shows the normalized wave vector diagram of three lattice types according to Table 8.1. Note the asymptotic wave vector bend angles that resemble the original lattice types.

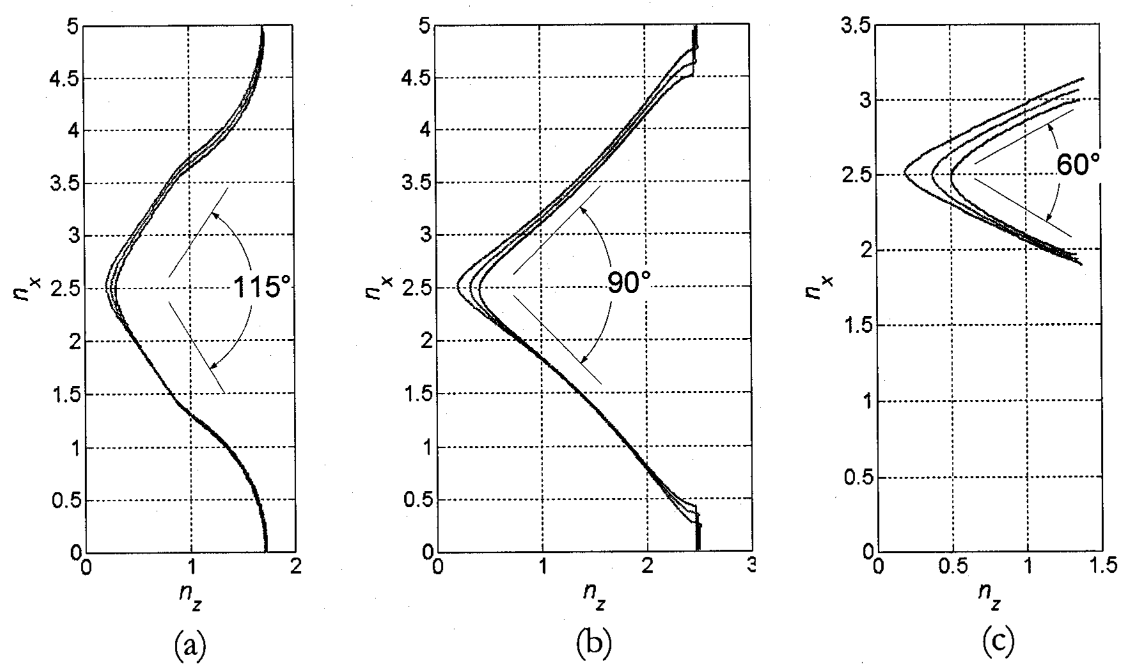

Figure 8.2.6 The normalized wave vector diagram of the photonic crystals of interest using the data of Table 8.1

8.3 The first and the second Brillouin zone dispersion comparison

It is not difficult to show analytically that dispersion is higher in the second Brillouin zone. Consider two symmetrical points (A and B) around the band edge (see Figure 8.3.1)

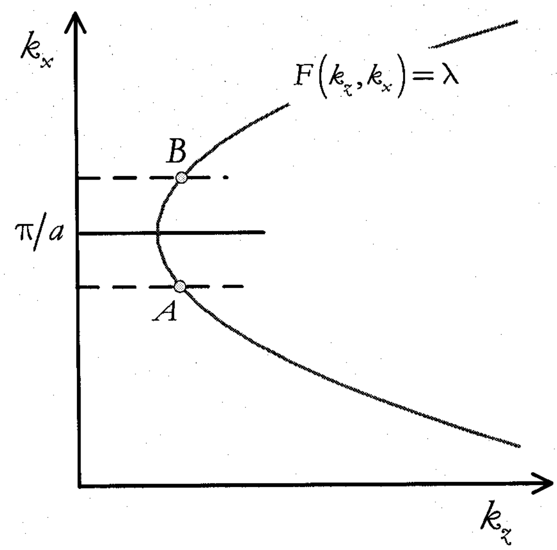

Figure 8.3.1 Constant wavelength contour near the bandedge

The following relation holds

$$k_{xB} = \frac{2\pi}{\Lambda} - k_{xA} \tag{8.7}$$

Differentially we can write

$$\Delta F = \Delta\lambda = \left.\frac{\partial F}{\partial k_x}\right|_A \Delta k_{xA} + \left.\frac{\partial F}{\partial k_z}\right|_A \Delta k_{zA} \tag{8.8}$$

Continuity of the tangential component of phase velocity at the interface with the slab region dictates that

$$\Delta k_x = \left(\frac{2\pi}{\lambda} - \frac{2\pi}{\lambda + \Delta\lambda}\right) n_{\text{eff}}(\text{slab}) \sin\varphi_1 \tag{8.9}$$

where φ_1 is the incident angle for operating point A and

$$k_{xA} = \frac{2\pi}{\lambda} n_{\text{eff}}(\text{slab}) \sin\varphi_1 \tag{8.10}$$

Eq.(8.9) can be approximated by

$$\Delta k_{xA} \approx \frac{\Delta\lambda}{\lambda} n_{\text{eff}}(\text{slab}) \sin\varphi_1 \tag{8.11}$$

Writing Eq.(8.8) for point B, we have

$$\Delta F = \Delta\lambda = \left.\frac{-\partial F}{\partial k_x}\right|_A \Delta k_{xB} + \left.\frac{\partial F}{\partial k_z}\right|_A \Delta k_{zB} \tag{8.12}$$

where symmetry around the band edge has been taken into account, and

$$k_{xB} = \frac{2\pi}{\lambda} n_{\text{eff}}(\text{slab}) \sin\varphi_1' \tag{8.13}$$

where φ_1' is the incident angle for the operating point B. Similar to Eq.(8.11) but for the operating point can be written as

$$\Delta k_{xB} \approx \frac{\Delta\lambda}{\lambda} n_{\text{eff}}(\text{slab}) \sin\varphi_1' \tag{8.14}$$

Subtracting Eq.(8.12) from Eq.(8.8) we have

$$\delta\Delta k_z = \Delta k_{zA} - \Delta k_{zB} = \left(\Delta k_{xB} - \Delta k_{xA}\right) \frac{\left.\partial F/\partial k_x\right|_A}{\left.\partial F/\partial k_z\right|_A} \tag{8.15}$$

where $\delta\Delta k_z$ is an indication of dispersion difference between point A and B. Using Eq. (8.10), (8.11), (8.13), (8.14) and (8.7) into Eq.(8.15) we have

$$\delta\Delta k_z = \left(\frac{2\Delta\lambda}{\lambda}\right)\left(\frac{\pi}{\Lambda} - k_{xA}\right)\left(\frac{\partial F/\partial k_x|_A}{\partial F/\partial k_z|_A}\right) \tag{8.16}$$

All three parameters in Eq.(8.16) are positive, so the dispersion difference is positive too. In conclusion, we have shown than dispersion in the second Brillion zone is higher than the first Brillouin zone, (or the dispersion difference is positive).

8.4 Design equations

Figure 8.4.1 shows the schematic diagram of a photonic crystal **k**-vector superprism and the parameters used in this section[1].

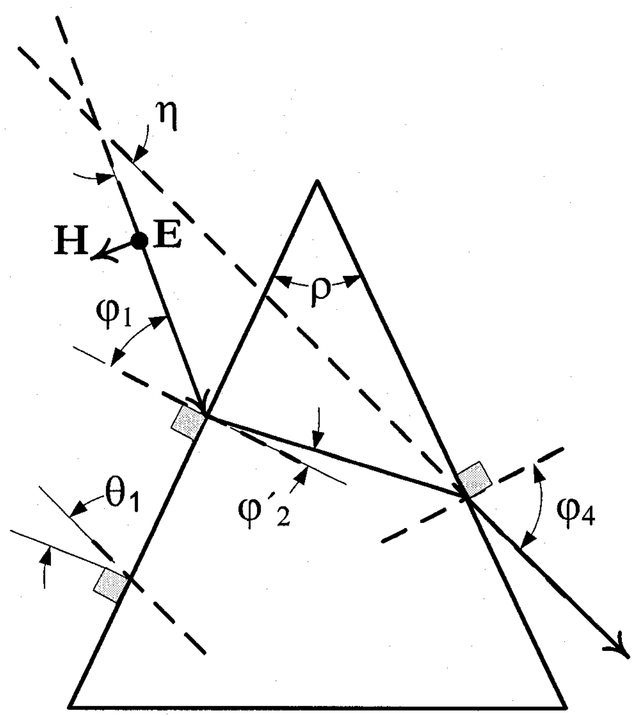

Figure 8.4.1 The photonic crystal superprism geometry with slanted photonic crystal

The conservation of the tangential component of the wave vector through different interfaces is the key factor determining the direction of refraction. The effective index of the slab mode and the normalized wave vector diagram of the photonic crystal are used to determine the refraction angle of the incident beam into the photonic crystal and from the photonic crystal into the slab. The rays evidently follow the group velocity directions, which usually differ from phase velocity directions (or that of the wave front). The phase velocity dispersion is defined as change of deviation angle $\eta = \varphi_4 - \varphi_1 + \rho$ versus wavelength ($\partial\eta/\partial\lambda$, see Figure 8.4.1).

Using the Gaussian approximation, the optical power density in the slab region can be written as

$$I(r,\theta,y) = \frac{2I_0}{\pi h_0 \theta_0 r} \exp\left(-2\theta^2/\theta_0^2\right) \exp\left(-2y^2/h_0^2\right) \tag{8.17}$$

where h_0 is the Gaussian effective height of the slab, θ_0 is the effective Gaussian angular width of the input/output waveguide and is given by [5]

$$\theta_0 = \frac{\lambda}{\pi n_{\mathrm{eff}}(\mathrm{slab})\, w_0} \tag{8.18}$$

where w_0 is the Gaussian effective width of the waveguide at the slab edge. In order to avoid excessive crosstalk, the nominal value for the output waveguide pitch $\Lambda_i = 3.5 w_0$ is chosen. Knowing the angular dispersion and Λ_i, the focal length of the output mirror can be found

$$f = \frac{\Lambda_i/2}{\sin\left(\left|\partial\eta/\partial\lambda\right|\delta\lambda/2\right)} \approx \frac{3.5 w_0}{\left|\partial\eta/\partial\lambda\right|\delta\lambda} \tag{8.19}$$

where $\delta\lambda$ is channel spacing. Knowing the focal length, and restricting the mirror aperture to $2\theta_0$, the minimum output aperture size will be

$$L = 2f \sin 2\theta_0 \tag{8.20}$$

or using Eq. (8.19),

$$L_{\min} \approx \frac{7\lambda}{\left(\left|\partial\eta/\partial\lambda\right|\delta\lambda\right) n_{\mathrm{eff}}(\mathrm{slab})\,\pi} \tag{8.21}$$

The selected aperture size will truncate the field amplitude at 1.8% of its peak value, producing negligible theoretical cross talk [6]. While the minimum output aperture size (or the output size of the prism) is restricted by the angular dispersion and the channel spacing, the real aperture size needs to take the group velocity dispersion into account.

For the i^{th} channel, the output beam extension on the output prism side l_{2i} is related to the input length of the prism l_1 via

$$m_i = \frac{l_{2i}}{l_1} = \frac{\cos\varphi'_{2i}}{\cos\left(\rho + \varphi'_{2i}\right)} \tag{8.22}$$

where ρ is the prism apex angle (see Figure 8.4.1). The input and output beam widths, L_1 and L_{2i} are related by the following equation (see Figure 8.4.2)

$$M_i = \frac{L_{2i}}{L_1} = \frac{\cos\varphi_1}{\cos\varphi_{4i}} \cdot \frac{l_{2i}}{l_1} = \frac{\cos\varphi_1}{\cos\varphi_{4i}} m_i \tag{8.23}$$

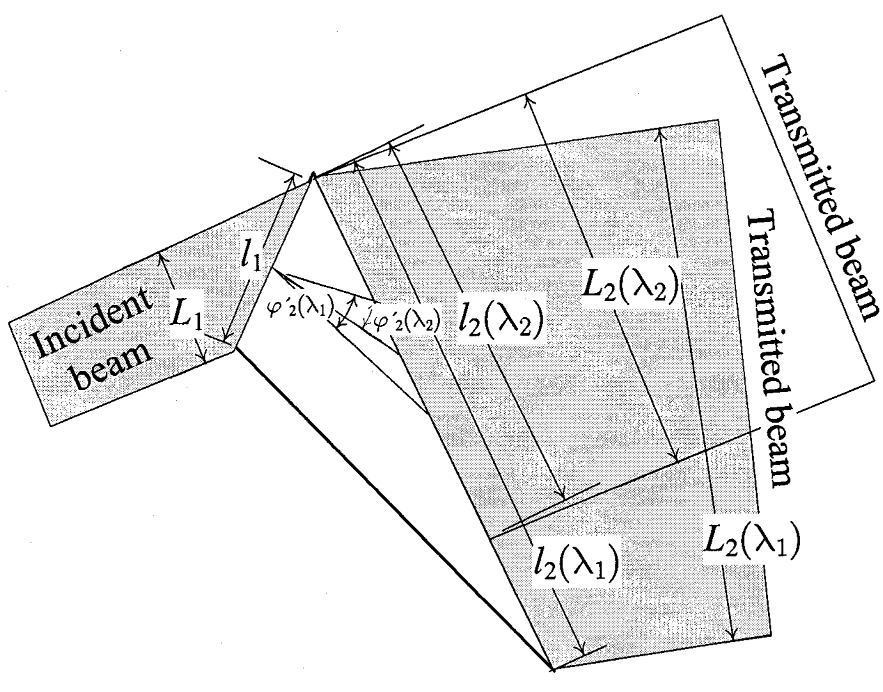

Figure 8.4.2 Relationship between prism facets and beam size that results in a minimum prism area

Note that at any specific incident angle (φ_1) the fraction in Eq.(8.23) is a function of wavelength because of implicit dependence of phase and group velocity dispersion in photonic crystal on operative point The minimum and the maximum of this coefficient play an important role in the design; let us define them as $M_{\min}$ and $M_{\max}$ respectively at the corresponding transmission angle of $\varphi_{4\min}$ and $\varphi_{4\max}$ (see Figure 8.4.1). In order that the prism facets are sufficiently large to cover the beam width and maintaining the required wavelength resolution, the input aperture size has to be greater than

$$L_{1\min} = \frac{L_{\min}}{M_{\min}} \tag{8.24}$$

where $L_{\min}$ is obtained from Eq.(8.21). Note that both $L_{\min}$ (because of phase velocity dispersion) and $M_{\min}$ (because of group velocity dispersion) are functions of wavelength, and the its maximum has to be found over all channels. Also the output aperture size has to be greater than

$$L_{2\min} = M_{\max} L_{1\min} \tag{8.25}$$

In the above equation, $M_{\max}$ is a function of wavelength and its maximum has to be obtained over all channels. The input and output prism facets have to be greater than

$$l_{1\min} = \frac{L_{1\min}}{\cos\varphi_1}, \quad l_{2\min} = \frac{L_{2\min}}{\cos\varphi_{4\max}} \tag{8.26}$$

The minimum prism area accommodating the beam extension only can be written as

$$S = \sin\rho \frac{l_{1\min} \times l_{2\min}}{2} \tag{8.27}$$

Or using Eqs (8.26), (8.24), (8.23) and (8.22), we have

$$\begin{aligned} S_{\min} &= L_{\min}^2 \left(\frac{M_{\max}}{M_{\min}^2} \right) \frac{\sin\rho}{2\cos\varphi_1 \cos\varphi_{4\max}} \\ &= \frac{L_{\min}^2 \sin\rho \times \cos\varphi_1 \times \cos\left(\rho + \varphi'_{2\max}\right)}{2\cos^2\varphi_{4\min} \times \cos^2\left(\rho + \varphi'_{2\min}\right)} \end{aligned} \tag{8.28}$$

Where we have neglected the variation of $L_{\min}$ with the wavelength. Assuming narrow spectral range as is typical for such applications, we can assume $\varphi_{4\min} \approx \varphi_4$, and assume group velocity angular dispersion at the input facet of the prism as $\partial\varphi_2'/\partial\lambda$, then

$$\varphi_{2\max}' = \varphi_{2\min}' + N\delta\lambda \left|\partial\varphi_2'/\partial\lambda\right| \tag{8.29}$$

Where N is the number of channels. Assuming $\left|\varphi_{2\min}'\right| \gg \left|N\delta\lambda\left(\partial\varphi_2'/\partial\lambda\right)\right|$ and applying these approximations into Eq.(8.28), we have

$$S_{\min} = \frac{L_{\min}^2 \sin\rho \times \cos\varphi_1 \times \left[1 + \tan\left(\rho + \varphi_{2\min}'\right) N\delta\lambda \left|\partial\varphi_2'/\partial\lambda\right|\right]}{2\cos^2\varphi_4 \times \cos\left(\rho + \varphi_{2\min}'\right)} \tag{8.30}$$

The role of group angular dispersion is clear through the factor $\partial\varphi_2'/\partial\lambda$. In the cases that $\tan\left(\rho + \varphi_{2\min}'\right) N\delta\lambda \left|\partial\varphi_2'/\partial\lambda\right| \gg 1$, we may further simplify Eq. (8.30) to

$$S_{\min} \approx \frac{N^2}{\Delta\lambda} \frac{\left|\partial\varphi_2'/\partial\lambda\right|}{\left|\partial\eta_p/\partial\lambda\right|^2} \frac{49\lambda^2 \sin\rho \times \cos\varphi_1 \times \sin\left(\rho + \varphi_{2\min}'\right)}{2\pi^2 n_{\mathrm{eff}}^2(\mathrm{slab}) \cos^2\varphi_4 \times \cos^2\left(\rho + \varphi_{2\min}'\right)} \tag{8.31}$$

Where Eq. (8.21) has also been used, and $\Delta\lambda = N\delta\lambda$ is the desired spectral window (total device bandwidth). Although the prism area increases due to group velocity dispersion, it reduces by the square of the phase velocity dispersion. The prism area scales quadratically with the number of channels. This scaling law is an interesting feature of **k**-vector superprism when compared to the fourth power for the **S**-vector superprism [7]. This feature shows that **k**-superprism is more suitable for higher count demultiplexers (over a specific spectral window).

Eqs.(8.24), (8.25) and Eq. (8.20) can be used to design the input and output mirrors. The output mirror profile can be optimized to reduce the effect of coma on the side channels (due to lateral displacement of the beam at the output side of the prism because of group velocity dispersion).

8.5 Apex and slant angles

In this section we introduce a means to expand the input beam width tremendously, so the minimum output aperture size of Eq.(8.21) can be achieved by a reduced input aperture size.

The result would be a significant reduction in the prism size. We restrict ourselves to operating points in the second Brillouin zone.

Consider the un-slanted photonic crystal with the operating point well inside the second Brillouin zone (see Figure 8.2.2c). As is seen in Figure 8.2.2c, the reflected beam makes the angle of $\sim \rho'/2$ with the interface, where ρ' is the asymptotic wave vector bend angle. So in this case if we choose the apex angle of the prism as $\rho = \rho'/2$, the beam inside photonic crystal will be parallel to the opposite interface of the prism (see Figure 8.5.1).

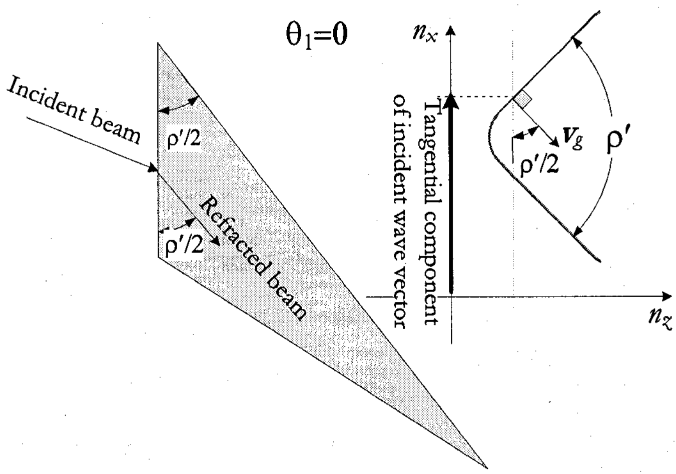

Figure 8.5.1 The refracted beam angle for a photonic crystal with the asymptotic wave vector bend angle of ρ' and the prism of apex angle $\rho = \rho'/2$, the lattice in the prism region is un-slanted $\theta_1 = 0$.

If we choose $\rho > \rho'/2$, then the beam first hits the base of the prism before the opposite side, but if we choose $\rho < \rho'/2$ the beam is expanded and hit the opposite side first (as we wanted). The beam expansion can be large, if ρ is chosen near $\rho'/2$. Alternately, one may keep $\rho = \rho'/2$ and try to slant the photonic crystal to use this phenomenon. The later situation is depicted in Figure 8.5.2. Both cases of positive and negative slant angles are feasible. Note that we have chosen the lattice parameters in order to have a small bandgap this fact places a restriction on the slant angle, i.e [8],

$$\theta_{1\max} = \tan^{-1}\left(\frac{n_{z0}}{n_{\text{eff}}(\text{slab})\sin\varphi_{1d}}\right) \tag{8.32}$$

We continue this chapter with the later alternative, *i.e.*, we assume $\rho = \rho'/2$ as a constant for all lattice types however we use θ_1 as a variable.

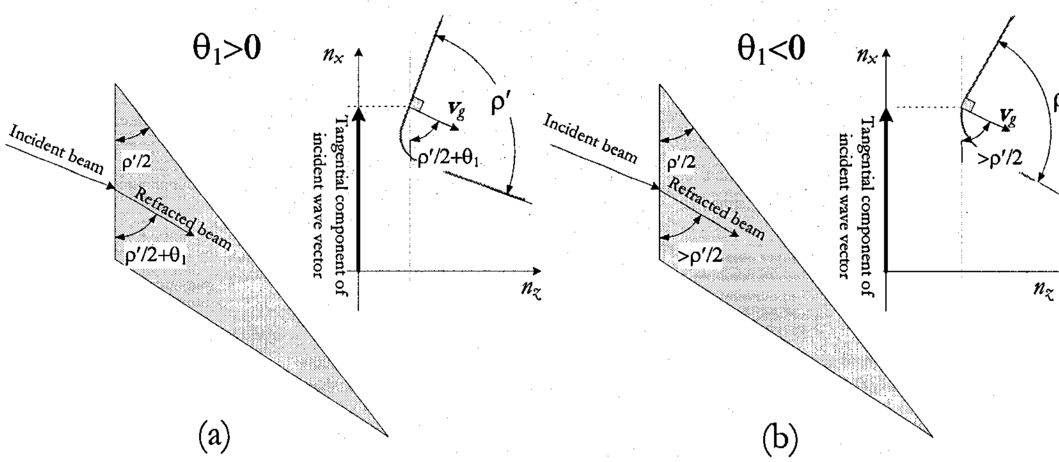

Figure 8.5.2. The refracted beam angle for a photonic crystal with the asymptotic wave vector bend angle of ρ' and the prism apex angle of $\rho = \rho'/2$, the lattice is slanted by θ_1 which is usually a small angle.

As can be seen from Figure 8.5.2, if we choose $\theta_1 > 0$, then in order to have refracted angle greater than $\rho'/2$, we have to chose the operating point deep into second Brillouin zone. But the drawback is that the dispersion will be lost as the operating point gets farther from the bandedge (the boundary of the first and the second Brillouin zone). However in the second case of $\theta_1 < 0$, the condition is satisfied if we makes the operating point nearer to the bandedge (where the wave vectors are far from their asymptotes too).

8.6 Numerical illustration

To provide a specific illustration, we design a 32 channel DWDM demultiplexer starting at $\lambda_{41} = 1537.40$ nm and ending at $\lambda_{11} = 1562.23$ nm (where indices are the ITU grids numbers). The channel spacing is 100GHz (or ~ 0.8 nm). We have tried in section 2 to select photonic crystal parameters suitable for the **k**-vector superprism (that also makes the comparison feasible). Using these selections and fixing the apex angle to $\rho = \rho'/2$, we vary the slant angle θ_1 and for each slant angle we seek to find the incidence angle (φ_1) that minimizes the prism area (whilst respecting all other constraints). Based on the photonic crystal parameters of Table 8.1 with minimum prism area as a figure of merit, the optimum superprism design parameters are provided in the Table 8.2.

Table 8.2 The optimum **k**-vector superprism parameters for various lattice types

Parameters	**1-D**	**2-D square**	**2-D hexagonal**
Slant angle $\theta_1\,(^\circ)$	-10.40	-8.25	-7.20
Apex angle $\rho\,(^\circ)$	57.5	45	30
Incident angle $\varphi_1\,(^\circ)$	62.13	60.51	60.55
Deviation angle $\eta\,(^\circ)$	39.61	36.99	32.17
Input aperture size $L_1\,(\mu m)$	4.94	11.16	22
Output aperture size $L_2\,(\mu m)$	1622	833.7	658
Input prism size $l_1\,(\mu m)$	10.56	22.67	44.77
Output prism size $l_2\,(\mu m)$	2227	1315	1290
Minimum Prism area $S_{min}\,(\mathrm{mm}^2)$	0.0099	0.0105	0.0114

As the results of the above table indicate, the minimum area of the superprism is around $0.01\ \mathrm{mm}^2$. The smallest superprism is 1-D, followed closely by 2-D square and then comes 2-D hexagonal (by about 45% greater than the smallest area). The operating points in all cases are located at the second Brillouin zone, where the dispersion is higher.

The optimization routine by minimizing the superprism area finds the condition that maximizes the phase velocity dispersion and minimizes the group velocity dispersion as much as possible. Comparing different photonic crystals in this regard, the best photonic crystal is the one with maximum phase velocity and minimum group velocity (see Eq.(0.31)). But these are contradictory requirements. *i.e.*, photonic crystals that show high phase velocity dispersion (such as the hexagonal lattice) usually show high group velocity dispersion too (see Figure 8.2.5). Interestingly enough, the slab 1-D photonic crystal wins the race with the minimum phase velocity and group velocity dispersions.

8.7 Discussion

The smallest superprism area is achieved by minimizing the group velocity dispersion and maximizing the phase velocity dispersion at the same time. The magnitude of the beamwidth expansion factor (Eq.(8.23)) is an inverse indication of the degree of group velocity dispersion. As we expected the 1-D photonic crystal with the lowest group velocity dispersion must have the largest beamwidth expansion factor. Figure 8.7.1 shows the beamwidth expansion factor versus the multiplexer channels for various photonic crystals. The multiplexers' parameters are adopted from Table 8.2. The beamwidth expansion factor together with associated phase velocity dispersion are two factors determining the superprism area. Indeed the benefit that the 1-D photonic crystal gets from the beamwidth expansion factor compensates the smallness of its phase velocity dispersion. As the combined result shows, the 1-D photonic crystal provides the smallest superprism area. The 2-D square lattice by having lower beamwidth expansion factor but having higher phase velocity dispersion, provides a minimum superprism area nearly the same as the 1-D case. But 2-D hexagonal lattice that has the lowest beamwidth expansion factor cannot reach 1-D case even with its highest phase velocity dispersion.

The various channels, besides of having various beamwidth, have been directed in different directions (due to phase velocity dispersion) and have been shifted along the output prism facet (due to group velocity dispersion). Considering the proposed structure of Figure 8.1.1, these factors will lead to increased aberration in the output image.

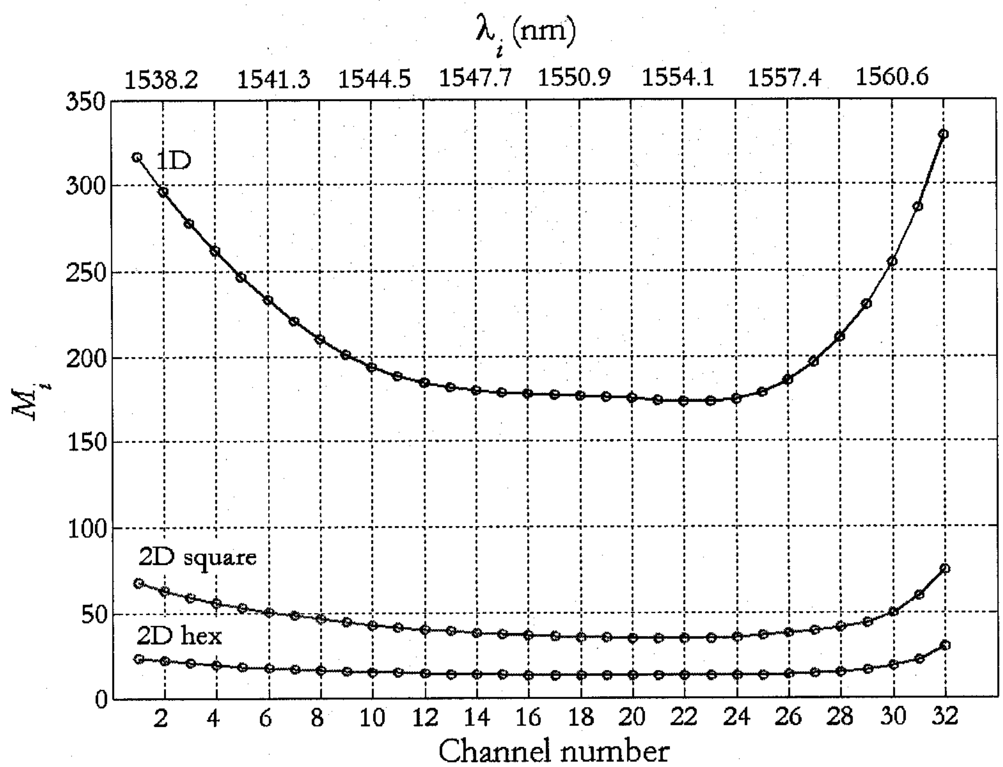

Figure 8.7.1, The beamwidth expansion factor for various superprism design of Table 8.2

Phase velocity dispersion which is achievable near the band edge may be substantial, but there is no guarantee of uniformity over the window of interest, especially if the window is relatively large. Figure 8.7.2 shows how the angular dispersion versus the multiplexer channel numbers (or versus wavelength in the desired window of spectrum). Given that we need to demultiplex onto the standard DWDM grid, we need to compensate this non-uniformity. The easiest way to do this is to make the output channel spacing non-uniform [1]. It is interesting that 1-D case shows the most uniform phase velocity dispersion however small.

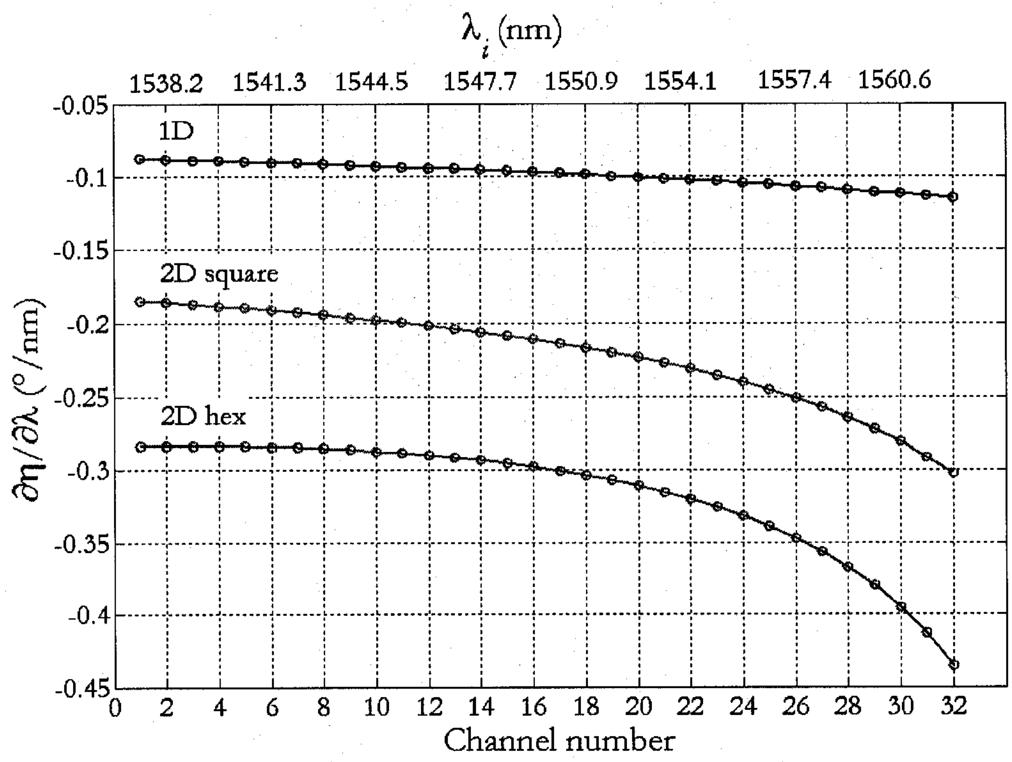

Figure 8.7.2. Angular dispersion as a function of channel number for the devices specified in Table 8.2

There are many sources of loss in this system, some of which could be mitigated. Side wall roughness and pattern uniformity of the photonic crystal structure have to be kept as small as possible. It has been shown that for the minimum feature size of 300 nm, the scattering loss of a ridge waveguide can be small (3.38 dB/mm)[9]. It has also been shown that the loss in 2-D photonic crystal waveguides (with a feature size of 120 nm) using SOI technology is low (3.5 dB/mm) [10] and is mostly due to fabrication imperfections, which also introduce similar loss in ridge waveguides [10;11].

Some of the fabrication imperfection losses can be minimized for 1-D photonic crystal case by aligning the lattice lines along the raster lines on the electron beam writer, then the patterns could be written much more smoothly via electron beam lithography. In this way, the photonic crystal side wall roughness which is an important source of scattering loss would be smaller. This task can be done on the mask level, as we have done in chapter 10.

Considering the absence of lateral mode confinement in our proposed structure, we therefore expect to obtain less scattering loss through the superprism region than has been previously reported for ridge waveguides. Substrate leakage loss can also be minimized by choosing thick enough substrates. Nevertheless considering the small size of the superprism, the main source of loss (also being a matter of concern to others [12]) is the beam coupling into and out of the photonic crystal to the free space propagation regions (the slab regions). Maximizing dispersion usually involves working near the band edge, where reflection is usually high. Approaches such as smoothing the transition by small airholes or projected airholes [13] have been explored for slab 2-D photonic crystals in order to maximize transmission into photonic crystals. Similar techniques together with adding a buffer layer which can act as an antireflection coating could be further explored. We have not yet attempted to calculate the coupling loss for this structure due to the absence of a suitable 3-D modeling technique that would be tractable for this relatively large structure and high index contrast.

8.8 Conclusion

In this chapter a complete optical design of a demultiplexer based on photonic crystal **k**-vector superprism has been proposed. A base for comparison among various photonic crystals has been introduced. We select parameters for three different photonic crystals which is a suitable choice for making the **k**-vector superprism and also make a comparison feasible. We have developed design equation for **k**-vector superprism. We have discussed various operating point on the group velocity dispersion and show that there is a great advantage to work in the second Brillouin zone and select the parameters so the beam width expand through phonic crystal. Exploiting the beam expansion capability of the prism, an optimal design has been obtained that maximizes the phase velocity dispersion and minimizing the group velocity dispersion as much as possible. The optimum design adjusts the prism area to just fit the path of the beam through the prism within a margin. The 1-D photonic crystal has the smallest superprism area of 99,200 μm^2, which provides sufficient resolution to demultiplex 32 channels in the *C* band with a 0.8 nm (100Ghz) channel spacing. The 2-D square lattice is very close to the smallest size, while the best 2-D hexagonal superprism is larger by 45% compared to the 1-D counterpart. The desired situation of having small superprism area consists of having maximum phase and minimum group velocity dispersion seem contradictory. It is in this context that 2-D hexagonal with high dispersion (both phase and group) has the largest superprism area. We have also shown that in the linear regime, the superprism area is a quadratic function of channel count. Finally we have addressed dispersion non-uniformity and have shown that 1-D photonic crystal is the most uniform one.

References

[1] A . Bakhtazad and A. G. Kirk, "1-D slab photonic crystal **k**-vector superprism demultiplexer: analysis, and design," *Optics Express*, vol. 13, no. 14, pp. 5472-5482, July2005.

[2] C . Y. Luo, M. Soljacic, and J. D. Joannopoulos, "Superprism effect based on phase velocities," *Optics Letters*, vol. 29, no. 7, pp. 745-747, Apr.2004.

[3] Z engerle R., "Light propagation in single and doubly periodic planar waveguides," *Journal of Modern Optics*, vol. 34, no. 12, pp. 1589-1610, 1987.

[4] M . Gerken and D. A. B. Miller, "Relationship between the superprism effect in one-dimensional photonic crystals and spatial dispersion in nonperiodic thin-film stacks," *Optics Letters*, vol. 30, no. 18, pp. 2475-2477, Sept.2005.

[5] U nger H.G., *Planar Optical Waveguides and fibers* Oxford, UK, Clarendon Press, 1977.

[6] O kamoto Katsunari, "Planar Lightwave Circuits," in *Fundamentals of Optical Waveguides* Academic Press, 2000, pp. 341-400.

[7] B . Momeni and A. Adibi, "Systematic design of superprism-based photonic crystal demultiplexers," *Ieee Journal on Selected Areas in Communications*, vol. 23, no. 7, pp. 1355-1364, July2005.

[8] A . S. Jugessur, A. Bakhtazad, A. G. Kirk, L. Wu, T. F. Krauss, and R. M. De la Rue, "Compact and integrated 2-D photonic crystal super-prism filter-device for wavelength demultiplexing applications," *Optics Express*, vol. 14, no. 4, pp. 1632-1642, Feb.2006.

[9] P . Dumon, W. Bogaerts, V. Wiaux, J. Wouters, S. Beckx, J. Van Campenhout, D. Taillaert, B. Luyssaert, P. Bienstman, D. Van Thourhout, and R. Baets, "Low-loss SOI photonic wires and ring resonators fabricated with deep UV lithography," *Ieee Photonics Technology Letters*, vol. 16, no. 5, pp. 1328-1330, May2004.

[10] A . Jafarpour, E. Chow, C. M. Reinke, J. Huang, A. Adibi, A. Grot, L. W. Mirkarimi, G. Girolami, R. K. Lee, and Y. Xu, "Large-bandwidth ultra-low-loss guiding in bi-periodic

photonic crystal waveguides," *Applied Physics B-Lasers and Optics*, vol. 79, no. 4, pp. 409-414, Sept.2004.

[11] T . Baba, A. Motegi, T. Iwai, N. Fukaya, Y. Watanabe, and A. Sakai, "Light propagation characteristics of straight single-line-defect waveguides in photonic crystal slabs fabricated into a silicon-on-insulator substrate," *Ieee Journal of Quantum Electronics*, vol. 38, no. 7, pp. 743-752, July2002.

[12] T . Matsumoto and T. Baba, "Photonic crystal **k**-vector superprism," *Journal of Lightwave Technology*, vol. 22, no. 3, pp. 917-922, Mar.2004.

[13] T . Baba and D. Ohsaki, "Interfaces of photonic crystals for high efficiency light transmission," *Japanese Journal of Applied Physics Part 1-Regular Papers Short Notes & Review Papers*, vol. 40, no. 10, pp. 5920-5924, Oct.2001.

Chapter 9

LENS DESIGN WITH SLAB 1-D PHOTONIC CRYSTAL

An aspheric collimating slab waveguide lens is designed using a diverging slab 1-D photonic crystal. An approximation method for analysis of such structures has been developed. A lens design procedure (which minimizes area) is also introduced. For illustration purposes, we use Silicon on insulator technology with the minimum feature size of 100 nm. We show that a fast lens with 130 μm focal length, $f/\# = 1.3$ is achievable with an etching area of only 658 μm^2.

9.1 Introduction

There are numerous optical devices which require some form of focusing element to influence the propagation of an optical beam. In particular, a lens which can focus the optical signal into planar lightwave circuit waveguides may find application in micro-opto-electromechanical (MOEM) switches, alignment of waveguides to fiber optic terminations, and the integration of planar light wave circuits with photodetectors and laser diodes. More specifically we are interested to design a collimating lens for a superprism with makes use of the engineered dispersion of slab photonic bandgap materials for very small multiplexers [1]. We have shown recently that a superprism can be realized with a slab 1-D photonic crystal structure [2].

There is a lot of interest in light propagation in photonic crystals. The light propagation in a photonic crystal is governed by its dispersion surface (for 1-D photonic crystals, the wave vector diagram), which corresponds to the index ellipsoid in conventional crystalline optics. Anomalous dispersion near the band gaps leads to the superprism phenomenon which is based on the super dispersion observed in this region of the band diagram [1]. The curvature of the band diagram (or in 1-D case wave vector diagram) also makes the collimation of light possible when the structure is designed correctly, such that the wave front encounters different parts of the band diagram in a given way [3]. Wavefront refraction through non-uniform anisotropic media can be modeled by matching the phase velocity normal to the gradient of the inhomogeneity at each step and propagating along the local group velocity to the next point. This process generally can be described by the solution of Hamiltonian equation [4]. In general, even if collimated rays propagate through photonic a crystal, their phase velocity direction is not collimated. It means that as soon as the rays leave the photonic crystal, the collimation is destroyed. This fact makes wavefront engineering using a quasi-periodic photonic crystal a difficult task.

Our approach for controlling the wavefront using a quasi-periodic photonic crystal is to maintain the group and phase velocities in the same direction inside the photonic crystal. In the 1-D photonic crystal wave diagram there is a unique point which possesses the property that group and phase velocities are in the same direction regardless of the period. Figure 9.1.1 shows a typical wave vector diagram for a slab 1-D photonic crystal for different grating periods. Points A are the points where the incident wave vector is parallel to 1-D photonic crystal grooves (wave vector normal to the grating vector). There is also points B, with the same property, however, there are periods where point B is on the band gap region, or the modes belong to the second band. We restrict ourselves in this appendix to points A. The change of n_z versus grating period at points A provides us with a unique opportunity to design a special kind of graded index (GRIN) lens, which is very difficult to achieve in other ways [5;6].

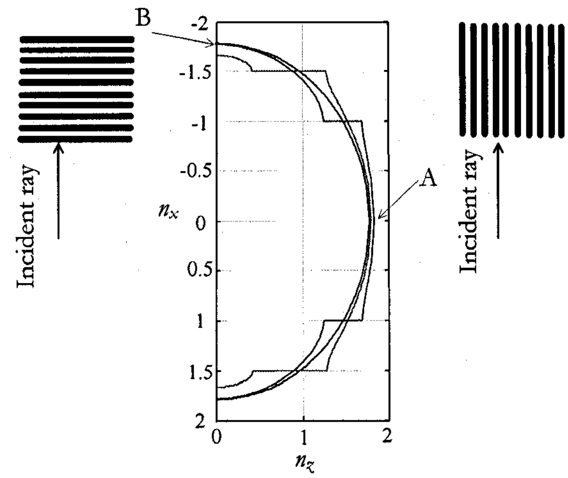

Figure 9.1.1 A typical normalized wave vector diagram for a 1-D photonic crystal at different wavelengths

When considering a collimator, the need to have 1-D photonic crystal lines parallel to the rays emitted from a point source means that the photonic crystal must be quasi-periodic in direction of the ray. For a diverging ray, we need a diverging photonic crystal. Figure 9.1.2 shows a schematic of such a structure; a diverging slab 1-D photonic crystal spreading along an arc of circle of center o with radius ρ. In section two we review the radial effective index method which we have developed to handle such structures.

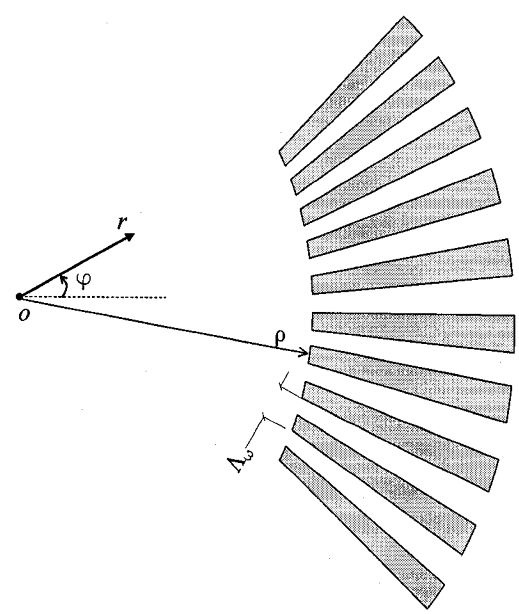

Figure 9.1.2. Schematic representation of a diverging photonic crystal

Mode-index (also called homogenous refracting) waveguide lenses have been proposed since the earliest days of integrated optics [7]. In homogeneous thin-film lenses, guided light is refracted at the boundary between two regions of disparate waveguides. It can be shown that Snell's law is applicable if one uses the effective refractive index of the propagating mode instead of the refractive index of the guide material. It follows that classical lens design techniques can also be used in the design of waveguide lenses.

As we will show in section two, maintaining the period of the diverging 1-D photonic crystal (see Figure 9.1.2) along the azimuthal (φ) direction, the effective refractive index only varies slowly in the radial direction. Since the radial profile cannot be engineered, limiting the design to a constant period along the azimuthal direction places a limitation on the lens design. Dropping the restriction of a constant period in this axis allows the effective refractive index to be controlled in the azimuthal direction. It is interesting to note that this kind of lens cannot be categorized as either an axial or a radial GRIN lens. The conventional radial GRIN lens has a radial refractive index around $\varphi = 0$, and no variation along $\varphi = 0$ line. On the other hand axial GRIN lenses have a variable refractive index along $\varphi = 0$ direction, but have no radial variation around $\varphi = 0$ axis. This has required us to develop a new lens design technique for this structure.

9.2 Radial effective index method

The radial effective index method has been developed in order to model a wave propagating in a diverging slab 1-D photonic crystal. The cross section of a unit cell of a diverging 1-D photonic crystal is depicted in Figure 9.2.1.

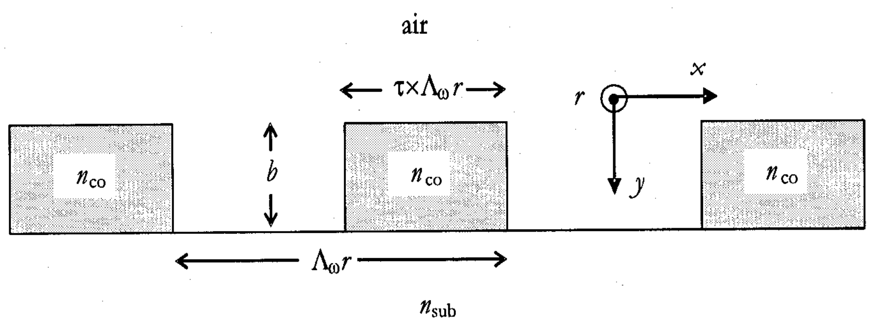

Figure 9.2.1 The cross section refractive index distribution of each core

We must solve the three dimensional Helmholtz equation directly. The radial effective index method combines the two previously developed methods. First the conventional effective index method is applied to obtain an equivalent vertical slab waveguide and then the azimuthal effective index method [8] is used for r and φ directions. The scalar Helmholtz equation in circular cylindrical coordinates considering z variation into account is as follows

$$\frac{\partial^2 U}{\partial r^2}+\frac{1}{r}\frac{\partial U}{\partial r}+\frac{1}{r^2}\frac{\partial^2 U}{\partial \varphi^2}+\frac{\partial^2 U}{\partial z^2}+k_0^2 n^2(\varphi,z)U=0 \tag{9.1}$$

where $n^2(\varphi,z)$ is the index distribution of the guide in circular cylindrical coordinates. We propose a solution of the form

$$U(r,\varphi,y)=F(y)\Psi(r,\varphi) \tag{9.2}$$

The first is a function of y exclusively, and the second is a function of r and φ. Substituting the above solution into Eq.(9.1) and grouping terms, we can obtain

$$F\left(\frac{\partial^2 \Psi}{\partial r^2}+\frac{1}{r}\frac{\partial \Psi}{\partial r}+\frac{1}{r^2}\frac{\partial^2 \Psi}{\partial \varphi^2}+k_z^2\Psi\right)+\frac{\partial^2 F}{\partial y^2}\Psi+k_0^2 n^2 F\Psi-k_y^2 F\Psi=0 \tag{9.3}$$

where we have added and subtracted $k_z^2 F\Psi$ from the equation. Now similarly to the familiar effective index methods, we multiply both sides of the above equation into $r\Psi(r,\varphi)$ and integrate with respect of r and φ to get

$$\frac{d^2F}{dy^2}+\left(k_0^2 n_{\text{eff}}^2(y)-k_y^2\right)F=0 \tag{9.4}$$

where

$$n_{\text{eff}}^2(y)=\frac{\frac{1}{k_0^2}\int_0^\infty\int_0^{2\pi}\left(r\Psi\frac{\partial^2\Psi}{\partial r^2}+\Psi\frac{\partial\Psi}{\partial r}+\frac{\Psi}{r}\frac{\partial^2\Psi}{\partial\varphi^2}+k_y^2|\Psi|^2 r\right)d\varphi dr+\int_0^\infty\int_0^{2\pi}n^2|\Psi|^2 r d\varphi dr}{\int_0^\infty\int_0^{2\pi}|\Psi|^2 r d\varphi dr} \tag{9.5}$$

Eq. (9.4) can be considered as a one-dimensional Helmholtz equation for a horizontal slab waveguide with refractive index distribution given by Eq. (9.5). As a first approximation, we assume $\Psi(r,\varphi)=r^{-1/2}\exp\left(ik_z r\right)\Phi(r,\varphi)$ where $\Phi(r,\varphi)$ is one in the core regions and zero elsewhere. It is a guess based on the far-field circular wave propagation, which is taken for the wave pattern in this direction. Then ignoring some negligible terms, Eq.(9.5) will be the refractive index distribution of a three-layer horizontal slab dielectric waveguide. The structure of this equivalent waveguide is shown in Figure 9.2.2.

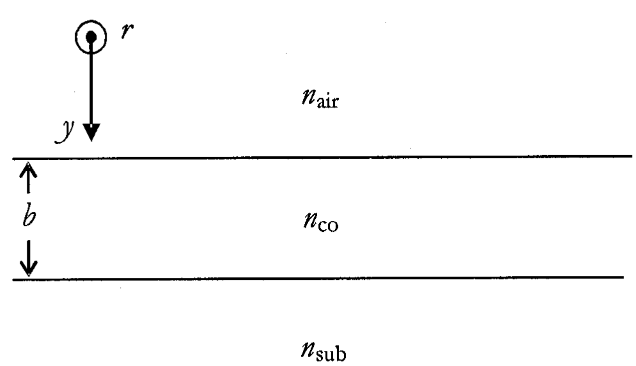

Figure 9.2.2 The equivalent horizontal dielectric waveguide in z direction

Similarly multiplying both sides of Eq.(9.3) into F and integrating with respect to y, we have

$$\frac{\partial^2\Psi}{\partial r^2}+\frac{1}{r}\frac{\partial\Psi}{\partial r}+\frac{1}{r^2}\frac{\partial^2\Psi}{\partial\varphi^2}+k_0^2 n_{\text{eff}}^2(\varphi)\Psi=0 \tag{9.6}$$

where

$$n_{\text{eff}}^2(\varphi)=\frac{\frac{1}{k_0^2}\int_{-\infty}^{+\infty}\frac{\partial^2 F}{\partial y^2}F^* dy+\int_{-\infty}^{+\infty} n^2|F|^2 dy}{\int_{-\infty}^{+\infty}|F|^2 dy} \tag{9.7}$$

Eq.(9.6) can be considered as a scalar Helmholtz equation for radial wave propagation in cylindrical waveguide. Note that although there is no y variation, however the propagation is along r-axis. Eq.(9.7) gives the equivalent refractive index distribution of the structure. Similarly as a first approximation to get $n_{\text{eff}}(\varphi)$, we take $F(z)$ to be one in the core region b (see Figure 9.2.1) and zero elsewhere.

The azimuthal effective index method tries to solve Helmholtz equation in the circular cylindrical coordinates. We suggest the solution of the form [8]

$$\Psi(r,\varphi)=\mathrm{R}(r)\Phi(r,\varphi) \tag{9.8}$$

We take the first function $\mathrm{R}(r)$ as a function of r exclusively, and the second $\Phi(r,\varphi)$ as a function of r and φ. Again, we perturb the refractive index distribution in order to make it suitable for the suggested solution. Indeed we do our perturbation in a way that the above solution be the exact solution of the new perturbed waveguide. Substituting Eq.(9.8) into Eq.(9.6) and grouping terms, we can obtain

$$\frac{1}{\mathrm{R}}\frac{d^2\mathrm{R}}{dr^2}+\frac{1}{\mathrm{R}r}\frac{d\mathrm{R}}{dr}+\frac{1}{r^2\Phi}\frac{\partial^2\Phi}{\partial\varphi^2}+k_0^2\left(n^2(\varphi)+n_{\text{pert}}^2\right)=0 \tag{9.9}$$

where

$$n_{\text{pert}}^2=\frac{1}{k_0^2}\left(\frac{1}{\Phi}\frac{\partial^2\Phi}{\partial r^2}+\frac{1}{r\Phi}\frac{\partial\Phi}{\partial r}+\frac{2}{\mathrm{R}\Phi}\frac{d\mathrm{R}}{dr}\frac{\partial\Phi}{\partial r}\right) \tag{9.10}$$

The first two terms of Eq.(9.9) are functions of r exclusively. We define them such that they are equal to $-k_{\text{eff}}^2(r)$. This function acts as a separation function and Eq.(9.9) can be written as two components

$$\frac{\partial^2\Phi}{\partial\varphi^2}+\left\{r^2\left[k_0^2\left(n^2(\varphi)+n_{\text{pert}}^2\right)-k_{\text{eff}}^2\right]\right\}\Phi=0 \tag{9.11}$$

$$\frac{d^2 R}{dr^2}+\frac{1}{r}\frac{dR}{dr}+k_0^2 n_{\text{eff}}^2(r)R=0 \tag{9.12}$$

where we define

$$n_{\text{eff}}^2(r)=\frac{k_{\text{eff}}^2(r)}{k_0^2} \tag{9.13}$$

Now we assume that Φ varies very slowly along r. This means that, Eq.(9.11) can be solved assuming r to be constant, and n_{pert}^2 (Eq.(9.10)) can be neglected. Then for a given r, the partial differential equation (9.11) can be replaced by an ordinary one as

$$\frac{d^2\Phi}{r^2 d\varphi^2}+\left[k_0^2 n^2(\varphi)-k_{\text{eff}}^2\right]\Phi=0 \tag{9.14}$$

The above equation is the equation of the field in a one-dimensional slab whose index $n^2(\varphi)$ repeats itself periodically along φ with period 2π. For the waveguide of Figure 9.1.2 , Eq.(9.14) represents a multilayer dielectric waveguide. Figure 9.2.3 shows a schematic of this waveguide. A solution of the wave equation (9.14) can be obtained using the transfer matrix method (see for example [9]). The field Φ must also repeat itself with period 2π. Usually 2π is not a multiple of Λ_ω, however since $\Lambda_\omega \ll 2\pi$, the mismatch can be ignored.

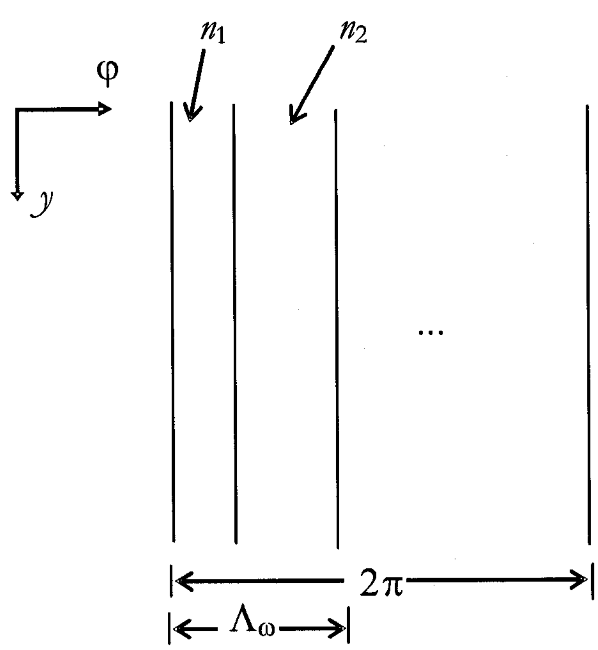

Figure 9.2.3 One period of the equivalent waveguide in φ direction.

The solution of Eq.(9.14) yields a value for k_{eff}^2/k_0^2 which is the effective index of the cylindrical sheet of radius r (see Eq.(9.13)). The known value of $n_{\text{eff}}^2(r)$ can be substituted in Eq.(9.12), which describes the circular-symmetric field of a cylindrical guide whose circular symmetric index $n_{\text{eff}}^2(r)$ varies only in the radial direction. For the waveguide of Figure 9.1.2, if we evaluate $n_{\text{eff}}^2(r)$ at discrete r it will be a multi-shell circular cylindrical structure (see Figure 9.2.4)

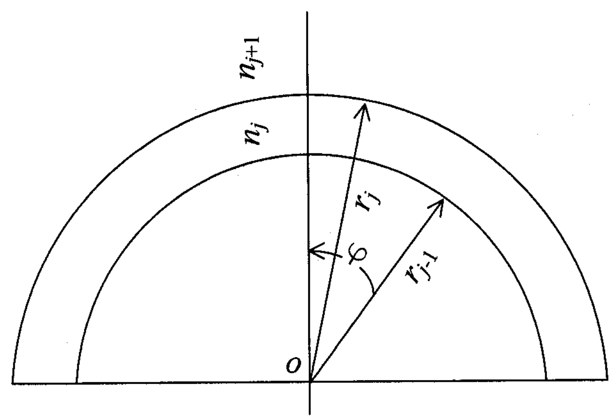

Figure 9.2.4. The equivalent stratified media in r direction.

If we assume that $n_{\text{eff}}^2(r)$ does not vary with r rapidly, then it can be shown that the following analytic approximation is suitable [10]

$$R(r)=C\sqrt{\frac{\sigma(r)}{r\,n_{\text{eff}}(r)}}\;\mathrm{H}_0^{(1)}\left[\sigma(r)\right] \tag{9.15}$$

where $\sigma(r)$ is the optical path length,

$$\sigma(r)=\int_0^r k_0 n_{\text{eff}}(r)\,dr \tag{9.16}$$

and C is a constant and $\mathrm{H}_0^{(1)}$ is the Hankel function of the first kind of order zero. Since r is usually taken to be much greater than wavelength, the exponential asymptotic approximation of the Hankel function can be used, so the r dependency can be reduced to a simple form

$$R(r)=\frac{C'}{\sqrt{k_0\,r\,n_{\text{eff}}(r)}}\exp\left[i\sigma(r)\right] \tag{9.17}$$

where C' is another constant. It is expected that $n_{\text{eff}}(r)$ is very smooth function of *r*.

9.3 Collimating waveguide lens

In this section we illustrate our approach to design a lens for converting the radiation field emitted by a waveguide into the slab region into planar wave front (expanding the beam width). Using the Gaussian approximation for the far field pattern of a rectangular dielectric waveguide in the slab region, the optical intensity can be written as

$$I(r,\varphi,y)=\frac{2I_0}{\pi h_0\varphi_0 r}\exp\left(-2\varphi^2/\varphi_0^2\right)\exp\left(-2y^2/h_0^2\right) \tag{9.18}$$

where h_0 is the Gaussian effective height of the waveguide, φ_0 is the effective Gaussian angular width of the waveguide and is given by [11]

$$\varphi_0=\frac{\lambda_0}{\pi n_{\text{eff}}(\text{slab})\,w_0} \tag{9.19}$$

where w_0 is the Gaussian effective width of the waveguide at the slab edge, and $n_{\text{eff}}(\text{slab})$ is the effective index of the slab. Restricting the lens aperture to $2\varphi_0$,the lens $f/\#$ can be expressed as

$$f/\#=\frac{f}{L}=\frac{1}{2\tan 2\varphi_0}\approx\frac{w_0 n_{\text{eff}}(\text{slab})\pi}{4\lambda_0} \tag{9.20}$$

Using the TE mode of a silicon-on-insulator (SOI) rectangular waveguide with a silicon thickness of 0.6 μm, and $w_0=0.82\ \mu\text{m}$, the effective index of slab waveguide would be $n_{\text{eff}}(\text{slab})=3.2738$, and then $\varphi_0=10.5°$. The required lens must span $\pm 21°$ with $f/\#=1.3$. For illustration purposes, we chose $L=100\,\mu\text{m}$. So in short, we are going to design a lens to expand a Guassian beam of width 0.82 μm propagating in the slab region to a width of 50μm propagating in the same region.

Using the radial effective index method of Section 2, we have calculated the effective index of the diverging slab 1-D photonic crystal for rays propagating radially. Figure 9.3.1 shows the radial effective index versus period at $\lambda_0=1.55\ \mu\text{m}$, the duty factor τ is assumed to be 0.5

(TE mode is assumed). The large change in effective index versus period makes lens design and its optimization a feasible task.

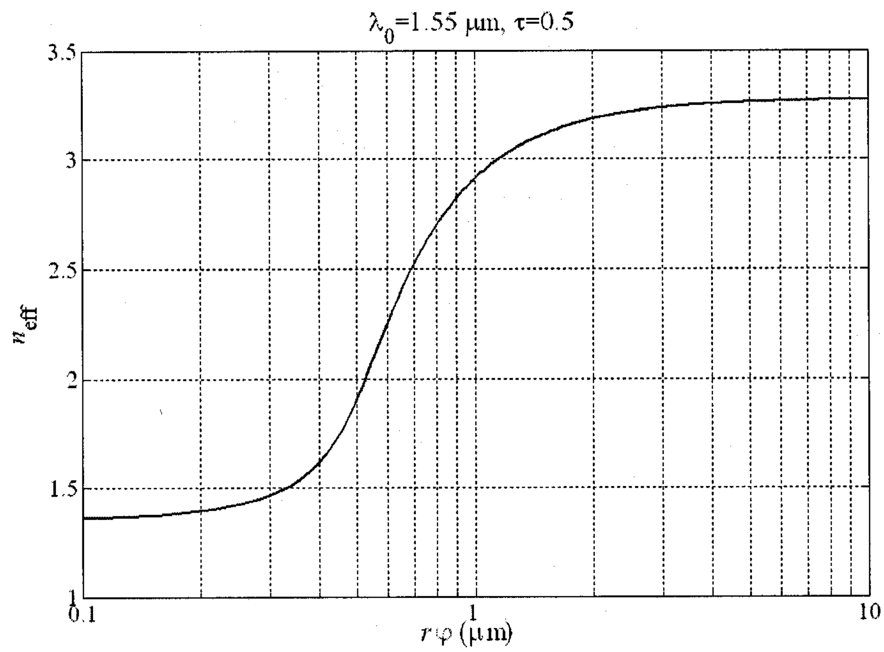

Figure 9.3.1. Radial effective index of diverging slab 1-D photonic crystal versus period

Whilst we restrict ourselves to lenses with circular front entrance (eliminating refraction, so that we are certain of the radial direction of the rays in the photonic crystal) we are free to choose the back surface curvature and the variation of the photonic crystal period with angle. In this way many designs are feasible. In order to narrow the design space we use the criterion of minimizing lens area in order to minimize etching area. Other optimization critera can also be chosen and there are usually some practical restrictions to be imposed. For example we cannot have structures finer than the minimum feature size of fabrication technology. We have assumed this to be 100nm, so periods lower than 200 nm are not permitted. Also effective refractive index lower than ~1.8 is not preferred due to loss of lateral confinement which leads to excessive coupling losses with the slab mode.

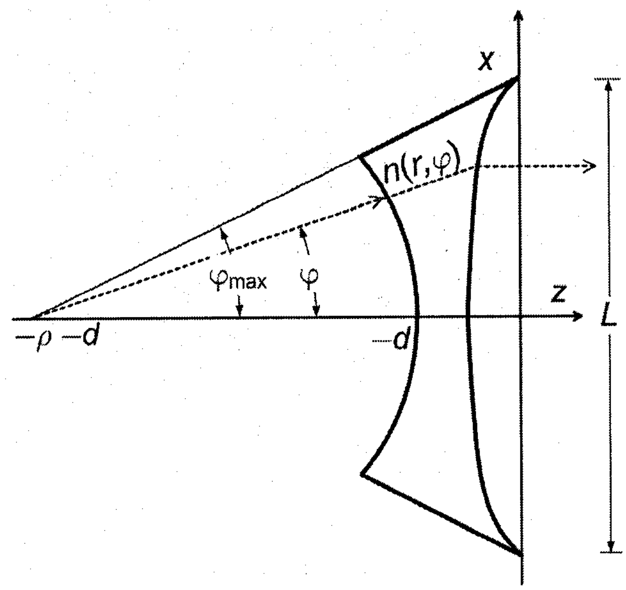

Figure 9.3.2. The proposed aspheric lens with some parameters defined.

We express the back surface profile in polar coordinate with the focal point as an origin, so

$$x = R(\varphi)\sin\theta, \quad z = R(\varphi)\cos\varphi - \rho - d \tag{9.21}$$

In order for the rays to be collimated, they need to undergo refraction of φ. Considering the refractive index of $n(\varphi)$, we need

$$n_{\text{slab}}\cos\theta = n(R,\Lambda)\cos(\varphi-\theta) \tag{9.22}$$

where θ is the angle of the back surface of the lens at φ. Solving for θ, we have

$$\tan\theta = \frac{n_{\text{slab}}/n(R,\Lambda) - \cos\varphi}{\sin\varphi} \tag{9.23}$$

then using Eq.(9.3), we have,

$$\dot{R} = \frac{R n_{\text{slab}}\sin\varphi}{n_{\text{slab}} - n(R,\Lambda)} \tag{9.24}$$

where dot stands for differentiation with respect of φ. Making optical path length from rays originating from o to $z=0$ equal, we have

$$\int_r^{R(\varphi)} n(r,\Lambda)\,dr + n_{\text{slab}}\left(\rho+d-R(\varphi)\cos\varphi\right) = \text{Const.} \tag{9.25}$$

Eqs. (9.24) and (9.25) need to be solved together. We also know that

$$\rho+d=\frac{L}{2\tan\varphi_{\max}} \tag{9.26}$$

There are also some restrictions,

$$\Lambda(\varphi)\geq\delta/\rho,\ \text{ and }\ \rho<R(\varphi)<(\rho+d)/\cos\varphi \tag{9.27}$$

where δ is the photonic crystal minimum period. The area of the lens can b=obtained as

$$S=\int_0^{\varphi_{\max}} R(\varphi)^2\,d\theta-\rho^2\varphi_{\max} \tag{9.28}$$

Now we will set up an optimization problem, there are two independent variables,

$$\begin{aligned} &0<d<\frac{L}{2\tan\varphi_{\max}}\\ &\Lambda_m>\frac{\delta}{L/2\tan\varphi_{\max}-d} \end{aligned} \tag{9.29}$$

where $\Lambda_m=\Lambda_\omega(\varphi_{\max})$. Knowing d and Λ_m, we need to solve Eqs. (9.24) and (9.25) to obtain $R(\varphi)$ and $\Lambda(\varphi)$, checking the restrictions (9.27), then we minimize the lens area of Eq.(9.28).

In order to solve Eqs. (9.24) and (9.25) together we proceed as follows

- Knowing d one can calculate ρ (from Eq.(9.26)) and note that $R_m = L/(2\sin\varphi_{max})$.
- Knowing d and Λ_m and ρ, The constant of Eq.(9.25), can be calculated.
- then $\dot{R}_m$ can be calculated (from Eq.(9.24)).
- Knowing $\dot{R}_m$, $R(\varphi_{max} - \Delta\varphi)$ can be estimated, and solving Eq.(9.25), $\Lambda(\varphi_{max} - \Delta\varphi)$ can be evaluated.
- Knowing $R(\varphi_{max} - \Delta\varphi)$ and $\Lambda(\varphi_{max} - \Delta\varphi)$, $\dot{R}_m(\varphi_{max} - \Delta\varphi)$ can be evaluated (from Eq. (9.24)).

The last two stages can be iterated until we obtain $\varphi = 0$.

The result of an optimization is as follows:

$$d = 84.36\ \mu\text{m}\,,\ \Lambda_\omega(\varphi_{max}) = 0.0122\ \text{rad}\,,\ r = 45.89\ \mu\text{m and } S = 1316\ \mu\text{m}^2.$$

Considering that the duty factor is assumed 0.5, the etching area is only 658 μm^2. Figure 9.3.1 shows the top view of the optimized lens, while Figure 9.3.2 shows its period variation with angle.

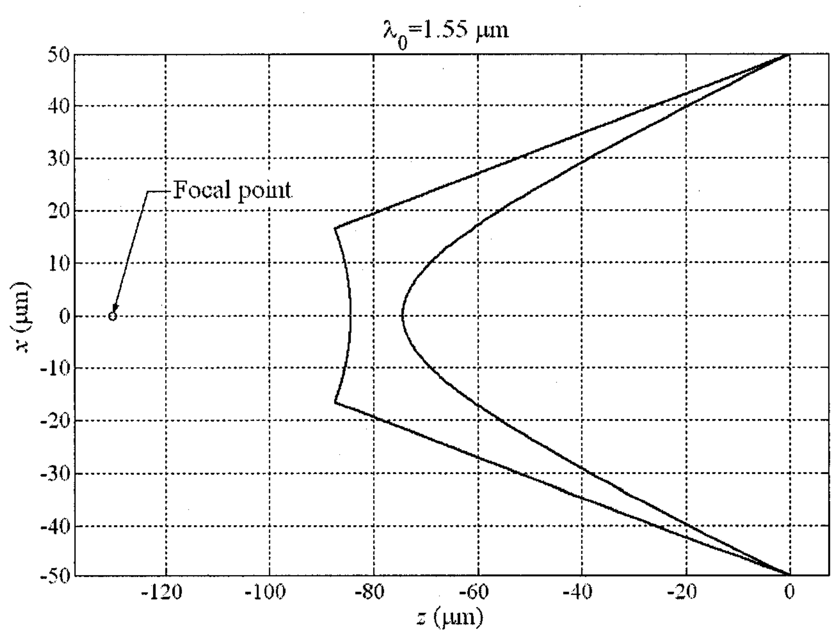

Figure 9.3.1. Aspherical concave lens as a beam expander being designed to have minimum area. The period variation is given in Figure 9.3.2.

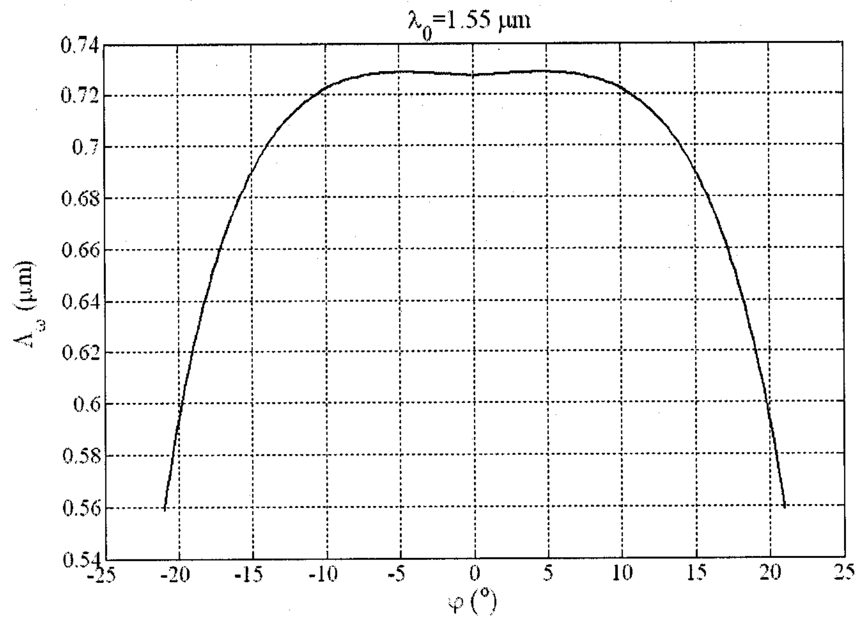

Figure 9.3.2. The period variation of the aspheric concave beam expander designed to have minimum area.

9.4 Conclusion and discussion

We have proposed the use of quasi-periodic slab 1-D photonic crystals for wavefront engineering. By keeping the 1-D patterns parallel to the rays, we have avoided the difficulty of misalignment between the group and phase velocities in photonic crystals. For diverging rays, the 1-D photonic crystal pattern is a diverging one. A suitable approximation method has been developed to obtain the effective index for the radially propagating rays. As a result we have been able to introduce a design procedure for asheric lenses for collimating light emitted from a waveguide into the slab region. Many lens configurations are possible. We imposed a criterion of minimum area and as a result, we obtained a unique lens design, with a focal length of 130 μm and operating at 100 μm.

Whilst we designed the lens for a single wavelength, since our structure is inherently dispersive, collimation will not to be perfect at different wavelengths. Figure 9.4.1 shows chromatic aberration (wave-front aberration) for the lens designed in section 3. Whilst the aberration seems huge considering traditional lenses, however for DWDM applications in which we are only interested in narrow band of wavelengths, it is seems tolerable. Note that 64 channels of 100 GHz bandwidths only cover $\pm 1.65\%$ of central wavelength of $\lambda_0 = 1.55\,\mu m$.

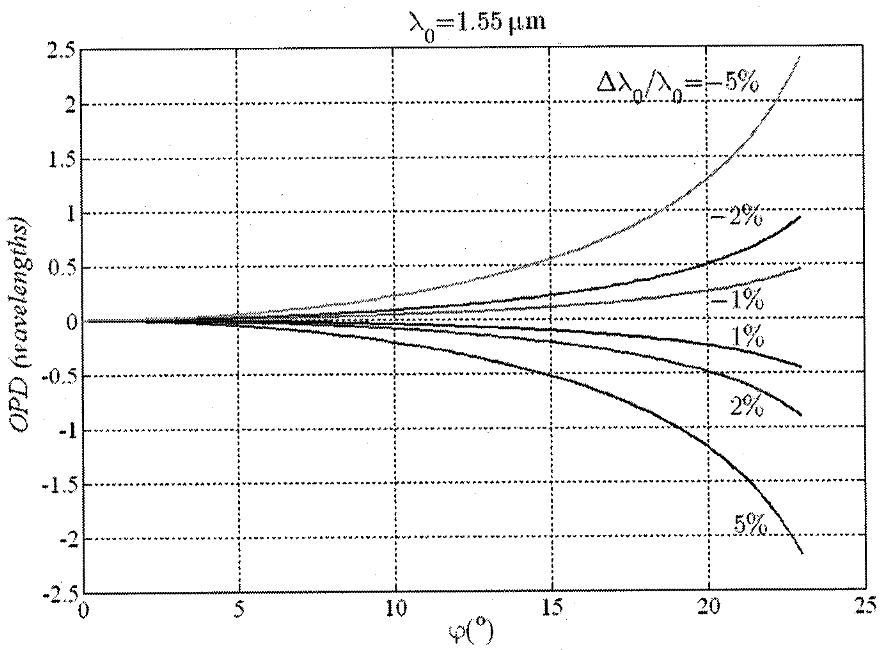

Figure 9.4.1 Chromatic aberration (wave-front aberration) for various wavelength deviations

It is to be expected that the proposed lens will have high coma aberrations. Since all rays are assumed to emanate from the focal point, significant errors may arise for objects located at different positions. Further study is underway to evaluate coma aberration of such lenses. The lens is also designed to operate correctly only for TE polarization.

References

[1] L . J. Wu, M. Mazilu, and T. F. Krauss, "Beam steering in planar-photonic crystals: From superprism to supercollimator," *Journal of Lightwave Technology*, vol. 21, no. 2, pp. 561-566, Feb.2003.

[2] A . Bakhtazad and A. G. Kirk, "1-D slab photonic crystal **k**-vector superprism demultiplexer: analysis, and design," *Optics Express*, vol. 13, no. 14, pp. 5472-5482, July2005.

[3] H . Kosaka, T. Kawashima, A. Tomita, M. Notomi, T. Tamamura, T. Sato, and S. Kawakami, "Self-collimating phenomena in photonic crystals," *Applied Physics Letters*, vol. 74, no. 9, pp. 1212-1214, Mar.1999.

[4] P . St. J. Russel and T. A. Birks, "Bloch wave optics in photonic crystals: physics and applications," in *Photonic Bandgap materials.* C. M. Soukoulis, Ed. Kluwer Academic Publishers, 1996, pp. 71-106.

[5] K . Tatsumi, T. Nakaguchi, and S. Ito, "Wide Field Angle Bi-Aspherical Wave-Guide Lens in Linbo3 Fabricated by Proton-Exchange," *Electronics Letters*, vol. 24, no. 9, pp. 546-548, Apr.1988.

[6] W . H. Southwell, "Index Profiles for Generalized Luneburg Lenses and Their Use in Planar Optical-Waveguides," *Journal of the Optical Society of America*, vol. 67, no. 8, pp. 1010-1014, 1977.

[7] P . J. R. Laybourn, G. Molesini, and G. C. Righini, "Homogeneous Refracting Lenses for Integrated Optical Circuits," *Journal of Modern Optics*, vol. 35, no. 6, pp. 1029-1048, June1988.

[8] E . A. J. Marcatili and A. A. Hardy, "The Azimuthal Effective-Index Method," *Ieee Journal of Quantum Electronics*, vol. 24, no. 5, pp. 766-774, May1988.

[9] J . Chilwell and I. Hodgkinson, "Thin-Films Field-Transfer Matrix-Theory of Planar Multilayer Waveguides and Reflection from Prism-Loaded Waveguides," *Journal of the Optical Society of America A-Optics Image Science and Vision*, vol. 1, no. 7, pp. 742-753, 1984.

[10] W . Streifer and C. N. Kurtz, "Scalar Analysis of Radially Inhomogeneous Guiding Media," *Journal of the Optical Society of America*, vol. 57, no. 6, p. 779-&, 1967.

[11] U nger H.G., *Planar Optical Waveguides and fibers* Oxford, UK, Clarendon Press, 1977.

Chapter 10

MASK DESIGN

This chapter is devoted to the technical aspect of the layout design for 1-D k-vector superprism. The mathematical equations governing the layout geometry are developed. The parabolic mirror is designed considering the critical angle of the silicon air junction. The tapering and the bend are also designed to minimize the loss. The theoretical coupling loss of the lens tapered fiber and the die are evaluated. The bending loss of our regular waveguide is discussed. Based on this analysis, one can select the minimum bending radius to keep the bending loss small. Some practical mask layout considerations are also mentioned.

10.1 The prism

The prism dimensions must be extended as far as the beam inside the photonic crystal demands. The input and output sides have to be greater than l and l' as has been shown in Figure 8.4.2. Additionally we need to keep a margin from what really is needed. It means that the dimensions on the mask are larger than what theory is suggested by a margin. A 10% margin seems reasonable, so the dimension on the mask is

$$l_1 = 1.1l, \quad l_1' = 1.1l' \tag{10.1}$$

The apex angle (ρ) must be also known initially. The prism geometry prior to any rotation is depicted in Figure 10.1.1.

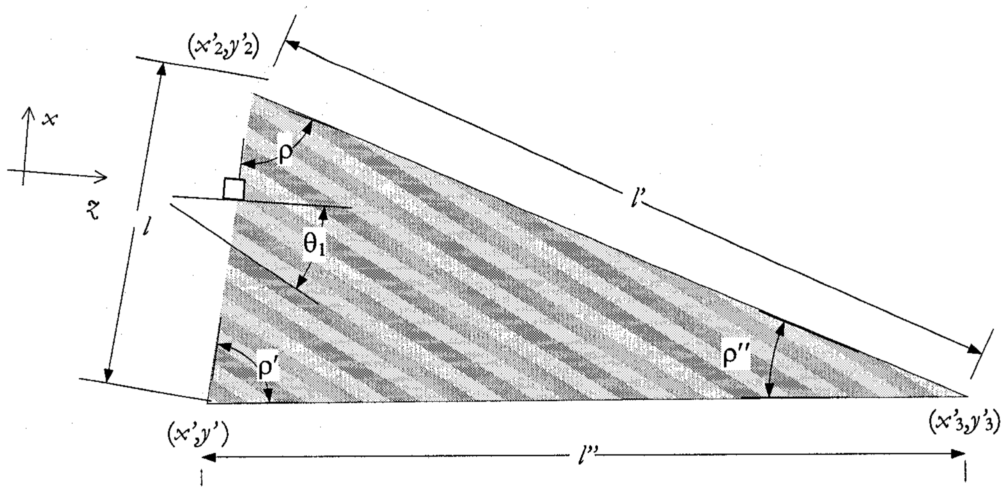

Figure 10.1.1 Prism geometry before any rotation

The other unknown parameters can be obtained as follows:

$$\begin{cases} l'' = \sqrt{l^2 + l'^2 - 2ll' \cos\rho} \\ \rho' = \sin^{-1}\left(l'/l'' \sin\rho\right) \\ \rho'' = \sin^{-1}\left(l/l'' \sin\rho\right) \end{cases} \tag{10.2}$$

The prism edge coordinates can be found from the following equations:

$$\begin{cases} x_1' = 0 & y_1' = 0 \\ x_2' = l\cos\rho' & y_2' = l\sin\rho' \\ x_3' = l'' & y_3' = 0 \end{cases} \tag{10.3}$$

As we have mentioned in chapter 8, it is beneficial to align the gratings to the raster lines of the electron beam writer, and this can be achieved at the mask level. The prism geometry after rotating to make grating parallel to the die border (coordinate z' and x') is shown in Figure 10.1.2.

The rotation angle that makes the grating parallel to z' axis, is

$$\omega = \pi/2 - \rho' - \theta_1 \tag{10.4}$$

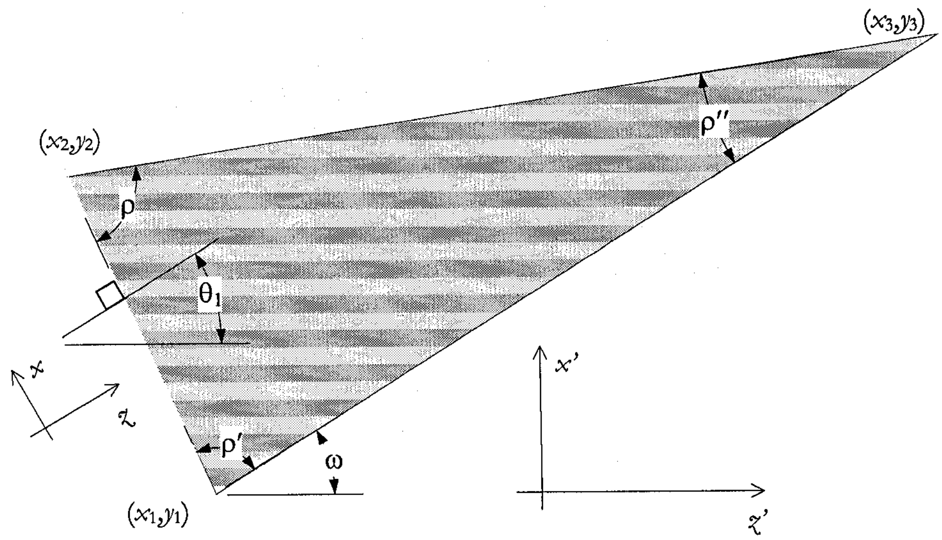

Figure 10.1.2. The prism geometry after rotating by ω

And if the grating is to be parallel to x' axis, then

$$\omega = -\rho' - \theta_1 \tag{10.5}$$

The new edge coordinate can be found by applying the rotation matrix over the original coordinates. The matrix for rotating by ω can be written as

$$T = \begin{bmatrix} \cos\omega & -\sin\omega \\ \sin\omega & \cos\omega \end{bmatrix} \tag{10.6}$$

10.2 Mirror

Using the total reflection angle of high refractive index materials and air, making a mirror is relatively easy. In our case of SOI technology, if the incident angle exceeds the critical angle of

$$\theta_c = \sin^{-1}\left(\frac{1}{n_{Si}}\right) = \sin^{-1}\left(\frac{1}{3.46}\right) = 16.78^\circ \tag{10.7}$$

there cannot be any refracted light as every ray undergoes the total reflection. If focusing is also needed, then the mirror must be the parabolic shape trench which is etched deep into silica. If the beam is shifted properly from the axis of the mirror (see Figure 10.2.1) , it is possible that the incident angle exceeds the critical angle θ_c of the silicon air interface of the trench, and the internal reflection at the interface make the trench a perfect mirror.

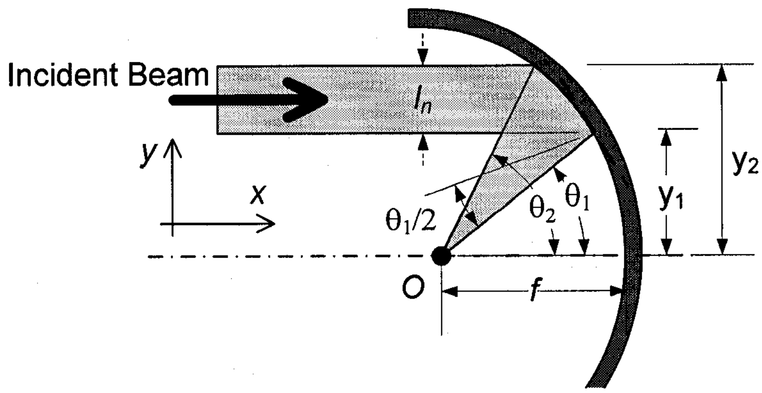

Figure 10.2.1, The parabolic mirror

A parabolic equation of the front surface of the mirror in polar coordinate can be expressed as

$$r = \frac{2f}{1+\cos\theta} \tag{10.8}$$

If we impose the restriction of

$$\theta_1 \geq 2\theta_c \tag{10.9}$$

it ensures that the beam will focus to the focal point and the mirror would be perfect. The beam has to be shifted form the mirror axis by

$$y_1 = \frac{2f\sin\theta_1}{1+\cos\theta_1} = 2f\tan\theta_1/2 \tag{10.10}$$

The mirror, at least, has to cover the beam width l_n, *i.e.*, it has to be extended from θ_1 to θ_2 (see Figure 10.2.1), where θ_2 can be found by solving the following equation

$$2f\tan\frac{\theta_2}{2} = 2f\tan\frac{\theta_1}{2} + l_n \tag{10.11}$$

or

$$\theta_2 = 2\tan^{-1}\left(\tan\theta_1/2 + l_n/2f\right) \tag{10.12}$$

These angles (of course with imposing some margins) are utilized to make a mirror on the final mask.

10.3 Superprism and the input mirror

Let's start from the rotated superprism of Figure 10.1.2, the input aperture sizes can be determined as follows:

$$L = l\sec\varphi_1 \tag{10.13}$$

Where φ_1 is the incident angle. The mirror distance to the superprism is somewhat arbitrary, but it is preferred to locate the mirror as close as possible to the input side (in order to reduce the total chip size and to reduce the propagation loss too). Let us start with the input mirror first. We find which edge of (x_1, y_1) or (x_2, y_2) is nearer to the input mirror. If φ_1 is positive, (x_2, y_2) is closer to the input mirror, otherwise (x_1, y_1). For the sake of illustration, let's assume $\varphi_1 > 0$. Then the start point of the mirror path can be found as

$$\begin{cases} x_{m1} = x_2 + \zeta\cos t_i \\ y_{m1} = y_2 + \zeta\sin t_i \end{cases} \tag{10.14}$$

Where

$$t_i = \varphi_1 + \frac{\pi}{2} + \rho' + \omega \tag{10.15}$$

Figure 10.3.1 depicts the input mirror geometry. The central input waveguide end point is then determined as

$$\begin{cases} x_w = x_{m1} + r_2 \cos t_r \\ y_w = y_{m1} + r_2 \sin t_r \end{cases} \tag{10.16}$$

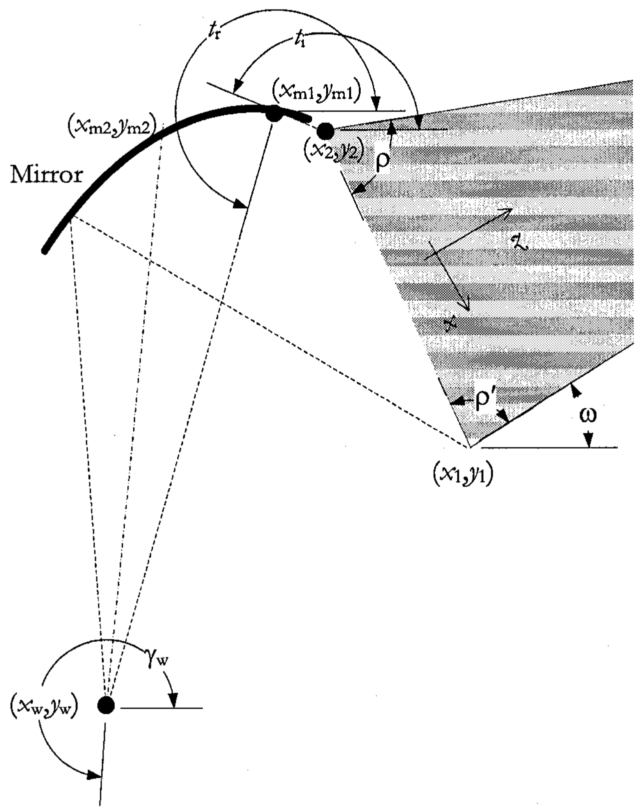

Figure 10.3.1 The input mirror geometry

Where

$$t_r = t_i - \pi + \theta_2 \tag{10.17}$$

and

$$r_2 = \frac{2f}{1+\cos\theta_2} \tag{10.18}$$

The central waveguide direction is toward the center of the mirror at (x_{m2}, y_{m2}) *i.e.,*

$$\gamma_w = \pi + t_r - \frac{\theta_2 - \theta_1}{2} \tag{10.19}$$

The equations which are mentioned in this section and depicted in Figure 10.3.1 are indeed a special case. More general cases (that works for all incident angles) are expressed with the following equations.

$$\begin{cases} t_r = t_i - \pi + \mathrm{sgn}(\varphi_1)\theta_2 \\ \gamma_w = t_i + \mathrm{sgn}(\varphi_1)\dfrac{\theta_2 + \theta_1}{2} \end{cases} \tag{10.20}$$

And

$$\begin{cases} x_{m1} = \dfrac{x_2}{2}\left[1 + \mathrm{sgn}(\varphi_1)\right] + \dfrac{x_1}{2}\left[1 - \mathrm{sgn}(\varphi_1)\right] + \zeta \cos t_i \\ y_{m1} = \dfrac{y_2}{2}\left[1 + \mathrm{sgn}(\varphi_1)\right] + \dfrac{y_1}{2}\left[1 - \mathrm{sgn}(\varphi_1)\right] + \zeta \sin t_i \end{cases} \tag{10.21}$$

Note that the input waveguides are tilted toward left if $\pi/2 < \gamma_w < 3\pi/2$, and they tilted toward right otherwise (*i.e.,* $-\pi/2 < \gamma_w < \pi/2$). In other words, in the former case the inputs are terminated at the right edge of the die, but in the later case they will end at the right edge. Usually it is preferred to have the input waveguides at the left edge of the die. We can either rotate the structure another 180° or 90°. In the later case, the 1-D photonic crystal will be vertical instead of horizontal. The situation will get more complicated when the output waveguide situation is also considered. In other words, the output waveguides must be terminated to the left edge of the die. In the worst case scenario, there might be some cases that we have to remove the restriction of making 1-D superprism vertical or horizontal.

10.4 The input waveguides loci and directions

The center point of the mirror can be written as

$$\begin{cases} x_{m2} = x_w + r\cos\gamma_w \\ y_{m2} = y_w + r\sin\gamma_w \end{cases} \tag{10.22}$$

Where r is the equivalent spherical radius of mirror and can be expressed as

$$r = \frac{2f}{1+\cos\overline{\theta}}, \qquad \overline{\theta} = \frac{\theta_1+\theta_2}{2} \tag{10.23}$$

The loci of the input waveguides make a circle with radius r centered at (x_{m2}, y_{m2}). The direction of inputs is toward the center of the mirror. The input waveguide pitch (Λ_i) is somewhat arbitrary, but it is recommended to be the same as the output waveguide pitch (see Figure 10.4.1)

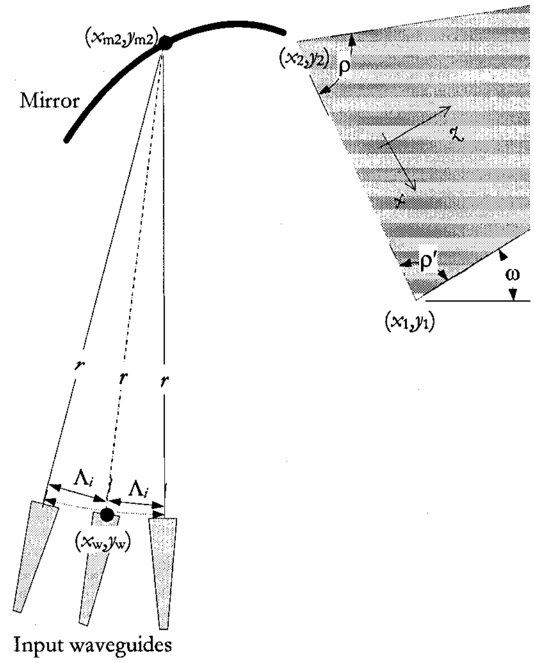

Figure 10.4.1 The input waveguides geometry

10.5 Superprism and the output mirror

We start from rotated superprism of Figure 10.1.2 again. The output aperture sizes can be found below:

$$L' = l' \sec\varphi_4 \tag{10.24}$$

Where $\varphi_4 = \eta - \rho + \varphi_1$ is the transmission angle and η is the prism deviation angle. Again we have to find which edge $(x_{1,}y_1)$ or $(x_{3,}y_3)$ are nearer to the output mirror. Clearly if φ_4 is positive $(x_{1,}y_1)$ is closer, otherwise it is $(x_{3,}y_3)$. For the sake of illustration, we assume $\varphi_4 < 0$. Then the first point of the mirror can be found as

$$\begin{cases} x'_{m1} = x_3 + \zeta' \cos t'_i \\ y'_{m1} = y_3 + \zeta' \sin t'_i \end{cases} \tag{10.25}$$

Where

$$t'_i = \varphi_4 + \frac{\pi}{2} - \rho'' + \omega \tag{10.26}$$

See Figure 10.5.1. The central input waveguide end point is then determined as

$$\begin{cases} x'_w = x'_{m1} + r'_2 \cos t'_r \\ y'_w = y'_{m1} + r'_2 \sin t'_r \end{cases} \tag{10.27}$$

Where

$$t'_r = t'_i - \pi - \theta'_2 \tag{10.28}$$

And

$$r'_2 = \frac{2f'}{1 + \cos\theta'_2} \tag{10.29}$$

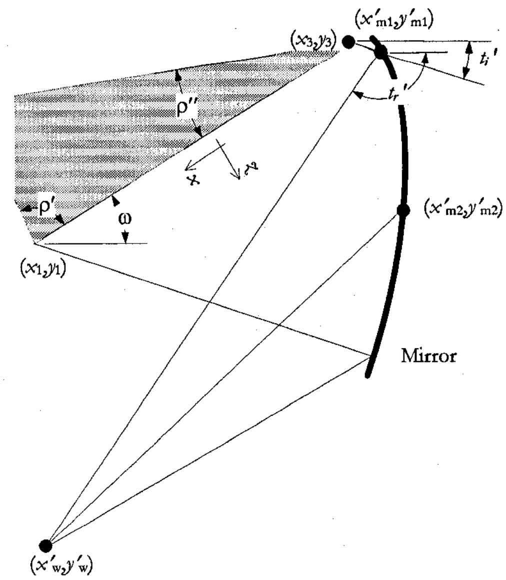

Figure 10.5.1 The output mirror geometry

The central output waveguide direction is toward the center of the mirror at $\left(x'_{m2}, y'_{m2}\right)$ *i.e.*,

$$\gamma'_w = t'_r - \pi - \frac{\theta'_2 - \theta'_1}{2} \tag{10.30}$$

The following equations show the general cases.

$$\begin{cases} t'_r = t'_i - \pi + \operatorname{sgn}\left(\varphi_4\right)\theta'_2 \\ \zeta'_w = t'_i + \operatorname{sgn}\left(\varphi_4\right)\dfrac{3\theta'_2 + \theta'_1}{2} \end{cases} \tag{10.31}$$

And

$$\begin{cases} x'_{m1} = \dfrac{x_1}{2}\left[1 + \operatorname{sgn}\left(\varphi_4\right)\right] + \dfrac{x_3}{2}\left[1 - \operatorname{sgn}\left(\varphi_4\right)\right] + \zeta' \cos t'_i \\ y'_{m1} = \dfrac{y_1}{2}\left[1 + \operatorname{sgn}\left(\varphi_4\right)\right] + \dfrac{y_3}{2}\left[1 - \operatorname{sgn}\left(\varphi_4\right)\right] + \zeta' \sin t'_i \end{cases} \tag{10.32}$$

Note that the output waveguides are tilted toward the left if $\pi/2 < \gamma'_w < 3\pi/2$, and they tilted toward the right otherwise (*i.e.*, $-\pi/2 < \gamma'_w < \pi/2$). This means in the former case the outputs are terminated at the right edge of the die, but in the later case they will end at the left edge. Usually it is preferred to have the output waveguides at the right edge of the die (see Figure 10.5.2).

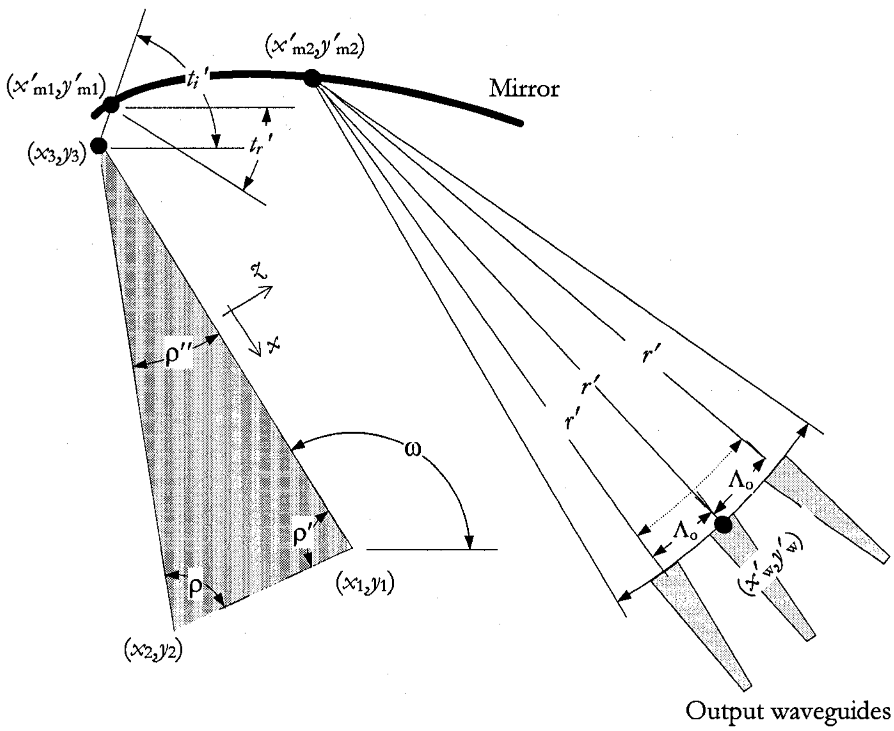

Figure 10.5.2 The output side of the mirror and the output waveguide. Note that the prism is rotated another 90 degrees to bring the output waveguide to the right side of the die

10.6 The output waveguides loci and directions

The coordinates of the center point at the mirror can be written as

$$\begin{cases} x'_{m2} = x'_w + r' \cos \gamma'_w \\ y'_{m2} = y'_w + r' \sin \gamma'_w \end{cases} \tag{10.33}$$

Where r' is the equivalent spherical radius of the output mirror and can be expressed as

$$r' = \frac{2f'}{1+\cos\overline{\theta}'}, \qquad \overline{\theta}' = \frac{\theta_1' + \theta_2'}{2} \tag{10.34}$$

The loci of the output waveguides make a circle with radius r' centered at (x'_{m2}, y'_{m2}). The directions of all inputs are toward the center of the mirror. The input waveguide pitch (Λ_o) is determined by the design (see Figure 10.5.2).

10.7 The input and output waveguide path to the alignment line

For the uniformity, we have to align the input and output waveguides at the die borders with a constant separation. The paths have to be designed. The procedure can be reduced to just drawing a number of patterns starting from midpoint of the mirrors (x_c, y_c) (for the input mirror it is (x_{2m}, y_{2m}), and for the output mirror it is (x'_{2m}, y'_{2m})), spanning around the central direction of γ (for the input mirror it is γ_w,and for the output it is γ'_w), and terminating at any point at the border but having specific pitch (the distances between neighboring patterns are the same and it is known as the border pitch). See Figure 10.7.1.

The patterns to be drawn are at angle γ_i $(i = 1, 2, \cdots, N)$ that is dependent on the central rotation angle of the waveguides as follows

$$\gamma_i = \begin{cases} \gamma - \frac{\Lambda}{r} \times \frac{N-1+2i}{2} & \text{first quadrant, } 0 < \gamma < \pi/2 \\ \gamma + \frac{\Lambda}{r} \times \frac{N-1+2i}{2} & \text{second quadrant, } \pi/2 < \gamma < \pi \\ \gamma - \frac{\Lambda}{r} \times \frac{N-1+2i}{2} & \text{third quadrant, } \pi < \gamma < 3\pi/2 \\ \gamma + \frac{\Lambda}{r} \times \frac{N-1+2i}{2} & \text{fourth quadrant, } 3\pi/2 < \gamma < 2\pi \end{cases} \tag{10.35}$$

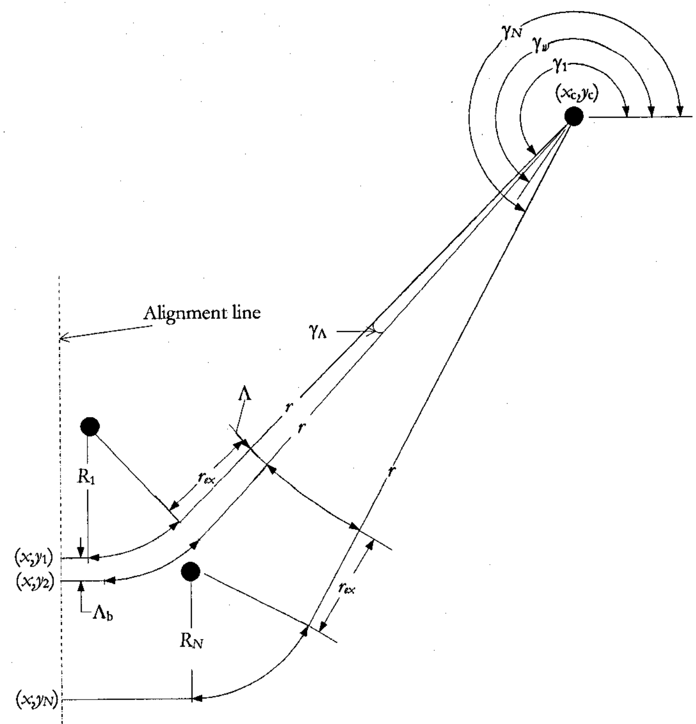

Figure 10.7.1 The pattern to the die border for the input and output waveguides

The purpose of locating the bends at radius $r+r_{ex}$ (or including extra straight pattern r_{ex} after radius r) is twofold. First, there are tapering at the waveguide/slab junction for the sake of beam shaping, and this length play the role of a buffer between the taper region and the bend region. Furthermore, it is usually preferred to have an extra waveguide length for fanning out the patterns (it makes them more separated, so providing the desired pith at the die border would be easier).

Let's start making the patterns, assuming the bend radius is R_i. The coordinates of the pattern at the alignment line is

$$\begin{cases} x_i = x_c + (r + r_{ex})\cos\gamma_i + R_i \cos\gamma_i + l_i \\ y_i = y_c + (r + r_{ex})\sin\gamma_i + R_i\left(1 - \left|\sin\gamma_i\right|\right)\operatorname{sgn}\left(\sin\gamma_i\right) \end{cases} \tag{10.36}$$

Where l_i is the extra distance needed to align the patterns to the alignment line of Figure 10.7.1. There are also some restrictions as follows

$$
\begin{aligned}
&x_i = x_1,\ i = 2,\cdots,N \\
&y_i = y_{i-1} + \Lambda_b \operatorname{sgn}(\sin\gamma),\ i = 2,\cdots,N \\
&R_i \geq R_{\min},\ i = 1,\cdots,N_{\min}
\end{aligned}
\tag{10.37}
$$

Where Λ_b is the waveguide pitch at the border, and $R_{\min}$ is the minimum bending radius. The set of Eq.(10.36), together with restriction (10.37) can have many solutions, but let us select the following one

$$
R_1 = R_{\min} \text{ and } l_1 = l_{\min} \tag{10.38}
$$

Considering the y coordinates of the first and i^{th} pattern are at the alignment line, *i.e.*,

$$
\begin{cases}
y_1 = y_c + (r + r_{ex})\sin\gamma_1 + R_{\min}\left(1 - |\sin\gamma_1|\right)\operatorname{sgn}(\sin\gamma) \\
y_i = y_c + (r + r_{ex})\sin\gamma_i + R_i\left(1 - |\sin\gamma_i|\right)\operatorname{sgn}(\sin\gamma)
\end{cases}
\tag{10.39}
$$

By using the second restriction of Eq.(10.37), *i.e.*, $y_i = y_1 + (i-1)\Lambda_b \operatorname{sgn}(\sin\gamma)$, we have

$$
R_i = \frac{(r + r_{ex})(\sin\gamma_1 - \sin\gamma_i) + (i-1)\Lambda_b \operatorname{sgn}(\sin\gamma)}{\left(1 - |\sin\gamma_i|\right)\operatorname{sgn}(\sin\gamma)} + R_{\min} \tag{10.40}
$$

Now consider the x coordinates of the first and i^{th} pattern are at the alignment line, *i.e.*,

$$
\begin{cases}
x_1 = x_c + (r + r_{ex})\cos\gamma_1 + R_{\min}\cos\gamma_1 + l_{\min} \\
x_i = x_c + (r + r_{ex})\cos\gamma_i + R_i\cos\gamma_i + l_i
\end{cases}
\tag{10.41}
$$

By using the first restriction of Eq.(10.37), *i.e.*, $x_i = x_1$ we have

$$
l_i = (r + r_{ex})(\cos\gamma_1 - \cos\gamma_i) + R_{\min}\cos\gamma_1 - R_i\cos\gamma_i + l_{\min} \tag{10.42}
$$

Knowing R_i, and l_i, all other parameters of the patterns can be determined.

10.8 Waveguide dominant mode and Tapering

There are four reasons and locations that we implement tapering:

a) at the input border to increase the input coupling,
b) at the input slab junction to decrease the beam-width, and beam shaping,
c) at the slab output waveguide junction to match the beam-width at the focal point, and,
d) at the output edge to increase the output coupling.

The tapering width in cases b) and c) are mostly design related, whereas in cases a) and d), they are mask design problems. Considering our SOI wafer with 0.5 μm silicon height and the availability of lens tapered fiber with beam width of 2.5 μm, we have to design a tapering profile to minimize the coupling loss. For simplicity, we restrict ourselves to the linear tapering profile. Therefore, only two parameters have to be selected: the tapering width at the die border and the tapering length.

Figure 10.8.1 and Figure 10.8.2 show the first two quasi-TM modes of the main waveguides. Finite element methods are used to obtain the modal patterns and the effective index of the modes.

If the tapering width at the border is selected properly, then a long enough tapering will convert the modal profile at the die border to the main waveguide profile depicted in Figure 10.8.1. Any misalignment will cause higher order modes to be generated (see the second mode profile in Figure 10.8.2).

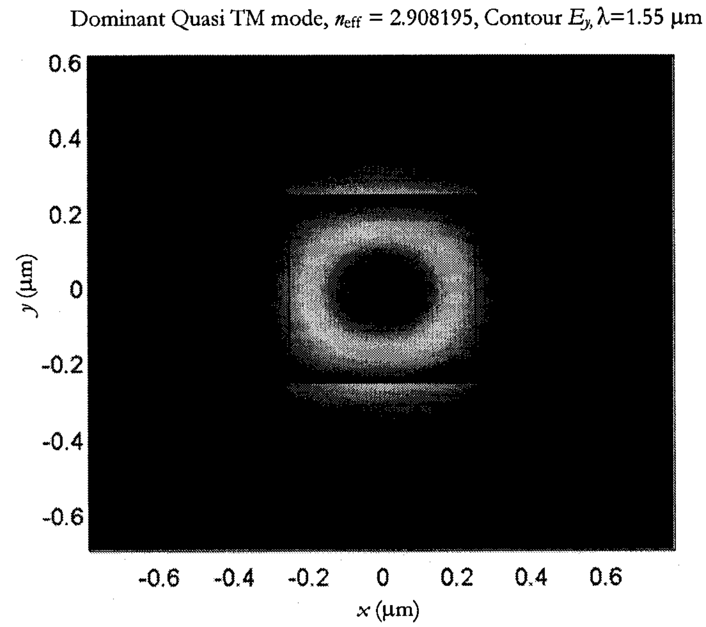

Figure 10.8.1. The dominant electric field component of the dominant quasi-TM mode of $0.5 \times 0.5\ \mu m^2$ waveguide

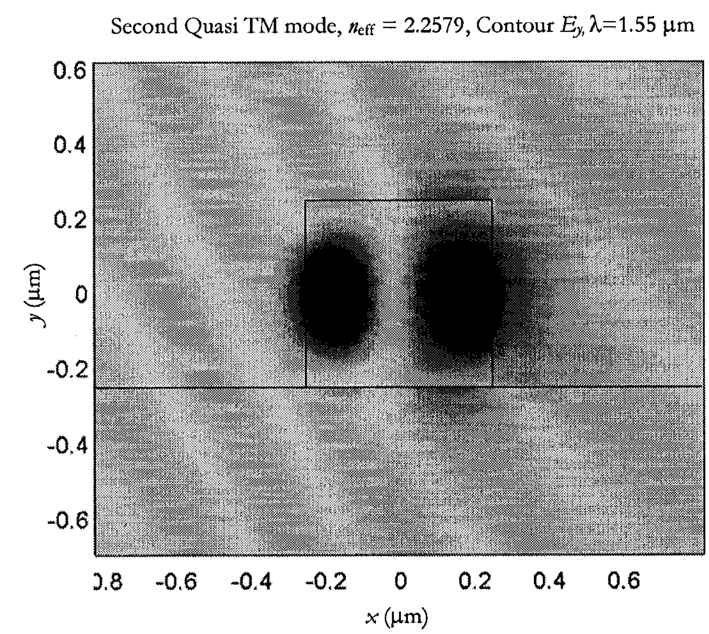

Figure 10.8.2. The dominant electric field component of the second quasi-TM mode of $0.5 \times 0.5\ \mu m^2$ waveguide

Figure 10.8.3 shows the theoretical coupling loss of the Gaussian beam of the lens tapered fiber (with the beam width of $2.5\mu m$) versus border waveguide width; the waveguide height is fixed at 0.5 μm. As can be seen, the coupling loss for the waveguide of 2×0.5 μm^2 is 1.2 dB per facet. In our layout the tapering width at the border is 2μm.

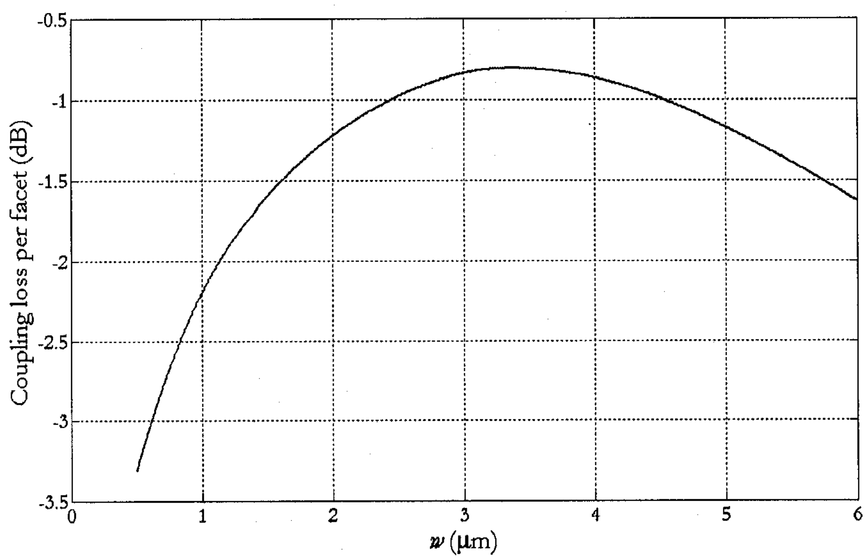

Figure 10.8.3 The coupling loss of the lens tapered fiber (with the focal beam width of 2.5μm) versus waveguide width, the waveguide height is fixed at 0.5 μm

Figure 10.8.4 shows the modal profile of the dominant electric field (E_y) for the dominant quasi-TM mode of the waveguide of dimension 2×0.5 μm^2. Our simulation shows that the waveguide of this size at wavelength of 1.55 μm supports 22 guiding modes. Although, many of these modes may be excited at the border (especially due to possible misalignment), few of them will survive after the tapering (which reduces the waveguide width at the border to the regular waveguide). As is shown later, although our regular waveguide supports more than the dominant mode, all the non-dominant modes are close enough to the cutoff and will not survive due to bending loss. In short, with this waveguide dimensions, practically only the dominant mode would prevail.

Dominant Quasi TM mode, n_{eff} = 3.126332, Contour E_y, λ=1.55 μm

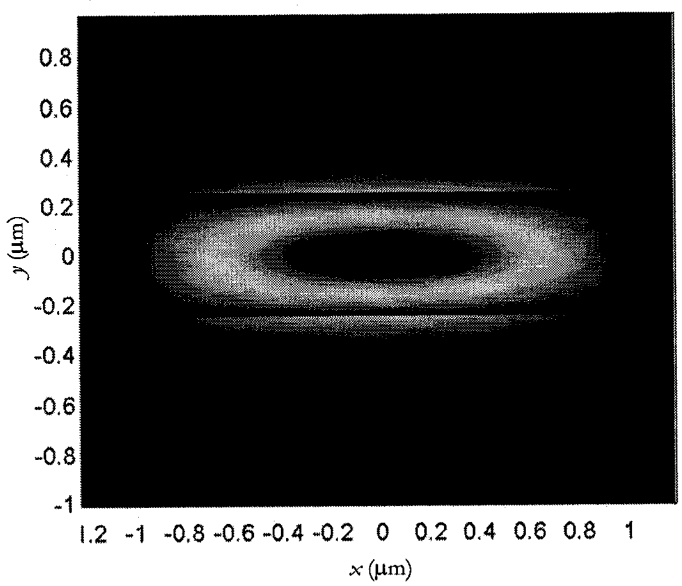

Figure 10.8.4, The dominant electric field component of the dominant quasi-TM mode of $2\times0.5\ \mu m^2$ waveguide

As is shown in Figure 10.8.3, the optimum waveguide width at the border is 3.37 μm. If we had chosen this waveguide width then our coupling loss would have been reduced to 0.81 dB per facet. The simulation tool is 3-D beam propagation method; the wavelength is 1.55 μm, and the polarization is quasi-TM.

The simulation shows that the tapering length of 100 μm is sufficient (less than 1% of power in the dominant mode is lost) to shrink the modal profile of the waveguide at the border (see Figure 10.8.4) to that of the dominant mode of our regular waveguide (see Figure 10.8.1).

10.9 Bend calculation

Bent waveguides are the key component in many integrated optical devices. As the curvature radius R becomes smaller, an optical path direction is changed at the shorter propagation distance. Therefore, the optical bending loss will increase as R declines. When guided light goes around a bend, to maintain a guided mode with equi-phase fronts on radial planes, the phase front will need to move more quickly at the outside of the bend than the inside.

Following this trend, to greater radii will lead to a point (at a certain radius R_c) where the phase velocity of the guided mode is equal to the velocity of the unguided light in the free space there. The matching of velocities there makes the opportunity for the guided light to couple to the unbounded radiation modes. This means that a part of the optical power in the guided mode $r > R_c$ (where R_c is the critical radius) radiates toward the outside of the arc. This mode conversion is the actual reason of the optical loss in the bent waveguides, which should be considered in designing the bent waveguides.

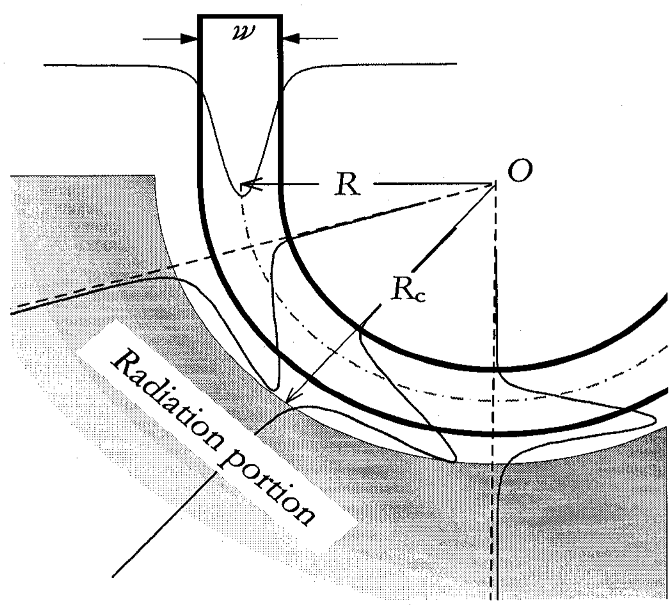

Figure 10.9.1 Field distribution of the guided mode in a bend

The bending loss has three origins: the radiation losses of the bend (imaginary part of the propagation constant of the mode in the bend), conversion loss between the straight to the bend, and vise versa. Although the bending loss (which is the most important factor among the others) is related to the length of the bend, the two others are not. To assess the bending loss we will consider the 180° bend at various bending radiuses. Our model is the two dimensional one (using effective indices of the corresponding slab at the proper polarization), and we have used finite element method for this purpose. The wavelength is 1550 nm, and the polarization is quasi TM. Figure 10.9.2 shows the modal profile of the regular waveguide bend which produces excessive loss as the center of the modal spot tends outward.

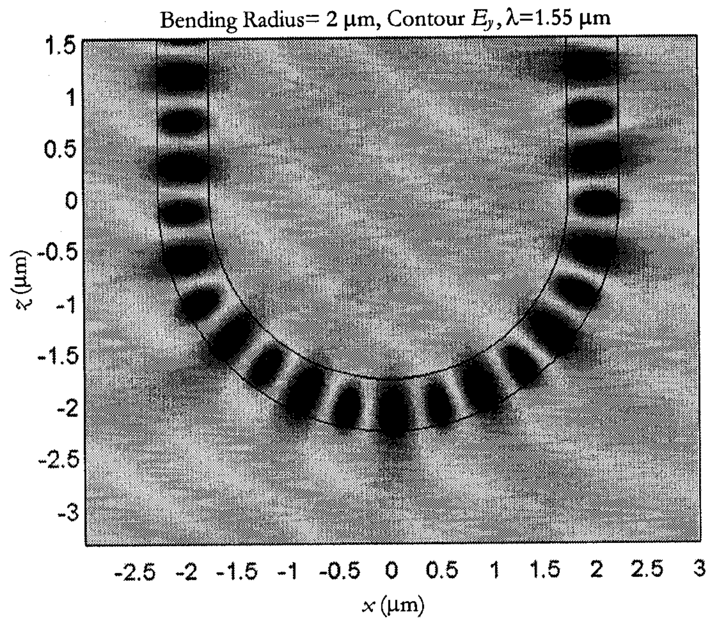

Figure 10.9.2 The field profile of a lossy bend

Figure 10.9.3 shows the loss in the 180° bend versus the bending radius. Note that at higher radius, the bend length is also high causing greater total loss, even though the radiation loss per length is small (corresponding to the imaginary part of the propagation constant in the bend). That is why at higher bending radius, the total loss will not decrease significantly. It seems the bending radius grater than $R_{bend} = 30\,\mu\text{m}$ produces smaller radiation losses.

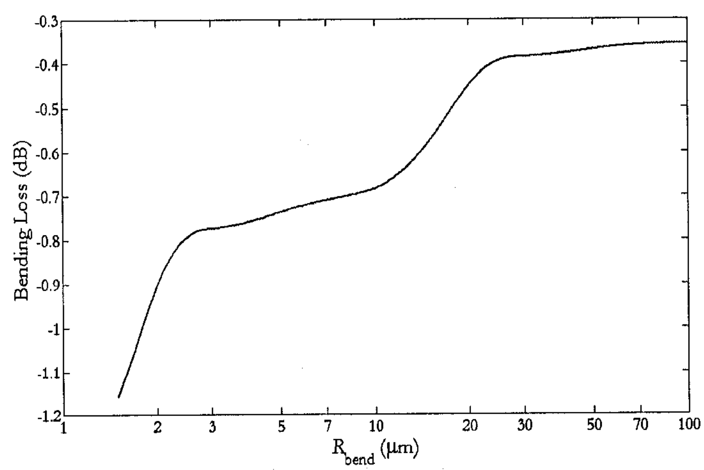

Figure 10.9.3 The bending loss of 180° bend versus the bending radius.

Figure 10.9.4 shows the field profile in a part of the 180° bend with the bending radius of 30 μm. As is clear, the mode is well confined, and the modal spot's outward tendency is insignificant.

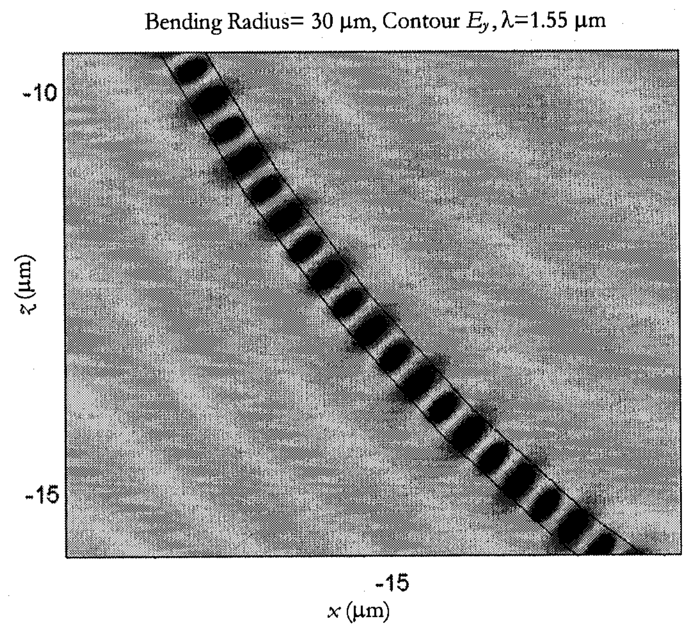

Figure 10.9.4 The field profile in a small portion of the 180° bend, with bending radius Of 30 μm.

An interesting feature of the bend is the ability to impose higher losses to the modes which are near enough to cutoff. The reason for this loss is the lower modal confinement close to cutoff that makes the greater amount of power to be extended beyond the critical radius R_c (see Figure 10.9.1). Figure 10.10.1 shows the field profile of the bend carrying second mode of the straight waveguide. The amount of loss is enough to assume that bends are a mode attenuator/filter (which imposes considerable losses to higher order modes near cutoff).

10.10 Alignment waveguide paths

In order to launch light into the chip, we have to align the input beam (or fiber) to the input waveguide. Similarly, in order to measure the output power from output waveguides we need alignment too. To simplify the optical alignment procedure, it is highly recommended making two extra waveguide paths. One connects the top of the input waveguide at the input facet to the

Bending Radius= 30 μm, Contour E_y, λ=1.55 μm

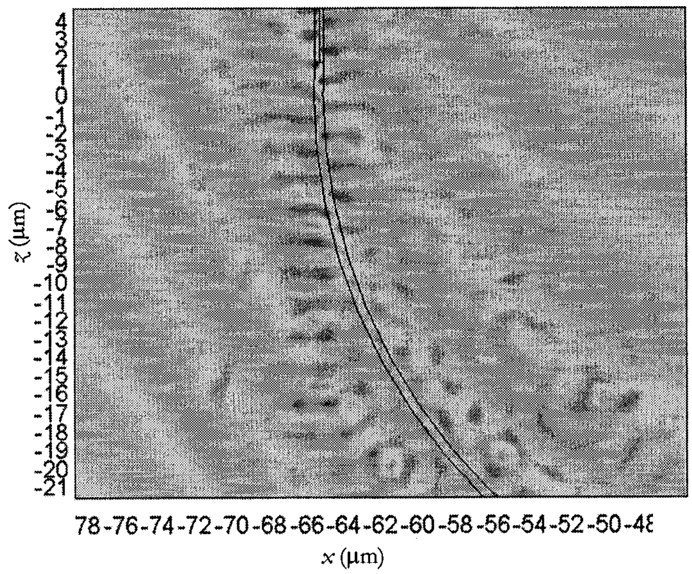

Figure 10.10.1 The second mode field profile in a portion of the 180° bend (the bending radius 0f 30μm

top of the output waveguide at the output facet and the other connects the bottom to the bottom. The alignment procedure then would consist of exciting the top and the bottom input waveguide and observe the corresponding outputs. If this procedure is followed properly, one can change the input excitation by only displacing the input lens tapered fiber, and then input waveguide excitation is easily achievable by moving the input fiber to the input waveguide (only one lateral alignment is left). Unfortunately we have not implemented this scheme in the layout that was submitted for fabrication. Figure 10.10.2 shows the schematic of such an arrangement.

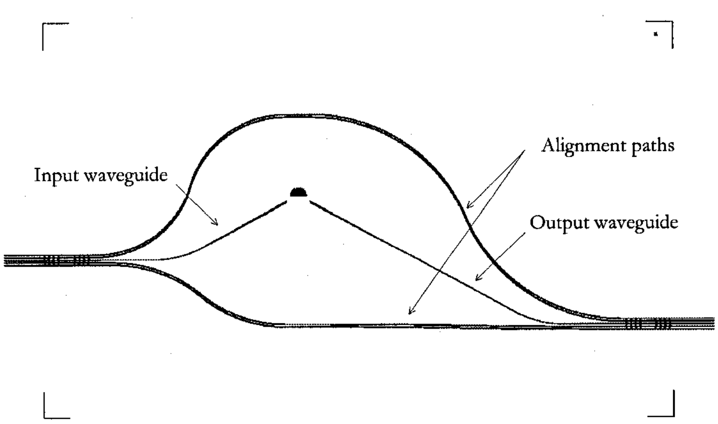

Figure 10.10.2 The alignment path

10.11 Chevrons

Chevrons are the inclined trenches (chevron shape) which are put between the input and the output waveguides in order to obscure this region and prevent the light propagation there. The region between waveguides if not obscured, can be a propagating region (very similar to the waveguide itself, a silicon region between two trenches). In practical alignment procedure, if there are no chevrons, then it will be very difficult to recognize whether the light is propagating in the intended waveguides or between the waveguides. Typical chevrons are depicted in Figure 10.11.1.

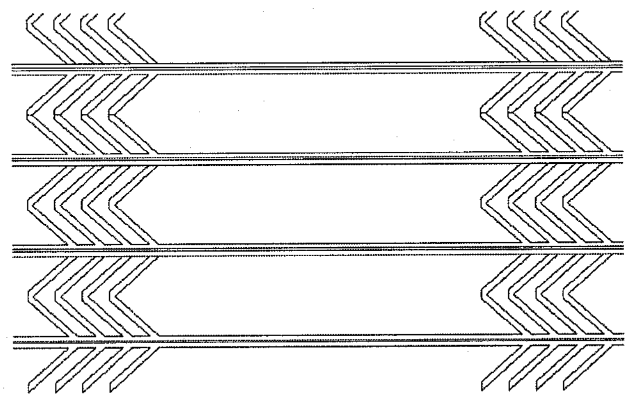

Figure 10.11.1 The chevrons.

10.12 Die borders and number

The input and output waveguides have to be extended beyond the input and output die edges. The die border is usually used as the cleaving guideline, and this extension (200 μm in our case) guarantees that the cleave line passes through the input and the output waveguide (See Figure 10.12.1). If we keep the separation of neighboring dies in a row as this extension (200 μm in our case), then by a single cleave we will have two facets.

We have also put die number at the left top corner of the die (see Figure 10.12.1).

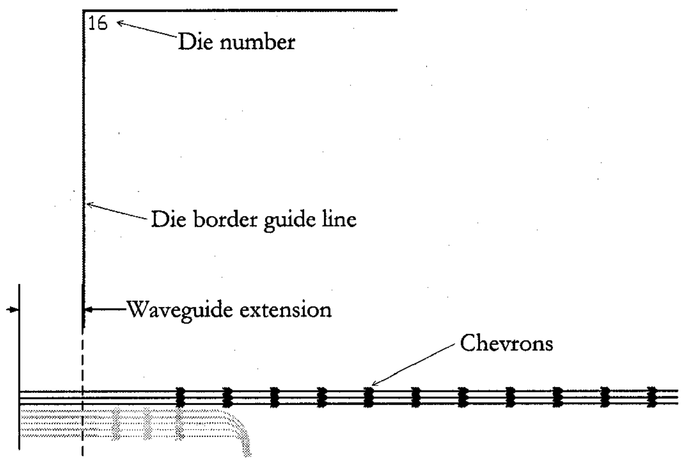

Figure 10.12.1 The position of input waveguides with regard to die border

10.13 A typical layout

A typical layout without the alignment waveguides is depicted in Figure 10.13.1. The straight waveguide has been made there as a reference for the propagation loss measurement.

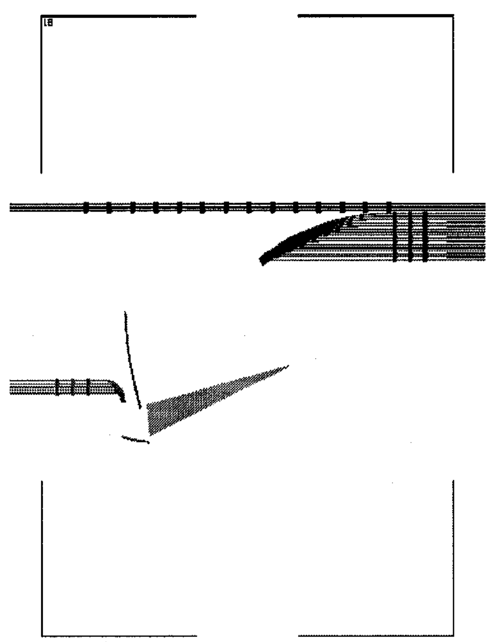

Figure 10.13.1 A typical layout

Chapter 11

EXPERIMENTAL RESULTS

In this chapter we review our attempt to design, fabricate, post-process and experimentally measure the performance of the k-vector superprism. Our goal was to resolve 16 DWDM channels with 0.8nm channel spacing. We will also discuss the challenges for forthcoming work.

11.1 Introduction

Demonstrating the capability of **k**-vector superprism for resolving fine wavelength separation was one of the first objectives of this thesis. More specifically, the goal was a 16 channel demultiplexer of 0.8 nm channel spacing.

Our first attempt to design the multiplexer using a moderate refractive index contrast material (such as PECVD silicon nitride over silica) failed due to the following important issues

1. The size of photonic crystal required to resolve a 16 channel of 0.8nm channel spacing was prohibitive for most electron beam writers.
2. Design and fabrication of the focusing elements was challenging, as has been addressed in chapter 9.
3. Furthermore a stress free thick silicon nitride layer was hard to achieve

The high refractive index contrast system of materials such as silicon on insulator (SOI) technology was a promising candidate because

1. The size of photonic crystal for the desired resolution would not be prohibitive.

2. Considering the high refractive index contrast of silicon and air, the focusing elements can be implemented as mirrors.

The thickness of the top silicon layer was selected to be as large as possible to enhance the vertical field confinement in 1-D photonic crystal. However the thickness must not be too large that it makes the input/output rectangular waveguides multimode. Details of this aspect of the design have been presented in chapter 10. We selected top a silicon layer thickness of 0.5 μm. A buried oxide layer thickness of 3μm was also selected to prevented the bond Bloch modes leaking to the substrate. We prepared a complete technical details of the design before purchasing the wafers from Soitec (http://www.soitec.com/). Reports of the successful implementation of such waveguides in other devices also made us confident of our choice [1].

Using the theory developed in chapter 8, we have designed several demultiplexers (a total of 10) fulfilling the requirements. The following ideas were to examine

- Quiescent points in the first, and in the second Brillouin zones.
- Positive and negative incident angles
- Bandgap width effect on dispersion

Using the equations developed in chapter 10, masks were designed for all cases. The masks data were sent to National Research Council (NRC) laboratories for the electron beam writing on the SOI wafers and reactive ion etching (RIE). All the top silicon layer (0.5 μm) was supposed to be etched uniformly. The etch profile has to be as vertical as possible.

Placing a cladding over the device (such as PECVD oxide) had the following pros and cons

a) The advantages were

1. By smoothing the transition of silicon and air in the 1-D photonic crystal area, the scattering loss could be reduced.
2. It physically protects the fine structures, (more discussion on this subject will be presented later in the chapter)

b) The disadvantages were

1. It reduces the refractive index contrast in the 1-D photonic crystal area, which would reduce the dispersion and increase the superprism size.
2. It adds another processing step
3. The uniformity of the oxide layer in the narrow trenches of the 1-D photonic crystal is doubtful.

At that time no cladding option was chosen. We will discuss the consequence of this decision later. The dies (total of 30 complete devices) were etched on 4 pieces of one inch by one inch wafers covered by the left over PMMA layer.

11.2 Wafer post-processing

For protection, the wafers were coated with ~2μm Shipley (1813) photoresist, and then soft baked at 95° for 30 min. For the sake of having smooth facets which is essential for light coupling into device, we followed the following procedure

1. We diced the samples into small pieces (less than 1cm by 1cm). Each piece contains at least a couple of dies.
2. We thinned the pieces to less than 150μm. The Allied polisher was used. Fifteen minutes polishing with 45μm diamond suspension granules followed by ten minutes polishing with 9μm diamond suspension granule led to a satisfactory result. The thinning uniformity is important to make the next cleaving step more certain.
3. We used the Sherbrooke University's scriber to scribe the samples and then cleaved them.

Electron Scanning Microscope (ESM) image of a typical facet are depicted in Figure 11.2.1.

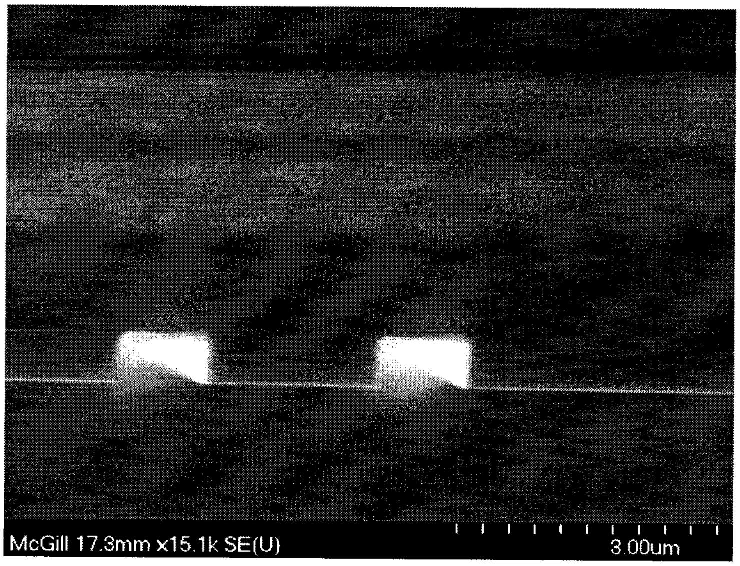

Figure 11.2.1 A typical cleaved facet ESM image

11.3 Optical characterization setup

The schematic of our optical characterization setup is shown in Figure 11.3.1.

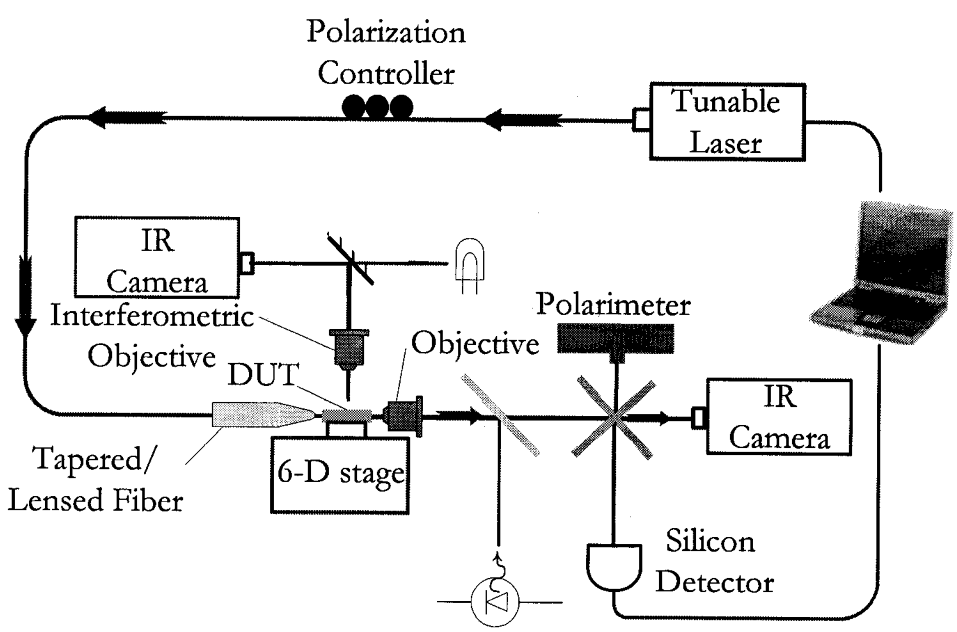

Figure 11.3.1 The optical characterization setup, (6-D stage stands for 6 degrees of freedom)

The laser source is an external cavity laser capable of tuning from 1460 to 1580 nm. The polarization controller is a three-plate type consisting of a ¼ wave plate, a ½ wave plate and a linear polarizer. The input fiber to the polarization controller is a single mode fiber and the output is a polarization maintaining fiber. The device under test (DUT) is excited by a tapered lensed fiber with the output beam-width of 2.5μm. The output power is read by an IR coated 60x objective lens (with a numerical aperture of 0.65). The 6-D stage is capable of moving the DUT on all directions (three translational, and three rotational). The replaceable top objective (at the top of the sample) is initially an interferometric objective (10x, with numerical aperture of 0.30) for leveling the DUT. Ensuring a level sample is crucial for reducing the total coupling losses.

The top objective is then replaced by an "infinity-corrected long working distance objectives". Initially with a 10x objective (with a numerical aperture of 0.28) for the azimuthal alignment of the fiber with the DUT input waveguide, and then by 50x objective (with numerical aperture of 0.45) for the translational alignments. The top IR camera is used the fiber/ DUT alignment with the condenser light. In addition, when the laser is on one can also trace the light inside the sample using the top IR camera. Figure 11.3.2 demonstrates the aligned a tapered lensed fiber with the input waveguides of the DUT. The image has been captured using 50x top objective and the top IR camera. Note that the waveguide width at the die border is 2μm.

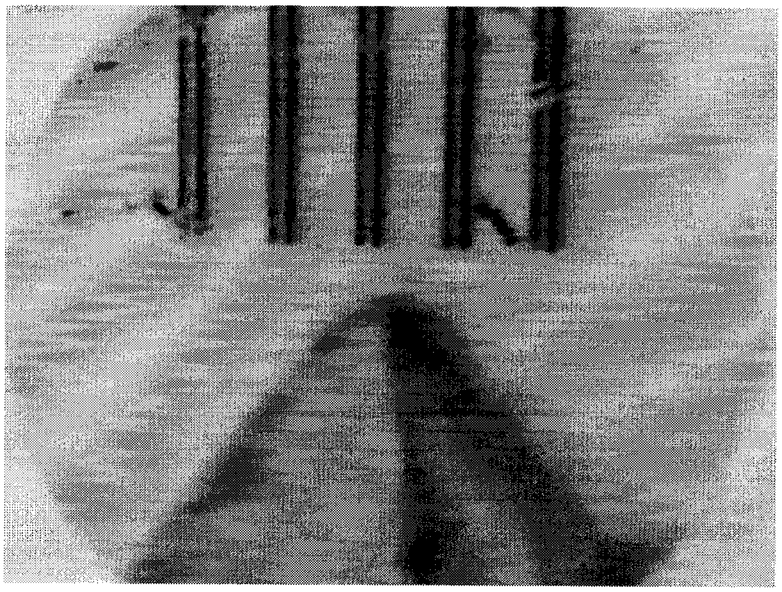

Figure 11.3.2 The images of an aligned tapered lensed fiber with the input waveguide of the DUT

The removable photo diode is for the alignment of the output objective with the output facet. The removable polarimeter is for reading the polarization. The computer and the silicon detector have been programmed to perform the transmission measurement automatically.

The side IR camera is for observing the output facet when the photodiode is on, and then the output mode when the laser is on. Figure 11.3.3 shows the experimental radiation profile of the mode of a $2\times0.5\mu m^2$ SOI waveguide at 1550 nm (Quasi TM mode) when it is excited by a tapered lensed fiber of 2.5 μm beam width. The image is captured with the IR camera and 60x lens. The image data has also been processed for compensating the nonlinearity of the IR camera. Comparing the image with the perfect modal profile of Figure 10.8.4 shows a good agreement which is an indication of good alignment. Our estimation of the total coupling loss is ~15dB (from the tapered lensed fiber to the chip and from the chip to the detector)

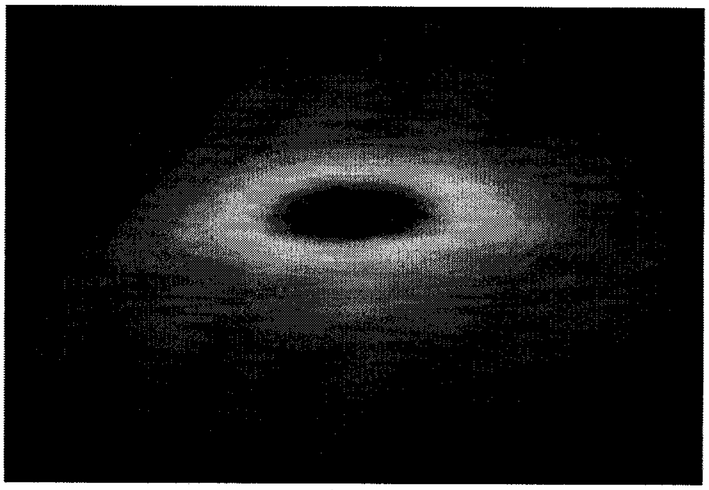

Figure 11.3.3 Experimental radiation profile of the mode of a $2\times0.5\mu m^2$ SOI waveguide at 1550 nm (Quasi TM mode) which is excited by a tapered lensed fiber of 2.5 μm beam width

Irrespective of our confidence regarding the light coupling into the device, unfortunately there was no meaningful light emerging from the prism region. Although our first inspection of the etched patterns indicated that they were satisfactory, this motivated us to make a more careful inspection of the etched patterns. In the next section we will summarize our observations.

11.4 Etching characterization

The etching of patterns with large feature sizes were mostly successful (as the following two figures depict).

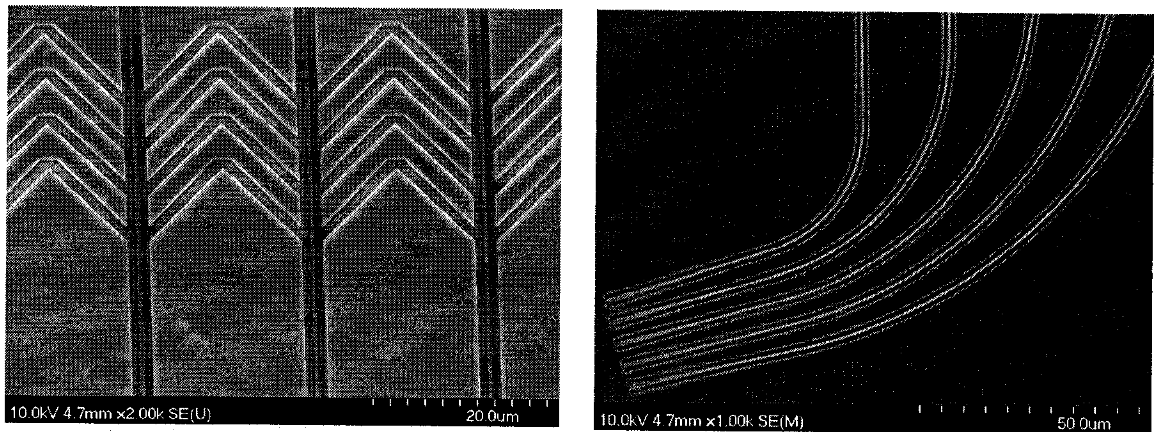

(a) (b)

Figure 11.4.1 (a) the etched chevrons and (b)the input waveguides/slab region on SOI sample

Figure 11.4.2a shows the etching of $0.5\mu m \times 0.5\mu m$ waveguide. As can be seen the etching height and side wall verticality seems acceptable. Figure 11.4.2b shows the side wall roughness of $0.5\mu m \times 0.5\mu m$ waveguide (which is not very satisfactory).

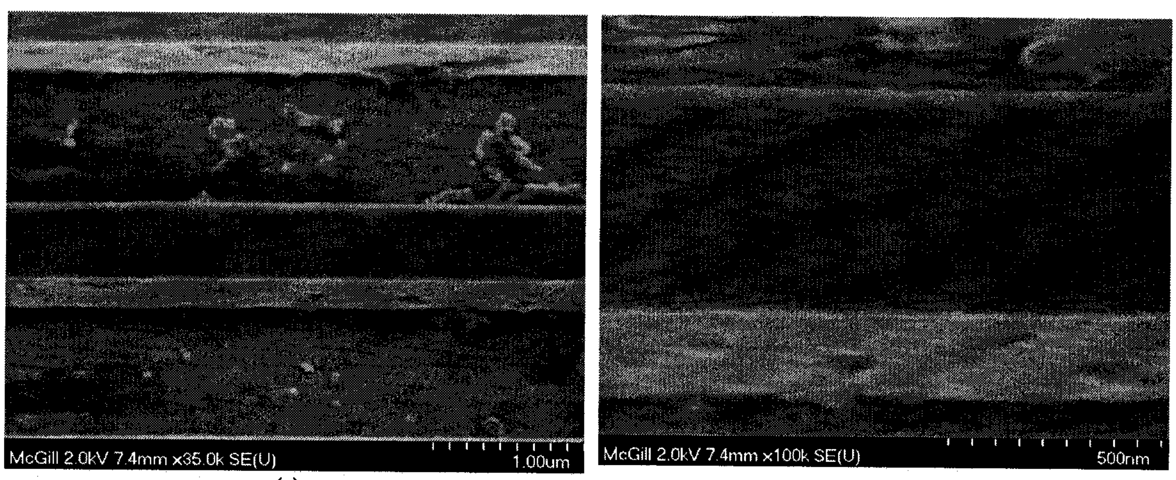

(a) (b)

Figure 11.4.2 (a) the etched $0.5\mu m \times 0.5\mu m$ waveguide (b) its sidewall roughness on SOI sample

However, our careful inspection of the fine patterns (gratings) on many samples revealed that there were systematic flaws (many of them catastrophic). In the following we will categorize them.

The first significant error is that the duty factor of the etched patterns is not according to the design value (which was 0.5 for all cases). As we will show in the next section, the performance of the **k**-vector superprism is very sensitive to this parameter. Figure 11.4.3 shows a typical cross section. As is seen, the duty factor in this case is about 0.4.

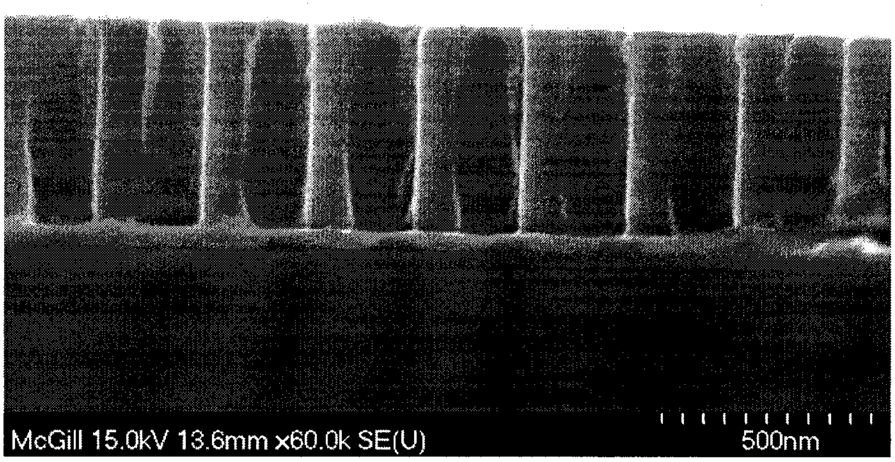

Figure 11.4.3 The cross section of a typical etched grating

The duty factor in many cases was smaller than 0.4 (as Figure 11.4:4a shows the case of a duty factor ~0.3) and in many other cases, it was greater than 0.5 (as Figure 11.4.4 b shows the case with duty factor of ~0.65). On some occasions, the observed duty factor was close to perfect, but unfortunately not over the entire part of superprism. However in the most observed cases, the trenches were over etched (the duty factor was lower than expected).

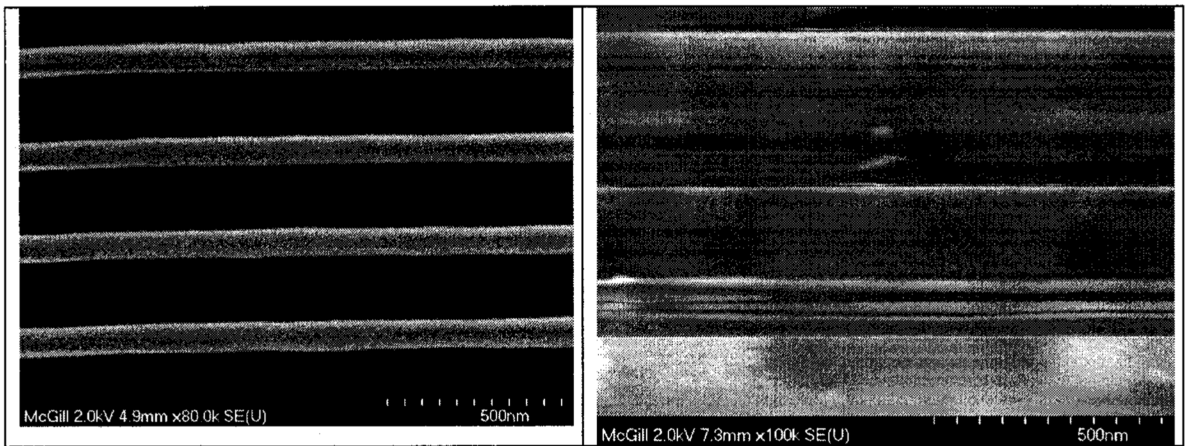

(a) (b)

Figure 11.4.4 The top view of the etched grating, (a) low duty factor of ~0.3 and (b) high duty factor of ~0.65.

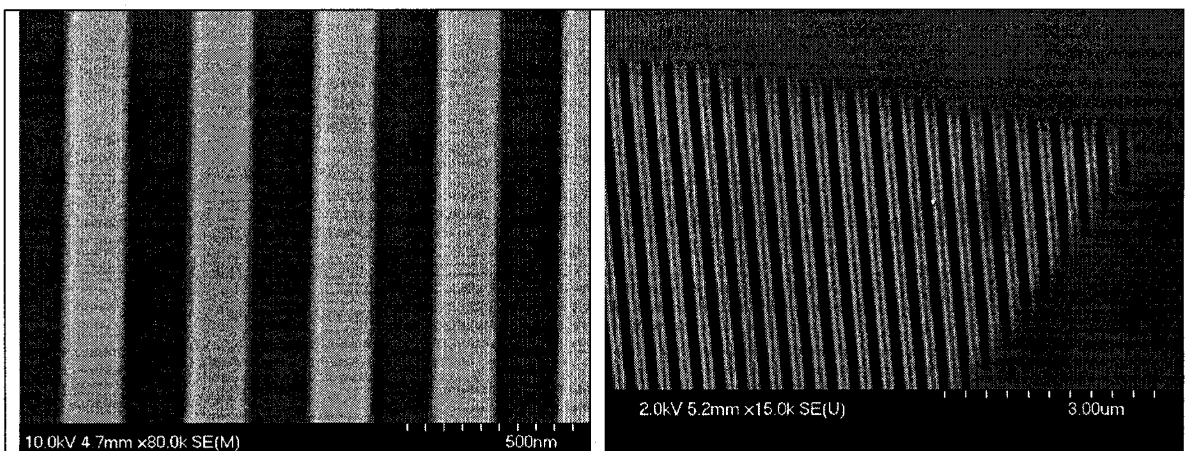

(a) (b)

Figure 11.4.5 (a) and (b) The top view of an almost perfect grating

The second error was the non-uniformity of duty factor along the prism region. In other words, the duty factor was changing over the prism area. Usually the duty factor variation (of about 0.1) occurs smoothly over the prism region. However in cases, the duty factor changed abruptly. Figure 11.4.6 shows such a situation.

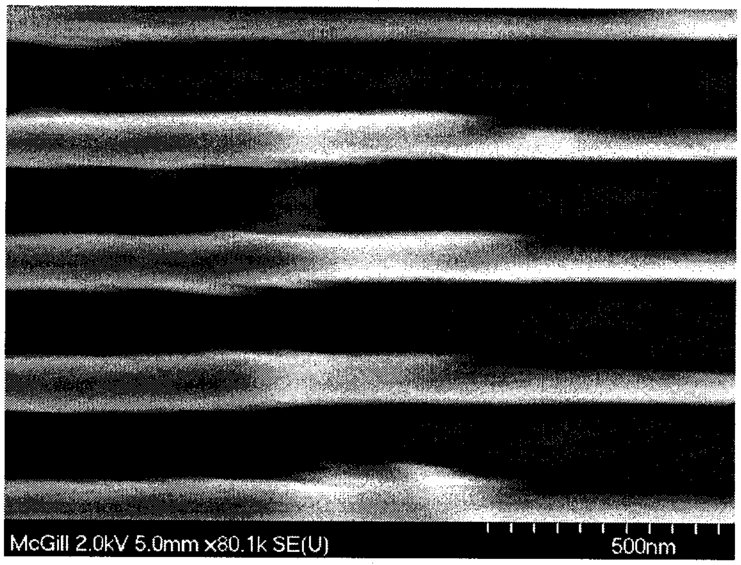

Figure 11.4.6. A sudden change of duty factor from 0.41 to 0.27.

The third error was dislocation of the grating patterns and misprinting. Figure 11.4.7 and Figure 11.4.8 shows two of such cases.

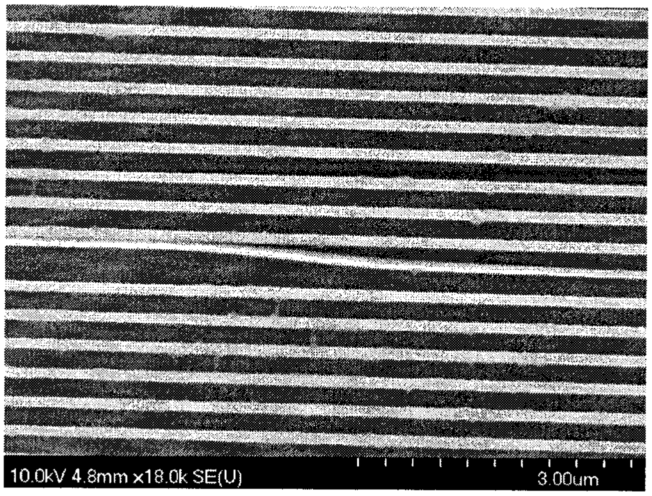

Figure 11.4.7 Grating pattern dislocation

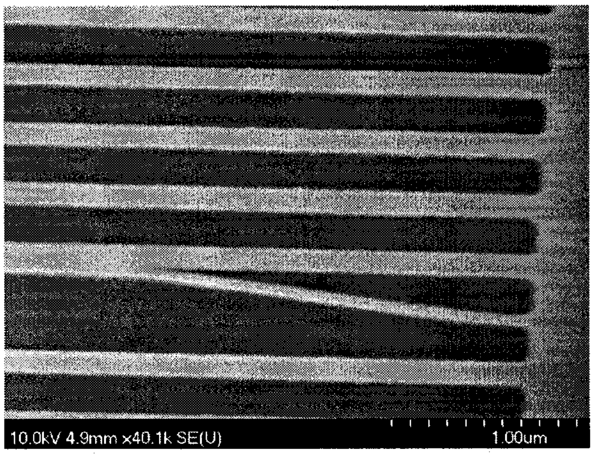

Figure 11.4.8. Grating pattern misprinting

The forth and the fifth are fabrication imperfections such as the bad and non-uniform etching. Figure 11.4.9 shows two typical cases of bad and/or non-uniform etchings.

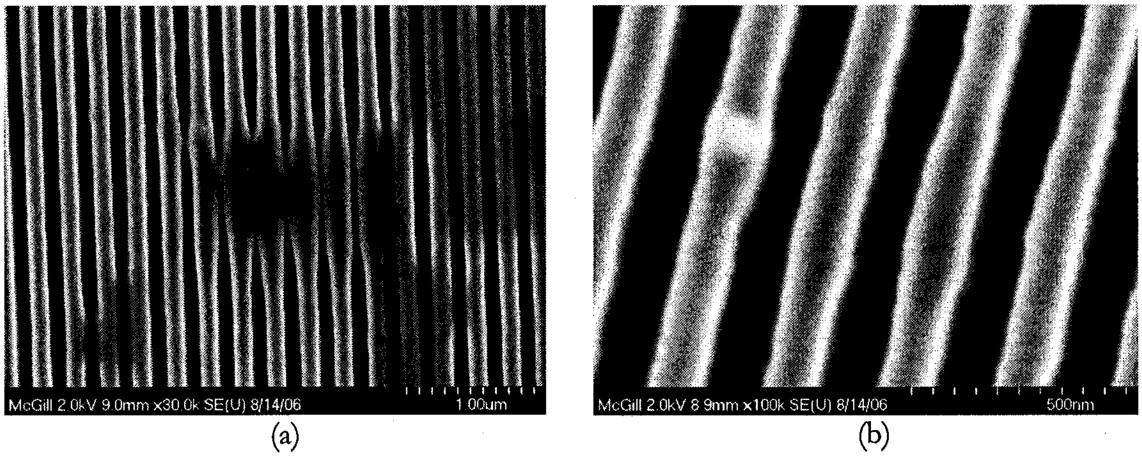

Figure 11.4.9 Typical (a) bad and (b) non-uniform etchings

The last error is also a fabrication imperfection. The etch pattern of the top silicon layer is not uniform and the side walls are not sufficiently smooth. This imperfection can be seen from cross section of Figure 11.4.3.

Although the three last defects are not disastrous (they will cause more scattering loss) the first three ones are catastrophic. In the next section, we will perform a sensitivity analysis of the **k**-vector superprism which shows the importance of having the duty factor under control.

11.5 Sensitivity analysis

The scaling law of photonic crystal is the duality of wavelength and dimensions. In other words, if we want an accurate central wavelength, accurate fabrication techniques are needed. To illustrate this more quantitatively, assume that the fabrication tolerances are on the order of 10nm. Assuming the 1-D photonic crystal of period 275nm, then approximately the central wavelength will be shifted by

$$\frac{\Delta\lambda}{\lambda_0}=\frac{\Delta\Lambda}{\Lambda},\quad \Delta\lambda=\frac{\pm 10}{275}\times 1550\simeq\pm 55\text{ nm} \tag{11.1}$$

Considering the channel spacing of 0.8nm, this is a large deviation. Furthermore unfortunately the **k**-vector superprism is also very sensitive to the duty factor of the 1-D photonic crystal. Figure 11.5.1 shows a typical bandgap variation of one of our design versus the duty factor. As can be seen for this case, a duty factor of less than 0.42 (*i.e.*, trench over etching greater than 22nm) causes the bandgap to disappear. Note that the total internal reflection happens if the duty factor becomes smaller. This may explain the reason that we could not observe any transmitted light out of the prism region.

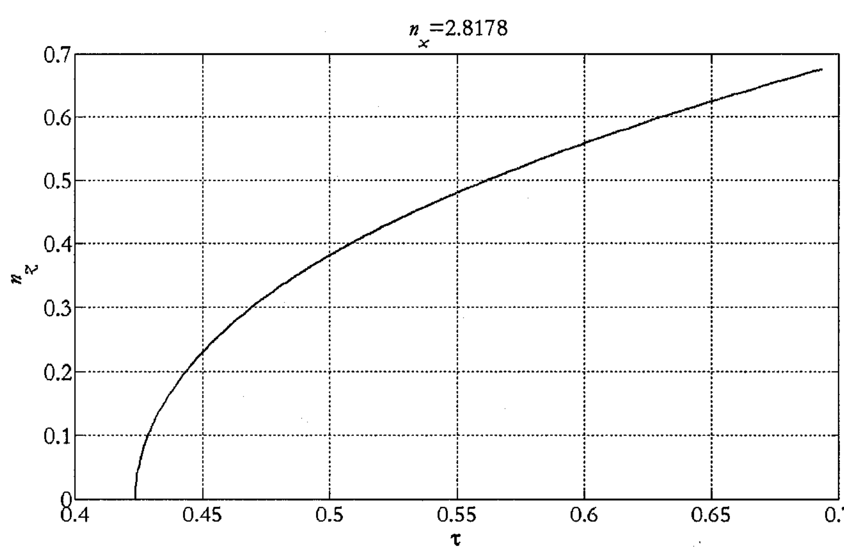

Figure 11.5.1 Normalized bandgap variation versus duty factor for a 1-D photonic crystal of period $\Lambda = 275\,\text{nm}$ and at the wavelength of $\lambda = 1549.82\,\text{nm}$

11.6 Challenges ahead and some recommendations

As we have demonstrated in the last section, the dimension and duty factor sensitivity of the 1-D **k**-vector superprism is behind the fabrication challenges. Precise control of the dimension and etching profile is crucial. The etching uniformity is also important.

The option of no cladding had the following consequences

- Exposure of the fine structure to potential external damage. The damages start to emerge after a soft cleaning of the sample (washing with edge bead remover, acetone, and isopropanol alcohol). Figure 11.6.1 shows a typical case.

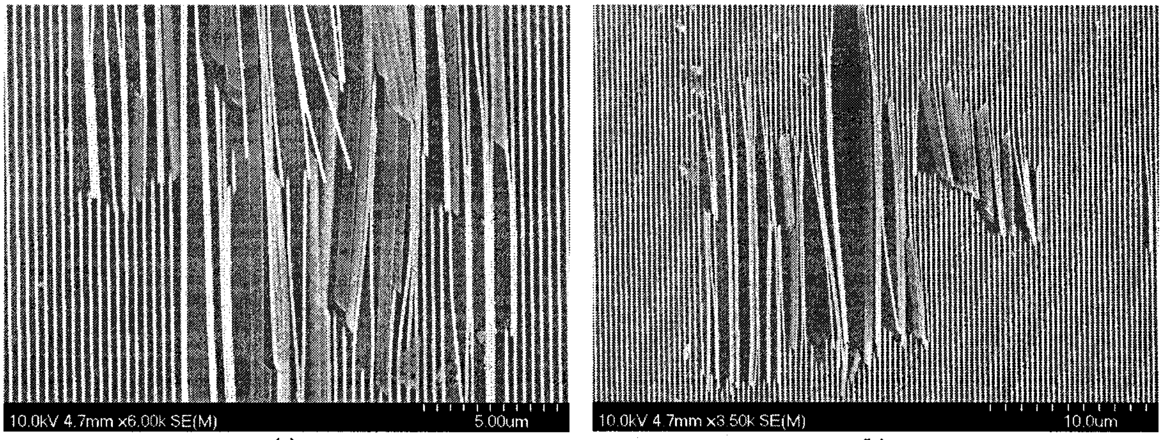

(a) (b)

Figure 11.6.1 (a) and (b) Typical grating damages right after soft cleaning

- The damage often became worse after the samples had undergone the stress of the thinning process (which includes using wax, heating the sample, removing and cleaning the wax). Some worse cases have been depicted in Figure 11.6.2

(a)

(b)

Figure 11.6.2 (a) Broken waveguide and (b) smeared waveguide due to the stress of post-processing

- The built in stress along the long grating lines could be a source of breakage. Figure 11.6.3 shows a typical site.

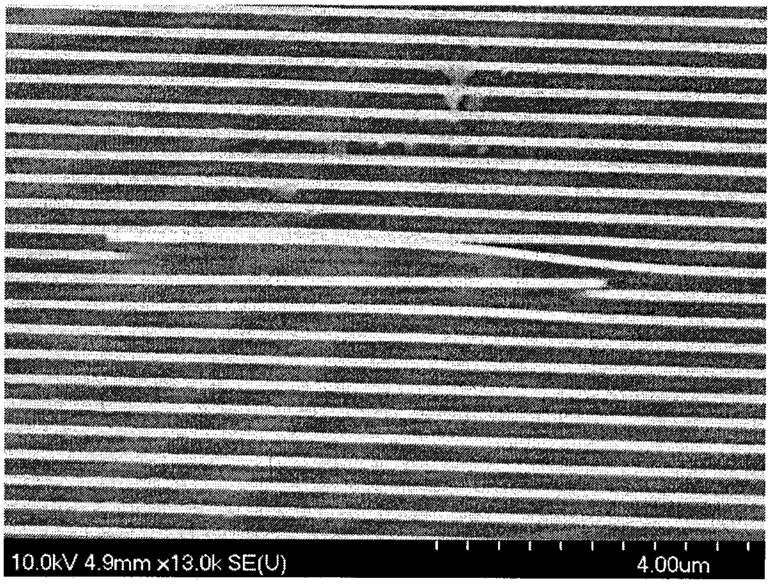

Figure 11.6.3 The stress along the grating lines which seems to be the source of breakage

- We could not use the dicing and side polishing technique which is a well established technique for making a good facet. Instead we worked with tiny fragile SOI samples of 150μm width.

For the sake of all of the above points we recommend the developing of a cladding layer over the entire device. The PECVD silicon oxide can be grown over the wafer, or methylsiloxane polymers can be spin coated over the sample. A special family of this polymer is capable of filling small ditches up to 100nm (Honeywell ACCUGLASS T-14 family, http://www.honeywell.com/). Considering modified refractive index distribution, we would need to change the design. The dispersion in the new design would be lower, and consequently the sensitivity would be lower, however the prism area would be larger. We need to control the accuracy of the electron beam writer and etching profiles. Electron beam exposure bracketing is also recommended.

References

[1] W . N. Ye, D.-X. Xu, S. Janz, P. Cheben, A. Delage, M. J. Picard, B. Lamontagne, and N. G. Tarr, "Stress-induced birefringence in silicon-on-insulator (SOI) waveguides," *Proc. SPIE*, vol. 5357, pp. 57-66, 2004.

Chapter 12

CONCLUSIONS

In this chapter we conclude the thesis. We summarize the main issues and our contributions. We also comment on possible future work.

12.1 Introduction

Planar lightwave circuits on the SOI platform using the well known patterning techniques of microelectronics are a good candidate technology making the future optical integrated circuits. Using a similar or at least a compatible technology, such an integrated device must contain all the components necessary for doing a specific task. It is in this context that the objective of this thesis which was to demonstrate the capability of superprism for making a miniaturized demultiplexer is situated. Usually, there is a long time that must elapse between an emerging idea and a realistic device. Although it is now about two decades since the superprism phenomenon was first observed [1], a practical device has yet to be demonstrated. There are many obstacles to overcome. The first astonishing superprism observation was on 3-D photonic crystal using high refractive index contrast of pseudo-2-D auto-cloned photonic crystal. The observed large degree of beam steering (later called the **S**-vector superprism) indeed occurred over a narrow range of spectrum, and the transmitted beam had lost a lot of its spatial coherence. Evolution of the 3-D photonic crystal superprism to the slab 2-D counterpart makes fabrication much easier but it also results in about 10 times dispersion reduction [2]. Then the first order calculation showed that loss of spatial coherence of the beam prevents the device from resolving fine wavelengths [3]. That analysis concluded that the size of the device makes the photonic crystal **S**-vector demultiplexer more suitable for CWDM applications. However, the dispersion across the wider CWDM bandwidth is so nonlinear that linear analysis is not sufficient for designing a practical device. There were attempts to improve the coherence recently, but the resulting bandwidth is not still suitable for CWDM applications [4;5].

The phase velocity dispersion was exploited for making superprisms in the millimeter wave range of the spectrum [6]. We then pioneered the exploitation of phase velocity dispersion in the optical spectrum using a 1-D photonic crystal [7]. We have shown that a DWDM demultiplexer is feasible and that the size of the device is very small when compared to the alternatives. This configuration was later called the **k**-vector superprism [8]. No experimental results for the **k**-vector superprism in the optical spectrum have yet been reported.

Any accurate design must be based on accurate modeling techniques. The plane wave expansion method with supercell definition has been used for obtaining the wave vector diagram of slab photonic crystals. The speed and accuracy of the method has been improved considerably using the block-iterative frequency-domain methods [9]. However obtaining the complete wave vector diagram requires the whole Brillouin zone to be scanned (for a given wavelength). Furthermore obtaining the wave vector at any quiescent point needs some sort of interpolation method to be applied which is not particularly accurate. There is also no trace of any leaky modes in the method due to the application of the supercell technique.

Since any optimization techniques usually rely on repeated simulations of the structure with different parameters, the current plane wave expansion method is not suitable for such a task due to its high computational demands. Loss of accuracy at the expense of speed is an acceptable trade off for such methods.

The high scattering loss of the light propagating through a photonic crystal and low coupling loss of the light into the photonic crystal are two drawbacks of the planar superprisms. Whilst the former can be mitigated using more accurate fabrication techniques, the later needs to be addressed through the design. Reliable transmission and reflection modeling of the bulk photonic crystal is necessary to obtain any practical designs. Full 3-D FDTD modeling of the structure exhausts the computer resources and there is no other reliable technique for this issue. Mode matching using bound and leaky modes is a valuable technique to obtain a reliable transmission and reflection coefficients. However, leaky modes of the slab photonic crystals are not well known, and the plane wave expansion method with supercell definition cannot trace them.

A focusing element is a crucial part of the superprism demultiplexers. It is the main component of our layout for **k**-vector superprism and it is necessary element for an **S**-vector when the output beam width becomes excessive. A waveguide lens with a relatively large $f/\#$ and bandwidth is required for our task. The superlenses with very short focal length [10] are not suitable for our task.

12.2 S-vector superprism

In chapter 6 we have developed general design equations for designing a demultiplexer using **S**-vector superprism phenomena based on the first band of photonic crystals. First, we obtained a criterion for obtaining the best lattice parameters. We have shown that average group velocity at the bandedge is a suitable indicator of the available dispersion. We have selected the lattice parameters taking the micro-fabrication limitation into account (we have assumed a minimum feature size greater than 75μm). A 3-D plane wave expansion method with supercell technique has been employed to insure a more realistic design than the equivalent 2-D counterparts. The 2-D hexagonal lattice provides an order of magnitude higher angular dispersion than 1-D photonic crystal. The angular dispersion of 2-D square lattice was near to the hexagonal one.

We have defined the minimum resolution length and calculated it for all channels. We have modified the conventional **S**-vector superprism geometry in order to reduce the total area of the superprism. Now the superprism area only accommodates the area necessary for the beams to propagate and resolve neighboring channels. Usually the dispersion is high enough that the Gaussian beams are resolved from the neighboring channels in the near field. We have derived a more accurate model to evaluate cross talk in the near Gaussian field. Based on our model, we have concluded that the resolution is more critically dependent on the beam divergence inside the photonic crystal than on angular dispersion. As result the 1-D photonic crystals provide the best resolution, despite their lower angular dispersion.

We have shown that a 4-channel CWDM demultiplexer with a theoretical cross talk level of 20 dB can be made with a the prism area of $1367\,\mu m^2$. A typical SOI wafer technology with a top silicon layer thickness of 260 nm has been used for our simulation. The input beam width is about 1.5 μm and the maximum output beam width is about 3 μm. This size is about 500 times smaller than AWG on the similar platform.

Our investigation also shows that it is not easy to design higher channel count demultiplexers based on the **S**-vector superprism phenomenon due to the high non-uniformity of the band diagram as it evolves with the wavelength. In chapter 7, we have introduced a novel concept for higher count (wider band) demultiplexers. We have shown that a stratified photonic crystal is capable of reducing the superprism area by five times. The slant angle in each layer has been selected for maximizing the dispersion for a particular channel, and for reflecting back the proceeding channels and refracts the succeeding ones. We have shown that we only need a 0.26 mm^2 photonic crystal area to resolve 8-channel CWDM demultiplexer (with 160nm bandwidth). The non-uniformity of the output channel width also shows tremendous improvement over the conventional superprism.

For having a practical CWDM demultiplexer based on the **S**-vector superprism, there are some issues to be addressed and also some ideas to explore more.

1. The main issue of the multiplexer is the coupling loss of the input beam into the photonic crystal bulk and from the bulk into the output waveguide. Working near the bandedge for the sake of having higher dispersion is causes the low coupling efficiency. Modeling is more complicated due to the Gaussian nature of the beams. For the input coupling, we have to consider the divergence of the incident beam, and the group of Bloch modes that are involved in the coupling. For the output coupling on the other hands we have to consider the Bloch modes which are involved in the propagation and the Gaussian modes which are allowed to propagates. Lack of any accurate model is clear. As we have shown in chapter 6, any practical design has to use the full 3-D modeling especially when the refractive index contrast is high. So the coupling issue has to be addressed in full 3-D modeling finally.

2. The rapid loss of spatial coherence is another factor that over sizes the conventional superprism. Although preconditioning is a novel idea [5], we need some other means with the bandwidth suitable for CWDM applications. Our stratification technique is also an idea that can be explored further by varying other lattice parameters of each section (we only change the slant angle).
3. The wave propagation in a stratified media in the limit can be considered as the wave propagation in the inhomogeneous media (*i.e.*a gradient refractive index medium). Any abrupt reflection can be replaced by a smooth turn (similar to radio wave reflection from the ionosphere or in a gradient refractive index lens). Hamiltonian optics has been suggested for the modeling of the light propagating in non-uniform photonic crystal [11], but it has to be explored more.
4. Polarization sensitivity of the photonic crystal is also problematic. An ideal demultiplexer has very low polarization dependence. However wave propagation in a conventional photonic crystal is sufficiently anisotropic, that a polarization beam splitter has been made from it [12]. Either polarization compensation elements must be developed or a new structure and/or new photonic crystal atoms must be found that show very low polarization sensitivity.

12.3 k-vector superprism

In chapter 8, a complete optical design of a demultiplexer based on photonic crystal **k**-vector superprism has been proposed. The first integrated layout for the high contrast material has been introduced.

Once again we have used the group velocity at the bandedge as the indicator for the available dispersion. Based on this indicator, we have selected the photonic crystal parameters in order to obtain the best **k**-vector superprism performance. We have developed design equations and design rules, for the **k**-vector superprism. We have discussed various operating points and showed that there is a great advantage to work in the second Brillouin zone and select the parameters so that the beam expands through the photonic crystal. As before, the superprism is large enough for the beam to expand and providing the desired resolution, and the nonlinearity of dispersion has been taken into account. An optimal design maximizes the phase velocity dispersion and minimizes the group velocity dispersion as much as possible. Interestingly, we have shown that the 1-D photonic crystal has the smallest superprism area of 99,200 μm^2, which provides sufficient resolution to demultiplex 32 channels in the *C* band with a 0.8 nm (100Ghz) channel spacing. The 2-D square lattice is very close to the smallest size, while the best 2-D hexagonal superprism is larger by 45%.

The maximum phase and the minimum group velocity dispersion is an ideal case for having small demultiplexer, but this appears to be an impossible condition. This is the reason that the 2-D hexagonal lattice with high dispersion (both phase and group) has the largest superprism area.

The chip size excluding the input and the output sections is approximately 4.5 times smaller than the etched grating demultiplexer on the same platform.

One of the main components of our proposed layout is the focusing element. In chapter 9 we have introduced a new class of lenses by introducing rotational periodicity of the lattice. By keeping the 1-D patterns parallel to the rays, we have avoided the difficulty of misalignment between the group and phase velocities in photonic crystals. The azimuthal effective index method has been modified in order to obtain the effective index for the radially propagating rays. Many types of lenses can be designed but we chose to design a lens for collimating light emitted from a waveguide into the slab region. We have shown that 658 μm^2 lens area is enough to collimate 100 μm beam. The focal length is 130μm. The lens performance appears to be good in simulation.

In chapter 10, the mathematical equations necessary to design the mask for the proposed layout has been presented. Many aspects of waveguide designs have been discussed there.

This multiplexer type has also some issues to be solved before become a practical device, and there are also some ideas to be explored.

1. Similar to the previous case, coupling into and out of the photonic crystal must be improved, but the case is less complicated than the **S**-vector case. The incident beam can be treated as a plane wave, the refracted wave as a Bloch mode (if the quiescent

point has been chosen correctly) and the transmitted wave as a plane wave again. There are some pioneering works in this regards (including projected holes, adiabatic tapering, and diffraction grating) [13-16].

2. A practical demultiplexer for DWDM channel spacings must bring under control the sensitivity of the structure to the temperature. Any wavelength drift must be a small fraction of channel spacing. For high count multiplexers, the low power than many inputs carry may be a source of significant heat due to propagation loss through the device. We should therefore investigate the sensitivity of the **k**-vector superprism to temperature, and if it is too sensitive, we need to develop about a means to reduce it.
3. Tuning the central wavelength of a **k**-vector superprism with input optical power, (or to an external source) is an interesting idea. Design imperfections or even the wavelength shift with temperature can be compensated using an external light source. Applying the proposed method to a study the Kerr-type nonlinearity of **k**-vector superprism, we have also pioneered an approach in this area too. But our method is only approximate and we need more accurate modeling, especially when the index contrast is high.
4. The possibility of implementing our photonic crystal lens in the **k**-vector layout is interesting to explore. The other types of the lens (plano-concave) can be designed which is more suitable for integrating with the prism. Figure 12.3.1 shows the concept. Note that the passing of the beam through different photonic crystal regions in the limit can be modeled using Hamiltonian optics [11].
5. Although the modeling which has been used for the lens design is a 3-D one, however, its small size makes it a possible candidate for FDTD analysis. It is possible to test the validity of our lens design with FDTD simulation.

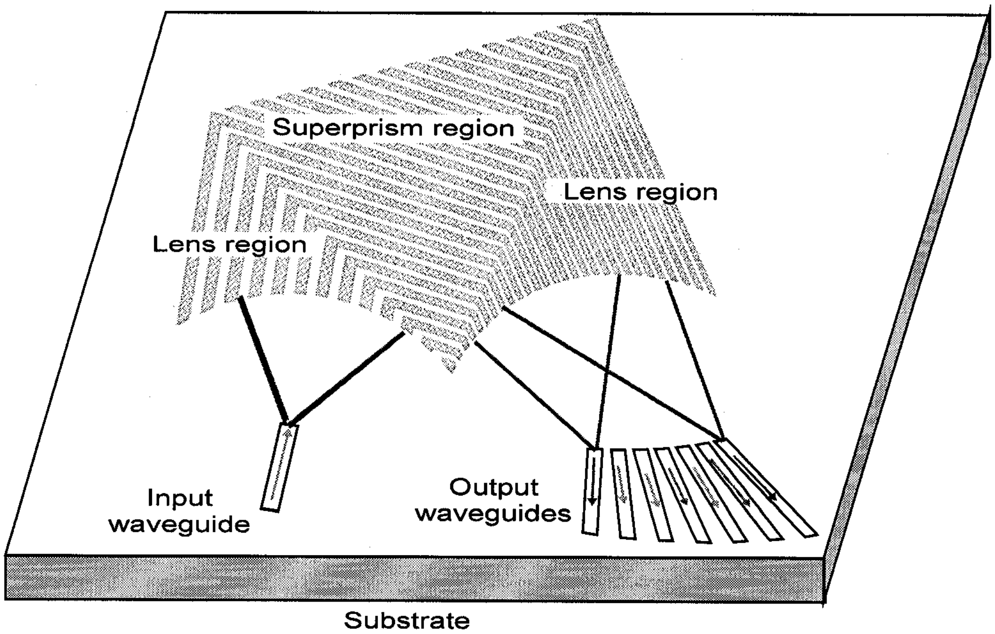

Figure 12.3.1 An integrated superprism and lens designed with 1-D photonic crystal.

12.4 Modal analysis

In chapter 4 we have presented an approximate analytical method for the analysis of slab 1-D photonic crystal. The method is an extension of the known weighted index method for rectangular dielectric waveguides, and is capable to be applied to some slab 2-D photonic crystal too.

Compared to the accurate finite elements results, the accuracy of the weighted index method is good in the low refractive index contrast systems ($\Delta n \approx 0.5$), but it deteriorates as the refractive index contrast becomes higher ($\Delta n \approx 2$).

The weighted index method has also been extended to handle the nonlinear slab 1-D photonic crystal. Merging the loop of the weighted index method with the loop of the nonlinear routine will speed up the method considerably. The resultant method is simpler, and converges virtually as fast as the conventional perturbation feedback method (through 4 to 8 iterations). Here are some ideas for further to exploration of the weighted index method.

1. The study of low contrast photonic crystals is an emerging field. The low scattering loss and the possibility of making large photonic crystals with various methods make it interesting [17]. For such an application the weighted index method is choice: accurate enough but very fast.
2. The application of the method in nonlinear periodic structure can be further explored. Investigating soliton wave propagation in 1-D photonic crystal is interesting [18].

In chapter 5, we presented a new method based on the conventional plane wave expansion method. The method is capable of obtaining a spectrum of slab 1-D photonic crystal mode including leaky mode (which is valuable for replacing the continuum of radiation modes in the conventional mode matching technique) However, the method as presented here is computationally more intensive than the state of art plane wave expansion method. Although we have to execute the plane wave expansion program numerous times, thanks to the Bloch variational iterative formula[9], the method is relatively fast. The method can trace the leaky modes through the Brillouin zone, and the fact that it needs less Fourier components in the non-periodic direction make it attractive. This method has a lot of capability to be explored, including

1. The full 3-D reflection and transmission can be modeled using the leaky modes obtained in chapter 5.
2. The method is basically is at the same level as the very first introduction of the plane wave expansion method, so one can expect that the efficiency of the method can be improved using more sophisticated eigenvalue solver.
3. The more accurate mode characterization of slab photonic crystal is doable (similar as 2-D rectangular dielectric waveguides) using the results of the method. This will shed light on the dark side of mode matching and what is behind it.

The last section we explain our achievements and present our comments regarding our experimental results.

12.5 Experimental results

In chapter 11, we have reviewed our attempt to design, fabricate, post-process and experimentally characterize the of the **k**-vector superprism.

Parametric mask design for the proposed **k**-vector superprism demultiplexer has been done. An SOI wafer with a top silicon layer of 0.5 μm thickness was selected for fabrication. Ten different demultiplexer designs for resolving 16 standard DWDM channels were developed. The mask data for thirty full demultiplexers were sent for fabrication. An optical characterization setup suitable for coupling light into and reading power out of the samples with submicron waveguides was designed and constructed. Unfortunately, the sensitivity of our design to fabrication imperfections and unsatisfactory fabrication quality prevented us from obtain any meaningful experimental results. For the next step of the project, we suggest the development of cladding through new device design. More accurate and careful fabrication is also needed.

References

[1] H . Kosaka, T. Kawashima, A. Tomita, M. Notomi, T. Tamamura, T. Sato, and S. Kawakami, "Superprism phenomena in photonic crystals," *Physical Review B*, vol. 58, no. 16, pp. 10096-10099, Oct.1998.

[2] T . F. Krauss, R. M. Delarue, and S. Brand, "Two-dimensional photonic-bandgap structures operating at near infrared wavelengths," *Nature*, vol. 383, no. 6602, pp. 699-702, Oct.1996.

[3] T . Baba and T. Matsumoto, "Resolution of photonic crystal superprism," *Applied Physics Letters*, vol. 81, no. 13, pp. 2325-2327, Sept.2002.

[4] J . Witzens, T. Baehr-Jones, and A. Scherer, "Hybrid superprism with low insertion losses and suppressed cross-talk (vol E 71, art no 026604, 2005)," *Physical Review e*, vol. 71, no. 3 Mar.2005.

[5] B . Momeni, J. D. Huang, M. Soltani, M. Askari, S. Mohammadi, M. Rakhshandehroo, and A. Adibi, "Compact wavelength demultiplexing using focusing negative index photonic crystal superprisms," *Optics Express*, vol. 14, no. 6, pp. 2413-2422, Mar.2006.

[6] S . Y. Lin, V. M. Hietala, L. Wang, and E. D. Jones, "Highly dispersive photonic band-gap prism," *Optics Letters*, vol. 21, no. 21, pp. 1771-1773, Nov.1996.

[7] A . Bakhtazad and A. G. Kirk, "Superprism effect with planar 1-D photonic crystal," *Proceedings of the SPIE*, vol. 5360, pp. 364-372, June2004.

[8] T . Matsumoto and T. Baba, "Photonic crystal **k**-vector superprism," *Journal of Lightwave Technology*, vol. 22, no. 3, pp. 917-922, Mar.2004.

[9] S . G. Johnson and J. D. Joannopoulos, "Block-iterative frequency-domain methods for Maxwell's equations in a planewave basis," *Optics Express*, vol. 8, no. 3, pp. 173-190, Jan.2001.

[10] T . Matsumoto, K. Eom, and T. Baba, "Focusing of light by negative refrction in a photonic crystal slab superlenss on silicon-on-insulator substrate," *Optics Letters*, vol. 31, no. 18, pp. 2786-2788, Sept.2006.

[11] P . S. Russell and T. A. Birks, "Hamiltonian optics of nonuniform photonic crystals," *Journal of Lightwave Technology*, vol. 17, no. 11, pp. 1982-1988, Nov.1999.

[12] L . J. Wu, M. Mazilu, and T. F. Krauss, "Beam steering in planar-photonic crystals: From superprism to supercollimator," *Journal of Lightwave Technology*, vol. 21, no. 2, pp. 561-566, Feb.2003.

[13] J . Witzens, M. Hochberg, T. Baehr-Jones, and A. Scherer, "Mode matching interface for efficient coupling of light into planar photonic crystals," *Physical Review e*, vol. 69, no. 4, p. Art. No. 046609 Part 2, Apr.2004.

[14] B . Momeni and A. Adibi, "Adiabatic matching stage for coupling of light to extended Bloch modes of photonic crystals," *Applied Physics Letters*, vol. 87, no. 17, p. Art. No. 171104, Oct.2005.

[15] T . Baba and D. Ohsaki, "Interfaces of photonic crystals for high efficiency light transmission," *Japanese Journal of Applied Physics Part 1-Regular Papers Short Notes & Review Papers*, vol. 40, no. 10, pp. 5920-5924, Oct.2001.

[16] T . Baba, T. Matsumoto, and M. Echizen, "Finite difference time domain study of high efficiency photonic crystal superprisms," *Optics Express*, vol. 12, no. 19, pp. 4608-4613, Sept.2004.

[17] C . Liguda, G. Bottger, A. Kuligk, R. Blum, M. Eich, H. Roth, J. Kunert, W. Morgenroth, H. Elsner, and H. G. Meyer, "Polymer photonic crystal slab waveguides," *Applied Physics Letters*, vol. 78, no. 17, pp. 2434-2436, Apr.2001.

[18] R . Morandotti, H. S. Eisenberg, Y. Silberberg, M. Sorel, and J. S. Aitchison, "Self-focusing and defocusing in waveguide arrays," *Physical Review Letters*, vol. 86, no. 15, pp. 3296-3299, Apr.2001.

Appendix A

A FINITE ELEMENT METHOD FOR ANALYZING OF SLAB 1-D PHOTONIC CRYSTAL

A vectorial finite element method is introduced for the analysis of a slab 1-D photonic crystal. The periodic boundary condition is imposed on the periodic direction, while essential boundary conditions are adopted for the two other transversal directions after inserting enough perfectly matched layer absorber in non periodic direction. Numerical results illustrate the method. Some comments on the other alternatives are also presented.

2.1 Introduction

The Finite Element Method (FEM) has already been used to model 2-D and 3-D photonic crystals [1;2]. Note that 1-D photonic crystal has an analytic solution [3]. Periodic boundary condition and Floquet theory can be implemented implicitly [1], or explicitly [2]. Using FEM, the modeling of periodic structures that has been done so far, is based on the assumption that the refractive index of the structure is uniform in non-periodic direction which may not be the case generally. In slab photonic crystals, the structure is periodic in one or two directions, while the refractive index in the third direction is arranged to confine light in that direction. In our case, the structure is periodic in *x* direction, uniform in *z* direction (direction of propagation) and inhomogeneous in *y* direction (light confinement direction which is normal to the slab).

There has been a lot of interest in the last two decades to implement FEM on dielectric waveguides with open boundaries. We have chosen edge type of FEM, which enables us to model full vectorial Helmholtz's equation. Edge type FEM guarantees the continuity of tangential field components across element interfaces, while allowing discontinuity in normal components, and by implicitly applying the divergence equation, it eliminates the so called spurious modes[4]. We have also employed Berenger's Perfectly Matched Layer (PML) as an absorbing layer [5]. This kind of artificial absorber shows less sensitivity to the wave incidence angle and frequency. Essential boundary condition is applied to enclose the computational domain in y direction (normal to the slab).

This appendix has been arranged in four sections. In section 2, the implementation of periodic boundary condition together with Floquet theory in implicit form is reviewed. In section 3, we will show how PML can be implemented and how the corresponding matrix elements are affected. In section 4, more comments alongside with some guidelines for further research are presented.

A.2 Periodic boundary condition

In explicit form, one can change the workable variable to Bloch eigenvector and use Maxwell's equations for Floquet's wave, while in implicit form Bloch eigen values are introduced through parameters in interpolation functions. They are equivalent in a sense that they lead to the same results. We have adopted implicit form for the sake of easiness. Rewriting Eq.(3.1) in a more familiar form for FEM implementation

$$\nabla_t \times \left(1/n^2\right)\left(\nabla_t \times \mathbf{H}_t\right) - \left(1/n^2\right)\nabla_t\left(\nabla_t \cdot \mathbf{H}_t\right) - \left(k_0^2 + k_z^2/n^2\right)\mathbf{H}_t = 0 \qquad \text{(A1)}$$

The weighted residual formulation of the Helmholtz Eq.(A1) is given by

$$\iint_A \left\{\left(\nabla_t \times \mathbf{W}\right)\cdot\left(1/n^2\right)\left(\nabla_t \times \mathbf{H}_t\right) - \mathbf{W}\cdot\left(1/n^2\right)\nabla_t\left(\nabla_t \cdot \mathbf{H}_t\right) - \left(k_0^2 + k_z^2/n^2\right)\mathbf{W}\cdot\mathbf{H}_t\right\} dA$$
$$-\oint_\Gamma \mathbf{W}\times\left(1/n^2\,\nabla_t \times \mathbf{H}_t\right)\cdot\mathbf{n}\,d\Gamma = 0 \qquad \text{(A2)}$$

where A is the area of the periodic unit cell (see Figure A.2.1), Γ represents the perimeter of A and $\mathbf{W}$ is some arbitrary weighting function.

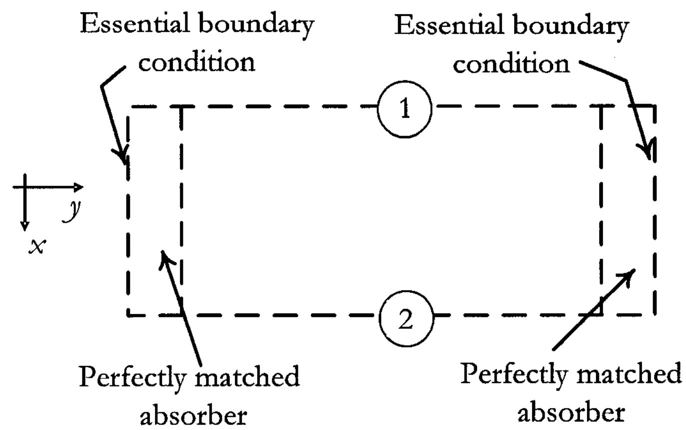

Figure 0.1. Unit cell of a singly periodic 2-D structure

In non-periodic cases the line integral in Eq.(A2) is eliminated by constraining the FEM trial functions ($\mathbf{H}_t$) and weight functions $\mathbf{W}$ to vanish wherever the essential boundary condition ($\mathbf{H}_t = 0$) on Γ applies, while the natural condition $(\nabla_t \times \mathbf{H}_t)\cdot\mathbf{n} = 0$ requires no further action. Such steps can also be taken here but do not account for the portions of Γ corresponding to the unit cell periodic closures. The latter are taken into account by employing Floquet's theorem. Thus, the degrees of freedom of $\mathbf{H}_t$ associated with non-overlapping geometric parts (1 and 2) of the unit cell in Figure 0.1 are related as follows

$$\mathbf{H}_t^2 = \mathbf{H}_t^1 \exp\left(-ik_x\Lambda\right) \tag{A3}$$

where k_x is the Floquet wave number. Constraining the weight functions with reciprocal factors $\exp\left(ik_x\Lambda\right)$ so that

$$\mathbf{W}_2 = \mathbf{W}_1 \exp\left(ik_x\Lambda\right) \tag{A4}$$

It follows that the line integral around Γ will be canceled because of equal and opposite normal vectors $\mathbf{n}$ on the first and the second boundaries. Thus instead of Eq.(A1) a residual

$$\iint_A \left\{\left(1/n^2\right)(\nabla_t \times \mathbf{W})\cdot(\nabla_t \times \mathbf{H}_t) - \left(1/n^2\right)\mathbf{W}\cdot\nabla_t(\nabla_t\cdot\mathbf{H}_t) - \left(k_0^2 + k_z^2/n^2\right)\mathbf{W}\cdot\mathbf{H}_t\right\}dA = 0 \tag{A5}$$

applies to the whole region A. On an element-by-element basis one may write

$$\mathrm{R} = \sum_e \mathrm{R}_e = 0 \tag{A6}$$

$$R_e = \iint_{A_e} \left\{ (1/n^2)(\nabla_t \times \mathbf{W}) \cdot (\nabla_t \times \mathbf{H}_t) - (1/n^2)\mathbf{W} \cdot \nabla_t (\nabla_t \cdot \mathbf{H}_t) - (k_0^2 + k_z^2/n^2)\mathbf{W} \cdot \mathbf{H}_t \right\} dA$$

(A7)

Provided $\mathbf{H}_t$ and $\mathbf{W}$ are continuous functions across inter-element boundaries, the line integrals due to such interfaces will cancel and need not to be included in Eq.(A7). The function $\mathbf{H}_t$ can be expanded within an element e as:

$$\mathbf{H}_t^e(\mathbf{r}) = \sum_{j(e)} H_j g_j^e \mathbf{N}_j^e \tag{A8}$$

where $j(e)$ signifies edge elements relating to the element e but counted on a global basis, while $\mathbf{N}_j^e$ are the vector interpolation functions. The constant g_j^e is introduced in order to impose the periodic constraints of Eq.(A3), as shown later. In the preferred weighted residual option, the weightings are selected from the interpolation functions

$$\mathbf{W}_i^e = c_i^e \mathbf{N}_i^e \tag{A9}$$

where the c_i^e are arbitrary constants. In this case the element residuals Eq.(A7) may be represented in matrix form by

$$\mathbf{R}_e = \mathbf{S}_e \mathbf{H}_e - \mathbf{T}_e \mathbf{H}_e - k_z^2 \mathbf{U}_e \mathbf{H}_e \tag{A10}$$

where the column vector $\mathbf{H}_e$ corresponds to $H_{j(e)}$. Assuming n^2 is constant within an element and given c_i^e and g_j^e the local matrix elements

$$S_{ij}^e = \frac{c_i^e g_j^e}{(n^2)^e} \iint_{\Omega_e} (\nabla_t \times \mathbf{N}_i^e) \cdot (\nabla_t \times \mathbf{N}_j^e) d\Omega \tag{A11}$$

$$U_{ij}^e = \frac{c_i^e g_j^e}{(n^2)^e} \iint_{\Omega_e} \mathbf{N}_i^e \cdot \mathbf{N}_j^e d\Omega \tag{A12}$$

$$T_{ij}^e = k_0^2 (n^2)^e U_{ij}^e \tag{A13}$$

are readily evaluated. Note that by choosing the edge elements as a vector interpolation function, the second term of the integrand in Eq. (A7) is zero, *i.e.*,

$$\nabla_t \cdot \mathbf{N}_i^e = 0 \tag{A14}$$

The constants c_i^e and g_j^e are specified so as to be consistent with the boundary and interface rules:

a) If edge $l(e)$ lies on an internal element boundary, c_l^e and g_l^e are chosen such that for any element e' sharing the edge l, $c_l^e = c_l^{e'}$, $g_l^e = g_l^{e'}$, otherwise the continuity of $\mathbf{W}$ and $\mathbf{H}_t$ is violated. A value of $c_l^e = 1$, $g_l^e = 1$ may conveniently be chosen for such edges and also for edges not shared by any other element.

b) If $l(e)$ is an edge for which $\mathbf{H}_t$ is prescribed ($\mathbf{H}_t = 0$ here), $c_l^e = 0$ is chosen to satisfy the requirement $\mathbf{W} = 0$ at that edge.

c) If $l(e_0) = l_0$ represents an edge at (x_0, y_0) on a periodic boundary (corresponding to geometric part 1 in Figure A.2.1), there is an edge $l(e_1) = l_1$ at $(x_0 + \Lambda_x, y_0)$ on the corresponding periodic cell closure (geometric part 2 in Figure A.2.1). In that case, Eqs. (A4), (A5) and (A9) show that $c_{l_0}^{e_0} = 1$ and $c_{l_1}^{e_1} = \exp(ik_x\Lambda_x)$ must be used in Eqs. (A11) and (A12) relating to the second edge. In a similar way, from Eq. (A4) $g_{l_0}^{e_0} = 1$ and $g_{l_1}^{e_1} = \exp(-ik_x\Lambda_x)$. Finally, the unknown variable H_{l_1} is set equal to H_{l_0} thereby eliminating it from the system of equations.

Note that it is required in the above discussion that the finite element mesh at periodic boundary pairs is identical. Figure A.2.2 shows such a mesh for the typical slab 1-D photonic crystal of chapter 5.

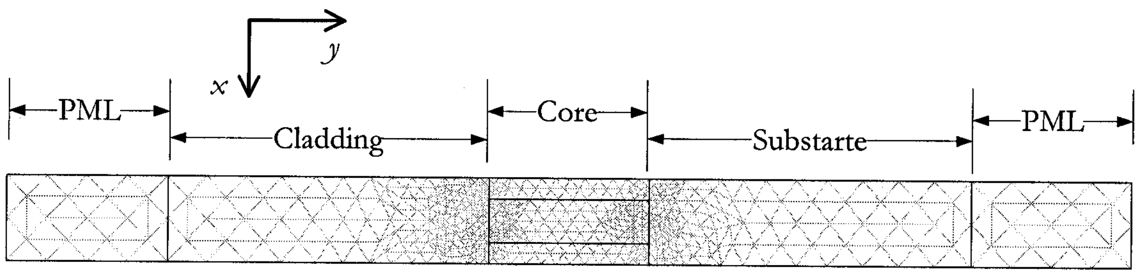

Figure A.2.2 A typical mesh for slab 1-D photonic crystal of chapter 5. The mesh density is lower than the practical one.

Summing the individual element residuals (Eq. (A10)) as in Eq. (A6) now amounts to a procedure which, element by element and edge by edge, assembles the global matrix equation

$$\mathbf{R} = \mathbf{SH} - \mathbf{TH} - k_z^2\mathbf{UH} = 0 \tag{A15}$$

where $\mathbf{H}$ is the column vector of the unknown nodal (H) values, ready for treatment as an eigen equation to solve for k_z^2 given k_0 and k_x

A.3 Perfectly matched layer (PML) boundary condition

Modeling of open problem space with FEM was at first done by truncating the computational window and imposing an artificial electric wall around it, a technique which as with the FD method gives erroneous results for waveguides operating near cut-off.

It can be shown that if we define ∇_t in the absorbing layer as

$$\nabla_t = \hat{\mathbf{a}}_x \frac{\partial}{\partial x} + \hat{\mathbf{a}}_y \alpha_y \frac{\partial}{\partial y} \tag{A16}$$

where α_y are parameter associated with the PML boundary condition. PML parameters have to be determined such that the wave impedance of the PML layer placed at the top and the bottom of the computational domain is exactly the same as that of the adjacent medium inside the computational domain. Hence, the PML medium will perfectly matches the computational domain medium which will allow the unwanted wave to leave the computational domain freely without any reflection. This necessary condition can be derived as [6]

$$\alpha_y = \frac{1}{1 - i\dfrac{\sigma_e Z_0}{k_0 n^2}} = \frac{1}{1 - i\dfrac{\sigma_m}{k_0 Z_0}} \tag{A17}$$

where $Z_0 = \sqrt{\mu_0/\varepsilon_0}$ is the characteristic impedance of vacuum while σ_e and σ_m are the electric and magnetic conductivity of the PML region, respectively. In the PML medium, if we let conductivity as a constant and define,

$$\alpha_y \equiv \frac{1}{s_y}, \; s_y = s_r - is_i \tag{A18}$$

Then for the plane wave propagating with wave number $k_r + ik_i$ propagating in the y direction, the wave attenuates as

$$\exp\left(-[s_i k_r + s_r k_i]\Delta y\right) \tag{A19}$$

And propagates as

$$\exp\left(i\left[s_r k_r - s_i k_i\right]\right) \tag{A20}$$

In the absence of evanescent wave ($k_i = 0$), the wave propagates with the wave number of $s_r k_r$, which results in approximately the same requirement on the mesh density outside of the PML.

In the PML medium, a parabolic profile is also commonly used for the conductivities, so [6]

$$\alpha_y = 1 + i\frac{3(\Delta y)^2}{2k_0 n d^3}\ln R_t \tag{A21}$$

where d is the width of PML , Δy is the distance from the beginning of PML and R_t is called the theoretical reflection coefficient at the PML-computational domain interface, which is set to a very small value during the simulations (say 10^{-10}).

For PML the definitions of matrix elements (Eqs.(A11) through (A13)) will not change, except for S_{ij}^e in Eq.(A11) which will be modified as below

$$S_{ij}^e = \frac{c_i^e g_j^e \left(\alpha_y^e\right)^2}{\left(n^2\right)^e} \iint_{\Omega_e} \left(\nabla_t \times \mathbf{N}_i^e\right)\cdot\left(\nabla_t \times \mathbf{N}_j^e\right) d\Omega \tag{A22}$$

where α_y is assumed to be constant through each element.

A.4 A Numerical result

Consider the known case of slab 1-D photonic crystal with the parameters depicted in Eq. (5.35) and repeated here.

$$\begin{aligned} &n_{\text{clad}} = 1,\ n_{\text{sub}} = \sqrt{2},\ n_{\text{core}} = \sqrt{12},\ \lambda = 1537.4 \text{ nm} \\ &\Lambda = 265\,\text{nm},\quad a = \tau\Lambda = \Lambda/2 = 132.5\,\text{nm},\ b = 500\text{nm} \end{aligned} \tag{A23}$$

Figure A.4.1 shows the unit cell with the convention of this appendix.

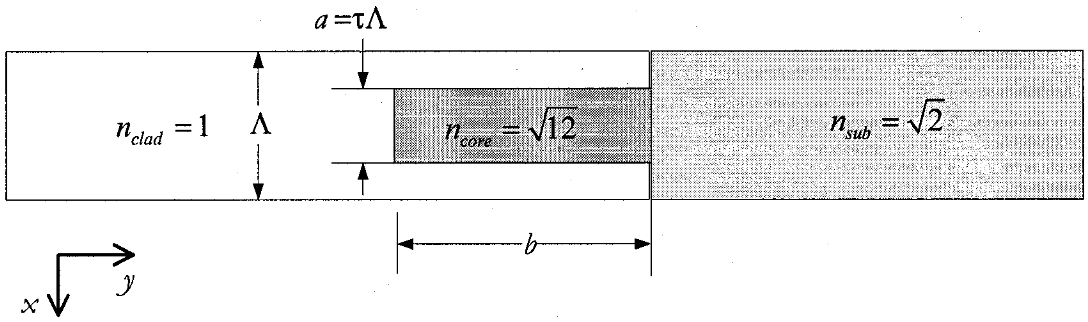

Figure A.4.1 a unit cell of slab 1-D photonic crystal with definition of some parameters.

We assume the cladding and substrate width of 1μm. If we want the wave attenuation (presumably plane wave) after 1 μm of PML layer reaches to 10^{-3}, then

$$s_i = \frac{\ln \alpha_{\mathrm{PML}} \times \lambda}{2\pi \Delta y_{\mathrm{PML}}} = \frac{3 \ln 10 \times 1.5374}{2\pi \times 1} = 1.69$$

Assuming the same value for s_r, then if we assume 10 elements per wavelength in the PML layer, the maximum element size in PML layer is

$$\frac{\lambda}{s_i 10 n} = \frac{1.5374}{1.69 \times 10 \times \sqrt{2}} \approx 64\,\mathrm{nm}$$

Under these conditions, Figure A.4.2 shows the magnetic field profile at $k_x = 0$ (resonance) and $k_x = \pi/\Lambda$ (anti-resonance) at the wavelength of $\lambda_{10} = 1537.40$ nm. The normalized wave vector in the z direction was obtained as $n_z = 2.303$ and $n_z = 0.230$ for resonance and anti-resonance cases respectively.

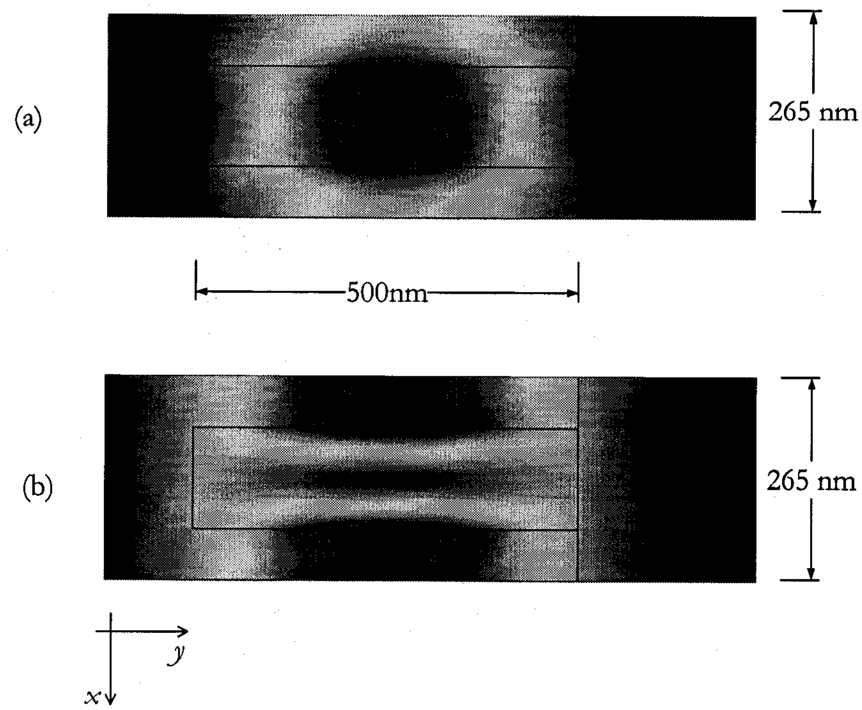

Figure A.4.2 The Total magnetic field of (a) resonant case $k_x = 0$, and (b) anti-resonant case $k_x = \pi/\Lambda$ over one period

Note the shift of magnetic field concentration at resonance and anti-resonance case. Although the method is very accurate however, it suffers from the existence of non-physical modes (spurious). Usually for each obtained eigen-value, one has to check the modal profiles to be sure that the obtained mode is physical.

A.5 Discussion and suggestions for further studies

In following, we will discuss some other aspects of the formulation and suggestions for further research on this topic.

As it is mentioned earlier, there are two equivalent methods to implement periodic boundary conditions and Flouqet's theorem in FEMs for analyzing periodic structures.

- Implicit method, which uses the conventional Helmholtz equation and apply Flouqet's theory with new parameters in interpolating functions, leads us to an eigen value equation of Eq.(A15), in which all matrix coefficients **S**, **T** and **U** ar e qu adratic functions of Flouqet wave number β_x [1]. If we want to calculate the wave vector diagram (k_z versus k_x at constant k_0) we need to determine all matrix coefficients **S**, **T** and **U** repetitively in every steps of the calculation.
- Explicit forms utilizing Bloch eigenvectors as a workable variables leads us to matrix coefficients which is independent of Flouqet wave number[2]. The following Bloch eigen mode is introduced

$$\boldsymbol{\Psi} = \exp(ik_x x)\mathbf{H}_t \tag{A24}$$

where $\boldsymbol{\Psi}$ is a periodic function in x direction, *i.e.*,

$$\boldsymbol{\Psi}(x, y) = \boldsymbol{\Psi}(x + \Lambda, y) \tag{A25}$$

The proper differential equation corresponds to Eq. (3.1) can be obtained by modifying the gradient operator as

$$\nabla_t \to \nabla_t + ik_x \hat{\mathbf{a}}_x \tag{A26}$$

and changing variable to Bloch eigen mode. More study is needed to find similar eigen value equation as of Eq. (A15). This approach has not been implemented yet using edge elements.

Technically specking, using absorbing layers of any kind at the structure boundaries makes the whole structure lossy. As a matter of fact, if we put them too close to the waveguide boundaries, then they will cause significant aberration of the field. Furthermore, using absorbing layers makes finding accurate cutoff wave number virtually impossible. True cutoff wave number will be obscured by the uncertainty, which exists in the contribution of absorbing layer in the imaginary part of obtained eigen values. This uncertainty will be magnified considering the fact that in vicinity of the cutoff, there is a little field confinement. The situation will be worse where there is little refractive index contrast. In this circumstance, band structure through cutoff (in our case through band gap region) is impossible using absorbing layers.

Alternatively, one can search for proper asymptotic physical boundary conditions. They have been implemented successfully for the single dielectric waveguide [7]. Using the radiation conditions, it is well known that the far field expression for electromagnetic waves exhibits the following form

$$F \sim \frac{\exp(ik_r\rho)}{\sqrt{k_r\rho}} \tag{A27}$$

where $k_r = \sqrt{(k_0 n_0)^2 - k_z^2}$ is the transversal wave number and $\rho = \sqrt{x^2 + y^2}$. n_0 is the refractive index of the free space in which the far field is propagating. Here we have an infinite array of waveguides with the field phase shifting of $\exp(-ik_x\Lambda)$, between consecutive waveguides. Similarity with the linear antenna array implies that an asymptotic equation for our case may also be found. Since the far field pattern of Eq.(A27) involves unknown eigen value k_z, using it for the boundary conditions causes the eigen value Eq.(A15) to behave nonlinearly. Iterative method is used to solve this nonlinear eigen value equation, however, Mcdougall proposes a method to avoid iteration [8].

References

[1] C . Mias, J. P. Webb, and R. L. Ferrari, "Finite element modeling of electromagnetic waves in doubly and triply periodic structures," *Iee Proceedings-Optoelectronics*, vol. 146, no. 2, pp. 111-118, Apr.1999.

[2] B . P. Hiett, J. M. Generowicz, S. J. Cox, M. Molinari, D. H. Beckett, and K. S. Thomas, "Application of finite element methods to photonic crystal modeling," *Iee Proceedings-Science Measurement and Technology*, vol. 149, no. 5, pp. 293-296, Sept.2002.

[3] Y ariv Amnon and Yeh Pochi, "Electromagnetic propagation in periodic media," in *Optical Waves in Crystals : Propagation and Control of Laser Radiation* Wiley Series in Pure and Applied Optics, 2003, pp. 115-219.

[4] J . Jianming, "Vector Finite Elements," in *The finite element method in electromagnetics,* 2nd ed Willey Interscience, John Wiley and Sons, Inc., 2002, pp. 273-337.

[5] J . P. Berenger, "A Perfectly Matched Layer for the Absorption of Electromagnetic-Waves," *Journal of Computational Physics*, vol. 114, no. 2, pp. 185-200, Oct.1994.

[6] S . S. A. Obayya, B. M. A. Rahman, and H. A. El-Mikati, "New full-vectorial numerically efficient propagation algorithm based on the finite element method," *Journal of Lightwave Technology*, vol. 18, no. 3, pp. 409-415, Mar.2000.

[7] H . E. Hernandezfigueroa, F. A. Fernandez, and J. B. Davies, "Finite-Element Approach for the Modal-Analysis of Open-Boundary Wave-Guides," *Electronics Letters*, vol. 30, no. 24, pp. 2031-2032, Nov.1994.

[8] M . J. Mcdougall and J. P. Webb, "Infinite Elements for the Analysis of Open Dielectric Wave-Guides," *Ieee Transactions on Microwave Theory and Techniques*, vol. 37, no. 11, pp. 1724-1731, Nov.1989.